Nonlinear Optical Enhancement from Aggregate and Ensemble Effects in Organic Systems

by

Jeffery Edward Raymond

A dissertation submitted in partial fulfillment
of the requirements for the degree of
Doctor of Philosophy
(Macromolecular Science and Engineering)
in The University of Michigan
2011

Doctoral Committee:

Professor Theodore G. Goodson III, Chair
Professor James D. Duderstadt
Professor Robert Zand
Associate Professor Max Shtein

Technorods

By Jeffery E. Raymond, 2008

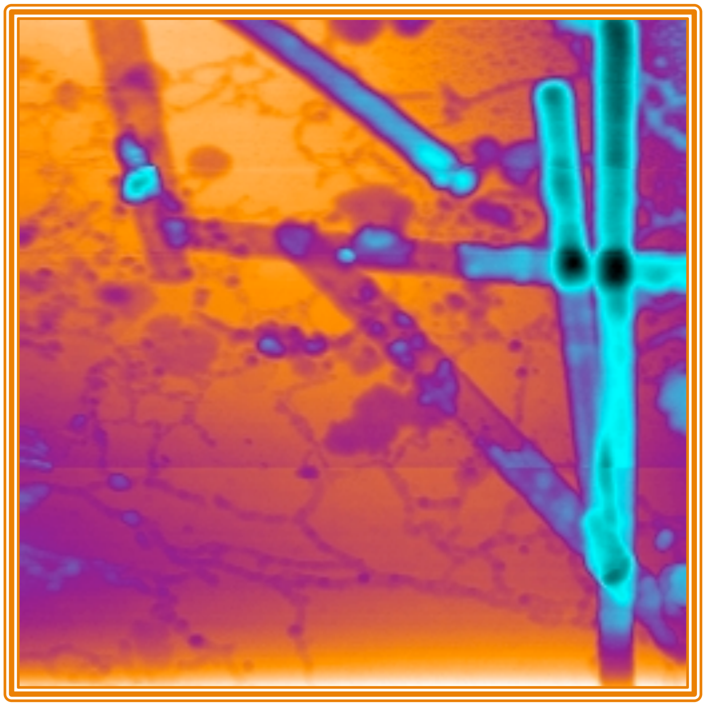

Dedication

To Daniel Anderson, Michael Harris and Jody Sherwood.
Thank you for asking the hard questions and keeping me honest in my answers.

Acknowledgements

This work would not have been possible with out the following individuals: Professor Theodore G. Goodson III, Ph.D. Advisor, for providing a great research environment with many opportunities to perform great science; Professor Robert Zand, Committee Member, Graduate Seminar Mentor, for helping me through the Macromolecular Program; Professor James D. Duderstadt Committee Member, Science Policy Mentor, for opening my eyes to the bigger picture; Professor Max Shtein, Committee Member, for continued discussions on applicability of research. Dr. Oleg Varnavski, Primary Research Mentor, for teaching me ultrafast optics; Professor Ramikrishna Guda, Research Mentor, for helping with mastery of pump-probe techniques; Dr. Ajit Bhaskar, Research Mentor, for helping me get my “sea legs” as a new student and helping me gain mastery in multiphoton spectroscopy; Dr. Zin Seok Yoon, Research Mentor, for helping me laugh in the laboratory; Nonna Hamilton, Program Administrator, for being a wonderful person and giving herself fully to her students; Linda VanBlaircum, Research Administrator, for making all of the little things run smoothly; the following collaborators for making and sharing materials that made this work possible - Professor Robert Twieg - Dr. Augustine Urbas - Dr. Thomas Cooper - Professor Juan Casado - ProfessorKazuya Ogawa - Professor Yoshiaki Kobuke - Professor George Newkome - Professor Julie Biteen - Professor Raoul Kopelman.

Preface

Having spent time in industry, academics, the military and federal laboratories, it has become clear to me that ultimately research is not about disciplines, facts or even publication record. It is about problem solving, diligence, creativity, analysis and communication. This includes communicating with peers and mentors, bosses and staff, in and out of discipline. Specifically, I have found that research, for me, is really about fostering individual relationships with a community of motivated and curious individuals. It is my hope that this body of work displays at least a small portion of all of these attributes.

Table of Contents

List of Figures

List of Tables

List of Appendices

Abstract

Organic optoelectronics provide several advantages over traditional Si based systems. These advantages are typically cost, ease of manufacturing, and environmental impact. One area of particular interest in the field of optoelectronics is that of two-photon absorption (TPA), a nonlinear optical process. In recent years it has become apparent that many dyes can exhibit good two-photon properties. However, attempts to generate further enhancement by self-assembly into nanoparticles has been difficult. This is in large part due to a lack of good optical characterization method for single nanoparticles at resolutions appropriate for determining structure-function relationships on a per particle basis. The work presented here will show organic macromolecular and aggregate systems assembled in such a way as to enhance the nonlinear optical properties orders of magnitude above the constituent building blocks. A focus will be placed on the development of tools appropriate for observing multiphoton response in individual nanoparticles on a single particle basis, namely work done to advance Two-Photon Near Field Optical Microscopy (TPA-NSOM). This discussion will show advances to both two-photon absorption NSOM and two-photon NSOM fluorescence, as well as how these techniques can quantitatively assess per particle and per molecule two-photon enhancement. Additionally, ultrafast excited state behavior of organic nanomaterials will inform us how these enhancements occur. Several systems, including macrocycles which mimic natural light harvesting, liquid crystalline materials, molecular wire arrays and "click" assembled metallated structures will be studied. It will be shown that the self assembly of dimers into macrocycles can enhance the two photon response by two orders of magnitude, dimer assembly into nanoparticles can give a five-fold two-photon enhancement, and that nanorods can be self assembled from marginal two-photon materials into

nanoparticles with a fourty-fold two-photon emission enhancement. The viability of TPA-NSOM for determining single particle TPA response will be displayed for several systems, with optical resolutions approaching 10 nm.

Chapter 1

Introduction

1-1 Document Scope

This document is in keeping with the Rackham Graduate School requirements for a publication dissertation. As such, the majority of the experimental details, background material, references and findings are presented directly in the following chapters as part of the authors published and 'in press' body of work. In addition to the minimum requirements of this format, some additional material will be presented for consideration in this work. A discussion of the inputs and outputs of the analytical methods used and how to interpret data from these techniques, included as they are introduced at the beginning of each chapter. A discussion of the capabilities of the materials studied as extended to a real world application is provided in appendix C. Unpublished NSOM and TPA-NSOM studies are provided in chapter 8, including an author generated standard operating procedure for performing NSOM with the Veeco Aurora 3 system. In appendix A a technical set of instructions on the operation of a two photon near field imaging system is presented. Additionally, appendix B presents a method for the generation of near field scanning optical microscope probes for two photon applications.

1-2 Two Photon Background

While the technical details of two-photon spectroscopy are presented extensively in chapters 2, 5, 6, 7 and 8, it is also important to understand the history and development of two-photon spectroscopy. Göppart-Mayar [1] predicted in her seminal PhD thesis that two-photon absorption should be possible, and would obey a I^2 power law. However, the intensities and wavelengths required to induce this process were beyond the capabilities of the excitation sources of the era. With the advent of lasers [2], Kaiser and Garret [3] were able to display two-photon absorption in heavy metal salts. in 1961. Much later, Watt Webb [4] pioneered the use of two photon dyes for use in two-photon scanning confocal microscopy. Today, with the commercial availability of pulsed turn-key laser systems, two-photon imaging is one of the more prevalent optical *in situ* bio-imaging techniques [5].

1-3 Near Field Imaging Background

The far field diffraction limit (~wavelength/2) for light was proposed originally by Raleigh in 1872 [6]. Shortly after, Abbe [7] proposed a theory on image formation which described what type of images could be produced optically while also outlining the physical requirements for obtaining images at higher resolutions. In 1928, Singe proposed the first near field optical imaging system based on Abbe's criterion [8]. Near field imaging was first displayed in 1972 using RF light to image features with a resolution of wavelength/20, overcoming the far field diffraction limit by a full order of magnitude [9]. However, the first near field image to be produced using visible wavelength light was published by Pohl et. al. at IBM laboratories in 1982 [10]. Several companies now produce commercially available NSOM systems, largely as modular options for other

Near field scanning optical microscopy (NSOM) is a technique where the aperture for light delivery is within a few nanometers of the sample and has a diameter much smaller than the wavelength of the light used. The technical aspects of NSOM are detailed implicitly in chapters 2, 6, 7 and 8, as well as in appendices A and B.

1-4 Solid State TPA and TPA-NSOM

This body of work is concerned mainly with the experimental and empirical determination of organic photonic materials for nonlinear optical (NLO) applications. Two-photon absorption, a NLO process, has been shown to occur readily in a variety of dyes [11]. However, it was still unclear how TPA might be further enhanced through self-assembly into nanoparticles that have superior TPA per molecule when compared to either the solution or bulk phases of a material.

A particular focus of this work is enhancing the two-photon absorption (TPA) of these systems through self-assembled multichromophore interactions. In order to accomplish this goal, the development of a top-down two photon near field optical microscopic (TPA NSOM) technique was required. The implementation, capabilities, operation and instructions on TPA-NSOM probe building for coupling to fs pulsed light can be found throughout this document in chapters 2, 6, 7, 8 and appendices A and B.

While some of the journal articles contained in the following chapters relate to other nonlinear optical properties, such as three-photon absorption (chapter 9) and excited state absorption (chapters 10 & 11), the bulk of this work is focused on two-photon enhancement from self assembled nanomaterials and, even more specifically, single particle enhancement imaging where TPA-NSOM is employed.

1-5 Highlights from TPA-NSOM Studies

TPA-NSOM of Organic Nanowires. In chapter 2 [12], a liquid crystal donor-pi-acceptor is self assembled into 1-D organic nanorods. *TPA-NSOM will be shown to be able to resolve fluorescence signals with resolutions less than 30 nm*. This allows for the direct investigation of individual nanorods and results in the discovery that TPA enhancement is only observed from the outer surface (~30 nm) of a 250 nm rod where a 10-fold TPA emission enhancement was observed. This TPA-NSOM finding allowed for a well informed decision to assemble smaller rods and resulted in a lower aspect ratio 60 nm nanorod where all of the molecules in the structure could be seen to have enhanced TPA emission. *This study shows that aggregation induced TPA enhancement and investigation by TPA-NSOM resulted in a material that had 40 times more TPA emission per molecule than the individual molecules in solutions.* A follow up study (chapter 8) displays, through one photon absorption NSOM, that a Pt-core analog of the liquid crystal rods is capable of having enhanced nonlinear optical properties as well.

TPA-NSOM of Porphyrin Nanoparticles. Chapters 3, 4 and 5 [13-15] display the bulk two-photon enhancement which can be achieved through the selective self-assembly of porphyrin dimers in to macrocycles which mimic naturally occurring light harvesting complexes. *Through ultrafast investigations, it becomes clear that the coupling of S1 and S2 bands between chromophores is the primary cause of TPA enhancement near two orders of magnitude over the individual dimers.* Of the two investigated macrocycle species, it will be shown that the fluorene bridged dimer (chapters 3 & 4) have much stronger TPA enhancement through ensamble effects. *The 19-mer macrocycle detailed in chapter 3 had the largest single molecule TPA cross-section at the time of publication (1 million GM).* The 19-mer could not be effectively self assembled further into stable particles; however, the dimer could be reliably converted into 160 nm nanoparticles (chapter 6). The intent was to generate at least some of the enhancement observed in the macrocycle, even if the regular ordering of chromophores the macrocycle allowed for was lost [16]. *Through TPA-NSOM alone, per particle TPA was obtained and a 5-fold enhancement was found to exist in the particles when compared to the lone dimer in solution. This study also provided the highest resolution optical absorption images to be published, with edge resolutions approaching 10 nm.*

Developing TPA-NSOM Standards. The absorption TPA-NSOM detailed in chapter 6 needs no standard, as change in intensity is the only signal needed to evaluate the absolute per particle TPA response. In contrast, emission TPA-NSOM requires a well known TPA standard, just as emission based TPA measurements do. *To that extent, chapter 7 shows the systematic development of a TPA-NSOM standard (Rhodamine labeled nanoparticles) with which to quantitatively analyze individual particles for absolute per particle TPA response [17].*

TPA-NSOM of Synthetic Peptide Plaques. In chapter 8, TPA-NSOM is used to show how individual nanoplaques of sythetic peptides can be compared, despite having virtually identical AFM profiles and particle sizes.

TPA-NSOM of Gold Nanofilms. Also in chapter 8, TPA NSOM is used to characterize holes in a gold film with sizes on the order of 100 nm. Two photon near field transmission and reflection imagining is used to show the continuation of light through the subdiffraction holes despite a strong two photon absorption by the film.

TPA-NSOM of Silver Microdendrites. The final study presented in chapter 8 is an ongoing work where plasmonic self assembled silver microdendrites can be shown to emit brightly by TPA-NSOM. *TPA-NSOM is then used to determine the exact source of the emission, a silver oxide coating which is plasmonically enhance by simultaneously targeting the underlying silver plasmonic band with two photon excitation and the silver oxide two photon excitation band.* This is in spite of silver oxide being a very weak TPA material with virtually no emission. TPA-NSOM of nanoscale structure in the microdendrite was then used to determine that the emission was enhanced further through oxidation of the non-radiative regions.

Other Work Related to Multichromophore NLO Processes. Not directly related to the TPA-NSOM that is the focus of this manuscript, several other investigation have been made by the author and have been included for completeness. In chapter 9 [18] a small organic molecular wire is shown to be capable of three-photon fluorescence (3PA). Through steady state and ultrafast studies, this 3PA will be found to be due to virtual state stabilization similar to the S1 stablization of TPA introduced in chapters 3 and 4. In chapter 10 [19], longer molecular wires are seen to have ultrafast excited states that have very fast charge recombination (<1 ps). Chapter 11 [20] displays a self-assembled mixed metal macrocycle and, through ultrafast transient investigation, reveals that the material has a photoswitching lifetime of ~10 ps and possesses highly efficient energy transfer at longer times.

Other Work Relating to NSOM. Again, while not directly related to the TPA-NSOM that is the focus of this body of work, several studies related to regular NSOM imaging are also presented for completeness. In chapter 8, a standard operating procedure is given for the Veeco Aurora 3 NSOM system. Three additional studies are also provided: surface emission from gold-azide nanoparticles, core-interface emission from silver-stilbene nanoparticles and enhanced absorption from Pt-core liquid crystal nanorods.

1-6 Overarching Theme

Through a combination of TPA-NSOM, bulk TPA, ultrafast and steady state techniques it will be shown that TPA enhancement is possible through self assembly in the nanoregime. Through repeated assessment of individual particles via TPA-NSOM, per particle and per molecule TPA cross-sections will be shown to be enhanced through these self-assembly processes. The superior resolution of TPA-NSOM will be shown conclusively to be one of the most viable tools for assessing the structure-function relation ship of individual particles and features at the nanoscale.

1-7 References

(1) Göppert-Mayer, M. Ann. Phys. 1931, 401(3), 273-294
(2) (a) Gould, G. 1959, The Ann Arbor Conference on Optical Pumping, the University of Michigan, pp. 128 (b) Maiman, T. Nature 1960, 187, 493-494
(3) Kaisar, W.; Garret, C G.B. Phys. Rev. Lett 1961, 7, 229–231
(4) Denk, W.; Strickler, J.H.; Webb, W. W. Science 1990, 6, 73-76
(5) Rubart, M. Circ. Res. 2004, 95, 1154
(6) Raleigh, L. Notes of the Royal Astrological Society 1872, 33 , 59-63
(7) Abbe, E. Arch. mikrosk. Anat. Entwichlungsmech. 1873, 9, 413-468
(8) Synge, H.; Phil. Mag. 1928, 6, 356
(9) Ash, E.; Nicholls, G. Nature 1972, 237, 510
(10) Pohl, D.; Denk, W.; Lanz, M. Appl. Phys. Lett. 1984, 44, 651
(11) Makarov, N.; Drobizhev, M.; Rebane, A. Opt. Express 2008, 16(6), 4029
(12) Raymond, J.E.; Ramkrishna, G.; Twieg, R.J.; Goodson, T. J. Phys. Chem. Lett. 2008, 112(21), 7913
(13) Raymond, J.E.; Bhaskar, A.; Goodson, T.; Makiuchi, N.; Ogawa, K.; Kobuke, Y. J. Am Chem. Soc. 2008, 130(51), 17212
(14) Raymond, J.E.; Yoon, Z.S.; Donehue, J.E.; Kazuya, O.; Kobuke, Y.; Goodson, T. Adv. Func. Mater. 2011, invited paper, to be published in Q4 2011
(15) Raymond, J.E.; Yoon, Z.S.; Yotsutuji, T.; Ogawa, K.; Kobuke, Y.; Goodson, T. J. Phys. Chem. Lett. 2011, submitted
(16) Raymond, J.E.; Goodson, T. J. Phys. Chem. Lett. 2011, 2(4), 329

(17) Raymond, J.E.; Goodson, T. Proc. SPIE 2009, 7413(0Y), 1

(18) Raymond, J.E.; Casado, J.; Navarrete, J.T.L; Takimiya, K.; Goodson, T. J. Phys. Chem. Lett. 2011, 2, 2179

(19) Raymond, J.E.; Yoon, Z.S.; Casado, J.; Navarrete, J.T.L; Takimiya, K.; Goodson, T. ACS Nano 2011, submitted

(20) Raymond, J.E.; Yoon, Z.S.; Newkome, G.; Goodson T. Chem. Sci. 2011, submitted

Chapter 2

Two Photon Enhancement in Organic Nanorods

2-1 Original Publication Information

This chapter was originally published as the following document:

> "Two Photon Enhancement in Organic Nanorods"
>
> Jeffery E. Raymond, Guda Ramakrishna, Robert J. Twieg, and Theodore Goodson.
>
> *The Journal of Physical Chemistry C*, **2008**, *volume 112,* issue 21, pp 7913-7921.

Modifications to the original document are cosmetic and used only to conform the format of this document or provide uniformity of enumeration.

2-2 Qualifying Statement

In this study, liquid crystal donor-pi-acceptor molecules will be used to generate nanorods where two-photon action cross sections are 40 times larger per molecule than the solution phase materials. TPA NSOM will be shown to be able to differentiate the less viable structures and inform the author on how to adjust assembly to obtain large cross section increases. Steady state, two photon, NSOM and TPA-NSOM will all be introduced in this chapter.

Ultraviolet-Visible Absorption Spectroscopy. Often abbreviated as UV-vis spectroscopy, ultraviolet-visible absorption spectroscopy is one of the most common spectroscopic techniques available. A white light source (often a Xenon lamp) is used to probe a liquid solution of sample and solvent, resulting in the extraction of wavelengths which are appropriate for electronic excitation in the material. These wavelengths relate to allowed electronic transitions in the material when it is in its ground state. While this technique can be displayed as a transmission spectrum, it is more often displayed as an absorption spectrum. This absorption spectrum is a function of the material's inherent absorption at a given wavelength and the amount of material interacting with the light (often relayed in terms of concentration and path length). Response obeys the following equation, referred to as the Beer's-Lambert Law.

$$A = -\log(I/I_0) = -\log(T) = \varepsilon \bullet \ell \bullet c \qquad \text{(I.)}$$

Where A is absorption, I is observed intensity, I_0 is incident intensity, T is transmission (also defined as I/I_0), ε is the molar extinction coefficient at the wavelength incident, l is the path length and c is the concentration in molarity of the solution.

The metric of import here is the molar extinction coefficient, and it is often expressed in unit of $M^{-1}cm^{-1}$. It represents allowed electronic transitions in a material from the ground state and hence a promotion of an electron from a given principle quantum number (n) to some higher quantum number (n+m). When interpreting these spectra for organic chromophores, the reddest major peak observed is often assigned to a $\pi \rightarrow \pi^*$ transition and the UV peaks are taken to represent $\pi \rightarrow \sigma^*$ transitions. While this is not a rule, it is a good starting point. Often UV-vis spectra are a bit more ambiguous when the species in question is a metal-ligand complex or a macromolecule. The presence of a metal complex or multiple chromophores often leads to molecular orbital splitting and the broadening of absorption regions. The actual energy absorbed in UV-vis spectroscopy can be taken as the energy difference between the starting orbital of the excited electron and the orbital it is promoted to. Fine features can sometimes be observed in the absorption spectra as well, often the result of classically disallowed electronic transition being partially allowed through coupling to an allowed state. We will see in several of the following publications that interband coupling is critical to the enhancement of nonlinear optical processes and these disallowed "dark states" are often electronic transitions with high two photon cross sections. Detection of the absorption in UV-vis is done through a diffraction grating and usually uses a photodiode (PMT) or charge coupled device (CCD).

Fluorescence Spectroscopy. A bit of a misnomer, most fluorescence spectroscopy is actually measuring all emission processes in a given wavelength range after photoexcitation. Two forms of fluorescence spectra are possible with the majority of fluorometers: emission spectra and excitation spectra. Emission spectra are the most common type of data encountered, where a white light source (often a Xenon lamp) is reduced to a single wavelength by way of a diffraction grating. A second diffraction grating, orthogonal to the first, in front of a photocathode selectively scans through a range of wavelengths and a spectrum for sample emission is generated, usually in units of photons counted. For most commercial fluorometers a known collection efficiency can be used to relate the counts observed to the total photons emitted. Similarly, higher end fluorometers are capable of giving you the total intensity of the light of excitation. This, combined with a known absorbance for the excitation wavelength, can provide the total photons absorbed. The ratio of these two values, photons emitted/photons absorbed, is known as the fluorescence quantum yield (ϕ_F). While emission from UV-vis excitation is typically from a single band relaxation, usually $S_1 \rightarrow S_0$, it is also possible to observe more complicated phenomena. This includes processes like phosphorescence ($T_1 \rightarrow S_0$) and multiband emission from molecules which have multiple emission modes from higher lying singlet states relaxing spontaneously to a ground state. Quantum yields, through integration, can be reported for any of these emission processes or for all of them combined. Emission quantum yield change and emission peak shift are some of the most common spectroscopic techniques for determining a change of environment for an emissive species. Quantum yield is always a function of wavelength and is often very sensitive to changes in sample concentration, pH, and temperature.

Two Photon Spectroscopy. Multiphoton spectroscopy, seen in this body of work, is the use of an ultrafast fs pulsed excitation source to drive a coherent excitation process in a chromophore or semiconductor to generate an excited state through the simultaneous absorption of two (or more) photons. As the excited state targeted is often observed as an absorption band in the visible range, most two-photon spectroscopy occurs in the NIR region. In the following chapters, the technique of particular interest is the two-photon excited fluorescence method (TPEF) in which emission spectra are obtained from two photon absorption and a two photon cross section is calculated. This technique requires that one know the fluorescence quantum yield of the investigated material as well as the quantum yield and two photon cross section of a TPA reference standard. Two photon cross sections are reported in units of $cm^4s/photon$. These units may seem a bit non-intuitive. However if one considers incident light on a substance as a plane wave, at any given point there will be an area of interaction, occurring twice in TPA, per photon incident with seconds tracking the time in which the interaction may occur. Typically this cross section is reported in units of GM (Geoppert-Mayer) where 1 GM = 10^{-50} $cm^4s/photon$. Spectra for two photon cross sections are often presented as pure cross sections or as action cross sections. An action cross section is a measure of two photon emissivity and is just the product of the fluorescence quantum yield and the pure two photon cross section. Two photon absorption is a nonlinear process where the absorption is related to the incident intensity squared, and can be thought of readily as the probability of a virtual state occurring from photon matter interactions cross the probability of the virtual state interacting with a second photon during its lifetime and being promoted to a real excited state. The author feels it is critical to point out some common errors in the TPEF measurement. First, it should be noted that the confidence of this measurement can only be as high as the confidence in the reference material. Secondly, quantum yield measurements can often have uncertainties of 10-20% (or higher) and any measurement based on these will suffer in accuracy accordingly. Thirdly, and perhaps the author's greatest concern, is the presumption that one photon steady state quantum yields are the same for two photon processes may not be an apt assumption. All together, this has led to different groups reporting cross sections for the same material that often vary by as much as an order of magnitude. This is addressed in chapter 5. However, the author also feels that the repeatability is still higher than the other conventional method of two photon cross section measurement (the z-scan method) in which a focal point is rastered through a material and absorption is measured. This is due to the z-scan method's low signal to noise ratio, the need to know implicitly the beam pulse quality, the geometric assumptions that have to be made in order to calculate the cross section and the non-TPA absorption (like ESA) which must also be removed from the signal.

Near Field Scanning Optical Microscopy. Near field scanning optical microscopy (NSOM, or sometimes SNOM) is a scanning probe microscopy technique where one simultaneously collects atomic force microscopy (AFM) and near field optical signal. The near field region for optical processes is the volume within just a few nanometers of the surface in question. While several near field optical techniques exist, this body of work will focus on just the pulled fiber method of NSOM. In brief, one photon NSOM uses a metallated single mode fiber optic cable, tapered and brought to within 1-2 nm of a surface. An excitation source is coupled into the fiber and is emitted onto the surface through an aperture in the fiber tip (often cut through the metal), which is typically 30-300 nm in diameter. The benefit of NSOM to other optical microscopies is that it has innate hyper resolution well below the normal diffraction limit of far field imaging and is restricted not by the wavelength of the excitation source, but the size of the aperture. The theoretical resolution of this type of illumination is one half of the aperture size. Collection is done by PMT and can be the result of fluorescence, absorption or scatter depending on the filter set selected. Collection can be done via top down collection through an aperture focused on the bottom of the sample or by overhead collection where an objective for collection is focused on to the top of the sample.

Shear Force Atomic Force Microscopy. AFM (topography) signal is acquired through non-contact mode shear force AFM. This type of collection requires the probe to be connected to an oscillator, often a quatz tuning fork, with induces a nanometer scale dither in the probe tip. The tip, when brought to a surface, will come to rest near the onset of van der Waal force interactions and software will instruct it to seek out a particular degree of attraction or repulsion. The tip will then adjust its height to have this uniform force regime when scanning across a surface, generating a height profile image. After each dither the probe adjusts its height depending on the force feed back which is felt on each pass of the surface. Typical AFM resolutions in this mode of operation are 2-3 nm in the x-y (depending on the amplitude of the oscillator) and <1 nm in z direction.

Two Photon NSOM. Unlike normal NSOM which is used to investigate one photon processes, two photon NSOM (TPA NSOM) requires a significantly higher flux to obtain meaningful data. This means that coated probes are not useful for this application as any metallation of the tip results in burning of the probe near the aperture. TPA NSOM must then include the use of special probes, whose manufacture are detailed in Appendix 2 of this work. In short, the probes must be pulled and attached to an oscillator such that the probe can maintain <1 nm proximity to the surface, withstand constant a constant influx of fs pulsed light (GW peak power) and also supply enough near field light at the aperture to trigger two photon processes. Collection modes are as that of one photon NSOM, though the filter sets are different. The signal collected by PMT for these images are counts per second.

2-3 Abstract

The nonlinear optical response in one-dimensional organic nanorods of N,N-dimethyl-4−4((4-(trifluoromethylsulfonyl)phenyl)ethynyl)aniline (DMFSPA) was investigated to probe the long-range interactions in the nanocrystals on the microscopic level. Differences in the linear and nonlinear optical properties are shown for two different morphologies of these organic crystals as well as for the chromophore in solution. The optimized nanocrystalline suspension had more than an order of magnitude increase in the two-photon excited fluorescence when compared to the solution phase of DMFSPA at similar chromophore densities. The one and two-photon properties of the nanocrystals and bulk crystals are compared by near-field scanning optical multiscope imaging. The images also provide insights into the formation of the nanorods during initial crystallization, changes in the optical response of the system with time, and the viability of these and similar

nanomaterials for consideration in solid-state organic device applications. In addition to providing an imaging regime by which to assess this and other solid-state nanocrystalline organics, our investigation provides a simple and elegant method for enhancing the nonlinear optical response of organic materials by transition to nanoscale morphologies, without the need for additional chemical modification or synthesis.

2-4 Introduction and Background

Many methods have been investigated for the generation of nanowires and nanorods from inorganic materials [1], while fewer avenues remain available for the formation of nanoscale solids consisting of purely organic materials. This detracts from the number of applications organic materials might be used for and limits the degree to which an organic fluorophore may be tuned without chemical modification to the molecule. It has recently been shown that small donor-π-acceptor molecules can be readily formed into one-dimensional (1D) nanocrystals via a simple, two-solution regime [2]. We show here that a rigid organic charge-transfer molecule, N,N- dimethyl -4–4((4-(trifluoromethylsulfonyl)phenyl)ethynyl) aniline (DMFSPA) (figure 2-1a), can be crystallized into either 60 or 250 nm diameter nanorods (figure 2-1b), enhancing the one- and two-photon optical response of the system. The linearity and regularity of the individual rods is an indication of their single crystal nature, primarily 1D growth mechanism and phase stability both in suspension and at ambient atmospheric conditions.

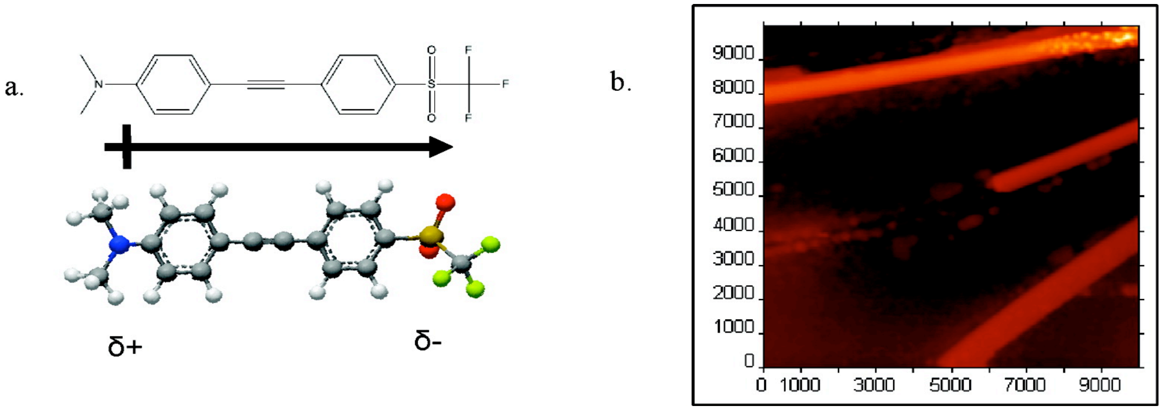

Figure 2-1 Molecular Model and Nanorods of DMFSPA

(a) The charge transfer molecule DMFSPA. (b) AFM image of nanorods from preliminary DMFSPA nanocrystallization. Diameters range from 300–800 nm with aspect ratios near 30. Units are in nanometers

While there are many factors that are important to the enhancement of the two-photon cross-section of a molecule, a system's macromolecular geometry has played a large role in most recent accounts of organic materials assessed for this purpose. Through the use of branched, cyclical, charge-transfer, and two-dimensional organic molecules, it has been shown that a variety of molecular architectures provide reasonable avenues for producing functional nonlinear optical (NLO) materials [3-5]. Two-photon cross-section enhancement in these systems can be attributed to a variety of factors such as extended π-electron systems, bond-order-alternation, exciton delocalization, multidirectional dipole enhancement and control of symmetry [4-8]. Concurrently, increasing exciton hopping and decreasing thermal degradation pathways has been shown to provide enhancement to a materials two-photon excited fluorescence (TPEF) by way of an increased fluorescence quantum yield [5,7-9]. Unfortunately, these materials often require special and sometimes cumbersome synthetic regimes in their generation. In an attempt to gain some of the benefits of these larger architectures and longer range effects, we propose a transition to the solid-state to induce dipole-lattice interaction that will enhance our TPEF. The vast majority of the TPEF studies on these molecular architectures have been done in the solution phase, leaving some question as to their viability for solid-state device applications. We address this by crystallizing a small liquid crystalline organic charge-transfer molecule from the solution phase into nanorods, thereby providing a regime by which any linear donor-π-acceptor molecule might see its NLO properties enhanced and its potential for application increased. In contrast to a general decrease in fluorescence normally seen in bulk crystals, a drastic TPEF increase was seen in the resultant nanorod suspension that appears to function by a different route than typical J-type aggregate response.

Enhancement of the TPEF of rigid organic donor-π-acceptor molecules by increasing their intermolecular electronic interactions in the nanoscale solid state, producing high local fluorophore concentrations and increased dipole moments, makes this type of nanorod particularly attractive for a large number of applications [3-6]. Solid-state TPEF is often diminished when compared to the fluorescence of a solution phase D−A fluorophore if crystal dimensions are on the order of magnitude of tens of microns or larger. This happens for a variety of reasons, such as reabsorption, reflection, diffraction, etc. However, for crystals with dimensions at the nanoscale, many of these issues are minimized or eliminated altogether.

In this paper, we report a system that shows increased quantum yield and two-photon cross-section upon formation of nanorods in suspension. While the electronic structure and excited states of similar molecules have been investigated previously [6,8,9], the solid-state TPEF enhancement of these systems has not been shown or imaged. The nanorod samples were imaged by a near-field scanning optical multiscope (NSOM), allowing for topographical imaging by atomic force microscopy (AFM). Fluorescence was simultaneously observed qualitatively by near-field fluorescence optical microscopy (FNSOM) and near-field two-photon fluorescence microscopy (TPA NSOM)

2-5 Experimental Section

Crystallization

The crystallization of all samples was done by addition of a tetrahydrofuran (THF) solution of the molecule to water under ambient conditions. For the 60 nm diameter rods, 100 µL of a 407 µM THF solution was added to 4.9 mL of water, generating a suspension with a chromophore density of 8.14 µM. In the case of the 250 nm diameter rods, 400 µL of a 102.9 µM THF solution was added to 4.6 mL of water, generating a suspension with a chromophore density of 8.13 µM. Magnetic stirring occurred for one minute on addition of the THF solution. No precipitation was observed and filtration was not used.

NSOM Sample Preparation

Solutions and suspensions were applied dropwise to acid-cleaned glass slides in a spin coater. Samples were then subsequently subjected to vacuum for 3 min to remove all solvent.

Imaging

Images were obtained by use of a CDP MoScan NSOM multiscope. All AFM images are from noncontact mode. All NSOM and fluorescence images have excitation wavelength given. All image collection wavelengths (where applicable) are at 560 nm. Scales are given in nm.

Steady-State Measurements

All compounds were used as received without further purification. Measurements on solutions were carried out in spectroscopic grade tetrahydrofuran (THF) purchased from Sigma-Aldrich. Measurements on suspensions were carried out in THF/water mixtures (ratios are indicated). All water used was ultrapure (type I) from a Millipore filtration system. For the time dependent quantum yield study, absolute quantum yield was not obtained and only relative values are given.

Two-Photon Absorption Cross-Section Measurement

To measure the two photon absorption cross-sections, we followed the TPEF method. The details of the lasers and optical setup have been described elsewhere

[10]. A 117 μM Coumarin 307 (Acros Organics) solution in methanol was used as the reference for the entire study. Quadratic dependence of TPEF intensity on input intensity was ensured at every wavelength. Two-photon cross-sections are calibrated to account for sensitivity of the photomultiplier tube (PMT) at the collection wavelengths of both the standard and the samples.

2-6 Steady State Properties

For organic charge-transfer aggregate systems, there is a tendency to refer to the systems studied in terms of there photochemical response, even when implicit crystallographic information has been obtained. The standard model used for these systems was first provided by the historical paper by Kashi et al. [11] and is primarily concerned with two types of interactions in a two molecule system, H-aggregation and J-aggregation. This description of associative dimerization provides a general method for assessing the intermolecular electronic interactions effect on absorption and emission properties of the system. The H-aggregate model assumes that the dipoles associate in a side-to-side manner and is often characterized by stronger π−π interactions, blue-shifted excitation, and a decreased fluorescence response due to excitation to a nonemissive triplet state. In contrast, J-aggregate behavior is characterized by a head-to-tail dipole association, and its strongly enhanced dipole moments lead to greater exciton delocalization, red-shifted excitation, and an increased fluorescence response for the system. While this is a good starting point for discussion of aggregate systems, it cannot and should not be used to implicitly describe aggregate systems of many molecules. Rather, it is more useful to use these models for description of extended dipole network behavior. Crystalline structures, by their very nature, demand some component of both types of interaction for these materials, and one cannot readily isolate response to a two molecule system. Therefore, it is more appropriate to discuss the H-type and J-type response of the system, keeping in mind that the system under investigation by necessity possesses both types of interactions, and that these descriptions are purely in reference to electronic transitions of the system governed by both short and long-range interactions.

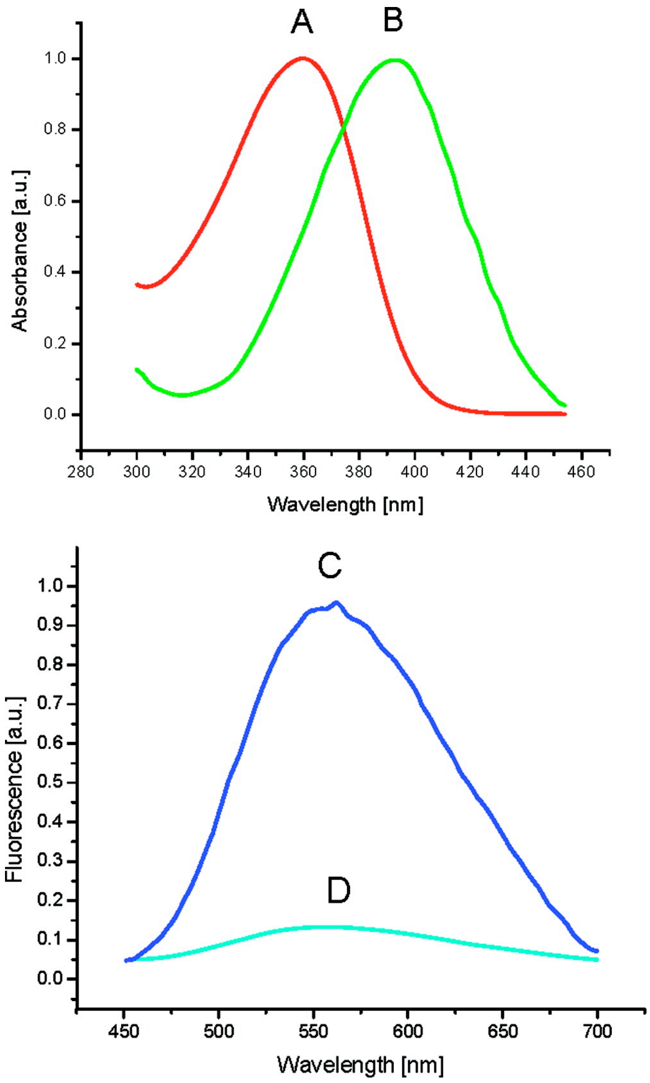

Figure 2-2. Steady State Absorption and Emission Spectra for the Suspension and Solution Phase DMFSPA

(A) Absorbance for 250 nm rod suspension in 8% THF. (B) Absorbance for solution phase. (C) Fluorescence intensity for 250 nm rod suspension in 8% THF. (D) Fluorescence intensity for solution phase.

The optical absorption and fluorescence results for the DMFSPA solution and a nanorod suspension are given in figure 2-2. Similar absorption intensities for the two samples stand in sharp contrast to the large fluorescence enhancement in the suspension sample. As will be discussed later, this is primarily due to a 10-fold increase in the quantum yield upon nanocrystallization. Both sets of spectra are normalized to the larger peak for clarity and have concentrations of 12.4 μM. The shift in the absorption maxima from 394 nm for the solution to 364 nm for the nanorod suspension would typically imply the generation of a nonemissive H-type aggregation response.

Falling within the general umbrella of aggregation-induced emission (AIE) [12-15], this sort of response is characterized by a dual emissive kinetic model in which the lattice interactions with the molecule allow a generally nonemissive excited triplet state to readily transition to a more emissive state [14, 15], making H-type absorption response in the system potentially more fluorescent than J-type response. Several organic systems have been shown to exhibit this type of 1P response, showing increased AIE with transition to smaller and smaller crystals.

Morphologies in nanoscale charge transfer systems depend on solvent selection, molecular architecture and dipole number/strength. For rigid donor-π-acceptor systems like ours, with accessible regions of aromatic groups, there is little chance that aggregate structures could be formed purely from π−π stacking or from dipole−dipole interactions alone. It is therefore necessary to think of DMFSPA nanorods, as mentioned above, as possessing both H-type and J-type character simultaneously, though certainly from a photochemical perspective one may be seen to dominate. Though a strict evaluation of the implicit crystal structure for the nanocrystalline and bulk materials studied is beyond the scope of the study presented here, it should be noted that other linear charge transfer molecules displaying primarily H-type excitation still possess a dipole dominated growth mechanism and have been shown by X-ray diffration to possess dipoles primarily oriented in the direction of growth [13, 16, 17]. This is presumed to be the case for our systems and is supported to a degree by imaging presented later in this study.

In addition to the local environmental enhancement generated by a regular array of dipoles, our molecule possesses a “rotorlike” component in its dimethylaniline donor group. Other studies on AIE have shown that locking the rotation of such groups in D–A systems where small organic molecules have assembled in suspension give increased fluorescence response [12,15,18-19]. This effect is attributable to (1) a decrease in the availability of nonemissive excited-state vibrational relaxation and (2) a more rigid architecture that allows the donor electron pair to more fully contribute to charge transfer in the molecule.

The gross increase in emission intensity and blue-shift in absorption for the nanorods studied, when compared to the solution, is an indicator that there is greater exciton delocalization, generation of a triplet state accessible lattice induced emissive state, and lower opportunity for thermal degradation of the excited state in the nanocrystalline phase molecules. A complete overlay of the absorption/emission data shows that the bulk, nanorod, and solution phase samples show clearly that each sample possesses a different excitation and relaxation regime that we attribute to differing intermolecular interactions.

2-7 Time-Dependant Quantum Yield Measurements

A significant change in absorption spectra, emission intensity and, consequentially, quantum yield was seen during the growth of these nanostructures with efficiency closely tied to THF concentration and suspension age. Figure 3-3 shows the absorption spectra over time for two different solutions with relative quantum yields at pertinent times for the processes listed. The sample that generated the 60 nm rods, 2% THF, shows a lower loss of ε and η from aging than that of the 250 nm rod sample. The quantum yield from the 8% THF, 250 nm rod sample increases from 42% of maximum initially to a maximum efficiency at 3 min. The quantum yield of the 250 nm rod suspension then decreases significantly to a value of 19% of maximum 30 min after formation. In contrast, a maximum quantum yield is seen in the 60 nm rods at 1 min with constant and less dramatic decrease in quantum yield over time giving a quantum yield of 73% of maximum after 30 min.

From these results, it can be taken that lower concentrations of “good” solvent, THF, allows for faster crystallization and longer retention of higher quantum efficiency nanocrystals. The images shown in Figure 2-4 display a complimentary aging study of the suspension by NSOM/AFM. Observing the rods five minutes after crystallization onset (figure 2-4a, b and c), it is clear that the nanorods are single crystals with diameters of 250 nm and lengths greater than several microns. The NSOM image (figure 2-4b) shows the presence of metastable “protorods” having spherical structures with diameters of approximately 60 nm. On several of the rods, these spheres can be seen attached to the rod ends, confirming a 1D growth mechanism requisite of rodlike morphologies at these scales. Further aging shows reduction in these “protorods” and continuous rod−rod aggregation. Note that, though the individual rod dimensions remain the same, the rod−rod aggregation size increases continually during this time. The TPA NSOM image displayed for the youngest sample (figure 2-4c) was generated by 840 nm excitation. By its very nature, the TPA NSOM image of these systems is limited by the TPA cross-section, quantum yield of the sample, and the quadratic relationship between 2P fluorescence and incident light intensity. Typical TPA NSOM imaging is performed on samples with cross-sections that are 2 to 3 orders of magnitude greater than the 250 nm rod samples with features sizes several times larger than the diameter of the observed rods. Despite these factors, the clear contrast at the rod locations is further indication of this systems robustness for evaluating organic two-photon fluorescent nanomaterials and correctly correlating emission with specific morphologies and nanostructures within a sample. The rods appear to bundle with advancing age, while the basic morphology and dimensions of the rods do not change, implying no further change in crystal structure and that the rod−rod aggregation is largely a surface−surface interaction between rods. Over time, it can be seen that the loss of quantum efficiency can be attributed to the aggregation/bundling of the rods with each other and not additional growth of the crystals or transitions to different morphologies.

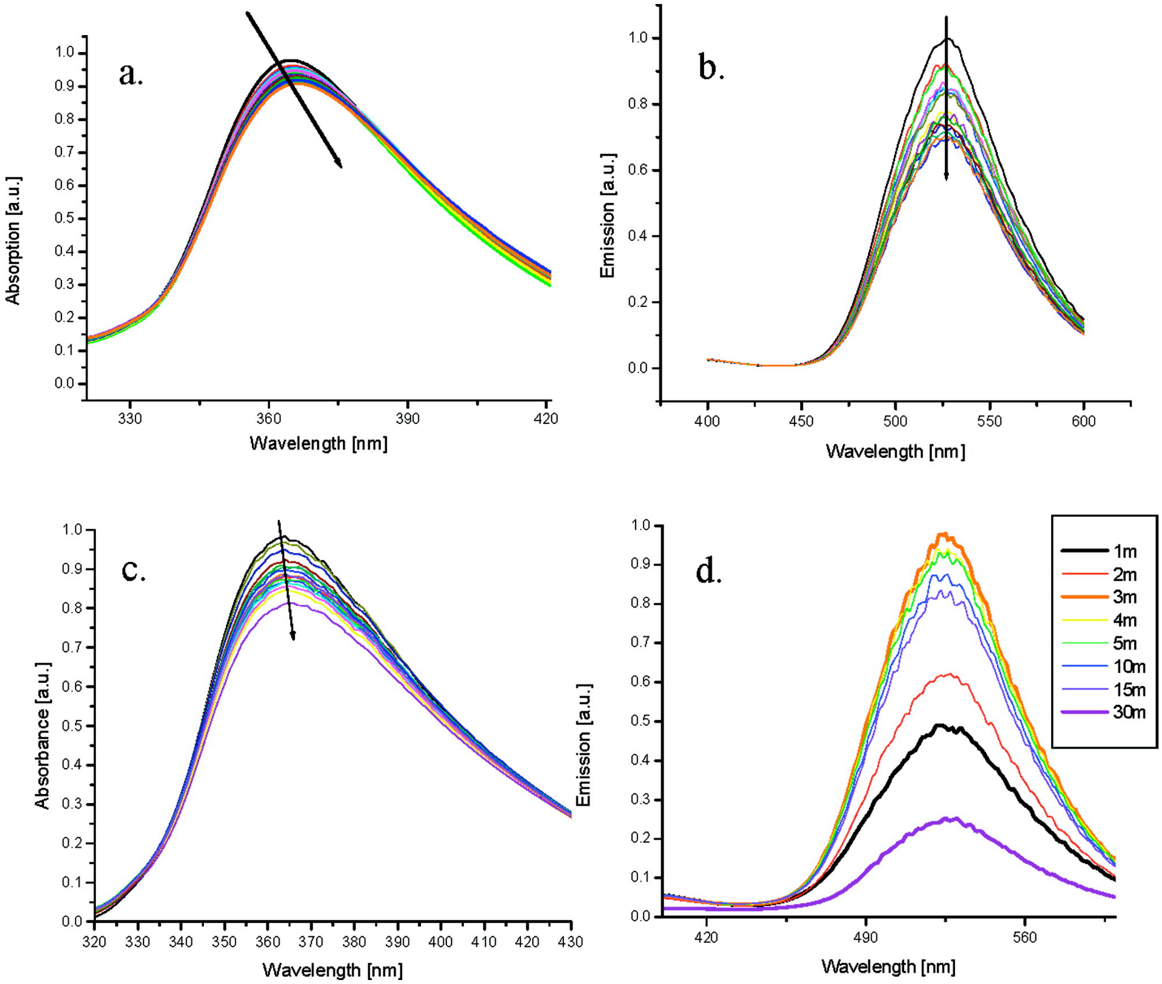

Figure 2-3. Absorption and Emission Spectra for the Two Characterized Rod Samples Aging Over 30 Minutes

(a) Absorption, 60 nm rods. (b) Emission, 60 nm rods. (c) Absorption, 250 nm rods. (d) Emission, 250 nm rods.

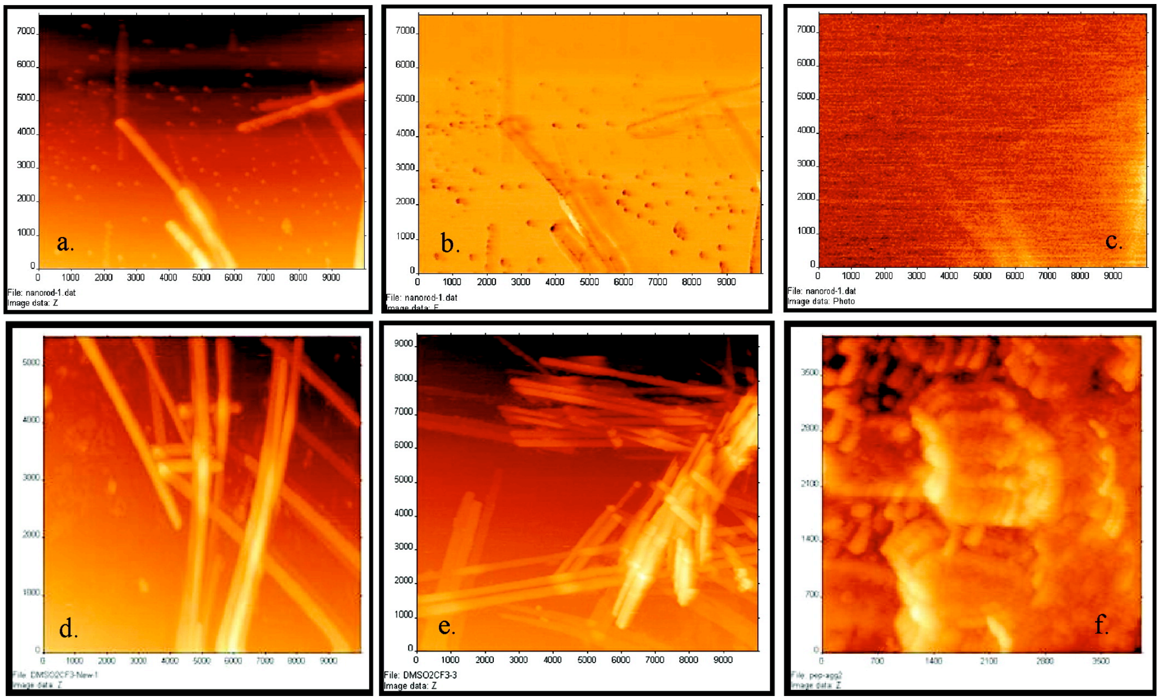

Figure 2-4. Quantum Yield Time Study Images

(a) AFM, (b) NSOM, and (c) TPA NSOM images of a 250 nm rod sample 5 min after crystallization. Subsequent AFM images of the same sample (d) 30 min, (e) 4 h, and (f) 48 h after crystallization. Scales are in nm.

2-8 Two-Photon Measurements

Two-photon excited fluorescence is a third order nonlinear process in which the fluorescence intensity is related quadraticly to the excitation intensity. The two-photon cross-section is therefore a higher order analog to the single photon absorption phenomenon related to the molar extinction coefficient of a material. Two-photon absorption benefits from being a process that uses less energetic photons and is typically enhanced by processes that increase a species' quasi-excited-state lifetime and allow for greater exciton delocalization.

Table 2-1. Spectra Peaks for Sample DMFSPA Systems

Sample	1P Absorption Maximum	1P Emission Maximum	1P Stokes Shift	2P Absorption Maximum	2P Emission Maximum	Change in Emission; 1P →2P
THF Solution	394 nm	560 nm	166 nm	845 nm	540 nm	20 nm
250 nm Rods	364 nm	560 nm	194 nm	840 nm	530 nm	30 nm
60 nm Rods	364 nm	560 nm	194 nm	835 nm	525 nm	35 nm

To fully assess the TPEF enhancement seen in the nanocrystalline samples, it is critical to characterize the molecule in solution as well as in the nanorod suspensions. Table 2-1 provides a summation of the absorption and emission spectra for the samples studied and shows a two-photon emission maximum near 525 nm for the 60 nm rod sample. This is a 35 nm blue-shift from the 1P emission. In contrast, the absorption maximum for the excited state allowed in the 2P excitation is lower energy than the 1P allowed excitation. These findings are in keeping with the dual emissive kinetic model, showing that the allowed 1P transition and 2P transitions are different but are provided similar lattice-induced energy levels that make a typically nonemissive excited state emissive [13,20]. The TPEF blue-shift is diminished in the larger rod sample with the 250 nm rods having a 30 nm emission blue-shift and the solution phase, giving only a 20 nm shift. This type of effect has been seen in other organic aggregate systems [12,13,18,20,21] and implies an increased Coulombic interaction of the molecule with its environment, which is the crystal lattice of the nanorod in the rod samples. This means that the two-photon emissive state is even more energetic for the rods and is closer in energy to the initial excited-state than in the solution. A summary of the TPEF materials investigated is given in table 2-2 and details the TPEF enhancement in the suspension in an implicit manner. For our most emissive sample, the 60 nm rods, the emission was enhanced close to 40 times that of the solution phase per chromophore.

Table 2-2. Optical and Nonlinear Optical Properties for the DMFSPA Samples

Sample	Solution Phase	250 nm Rods	60 nm Rods	60 nm Rods, Aged
Solvent	THF	23:2 Water to THF (8%)	49:1 Water to THF (2%)	49:1 Water to THF (2%)
Concentration	9.23 μM	8.23 μM	8.14 μM	8.14 μM
Sample Age	n/a	5 minute	5 minutes	48 hrs
ε ($mol^{-1}cm^{-1}$)	$2.02 * 10^4$	$2.00 * 10^4$	$6.34 * 10^4$	$0.74 * 10^4$
η	0.006	0.056	0.049	0.041
δ (GM)	90	99	419	84
η * δ enhancement	n/a	10.3 times	38 times	6.4 times
Aspect Ratio	n/a	~25	~20	~20

It is important to note that both the quantum yield and the two-photon cross-section for the 60 nm rod sample decrease with aging. From the earlier images shown in figure 2-4, it can be seen that the only difference between the rods at their highest quantum yield and later "ages" is their aggregation level. The rod size and morphology does not change with time, and the material is not chemically changed. Changes in quantum yield and two-photon absorption are therefore largely attributable to the aggregation. The same decrease in optical response seen with crystal defects in larger assemblies (i.e., dislocations, defects, reabsorption, etc.) is emulated by this process. Each point of contact made between rods may then be thought of as a small disturbance, disrupting the same organization that was responsible for the increased optical response of the system. The intermolecular electronic communication that helps to further enhance the dipole of these molecules can be thought of as "quenched" at these contact points, decreasing both quantum yield and two-photon cross-sections as the available avenues for exciton delocalization, as well as increasing the number of thermal degradation pathways through interaction with additional surfaces and a general decrease in the dipole-lattice interactions.

The end result of these enhancements in the 60 nm diameter rods of these molecules is an overall 38 fold increase in the TPEF of this material with the benefits of crystallization decreasing with time. The 250 nm rods also show a considerable increase of 10 times the TPEF of the solution phase. The two-photon emission (figure 2-5a) and cross-section (figure 2-5b) spectra for the 60 nm rod are comparable to the other samples studied with slightly lower emission wavelength for the 250 nm rods and the solution phase molecule. The TPEF enhancement of the rod samples is attributed to further polarization of the molecular dipoles by the regularly ordered and partially charged environment that the nanocrystal provides. The regular network of dipoles induces additional exciton delocalization, increasing the two-photon cross-section marginally for the 250 nm rod samples and grossly in the 60 nm rod samples. The quadratic relationships between the incident and the emission intensity for the 60 nm rods is shown representatively for the samples and as demonstrated in figure 2-5c to confirm the optical process as nonlinear.

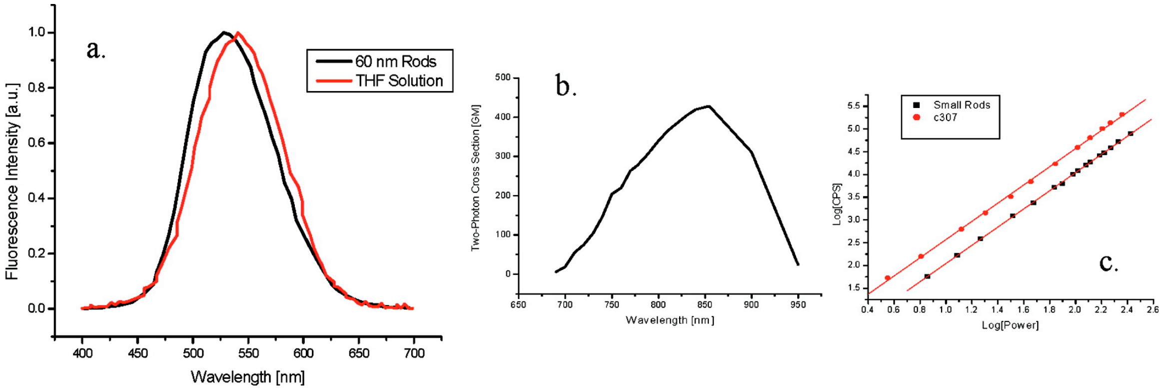

Figure 2-5. Two Photon Response from 60 nm Rods

(a) Two-photon emission spectra contrasting the 60 nm rod suspension to the solution sample. (b) Two-photon cross-section spectra of the 60 nm rod suspension, typical of all samples studied. (c) Graph depicting the quadratic relationship of the 60 nm rod samples two-photon excited emission, dependent on excitation intensity at 840 nm.

A decreased two-photon cross-section is reported for the aged rod sample (table 2-2) in addition to a decrease quantum yield and molar extinction coefficient. As stated previously, we attribute this decrease to excessive aggregation (similar to that shown in figure 2-4f) and solvent trapping in bundle cavities. The 250 nm rod sample has both a lower ε and two-photon cross-section when compared to the 60 nm rod sample, at similar chromophore concentrations. We propose that this enhancement is lower for the 250 nm rods due to a less emissive core. An argument for this will be detailed more fully in the following section.

2-9 Imaging

The viability of use of an NSOM multiscope for confirming our crystallization regime is readily shown (figures 2-1 and 2-4). The NSOM/AFM/TPA NSOM images generated simultaneously provide further confirmation of the curvature of sample features, regardless of depth of field. Although for this study FNSOM and TPA NSOM does not help with dimensional analysis, the contrast between emissive and less emissive materials can be seen. These imaging methods were critical to determining the cause of the quantum yield decrease with time and explaining the differing emission behavior for the two rod samples.

When the incident intensity and collection times for FNSOM imaging of the rods were drastically increased and the excitation intensity was decreased, a stark contrast between the two samples was observed. Noting the images in figure 2-6, we see that the emission from the 250 nm rods comes primarily from the outermost region of the sample, indicated by “edge” illumination. When fluorescence intensities are sampled radically across the rods and compared to integrations for a disk in the 60 nm rod sample and a ring in the 250 nm rod sample. The superimposed integrations use radii and ring thicknesses equal to the penetration depth for this material (31 nm). The comparison shows clearly that there is good correlation between the proposed interaction depth and the actual fluorescence response. Excitation for both images is at 370 nm, and fluorescence collection occurs at 560 nm.

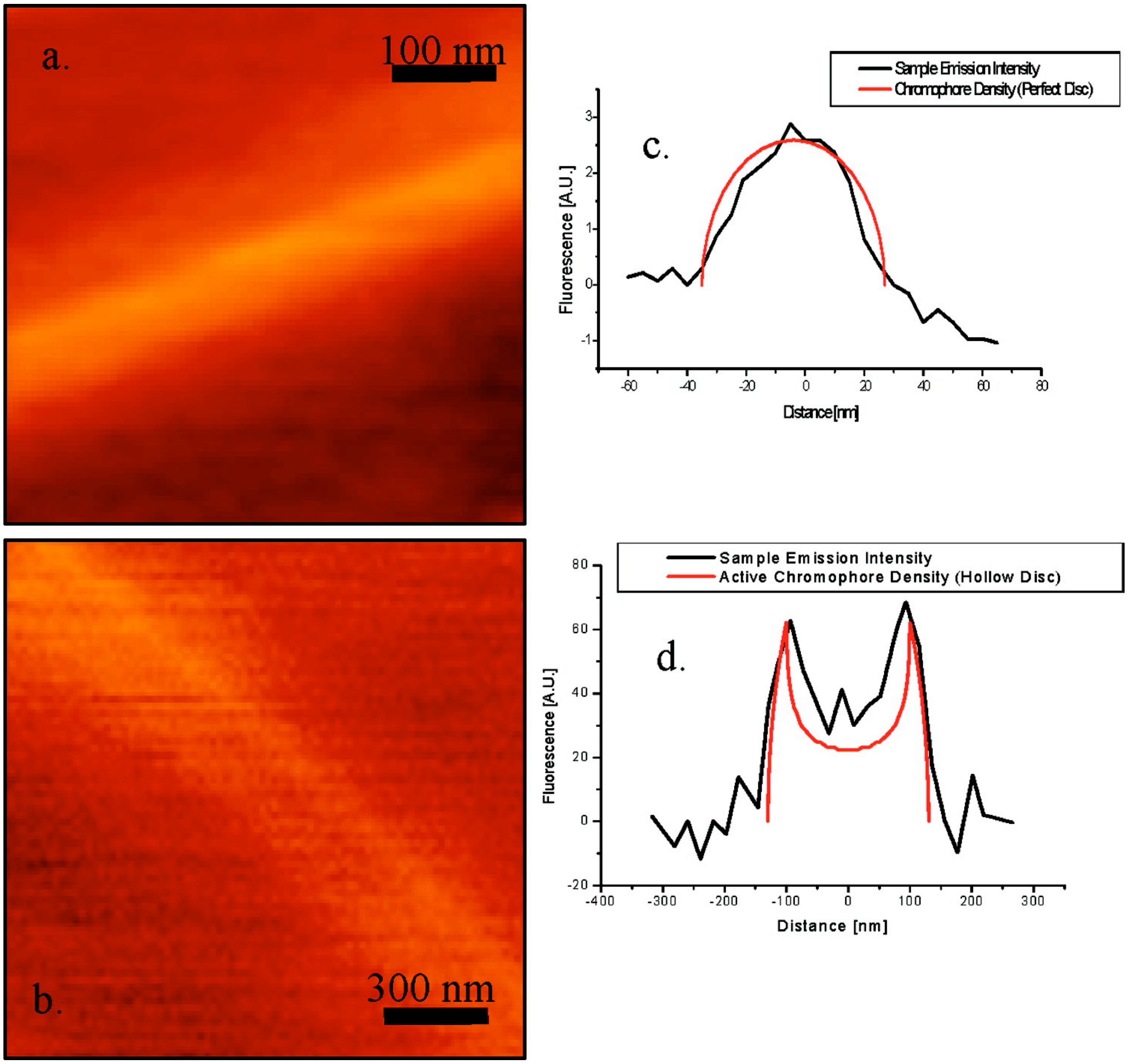

Figure 2-6. Rod Fluorescence Comparison

The 60 nm rod (a) shows a more homogeneous emission. The 250 nm rod (b) shows surface emission, characterized primarily by "edge" illumination. A line graph of the fluorescence intensities for the 60 nm (c) and the 250 nm (d) sample show good correlation to disk and thick ring models, confirming that only the outer region of the 250 rods participate in fluorescence.

Though spectroscopic data indicates a highly aligned nanocrystalline system with strong dipole coupling, an initial study was done to confirm that our system did in fact respond differently to different polarizations of light (figure 2-7). An arbitrary polarization was used for figure 2-7a-2 and a polarization 90° from that was used for figure 2-7b-2. Note that the “top” rod provides the majority of the emission in the parallel (a) image and that the “bottom” rod provides the majority in the perpendicular (b) image. From this, it can be taken that the associated rods have primary dipole moments that are uniform over each rods structure and positioned in opposite directions to each other in real space. Figure 2-7c shows an aged sample in which a rod bundle that appears to be “under” the other structures in the AFM image but provides the highest emission in the FNSOM image. Figure 2-7c,d was taken using a slightly different polarization regime in which emission was first maximized by changing the polarization of the excited light. Figure 2-7c.2 shows the parallel, maximum detection, “on” state for the observed bundle. In contrast, figure 2-7d-2 was taken using light perpendicular to the maximum, giving a “off” response from the bundle. The emission intensity scales have been left for both panels c and d images to show that the bundle emission in panel c is several times more intense than the background intensity. It can also be seen that the bundle intensity of the image in panel d is not detectable above background and that the background for both images are the same.

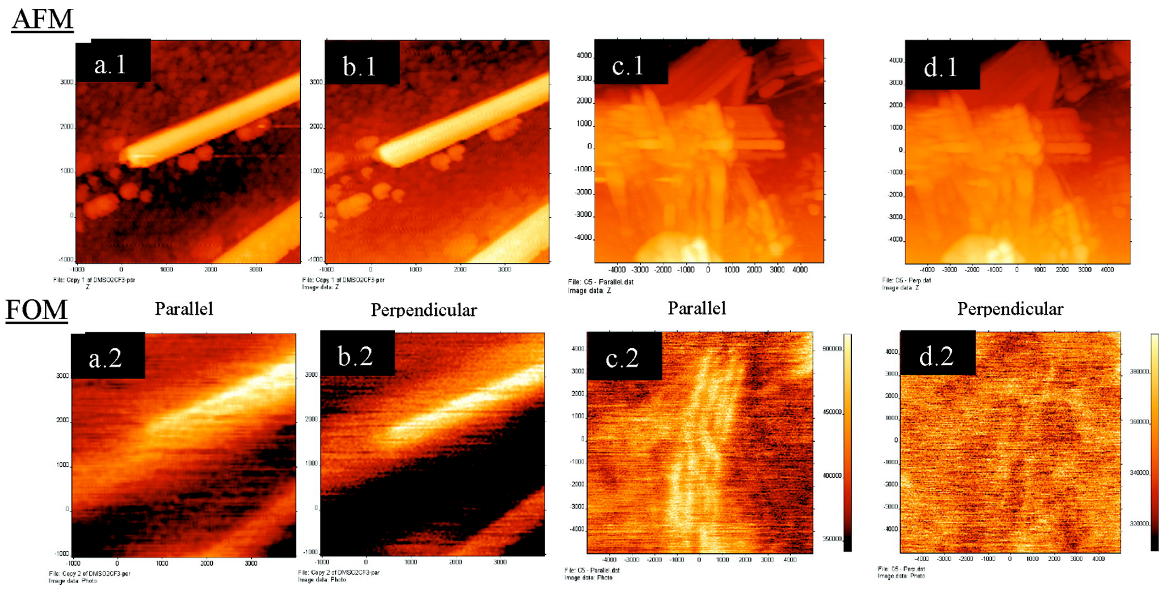

Figure 2-7. Polarized FNSOM Imaging of 250 nm Diameter Rods

Both the AFM image (1) and the FNSOM image (2) for each scan is provided to be certain that the exact same features were imaged in for both polarizations of light. Images (a) and (b) show a two rod system, stacked and off-set as indicated in the AFM image. Images (c) and (d) show a collection of rod bundles formed after 24 h of suspension.

For less regular crystallizations, generating various sizes and morphologies in the resultant crystals, it takes little imagination to anticipate its use in the determination of the most emissive products. This becomes particularly useful when considering materials that display TPA response. The generation of just a few strongly emissive morphologies in the presence of low emission structures may give a false indication of the response of system components that should be evaluated separately. Similarly, self-quenching materials, such as H-aggregates, may induce lower emission in adjacent materials. Figure 2-8 shows a sample that was agitated by sonication during crystallization. This product showed absorption similar to the nanorod samples but displayed only nominal emission. Images of the sample show that the product was a combination of nanorods and spheroids. The FNSOM image shows clearly that the spheres show no emission at the collection wavelength and may in fact be reabsorbing at the detection wavelength.

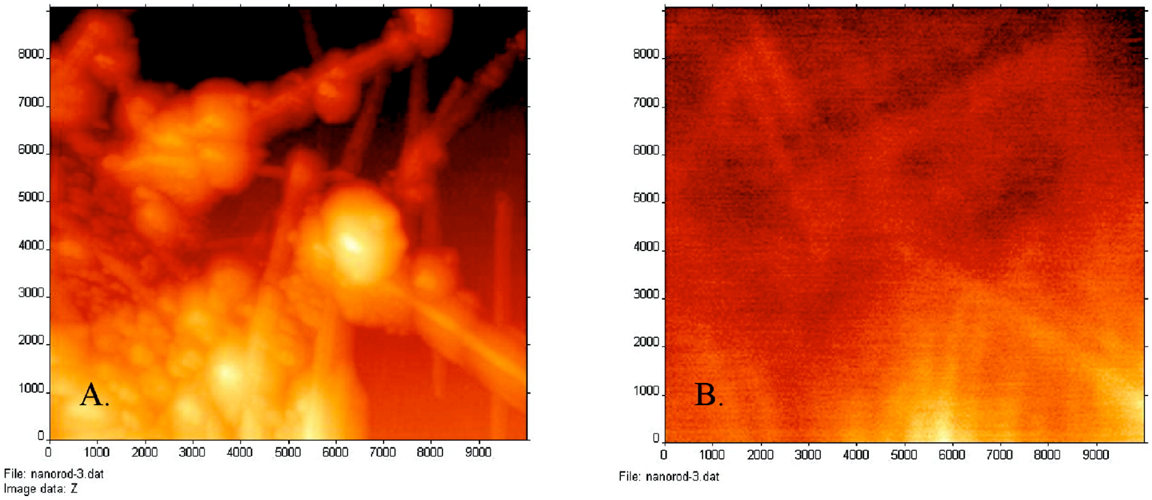

Figure 2-8 Sonicated Rods

The low emission sonicated rod sample shows two general morphologies in AFM mode (A). FNSOM imaging shows that the rod morphologies in the sample remain emissive (B). Negative contrast for areas containing high concentrations of the spherical morphologies show the nonemissive nature of the structures and their ability to inhibit rod fluorescence in their vicinity. Excitation wavelength is 370 nm.

Though the resolution for noncontact AFM is lower than more invasive imaging methods, the images of the 60 nm rod samples (Figure 2-9) clearly show that it is sufficient for resolving crystal features at this scale. Isolation of a single rod indicates that both curvature and dimensions can be resolved using this method for confirmation of nanostructure. Furthermore, it allows the viewing of structures by several complimentary methods simultaneously, ensuring that the same sets of features are being observed both topographically and optically. Resolution of features less than 20 nm can be difficult to obtain and confirm for both noncontact mode AFM and NSOM imaging. Here, the resolution provided by use of longer wavelength near-field optical response allows confident differentiation of structures at this level and provides information critical to correlating morphology to optical response. The structure observed in figure 2-9c was also imaged by TPA NSOM in a manner similar to figure 2-7. However, instead of changing polarization, system input intensity was varied from 5.1 mW (figure 2-8e) to 10.3 mW (figure 2-8f) in two subsequent scans with collection times roughly 50 times longer than in regular FOM. While the background showed an expected increase of roughly two with doubling of the input intensity, the intensity of the rods showed a 3.8 fold increase over background. This was calculated by subtracting the average background intensity from each image and comparing the intensity average along the axis of both rods. These images confirm that the primary mode of excitation occurring is nonlinear and not the result of a linear absorption-emission response; these images are some of the first two-photon images taken of isolated nanostructures that are not deposited in a composite thin film. Further refinement of this and similar imaging systems may make available an entirely new regime by which to study the NLO response of single nanocrystals in isolation.

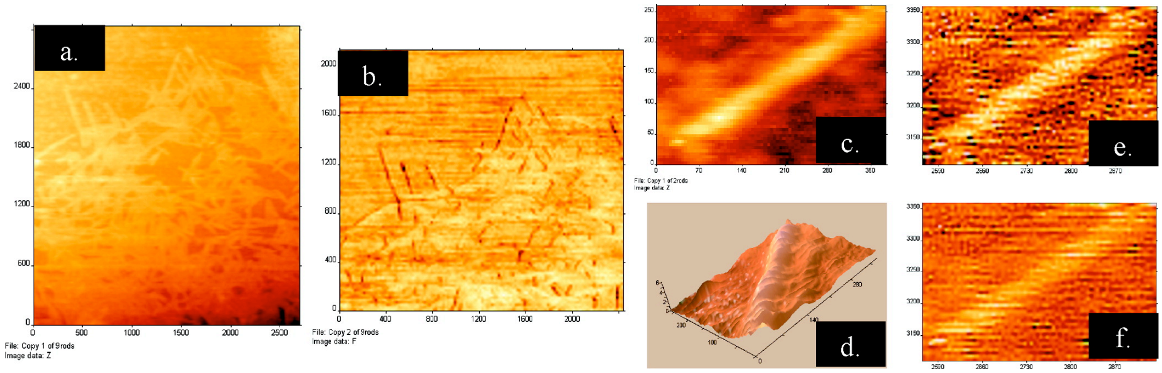

Figure 2-9. TPA NSOM of 60 nm Rods

(a) AFM and (b) NSOM images of a one hour old sample for the 60 nm rod sample characterized. Note that the NSOM image is generated with incident light at the two-photon cross-section maximum of 840 nm. (c) Isolation of a lone rod shows both dimensionality and curvature when the noncontact AFM image is viewed in a three-dimensional rendering (d). The TPA NSOM image of the isolated rod (e) is provides significantly more signal (≈4 times) when twice the excitation intensity is provided (f).

2-10 Conclusion

By generating functionally enhanced NLO organic nanomaterials from a simple two-solvent method, this study opens the way for similar enhancement in other charge transfer systems with little or no additional wet chemistry. The molecular system studied showed unique 1P and 2P fluorescence enhancement on transition to the solid-state, showing absorption and emission properties typical of neither H- nor J-aggregates. The increase in quantum efficiency and two-photon cross-section with properly controlled nanocrystallization leads to a total increase in the TPEF of this material close to one and half-orders of magnitude. In addition to this, the transition to solid state makes this type of sample preparation much more robust for thin-film impregnation applications. This solid-state transition is even more favorable when one takes into consideration that the functional lifetime of imbedded crystalline materials tend to be greater than similar quantities dispersed via solution in a polymer matrix, which is perhaps best exemplified in the difference between liquid crystal impregnated polymers with and without micelle formation [22]. This is particularly true for organic materials that have reactive functional groups, high potential for chelation, are prone to evaporation, or tend to phase separate. The normal drawback of a crystal dispersion, decreased fluorescent response, is therefore eliminated. AFM–NSOM–TPA NSOM imaging for analysis of donor-π-acceptor systems with nanoscale features has been shown in this study to be very illuminating when considering the size and stability of various morphologies.

2-11 Acknowledgements

T.G. would like to thank the Army Research Office for support of this investigation. A special thanks to Professor T. P. Radhakrishnan of the University of Hyderabad for useful discussions surrounding nanoscale aggregation.

2-12 References

(1) Dick, K. A.; Deppert, K.; Larsson, M. W.; Martensson, T.; Seifert, W.; Wallenberg, L. R. Nat. Mater. 2004, 4, 380–384. (b) Kang, Z. H.; Wang, E.; Mao, B. D.; Su, Z. M.; Gao, L.; Lian, S. Y.; Xu, L. J. Am. Chem. Soc. 2005, 127, 6534–6535. (c) Ween, X. G.; Wang, S. H.; Ding, Y.; Wang, Z. L.; Yang, S. H. J. Phys. Chem. B. 2005, 109, 215–220.

(2) Zhang, X.; Zhang, X.; Zou, K.; Lee, C.; Lee, S. J. Am. Chem. Soc. 2007, 129, 3527–3532.

(3) Varnavski, O.; Yan, X.; Mongin, O.; Blanchard-Desce, M.; Goodson, T., III. J. Phys. Chem. C. 2007, 111 (1), 149–162.

(4) Bhaskar, A.; Ramakrishna, G.; Hagedorn, K.; Varnavski, O.; Mena-Osteritz, E.; Bauerle, P.; Goodson, T., III. J. Phys. Chem. B. 2007, 111 (5), 946–954.

(5) (a) Ramakrishna, G.; Bhaskar, A.; Goodson, T., III. J. Phys. Chem. B 2006, 110 (42), 20872–20878. (b) Bhaskar, A.; Guda, R.; Haley, M. M.; Goodson, T. G., III. J. Am. Chem. Soc. 2006, 128 (43), 13972–13973.

(6) Varnavski, O.; Goodson, T., III.; Sukhomlinova, L.; Twieg, R. J. Phys. Chem. B 2004, 108, 10484–10492.

(7) Varnavski, O.; Leanov, A.; Liu, L.; Takacs, J.; Goodson, T., III. J. Phys. Chem. B 2000, 104, 179–183.

(8) Bhaskar, A.; Ramakrishna, G.; Twieg, R.; Goodson, T., III. J. Phys. Chem. C 2007, 111, 14607–14611.

(9) (a) Bhaskar, A.; Ramakrishna, G.; Lu, Z.; Twieg, R.; Hales, J. M.; Hagan, D. J.; Van Stryland, E.; Goodson, T., III. J. Am. Chem. Soc. 2006, 128 (36), 11840–11849. (b) Twieg, R.; Ebert, M.; Jungbauer, D.; Lux, M.; Reck, B.; Swalen, J.; Teraoka, I.; Willson, C. G.; Yoon, D. Y.; Zentel, R. Mol. Cryst. Liq. Cryst. Sci. Technol. 1992, 217, 19–24. (c) Burland, D. M.; Miller, R. D.; Reiser, O.; Twieg, R. J.; Walsh, C. J. Appl. Phys. 1992, 71, 410–417.

(10) Schwahn, D.; Richter, D.; Lin, M.; Fetters, L. J. Macromolecules 2002, 35 (9), 3762–3768.

(11) Kasha, M.; Rawls, H. R.; El-Bayoumi, M. A. Pure Appl. Chem. 1965, 11, 371–392.

(12) Hong, Y.; Dong, Y.; Tong, H.; Li, Z.; Haubler, M.; Lam, J.; Tang, B. Proc. SPIE 2007, 6470, 1–12.

(13) Bhongale, C.; Chang, C.-W.; Lee, C.-S.; Diau, E.; Hsu, C.-S. J. Phys. Chem. B 2005, 109, 13472–13482.

(14) Patra, A.; Anthony, S. P.; Radhakrishnan, T. P. AdV. Func. Mater. 2007, 17, 2077–2084.

(15) Li, Y.; Li, F.; Zhang, H.; Xie, Z.; Xie, W.; Xu, H.; Li, B.; Shen, F.; Ye, L.; Hanif, M.; Ma, D.; Ma, Y. Chem. Comm. 2007, 3, 231–233.

(16) Iyoda, M.; Hasegawa, M.; Enozawa, H. Chem. Lett. 2007, 36, 1402– 1407.

(17) Sonada, Y.; Goto, M.; Tsuziki, S.; Tamoaki, N. J. Phys. Chem. A 2006, 110, 13339–13379.

(18) (a) Tong, H.; Dong, Y.; Hong, Y.; Haussler, M.; Lam, J.; Sung, H.; Yu, X.; Sun, J.; Williams, I.; Kwok, H. S.; Tang, B. J. Phys. Chem. C 2007, 111, 2287–

2294. (b) Patra, A.; Hebalkar, N.; Sreedhar, B.; Sarkar, M.; Samanta, A.; Radhakrishnan, T. P. Small 2006, 5, 650–659.

(19) Tong, H.; Dong, Y.; Hong, Y.; Haussler, M.; Lam, J.; Sung, H.; Yu, X.; Sun, J.; Williams, I.; Kwok, H S.; Tang, B. Chem. Comm. 2006, 2, 1133–1135. Phys. Chem. B 2004, 108, 10484–10492.

(20) (a) Zhang, W.; Cozzolino, A.; Mahmoudkhani, A.; Tulumello, M.; Mansour, S.; Vargas-Baca, I. J. Phys. Chem. B 2005, 109, 18378–18384. (b) Wang, H. Z.; Zheng, X. G.; Mao, M. D.; Yu, X.; Gao, Z. L.; Yang, G. Q.; Wang, P. F.; Wu, S. K. Appl. Phys. Lett. 1995, 66 (1), 2777–2779. (c) Koren, A.; Curtis, M. D.; Francis, A. H.; Kampf, J. W. J. Am. Chem. Soc. 2003, 125, 5040–5050. (d) Qian, Y.; Li, S.; Zhang, G.; Wang, Q.; Wang, S.; Xu, H.; Li, C.; Li, Y.; Yang, G. J. Phys. Chem. B 2007, 111, 5861–5868. (e) Prakash, J. M.; Radhakrishnan, T. P. Cryst. Growth Des. 2005, 5 (5), 1831–1836.

(21) Belfield, K. D.; Bondar, M.; Hernandez, F. E.; Przhonska, O. V.; Yao, S. Chem. Phys. 2006, 320, 118–124.

(22) (a) Schuck, P. J.; Willets, K. A.; Fromm, D. P.; Twieg, R. J.; Moerner, W. E. Chem. Phys. 2005, 318, 7–11. (b) Galvan-Gonzalez, A.; Belfield, K. D.; Stegeman, G. I.; Canva, M.; Chan, K.-P.; Park, K.; Sukhomlinova, L.; Twieg, R. J. Appl. Phys. Lett. 2000, 77, 2083–2085.

Rightslink® by Copyright Clearance Center 6/28/11 3:03 PM

Title:	Two-Photon Enhancement in Organic Nanorods†
Author:	Jeffery E. Raymond et al.
Publication:	The Journal of Physical Chemistry C
Publisher:	American Chemical Society
Date:	May 1, 2008

Copyright © 2008, American Chemical Society

User ID

Password

☐ Enable Auto Login

Forgot Password/User ID?

If you're a copyright.com user, you can login to Rightslink using your copyright.com credentials. Already **a Rightslink user** or want to learn more?

No charge permission and attribution

Permission for this particular request is granted for print and electronic formats at no charge. Appropriate credit should be given. Please print this page for your records and provide a copy to your publisher. Requests for up to 4 figures require only this record. Five or more figures will generate a printout of additional terms and conditions. Appropriate credit should read: "Reprinted with permission from {COMPLETE REFERENCE CITATION}. Copyright {YEAR} American Chemical Society." Insert appropriate information in place of the capitalized words.

Copyright © 2011 Copyright Clearance Center, Inc. All Rights Reserved. Privacy statement.
Comments? We would like to hear from you. E-mail us at customercare@copyright.com

https://s100.copyright.com/AppDispatchServlet Page 1 of 1

Figure 2-10. American Chemical Society Permission to Publish in Thesis

Chapter 3

Synthesis and Two-Photon Absorption Enhancement of Porphyrin Macrocycles

3-1 Original Publication Information

This chapter was originally published as the following document:

> "Synthesis and Two-Photon Absorption Enhancement of Porphyrin Macrocycles"
>
> Jeffery E. Raymond, Ajit Bhaskar, Theodore Goodson, Naoyuki Makiuchi, Kazuya Ogawa, Yoshiaki Kobuke
>
> *The Journal of the American Chemical Society*, **2008**, *volume 130,* issue 51, pp 17212-17213.

Modifications to the original document are cosmetic and used only to conform the format of this document or provide uniformity of enumeration.

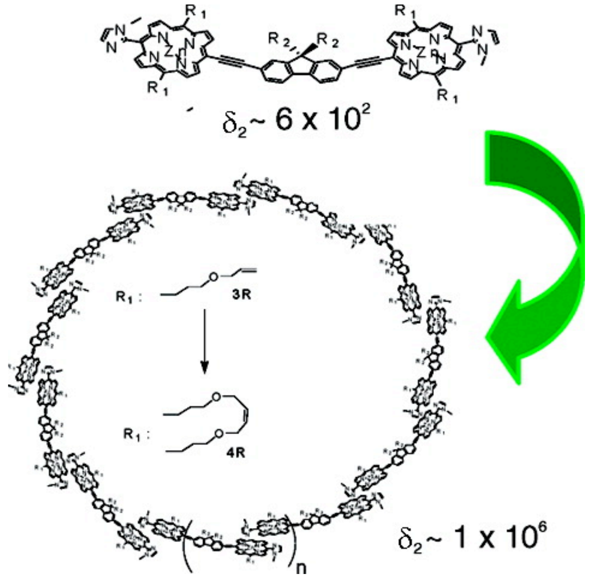

Figure 3-1. Table of Content Image as Published

3-2 Qualifying Statement

In this study a porphyrin dimer will be shown to self assemble into a macrocycle which mimics natural light harvesting systems. This results in a two-order of magnitude increase in the two photon cross section of the individual building blocks and shows the potential of two photon enhancement through self assembly. No new techniques are introduced.

3-3 Abstract

Improving the nonlinear optical properties of organic materials through transition to macromolecular architectures of highly conjugated chromophores has been shown to be a viable strategy for generating materials suitable for TPA applications. In this study we display a simple and elegant method by which to synthesize macrocycles of porphyrin dimers. Two-photon absorption studies show 2 orders of magnitude enhancement of cross-section of the material, giving a maximum δ_2 of 10^6 GM.

3-4 Introduction

It is now clear that dendrimers, 2-D arrays, and macrocycles offer new and enhanced effects for nonlinear and quantum optical applications [1-2], There is still a need to create superior self-assembled materials as building blocks for novel optical applications. New variations of the porphyrin molecule have recently been generated for this purpose. There have been reports of the use of porphyrins in polymers, linear arrays, dendrimers, and, in this report, cyclic aggregates [3]. In particular, it would be interesting to know the effect of the number of porphyrin dimer units in cyclic geometries on the two-photon cross section (δ_2). There is a large degree of interest in materials with large δ_2 values in the 700−900 nm range, a region where porphyrin assemblies have great promise. Indeed, for the porphyrin macrocycles in this report, δ_2 values in this critical region are observed to be as high as 1.0×10^6 GM.

3-5 Synthesis

The bisporphyrin dimer 3 was synthesized from ethynylimidazolylporphyrin 1 and 2,7-diiodofluorene 2 using a $Pd_2(dba)_3/AsPh_3$ catalytic system at 24% yield. When 3 was dissolved in a nonpolar solvent, chloroform, the long linear polymer 3P first formed by self-coordination. 3P was gradually converted to smaller cyclic arrays (3R) through a reorganization process at 45 °C [4], eventually converging to a mixture with a distribution maximum close to 3×10^4 Da (Supporting Information). To determine the exact molecular weights of the arrays by mass measurement, the coordination between dimers was fixed via a ring-closing metathesis reaction of meso-substituents to produce 4R [6]. After the reaction, GPC separation was performed, and the fractions were subjected to MALDI-TOF measurements. The bulk solution was found to contain several sizes of macrocycles, with the 11-mer (n = 1) through the 19-mer (n = 9) being separated into distinct fractions (Supporting Information). Molecular modeling, by way of a MOPAC calculation, found that the 17-mer and 18-mer macrocycles should be the cyclic species which contain the least amount of ring strain.

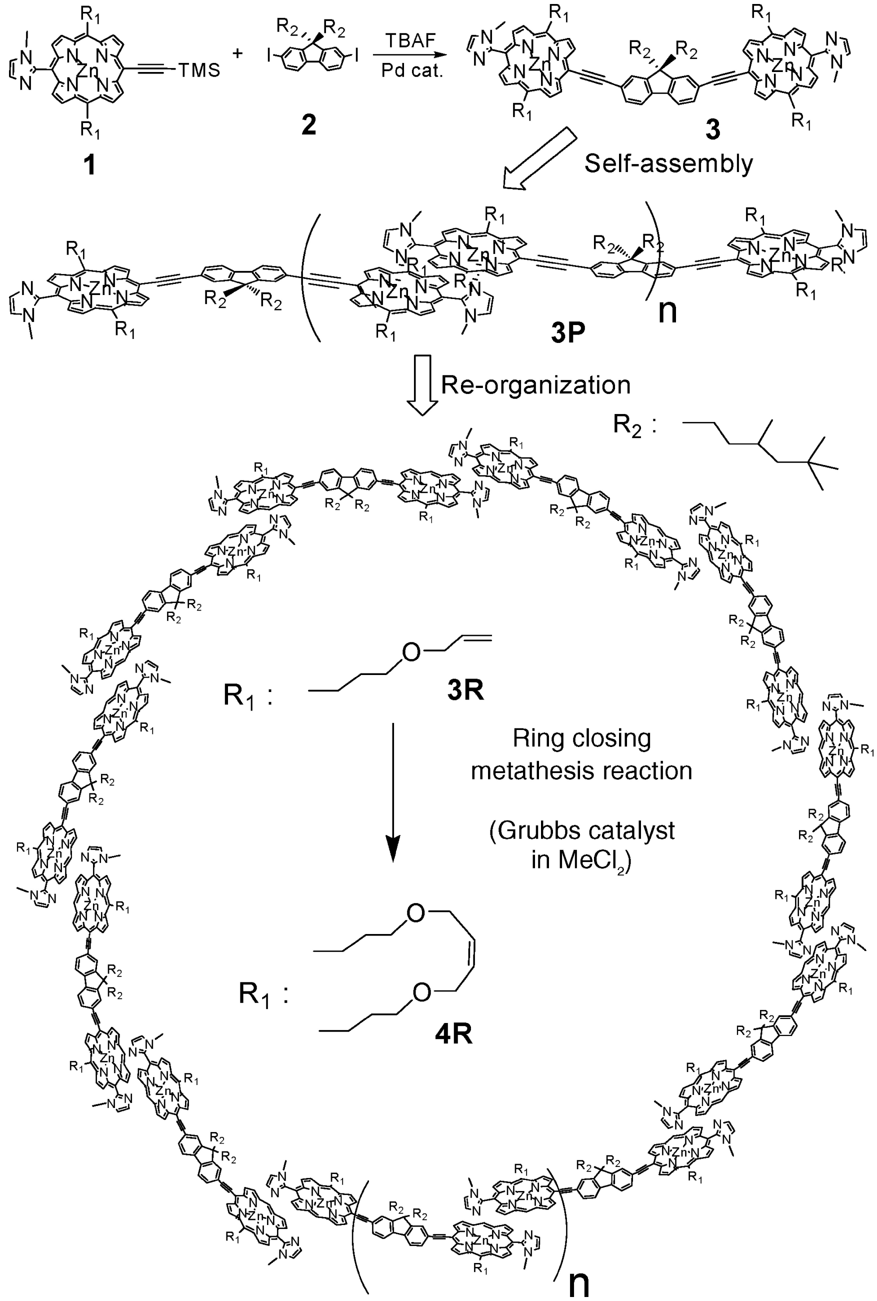

Figure 3-2. Synthesis of a Covalently Bonded Porphyrin Macrocycle by a Self-Assembly Pathway

3-6 Steady State Spectra

Steady-state absorption investigations (figure 3-3) for these systems show a significant red shift in the Soret band (25 nm) and a slightly less pronounced red shift (20 nm) in the Q-band for all of the macrocycles in comparison to the dimer. The distinct broadening of the Soret band seen is typical of other porphyrin assemblies. There is a significant decrease in quantum yield when transitioning from the lone dimer to the macrocycle species though the macrocycles still possess quantum yields comparable to previously investigated porphyrin polymers and macrocycles [3-5]. This is expected because of the arrangement of the porphyrins and slight disruption of resonance at the covalent linkage points. For smaller rings, since the acetylene bridge is less stressed than that of the porphyrin or fluorene regions, the strain at these bonds will be greater, leading to lower quantum yields.

The weakening of the planarity at the acetylinic regions is observed as a slight blue-shift in the Q-band absorption in the macrocycle systems, when smaller rings are compared to the less strained 17-mer species [5]. The subsequent increase in quantum yield (η), as the size of the macrocycle goes from an 11-mer to the 17-mer, confirms that the less distorted system sees less fluorescence inhibition. The 19-mer in turn sees another η decrease as the size and flexibility of the macrocycle becomes such that folding and bending of the macrocycle allows for even further distortion at acetylinic linkages and a greater number of intermolecular quenching sites within the molecule.

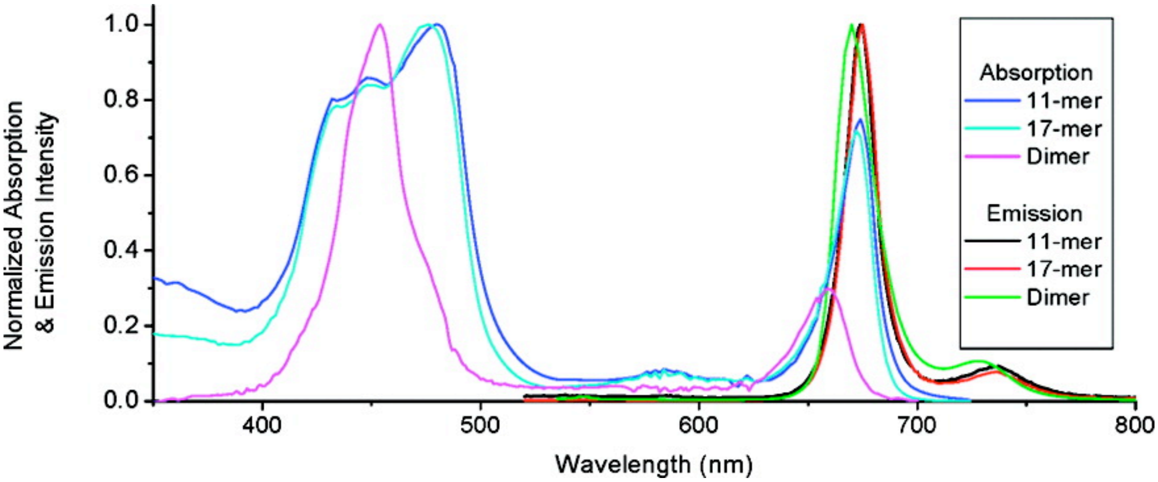

Figure 3-3. Steady-State Absorption and Emission Data for Porphyrin Macrocycles

A red shift in the absorption (20–25 nm) is seen in the porphyrin macrocycles when compared to the dimer. Only selected spectra are presented for clarity.

3-7 Two Photon Spectroscopy

A summary of the two-photon properties and quantum yields for the system studied are given in table 3-1. The two-photon absorption and emission properties of this system were investigated by the TPEF method with 100 fs pulses as outlined elsewhere in our previous reports [1-2]. The dimer in this investigation shows only a small 2P response when considered in isolation. However, upon cyclization and subsequent covalent linkage, a 2 order of magnitude increase in δ_2 and an order of magnitude increase in the two-photon fluorescence signal was observed. Though the acetylinic bridging between dimer units is not assumed to contribute to the two-photon cross section of the macrocycle implicitly, they are assumed to prevent dissociation of the imidazolyl linkages and make the assemblies more viable for use in a wider assortment of environments.

Table 3-1. TPA and TPEF Enhancement of Porphyrin Macrocycles

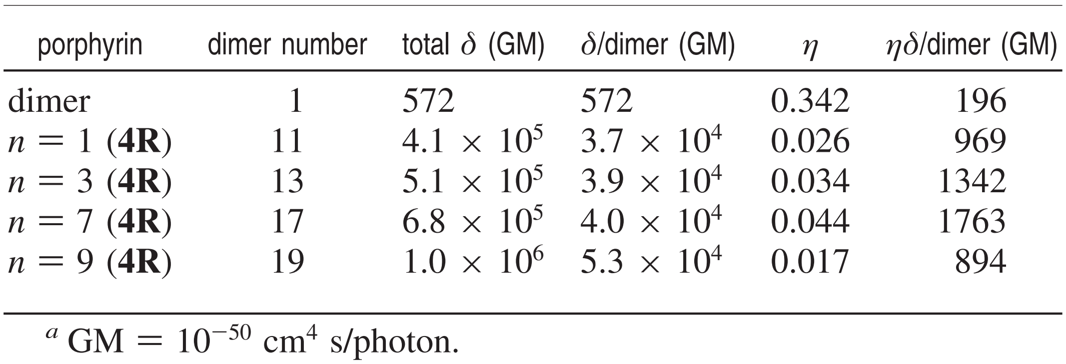

porphyrin	dimer number	total δ (GM)	δ/dimer (GM)	η	$\eta\delta$/dimer (GM)
dimer	1	572	572	0.342	196
$n = 1$ (**4R**)	11	4.1×10^5	3.7×10^4	0.026	969
$n = 3$ (**4R**)	13	5.1×10^5	3.9×10^4	0.034	1342
$n = 7$ (**4R**)	17	6.8×10^5	4.0×10^4	0.044	1763
$n = 9$ (**4R**)	19	1.0×10^6	5.3×10^4	0.017	894

[a] GM = 10^{-50} cm^4 s/photon.

The δ_2 for the cyclized systems is given in figure 3-4. For these systems it was found that the maximum two-photon cross sections occurred near 830 nm. It was also found that for cyclized porphyrin macromolecules the increased ring size leads to an increased dimer cross section, making the 19-mer a preferred candidate for TPA applications. This is one of the largest cross sections reported for porphyrin systems on the femtosecond time scale [3-5]. The maximum TPEF is attributed to the macrocycle with the lowest strain at it is linkage points, the 17-mer, and is also one of the largest values reported for porphyrin system at a $\delta_2 \times \eta$ value of 1.8×10^3 GM per dimer.

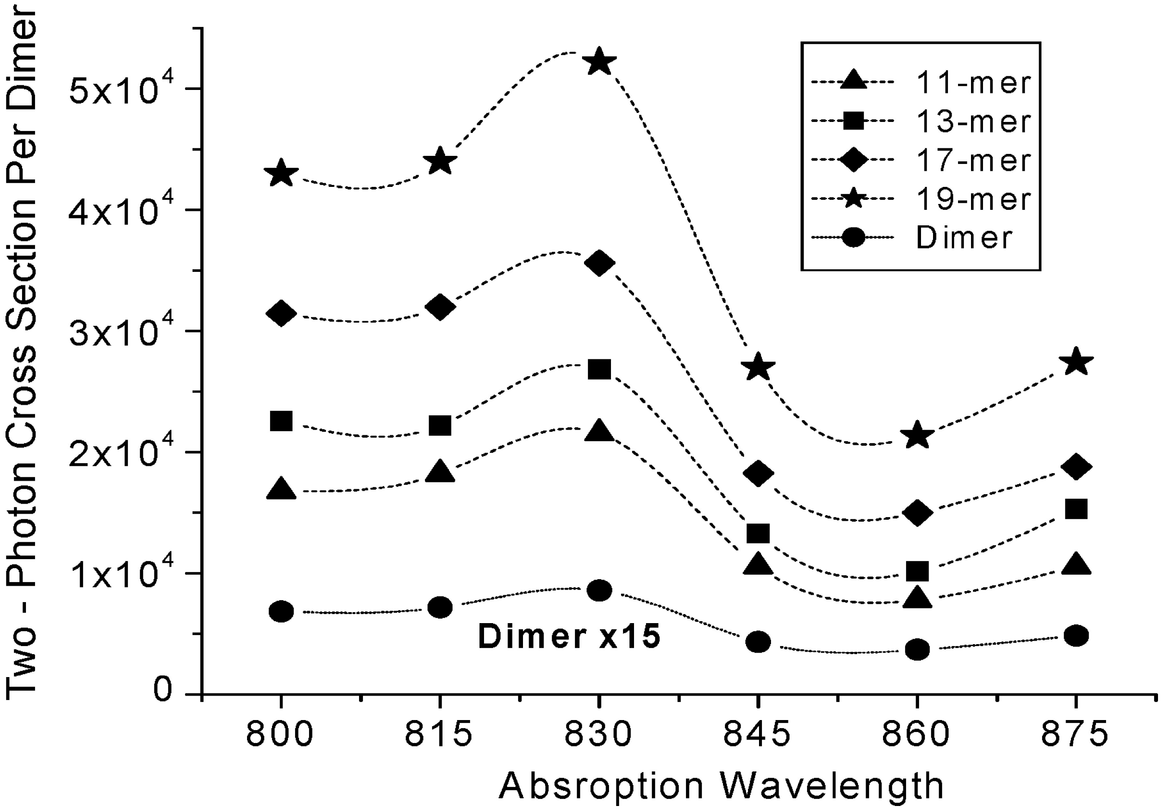

Figure 3-4 Two-Photon Cross Section Spectra per Dimer Unit for the Porphyrin Macrocycles Studied

The dimer is shown at 15 times it is actual value for contrast.

The δ_2 enhancement seen in this these macrocycles was attributed to several distinct factors. The complementary coordination of the imidazolyl group to the neighboring porphyrin's Zn(II) enhances the local dipole–dipole interaction in the macrocycle [3, 6] In forming cyclized molecules with covalent links preventing dissociation, we effectively enforce a minimal amount of variation in the coplanarity and distance between porphyrin rings with a rigid spacing unit between bound chromophores [7]. This binding in effect leads to lower dihedral angle disruption between the porphyrin units and fluorene and higher dimer symmetry [5]. All of these properties have been shown to contribute to strongly cooperative intramolecular interactions in multichromophore arrays and provide precedence for the enhanced δ_2 observed in this TPEF study.

3-8 Conclusion

In this study we show that by an elegant combination of self- assembly and a metathesis ring closing reaction, large porphyrin macrocycles can be generated and separated by size. An increase of 2 orders of magnitude for the δ_2 per dimer unit was observed in these porphyrin macromolecules. The macrocycles have greater promise for two-photon applications in multiple solvents and at wider pH ranges than aggregates which lack covalent bonds. These materials provide greater 2P response than linear counterparts, showing potential for use in both TPA and TPEF applications and providing a new avenue from which to probe porphyrin dimer−dimer interactions and flexible covalent bridges in imidazolyl−Zn(II) porphyrin systems.

3-9 Acknowledgment

Support for this project was provided by NSF-DMR-Polymers.

3-10 References

(1) (a) Williams-Harry, M.; Bhaskar, A.; Ramakrishna, G.; Goodson, T., III; Imamura, M.; Mawatari, A.; Nakao, K.; Enozawa, H.; Nichinaga, T.; Iyoda, M. J. Am. Chem. Soc. 2008, 130, 3252–3253. (b) Bhaskar, A.; Ramakrishna, G.; Lu, Z.; Twieg, R.; Hales, J.; Hagan, D.; Stryland, E.; Goodson, T., III J. Am. Chem. Soc. 2006, 128, 11840–11849. (c) Ispasoiu, R.; Balogh, L.; Varnavski, O.; Tomalia, D.; Goodson, T., III J. Am. Chem. Soc. 2000, 122, 11005–11006. (d) Bhaskar, A.; Ramakrishna, G.; Hagedorn, K.; Varnavski, O.; Mena-Osteritz, E.; Bauerle, P.; Goodson, T., III J. Phys. Chem. B 2007, 111, 946.

(2) (a) Ramakrishna, G.; Bhaskar, A.; Bauerle, P.; Goodson, T., III J. Phys. Chem. A 2008, 112 (10), 2018–2026. (b) Bhaskar, A.; Guda, R.; Haley, M. M.; Goodson, T. G., III J. Am. Chem. Soc. 2006, 128, 13972. (c) Goodson, T., III Acc. Chem. Res. 2005, 38, 99–107.

(3) (a) Ogawa, K.; Ohashi, A.; Kobuke, Y.; Kamada, K.; Ohta, K. J. Am. Chem. Soc. 2003, 125, 13356. (b) Ogawa, K.; Ohashi, A.; Kobuke, Y.; Kamada, K.; Ohta, K. J. Phys. Chem. B 2005, 109, 22003. (c) Lee, D.-I.; Goodson, T., III J. Phys. Chem. B 2006, 110, 25582–25585. (d) Drobizhev, M.; Stepanenko, Y.; Rebane, A.; Wilson, C.; Screen, T.; Anderson, H. J. Am. Chem. Soc. 2006, 128, 12432–12433.

(4) Shoji, O.; Okada, S.; Satake, A.; Kobuke, Y. J. Am. Chem. Soc. 2005, 127, 2201.
(5) (a) Ohashi, A.; Satake, A.; Kobuke, Y. Bull. Chem. Soc. Jpn. 2004, 77, 365. (b) Ikeda, C.; Satake, A.; Kobuke, Y. Org. Lett. 2003, 5, 4935. (c) Hong, Y.; Dong, Y.; Tong, H.; Li, Z.; Haubler, M.; Lam, J. W. Y.; Tang, B. Z. Proc. SPIE 2007, 6470, T1–T12. (d) Ahn, T.; Kim, K.; Noh, S.; Aratani, K.; Ikeda, C.; Osuka, A.; Kim, D. J. Am. Chem. Soc. 2006, 128, 1700–1704.
(6) Birge, R. R.; Pierce, B. M. J. Chem. Phys. 1979, 70, 165.
(7) (a) Varnavski, O. P.; Ranasinghe, M.; Yan, X.; Bauer, C. A.; Chung, S.-J.; Perry, J. W.; Marder, S. R.; Goodson, T., III J. Am. Chem. Soc. 2006, 128, 10988-10989. (b) Ranasinghe, M. I.; Varnavski, O. P.; Pawlas, J.; Hauck, S. I.; Louie, J.; Hartwig, J. F.; Goodson, T., III J. Am. Chem. Soc. 2002, 124, 6520–6521.

3-11 Supporting Information

As published online at pubs.acs.org.

General. 1H NMR spectra were obtained in CDCl3 with Me4Si as the internal standard (δ 0 ppm) and recorded on either JEOL JNM EX270 or JEOL ECP600. UV-vis spectra were obtained on either Shimadzu UV-1650PC or UV-3100PC. MALDI-TOF mass spectra were obtained on Perseptive Biosystems Voyager DE-STR or Shimadzu/KRATOS Axima-CFR Kompact MALDI with dithranol (Aldrich) or 2-[3-(4-tert-Butylphenyl)-2-methylprop-2-enylidene]-malononitrile DCTB (Aldrich) as the matrix. Reactions were monitored on silica gel 60 F254 TLC plates (Merck). The silica gel utilized for column chromatography was purchased from Kanto Chemical Co. Inc.: Silica Gel 60N (Spherical, Neutral) 60-210 mm and 40-50 mm (Flash). The alumina used for column chromatography was purchased from Merck: Aluminum oxide 90 active basic. Analytical GPC measurements were performed on a HEWLETT PACKARD 1100 SERIES with a JAIGEL 3H-A or 4H-A column for chloroform eluent.

1-Bromo-3,5,5-trimethyl hexane (5) [S1]. 3,5,5-Trimethylhexanol (4 ml, 23 mmol) was added into 5 ml of 47% hyrdobromic acid with 0.9 ml of sulfuric acid. The mixture was heated at 120 ^{o}C for 3 hours and extracted with hexane. The organic layer was washed with saturated NaHCO3 aqueous solution and evaporated to give **5** as yellow liquid (78.1%). 1H NMR (270 MHz, CDCl3) δ 3.35-3.49 (m, 2H, Br-CH2-), 1.81-1.91 (m, 1H, CH), 1.61-1.75 (m, 2H, CH2), 1.16 (m, 2H, CH2), 0.89-0.97(m,12H, Me+tBu) .

2,7-Diiodofluorene (6) [S2]. Fluorene (2.0 g, 12 mmol) was dissolved in a mixture of acetic acid (32 ml), water (6.5 ml), and sulfuric acid (1 ml) at 95 oC. Then, iodine (2.1 g, 8.3 mmol) and periodic acid (0.92 g, 4.0 mmol) were added at 80 oC and stirred at this temperature for one hour. The precipitate was corrected by filtration and washed with saturated $NaHCO_3$ aqueous solution and water. The crude was recrystallized from hexane to give **6** (2.72 g, 54%). 1H NMR (270 MHz, CDCl3) δ 7.88 (s, 2H, Ph), 7.70 (d, 2H, *J* = 8.1, Ph), 7.50 (d, 2H, *J* = 8.1 Hz, Ph), 3.84 (s, 2H, CH2).

9,9-Bis(3,5,5-trimethylhexyl)-2,7-diiodofluorene (2) [S1]. Under nitrogen atmosphere, **6** (0.8 g, 1.9 mmol), KI (0.032 g, 0.19 mmol), powdered KOH (0.53 g, 9.5 mmol), and **5** (0.866 g, 4.18 mmol) were added into 8 ml of DMSO at 0 oC. After stirring at room temperature for 5 hours, 50 ml of water was added and extracted with hexane. The organic layer was washed with water and evaporated. The crude was purified with silica gel column chromatography using hexane as an eluent (83%). 1H NMR (270 MHz, CDCl3) δ 7.62-7.68 (m, 4H, Ph), 7.40 (d, 2H, Ph), 1.83-1.99 (m, 4H, CH2), 1.18-1.27 (m, 2H, CH), 0.81-0.96 (m, 4H, CH2), 0.71-0.77(m, 24H, Me), 0.40-0.55 (m, 4H, CH2).

Species 3. Under argon atmosphere, **1** [S3] (110.5 mg, 148 μmol) and **2** (45.1 mg, 67.3 μmol) were dissolved in 58 ml of THF. Then, tetrabutylammonium fluoride in THF (300 μl, 296 μmol) was added. After 30 minutes, triethylamine (8 ml), $Pd_2(dba)_3$ (34.8 mg, 33.7 μmol), and $AsPh_3$ (41.2 mg, 135 μmol) were added. After stirring for 4 hours, the reaction solution was evaporated. The residue was dissolved in chloroform and washed with water. The crude was purified by preparative GPC (Tosoh G3000HHR, pyridine elution) to give **3** (15 mg, 12%). 1H NMR spectrum of **3**, which existed as a mixture of self-assembled polymer in CDCl3, showed broad signals. Therefore, we attempted to prepare free base **3FB** to identify the compound and confirm purity by 1H NMR. MALDI-TOF mass (dithranol) m/z 1759.7740 (M + H)+, calcd for C107H115N12O4Zn2 1759.7747 (M + H)+.

Species 3FB. Under an Ar atmosphere, **3** (5.0 mg, 2.8 μmol) in 4 ml of chloroform was added into a mixture of 12 N hydrochloric acid (1 ml) and methanol (5 ml). After stirring for 10 minutes at room temperature, diluted with water and extracted with chloroform. The chloroform layer was washed with saturated NaHCO3 aqueous solution and water. (quantitative). 1H NMR (600 MHz, CDCl3) δ 9.94 (q, 4H, J = 4.8 Hz, β), 9.56 (q, 4H, J = 4.8 Hz, β), 9.42 (d, 4H, J = 4.8 Hz, β), 8.76 (d, 4H, J = 4.8 Hz, β), 8.15 (d, J = 7.8 Hz, 2H, fluorene), 8.10 (s, 2H, fluorene), 8.05 (d, 2H, J = 7.8 Hz, fluorene), 7.68 (d, 2H, J = 1.8 Hz, im), 7.48 (d, 2H, J = 1.8 Hz, im), 6.01-6.14 (m, 4H), 5.42 (ddt, 4H, J = 17, 3.5, 1.6 Hz), 5.26 (ddt, 4H, J = 17, 3.5, 1.6 Hz), 5.04 (t, 8H, J = 7.6 Hz, CH2), 4.08 (ddd, 8H, J = 5.4, 2.7, 1.4 Hz, OCH2=), 3.65 (t, 8H, J = 5.9 Hz, OCH2), 3.38 (s, 6H, NMe), 2.75 (q, 8H, J = 7.6 Hz, CH2), 2.35-0.8 (m, 38H, trimethylhexyl), -2.28 (s, 4H, NH), MALDI-TOF mass (dithranol), m/z 1635.9470 (M + H)+, calcd for C107H119N12O4 1635.9477.

Re-organization (3R). A solution of 0.6 μM of 3 in 500 ml of chloroform was allowed for 5 days under dark at 45 ^{o}C. The solution was evaporated using vacuum pump at –40 oC.

Species 4R. 3R (5.3 mg, 3.0 μmol) was dissolved in 75 ml of dichloromethane. Under a nitrogen atmosphere, Grubbs catalysis $RuCl_2(=CH\text{-}p\text{-}C_6H_5)(PCy_3)_2$ [S4] was added into the solution and stirred for 6 hours at room temperature. The solution was diluted with chloroform and washed with water.

Steady State Measurements. The absorption spectra of the molecules were measured using an Agilent (Model # 8341) spectrophotometer. Their emission spectra were acquired using a Jobin Yvon Spex Fluoromax-2 spectrophotometer. The results presented in figure 3-9. The quantum yields of the molecules were measured using maximum absorption and integration of fluorescence. Tetraphenylporphyrin dissolved in toluene was used as the standard. The following relation was used to measure the quantum yield:

$$\Phi_F = (\Phi_F)_S \frac{\int J(\bar{v})d\bar{v}}{\int J_S(\bar{v})d\bar{v}} \frac{(J_a)_S}{J_a} \frac{n^2}{n_S^2} \qquad [I.]$$

These measurements may have some error due to sensitivity of the fluorescence spectrophotometer and other environmental conditions.

Two Photon Measurements. The two photon cross sections and fluorescence were obtained by the TPEF method (spectra given in figure 3-10). Excitation was obtained with light from a Spectra-Physics Mai Tai unit. The intensity was monitored by a Thor Labs DET 100A photo-voltmeter. Fluorescence was collected using a Hamamtsu R7518P PMT.

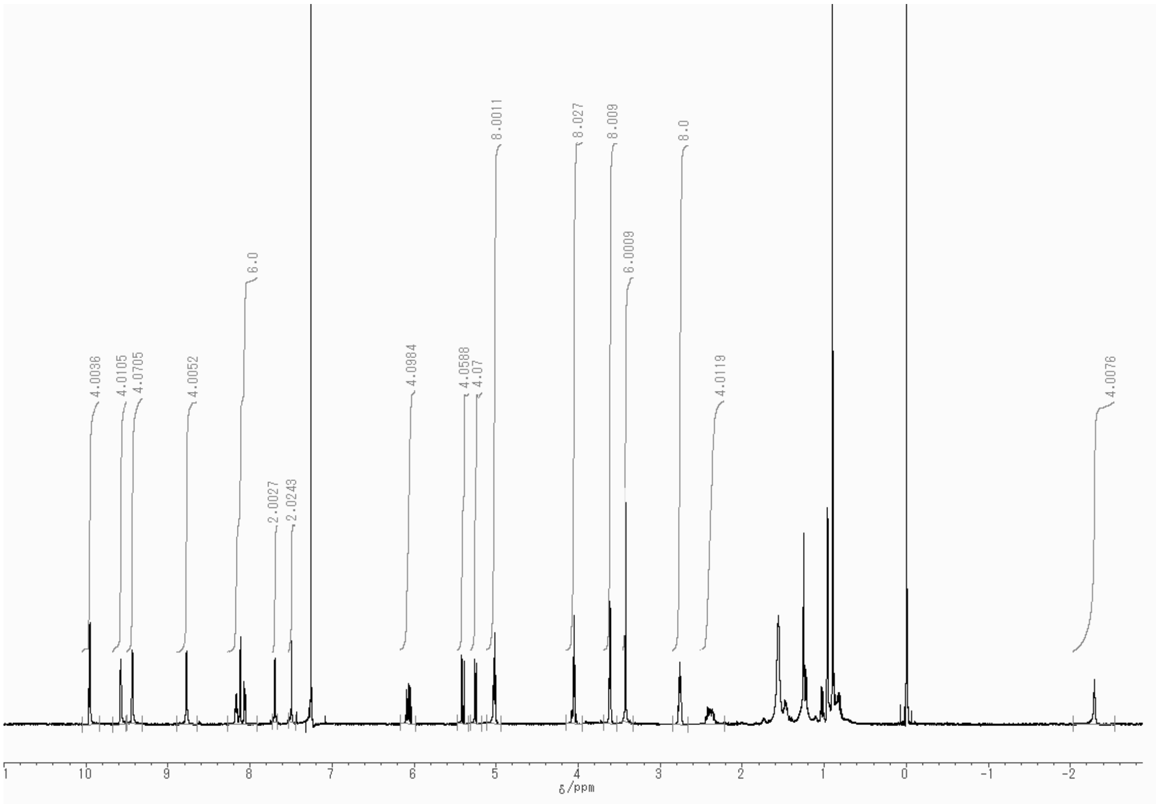

Figure 3-5. 600 MHz 1H NMR spectrum of 3FB in $CDCl_3$

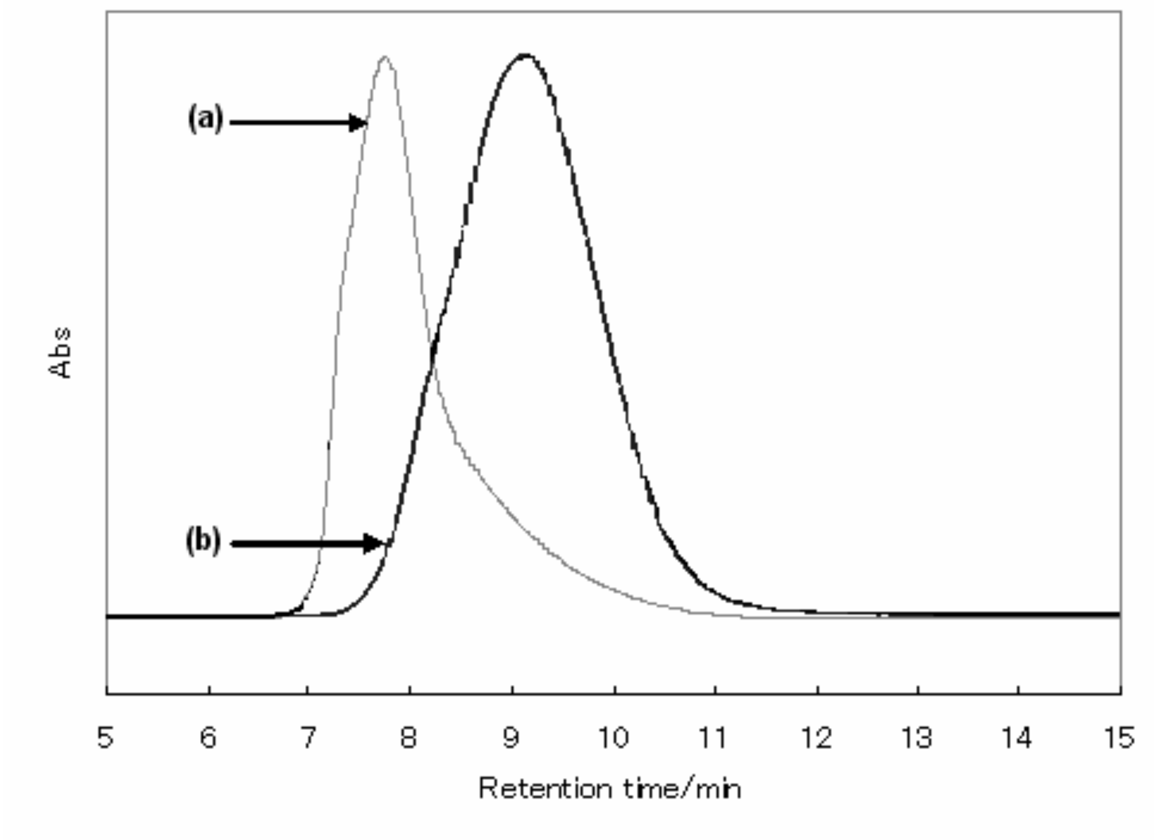

Figure 3-6. Analytical GPC Chromatograms Before (a) and After Reorganization (b)

Column: JAIGEL 4H-A (exclusion limit is 500,000 Da at the retention time of 7 min), Eluent: CHCl3 monitored at 420 nm.

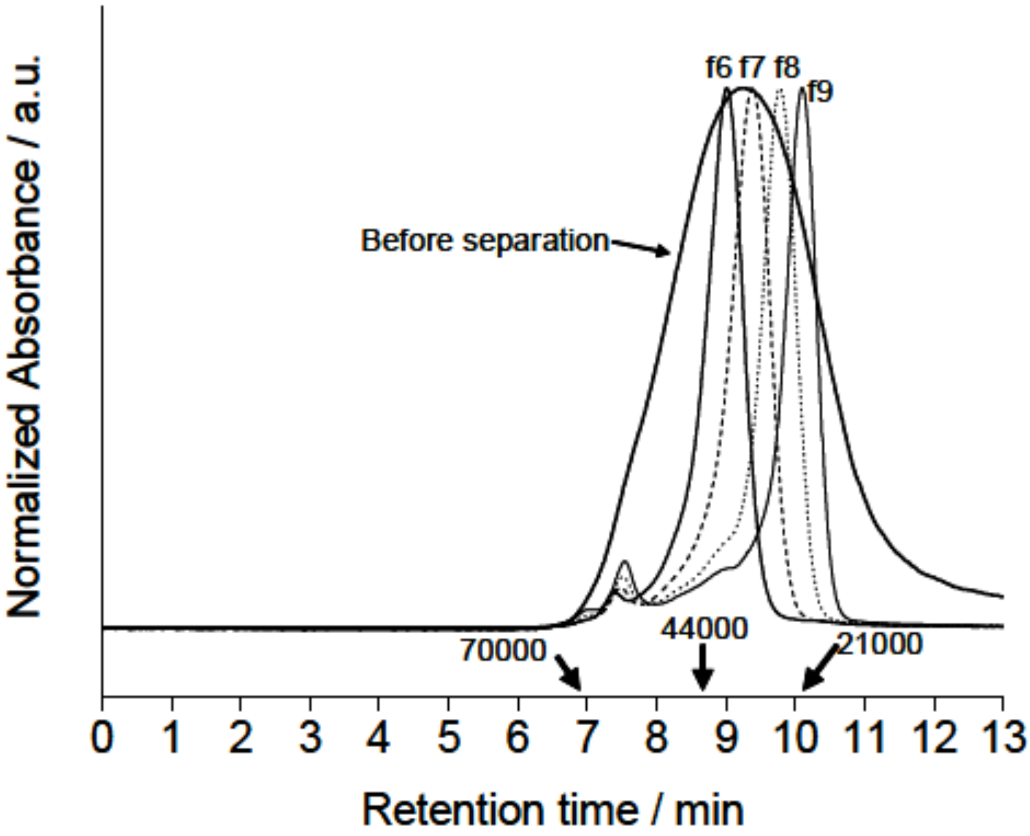

Figure 3-7. Normalized Anlytical GPC Before (bold black) and After Preparative GPC Separation (f6–f9)

The retention times of polystyrene standards are indicated by bold arrows with their molecular weight. Column: JAIGEL 3H-A (exclusion limit is 70,000 Da), eluent: CHCl3.

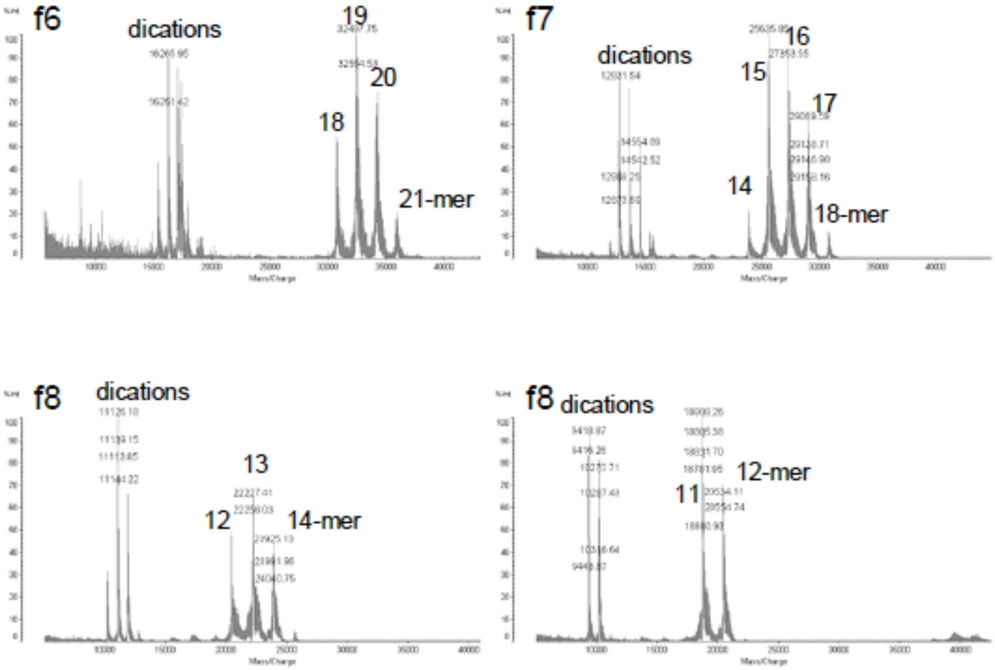

Figure 3-8. MALDI-TOF Mass Data of the Fractions f6–f9 After Preparative GPC Separation

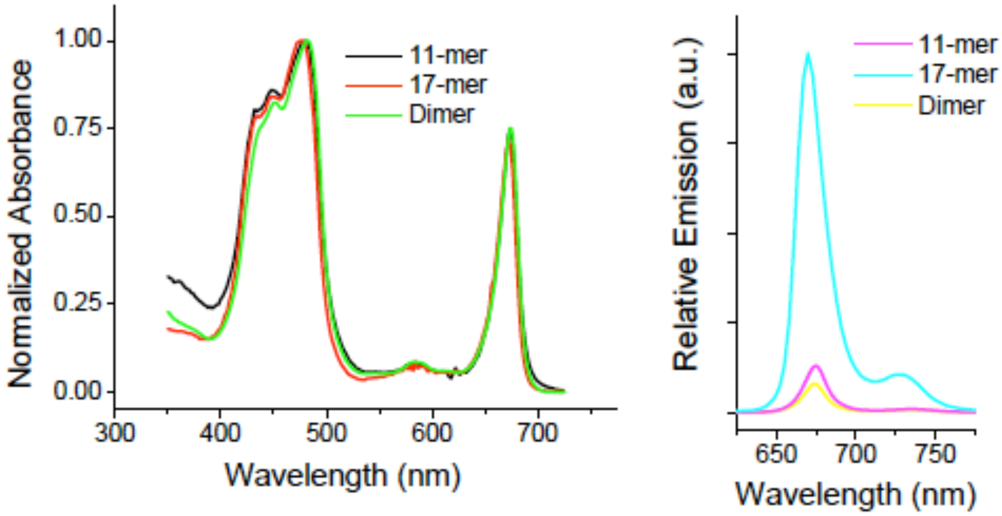

Figure 3-9. Representative Steady State Absorption and Emission Spectra

Only the 11-mer and 17-mer are shown for clarity in contrast to the dimer. Note the decrease in absorption blue-shift near 440 nm on transition to larger macrocycles, in keeping with decreased H-aggregate type behavior at for the larger cyclic.

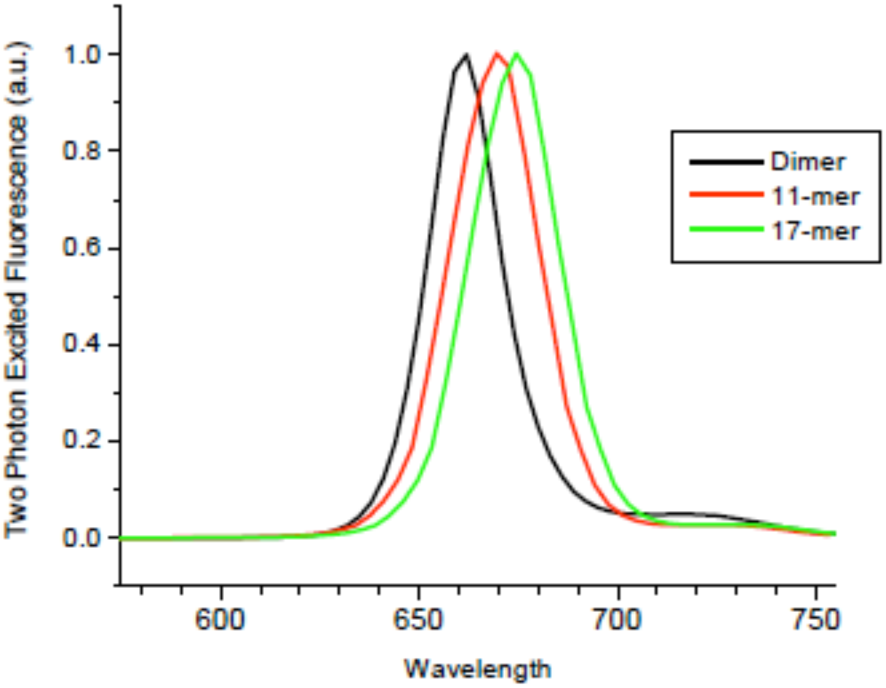

Figure 3-10. Representative Two-Photon Excited Fluorescence Emission Spectra

Only the 11-mer and 17-mer are shown for clarity of the dimer. The red-shift seen in the cyclic emissions is indicates more stable excited state in the cyclics.

3-12 Supplimental Information References

(S1) Kannan, R.; He, G. S.; Lin, T.-C.; Prasad, P. N.; Vaia, R. A.; Tan, L.-S. Chem. Mater. 2004, 16, 185.
(S2) Lee, S. H.; Nakamura, T.; Tsutsui, T. Org. Lett, 2001, 3, 2005.
(S3) Dy, J.; Ogawa, K.; Satake, A.; Ishizumi, A.; Kobuke, Y. Chem. Eur. J., 2007, 13, 3491.
(S4) Schwab, P.; Grubbs, R. H.; Ziller, J. W. J. Am. Chem. Soc., 1996, 118, 100.

Rightslink® by Copyright Clearance Center 6/28/11 3:07 PM

Copyright Clearance Center RightsLink®

ACS Publications High quality. High impact.

Title:	Synthesis and Two-Photon Absorption Enhancement of Porphyrin Macrocycles
Author:	Jeffery E. Raymond et al.
Publication:	Journal of the American Chemical Society
Publisher:	American Chemical Society
Date:	Dec 1, 2008

Copyright © 2008, American Chemical Society

User ID

Password

☐ Enable Auto Login

Forgot Password/User ID?

If you're a copyright.com user, you can login to Rightslink using your copyright.com credentials. Already **a Rightslink user** or want to learn more?

No charge permission and attribution

Permission for this particular request is granted for print and electronic formats at no charge. Appropriate credit should be given. Please print this page for your records and provide a copy to your publisher. Requests for up to 4 figures require only this record. Five or more figures will generate a printout of additional terms and conditions. Appropriate credit should read: "Reprinted with permission from {COMPLETE REFERENCE CITATION}. Copyright {YEAR} American Chemical Society." Insert appropriate information in place of the capitalized words.

Copyright © 2011 Copyright Clearance Center, Inc. All Rights Reserved. Privacy statement.
Comments? We would like to hear from you. E-mail us at customercare@copyright.com

https://s100.copyright.com/AppDispatchServlet Page 1 of 1

Figure 3-11. American Chemical Society Permission to Publish in Thesis

Chapter 4

Architecturally Induced Ultrafast Energetics in Self-Assembled Light Harvesting Mimics

4-1 Original Publication Information

This chapter is a publication submitted at the request of Advanced Functional Materials in 2011. It has been submitted as the following document for the purpose of being both an invited feature article and cover article for Advanced Functional Materials in a special issue devoted to electronic response in organic materials:

> "Architecturally Induced Ultrafast Energetics in Self-Assembled Light Harvesting Mimics"
>
> Jeffery E. Raymond, Zin Seok Yoon, Jessica E. Donehue, Ogawa Kazuya, Yoshiaki Kobuke, Theodore Goodson
>
> *Advanced Functional Materials*, sub **2011**, accepted for publication.

Modifications to the original document are cosmetic and used only to conform the format of this document or provide uniformity of enumeration.

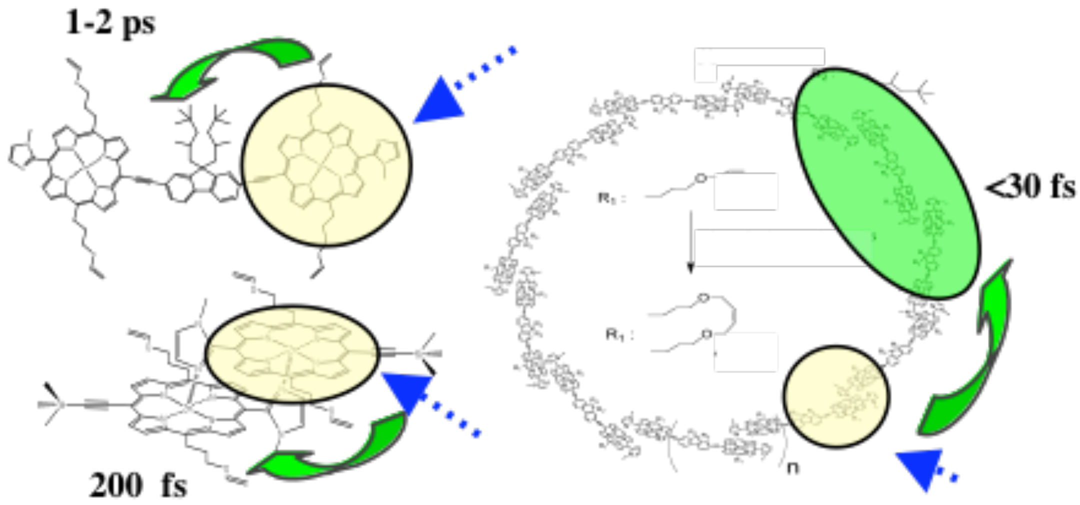

Figure 4-1. Table of Contents Image as Submitted with Table of Content Comment

Table of Content Comment: A giant, LH1 mimicking porphyrin macrocycle is shown to have ultrafast delocalization and interconversion at a time scale faster by an order of magnitude when compared to the individual building blocks of which it is composed. The strong coupling between excited states in this multiband system is shown, through ultrafast emission, anisotropy and absorption measurements, to induce extraordinary excited state delocalization (<100 fs) and two-photon response (~10^6 GM). These findings display that synthetic porphyrin macrocycles are capable of greatly exceeding natural light harvesting complexes both in termsdelocalization rate and nonlinear optical response.

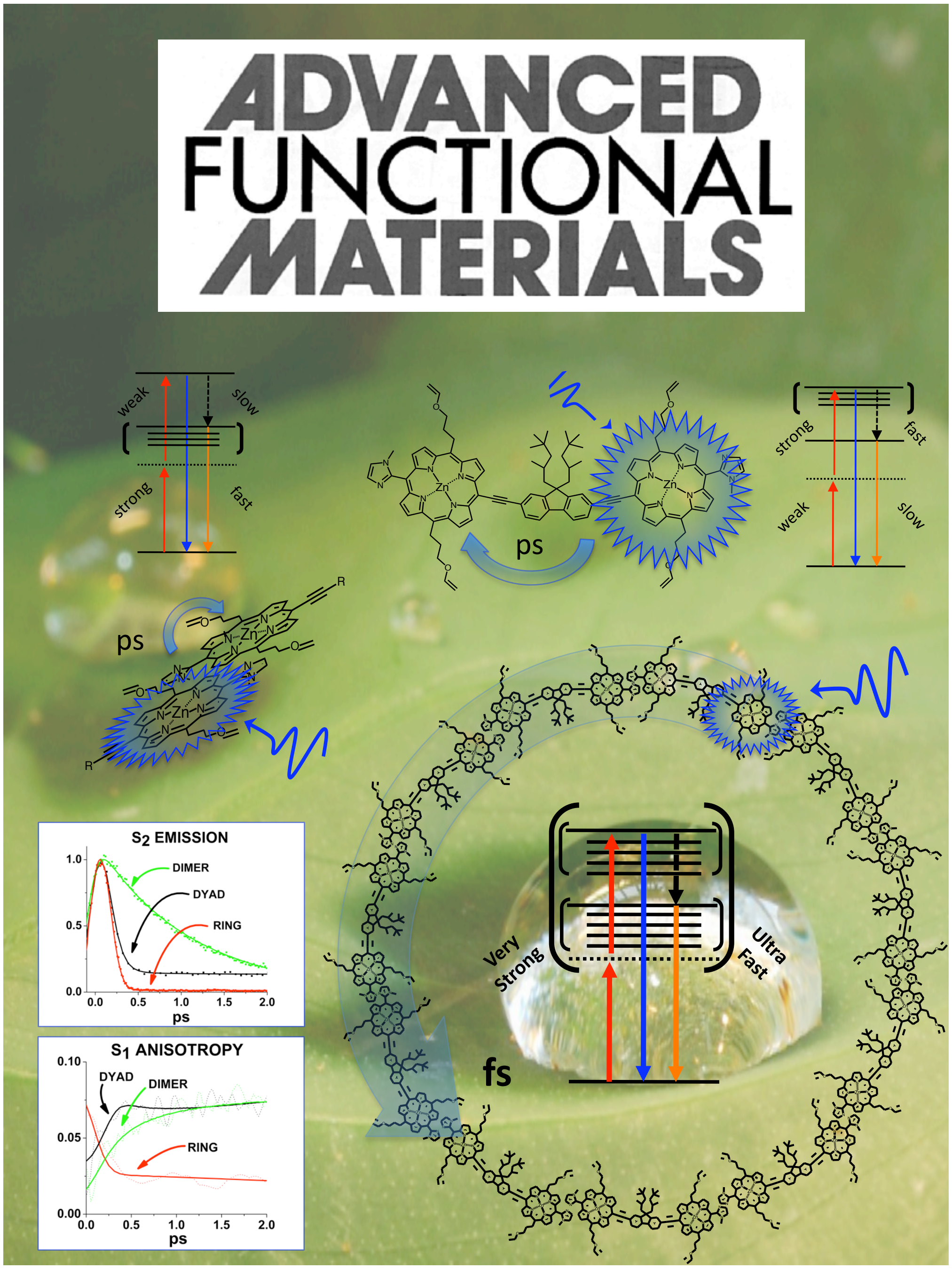

Figure 4-2. Cover Art as Submitted

4-2 Qualifying Statement

In this chapter, the two photon enhancement observed in chapter 3 is investigated by considering the ultrafast response of the porphyrin dimer, dyad and macrocycle species. It will be shown that a combination of inter- and intra-band couplings result in ultrafast (<30 fs) energy delocalization in the macrocycle species and provides a reason for the gross two photon enhancement. Introduced in this chapter is ultrafast fluorescence upconversion, anisotropy and transient absorption measurements.

Fluorescence Upconversion Spectroscopy. This form of fluorescence lifetime measurement is technically a type of pump probe spectroscopy in which the following process occurs: (1) a NIR femtosecond pulsed light source passes through a SHG crystal and the resultant visible light is used to excite the sample, (2) some of the NIR pulse is captured and taken to a delay stage, (3) the resultant emission is overlapped with the NIR pulse, (4) the NIR and emission wavelengths are measured at their sum frequency by a photomultiplier and (5) the process is repeated with small changes in the delay stage, assembling an emission curve in time point by point. Emission is measured in counts per second (CPS) and the time scale is determined by the step size between measurements, typically in the 5-10 fs range. The resultant emission is often fit with a multiexponential decay. In order to accurately report very fast emission lifetimes (<1 ps) it is necessary to deconvolute the instrument response function from the emission decay. Decay lifetimes down to approximately one fifth of the FWHM of the instrument response function (pulse width in time) can be determined. While this technique is much more labor intensive than other techniques where an emission probe is not needed, the benefit of being able to perform ultrafast anisotropy measurements more than compensates for this. Upconversion emission measurements will often return several lifetimes, each related to a competing relaxation process. The amplitudes to these decays provide a good gauge as to how much a given process contributes to the total excited state behavior.

Ultrafast Anisotropy Spectroscopy. Ultrafast anisotropy kinetics are recovered from the ultrafast upconversion kinetics by operating the system at two orthogonal polarizations of excitation. This generates two emission traces, one which gives counts for fluorescence which was excited with polarization parallel to the probe beam and then again with polarization perpendicular to the probe beam. Differences in the emission polarization lead to different degrees of sum frequency generation with the probe beam. Anisotropy signal is obtained comparing the signal intensity of each over time in the following relationship:

$$r = \frac{I_{para} - I_{perp}}{I_{para} + 2I_{perp}} \tag{I.}$$

Where r is the anisotropy, I_{para} is the intensity of the signal with parallel excitation and I_{perp} is that with perpendicular excitation.

The signal that is obtained is a unitless number typically in the 0.0 to 0.4 range. At the fs and early ps time scales this signal is an indication of the localization of the electron-hole pair that recombine to emit a photon. When the electron-hole pair recombine in a process that is similar to the excitation process, it is considered the emission of a localized exciton and will have polarization similar to the excitation polarization. A completely localized emission will give anisotropy (r) values of 0.4. When the electron-hole pair recombine from delocalized states then the emission will be purely random. In this instance the anisotropy will be zero. Most species will have some of both, each with it's own kinetic values (time constants) associated with it. This slight difference in the kinetic traces for I_{perp} and I_{par} will often give rise to an anisotropy decay over time. The time constants for anisotropy decay are then a very good measure of the delocalization lifetime and can provide critical excited state information relating to multichromophoric energetics, which are the focus of this body of work. At longer time scales, anisotropy measurements are often used in a different way. When emitters which have innate anisotropies of 0.4 are part of a larger molecular structure (such as labeled proteins or dye functionalized polymers) the anisotropy on the ns time scale is used to determine the rotational rate of the molecule. These kinetics can also be observed in smaller molecules at the ~100 ps time scale.

Ultrafast Transient Absorption Spectroscopy. In transient absorption spectroscopy, a pump-probe technique, the primary signal of consideration is the change in absorption of a material some time after excitation. In brief, an ultrafast excitation pulse is applied to the sample (pump) and immediately followed by a pulsed white light source (probe). Changes in the materials absorption are recorded and compared to the material's response to the white light prior to being pumped. This generates a visible spectrum of change in absorption values (ΔA) for each time measured. The lag in the probe pulse is generated by a delay stage. Each wavelength can then be fitted for the kinetic rise or decay of the signal, ΔA, and be assigned to newly allowed or denied electronic transitions in the species. Valleys in the spectra ($\Delta A < 0$) are typically associated with a ground state bleach (GB). This is to say that some transition which was allowed from the ground state before the pump pulse, $S_0 \rightarrow S_n$, is no longer as likely after the pump pulse interacted with the sample. This can be due to a now increased population in S_n or an overall decreased S_0 population (i.e. the excited electrons are not necessarily in S_n but have not returned to S_0 yet either). Peaks in the transient absorption spectra are typically attributed to excited state absorption (ESA). Excited state absorption is a process in which a newly excited electron finds itself in an orbital where it is possible to be promoted even further through absorption of another photon. This photon will have an energy equal to the energy gap between the first excited state reached and the second one to which the electron is promoted. Another type of ESA signal that can be observed in multichomophoric species is a sympathetic coupling between dipole moments. This is best thought of in a step-wise manner: (1) one chromophore becomes excited to a given state by the pump, (2) the new excited state now has a new dipole moment strength and direction, which may allow it to interact with neighbors, (3) the interaction with the excited electron makes promotions to higher energy levels more likely in the neighbor, and (4) when the probe light arrives, the neighbor sees increased absorption. The kinetic signals for transient absorption can be fitted in a multiexponential decay fashion, just like the previously detailed fluorescence lifetime measurements. This also requires deconvolution from the instrument response function to achieve accurate lifetimes for very fast (<1 ps) processes. Often the kinetics of an ESA region will match one or more GB regions as the ESA occurring is with excited states which are at the GB energy. Finally, it is important to be considerate before assigning cause for shifts in GB and ESA wavelength maxima with time. An example of this might be where GB seems to red shift with time and ESA blue shift. This is not an indication of a gross change of state in the system but rather normal response of a two level system where the average vibrational energy level in the GB is lower over time and the ESA wavelength needed to promote the GB energy electrons will change to compensate.

4-3 Abstract

Different zinc porphyrin architectures, including a giant macrocycle, are investigated by ultrafast fluorescence lifetime, anisotropy and transient absorption measurements. The measurements are carried out in order to relate the excited state response at very short time scales to the two order of magnitude two-photon enhancement observed in the macrocycle. A slipped cofacial assembly method is shown to enhance the electronic communication between acetyl-bridged chromophores. It is also shown that energy delocalization in these macrocycles is an order of magnitude faster than the ps time scale emission observed in the dimer species. It is found that the $S_2 \rightarrow S_1$ transition is further enhanced by an increase in contributing units in these macrocycles and that acetyl bridged porphyrins can be assembled to generate ultrafast excited state delocalization across the entire ring, despite not being connected via a conjugated pathway. The strong S_1-S_2 coupling provides for the phenomenal two-photon enhancement observed in these macrocycles which closely mimic naturally occurring light harvesting complexes.

4-4 Introduction

As attempts to generate porphyrin and pthalocyanine assemblies that deliver enhanced nonlinear optical (NLO) response grow more sophisticated, it is necessary to probe both the architectural and binding effects that drive energy transfer [1-3]. For applications such as remote sensing, light harvesting, organic semiconducting and quantum computing [2-5] it remains critical to understand how rapid excited state delocalization in advanced architectures contribute to NLO character. Of particular interest are porphyrin assemblies such as molecular wires, binary lattices and macrocycles where the ensemble interaction between building blocks generates optoelectronic responses unobtainable by single units [1,5]. Macrocycles which possess a slipped cofacial porphyrin interaction are of distinct import due to there mimicry of photosynthetic systems like those found in the naturally occurring light harvesting complexes such as LH1 and LH2 [1,6]. Previous studies have shown that the two-photon cross-section (TPACS, σ_2) per porphyrin can be enhanced by ~2 orders of magnitude when transitioning from a bridged dimer to a macrocycle with slipped cofacial interactions between units [1]. However, the implicit excited state behavior and electronic response which leads to this enhancement remains unclear.

In this article we report the excited state behavior observed in a collection of porphyrin structures which possess increasingly sophisticated Zn-porphyrin architectures. These molecules have been shown to have extremely high two-photon response when taken as nanoparticles [7] or macrocycles [1]. It is shown that neither the slipped cofacial architecture nor the fluorene bridging of porphyrins alone are sufficient to produce S_2 (B-band) exciton delocalization and relaxation to S_1 (Q-band) at time scales less than 100 fs. However, a combination of both the bridging and the slipped cofacial interaction turns a ps-scale S_2 lifetime (typified by hopping type energy transfer between porphyrins) [6,8] in a single dimer into an ultrafast delocalization capable of rapid emission from both the S_2 and S_1 states. It is also shown that the strong dipole interactions between macrocycle building blocks is effected by the entire structure and contribute to the fast interconversion from $S_2 \rightarrow S_1$. These same interactions are critical to the ~10^6 GM (cm^4/photon-second) two-photon cross-sections observed in our macrocycles, one of the highest values observed in organic single molecules [1]. Specifically, the strongly coupled transition dipole moments between bands combined with the existence of an increased density of states near the TPA virtual state energy will be shown to be of particular importance when assessing TPA enhancement [9-12].

4-5 Steady State Spectroscopy

Studied here is a bisporphyrin fluorene bridged dimer **1**, a slipped cofacial ethynylimidazolylporphyrin dyad **2**, and a covalently bound macrocycle **3** (figure 6-3). Specifically, macrocycles comprised of 11 (**3)** and 17 (**3a**) dimer units are investigated. Molarities of 15 uM for **1** and **2**, 3 uM for **3** and 2 uM for **3a** were used throughout this study in 7:3 dichloromethane/pyradine. Synthesis, one-photon and two-photon optical characterization of the macrocycle and dimer are outlined in our previous work [1].

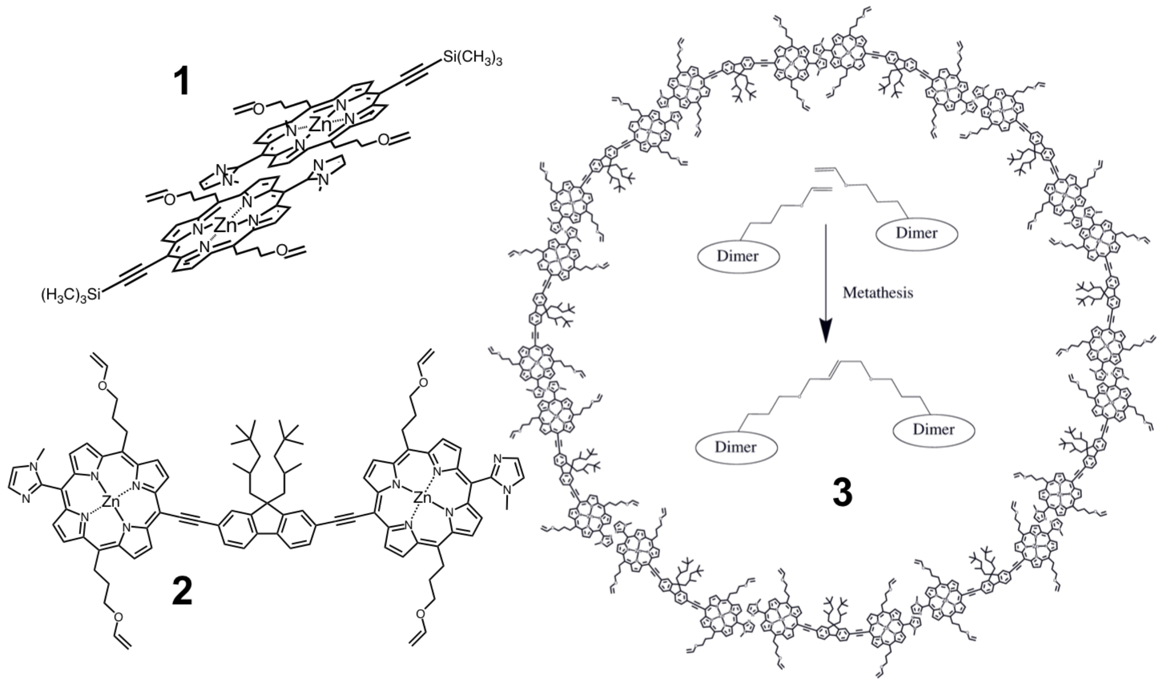

Figure 4-3. The Zinc Porphyrin Dyad (1), Dimer (2) and Macrocycle (3) Investigated in This Study

Two sizes of macrocycle are investigated in this stude: the 11 dimer (3) macrocycle and the 17 dimer (3a) macrocycle.

The absorption and emission spectra for all species are presented in figure 6-4 for comparison and are summarized in table 6-1. All of these porphyrin systems characterized display absorption in the 400-500 nm region as well as in the 600-700 nm regions. The higher energy absorption band is assigned to the $S_0 \rightarrow S_2$ transition and will be referred to as the S_2 or B-band region while the lower energy absorption band is assigned as the S_1 or Q-band. Steady state absorption spectra depict two available transitions for the B-band of the dyad and further splitting in the dimer. This response is typical of other bisporphyrin systems with cofacial associations being compared to a conjugated bridge between chromophores. The covalently bound dimer shows absorption and fluorescence maxima red-shifted with regards to the dyad assembly due to an extended conjugation between chromophores.

These transitions are seen collectively in the absorption of the macrocycle species, which is both broadened and red-shifted with regards to the dimer and dyad samples. This phenomenon can be explained by a coupling of the transition dipole moments of the B-band across multiple building blocks, as well as the additional band splitting induced by close proximity to other dimers. Red shifting of the Q-band is observed as we transition from dyad to dimer to macrocycle in these systems. This trend in the Q-band absorption, where the red shift is stronger than that observed in the B-band, signifies an even greater degree of chromophore interaction through increasing porphryin-porphyirn coupling via a conjugated bridge. Virtually no change in the integrated molar extinction coefficients in Q-band absorption per porphyrin is observed, however the integrated B-band extinction coefficients per porphyrin unit follow the trend Dyad < Dimer << 11-mer < 17-Mer, and is also attributable to strongly enhanced dipole interactions [2-4]. The broadening and peak shift of the macrocycle absorption supports an initial steady state excitation spanning approximately four porphyrin units (2 dimers). Moreover, the ε enhancement is still minor when compared to the large differences in σ_2 and does little alone to elucidate the two-order of magnitude enhancement of the two-photon properties observed for the macrocycle species over either the dyad or dimer. This leads to a need for ultrafast absorption and emission measurements in order to observe the excited state behavior in the femtosecond regime and fully understand how architecturally induced ensemble interactions may lead to nonlinear optical responses grossly in excess of isolated bis-porphyrin assemblies.

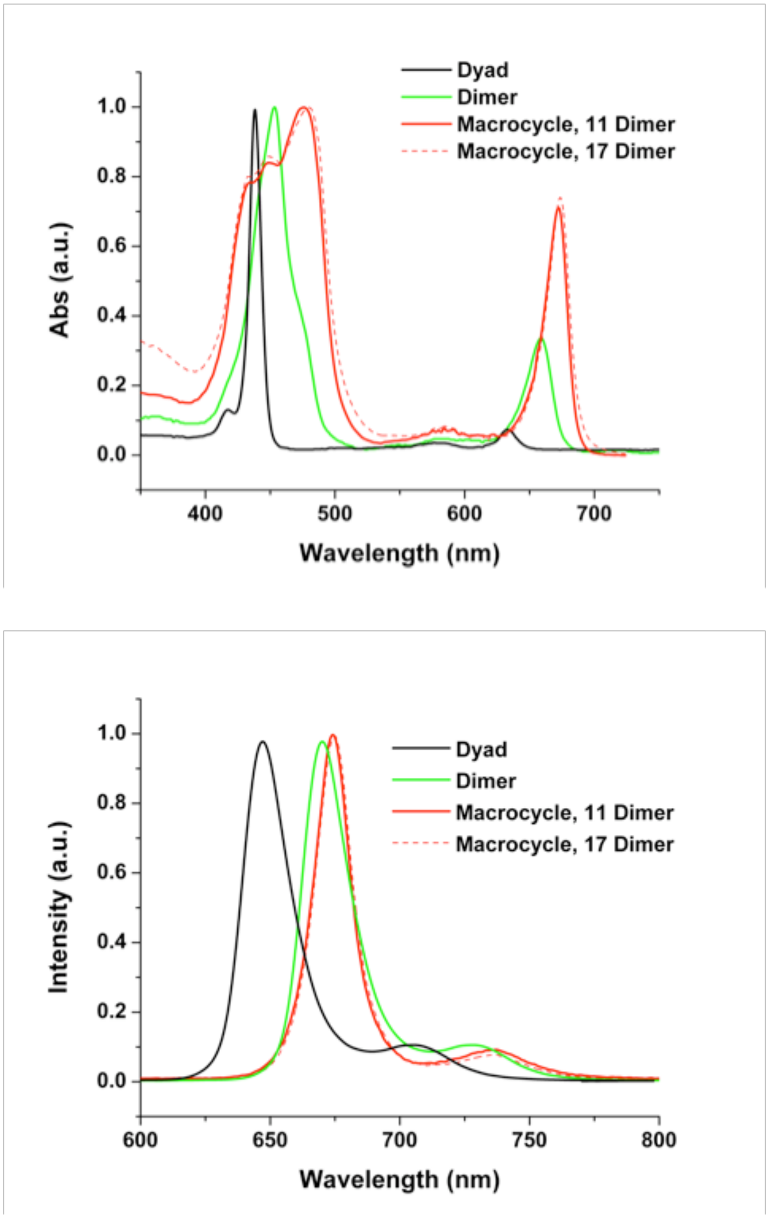

Figure 4-4. The Steady State Absorption Spectra for the Dyad 1, Dimer 2, 11-mer Cyclic 3, and 17-mer Cyclic 3a (Top) as well as Their Emission Spectra from 415 nm Excitation (Bottom)

Table 4-1. Linear, Nonlinear and Ultrafast Spectroscopic Results

Species	ε_B/dimer	σ_2/dimer	Abs λ_{max}	PL λ_{max}	PL Kinteics (ps)					Anisotropy Decay (ps)		
					τ_{1B}	τ_{2b}	$t_{max,Q}$	τ_{1Q}	τ_{2Q}	τ_{rB}	r_{0B}	τ_{rQ}
1	14.4	420	444	645	90	33	2.2	2	490	0.3	0.08	0.1
2	13.3	5721	461	670	1000	>500	5.8	3	1600	30	0.12	0.7
3	17.1	37000	487	673	< 30	-	0.2	1	30	0.1	0	<0.03

One photon molar extinction coefficients reported in units of 10^4 $M^{-1}cm^{-1}$, two photon cross sections reported in units of GM, wavelengths reported in units of nm and kinetics reported in units of ps.

4-6 Ultrafast Fluorescence Up-Conversion Spectroscopy

In order to investigate the excited state differences between the dimer, dyad and 11-mer macrocycle, we utilized ultrafast time-resolved fluorescence up-conversion spectroscopy [13]. In brief, this method uses a fs-pulsed excitation source to probe emission kinetics by way of wave mixing a fs-pulsed delay line with the sample fluorescence.

B-band emission shows that the porphyrin-porphyrin interaction of the cofacial configuration gives ultrafast emission lifetimes for **1** and **3** (figure 6-5), with a dyad τ_1 = 90 fs and a macrocycle τ less than the temporal resolution of our system (< 30 fs). However, it should be noted that the primary fluorescence lifetime (~95% of total emission) of the dyad is actually significantly slower, τ_2 = 33 ps, and should be taken as the majority indicator of the dyad emission lifetime. This stands in contrast to the nearly complete emission (>99%) of the macrocycle with a lifetime ~2 orders of magnitude faster than that of the dyad primary emission. The dimer species shows life times typical of other Zn-porphyrin dimers with a fast lifetime of τ_1 = 1 ps and secondary emission (<2%) associated with a very long lifetime, >500 ps. The two excited state lifetimes observed in the dyad and dimer species are the direct observation of two different relaxation regimes. Only for a portion of the population in the dyad system can a rapid transition to a lower energy level be observed. However, for the dimer, the major component of emission is in the ultrafast regime and points towards energy transfer which can be typified as having a degree of delocalized character. The macrocycle system stands unique in its complete depletion of the S_1 state, with emission in the tail region a trivial contribution to overall emission (<1%), and implies an extremely strong coupling between the S_1 and S_2 bands. These findings are further supported by the investigation of the fluorescence lifetime behavior from Q-band emission (figure 2). The rapid rise time (t_{max} ~ 200 fs) in fluorescence for the macrocycle Q-band indicates intermediate bands between the primary bands which rapidly allow for a transition from the S_2 to the S_1 band; significantly faster than the dyad (t_{max} ~ 2 ps) or the dimer system (t_{max} ~ 6 ps).

In addition to the rise time differences observed, emission lifetime trends for these systems are particularly poignant and can be taken in three parts:

(1) while all species possess two emission lifetimes, the macrocycle shows the most significant emission contribution from the fast lifetime component, indicating an enhanced rate of relaxation through architecturally induced chromophore coupling.

(2) The relaxation times for the majority emission from the macrocycle provide B- and Q-band lifetimes that are 1-2 orders of magnitude faster than either the dyad or dimer, pointing to one or more intermediate bands being present to induce a rapid relaxation regime in the macrocycle species.

(3) A somewhat subtler observation, not immediately apparent when accounting for lifetimes alone, can be made when a single amplitude weighted lifetime is assigned to the B-band emissions of both the dyad and dimer species. While both τ_1 and τ_2 are significantly shorter for the dyad species, almost all emission can be attributed to the longer lifetime and giving a total emission lifetime $\sim\tau_2$ (30 ps).

With similar treatement of the dimer, almost all emission attributable to the τ_1 component of the decay, gives a total emission lifetime of $\sim\tau_1$ (1.7 ps). The first implication of this third point can be taken as an indication that there is a greater B-band (S_2) interaction between chromophores in the dimer system when compared to the dyad [6-8]. The second is that the stacked dyad has the ability to display, to a small degree, behavior similar to the macrocycle (τ_1 < 100 fs) while the dimer has overall B-band emission which is faster than the dyad by more than an order of magnitude without having a sub-picosecond time constant. The combination of both effects can then be observed in the macrocycle, where no meaningful emission tail exists (dimer like) and a < 30 fs decay expresses 99% of total emission.

Conversely, the Q-band (S_1) emission lifetimes indicate that the dyad relaxes significantly faster than the dimer from the Q-band excited state, indicating a greater degree of Q-band coupling between porphyrins in the stacked configuration. Given that the B-band principle dipole moment is in the direction of the primary molecular axis in these chromophores and the Q-band's dipole moment orthogonal to this axis, it stands that this response is a direct result of B-to-B interaction in the more linear dimer, while Q-Q interactions dominate in the slipped-cofacial dyad [6,8]. The result of combining these properties in large macrocycles where multiple B-B couplings and Q-Q coupling can occur (along with B-Q coupling as the angle of interaction changes throughout the arc of the ring) is a species uniquely qualified to rapidly observe excited state relaxation from the $S_2 \rightarrow S_1 \rightarrow S_0$ with a tremendous amount of electronic communication between building blocks. MOPAC calculations [1] indicate that the 17-mer relax even faster from $S_2 \rightarrow S_1$, however as the 11-mer response is already at the limit of our detection (<30 fs) a direct comparison could not be made. A summary of the ultrafast emission kinetics are provided in table 6-1.

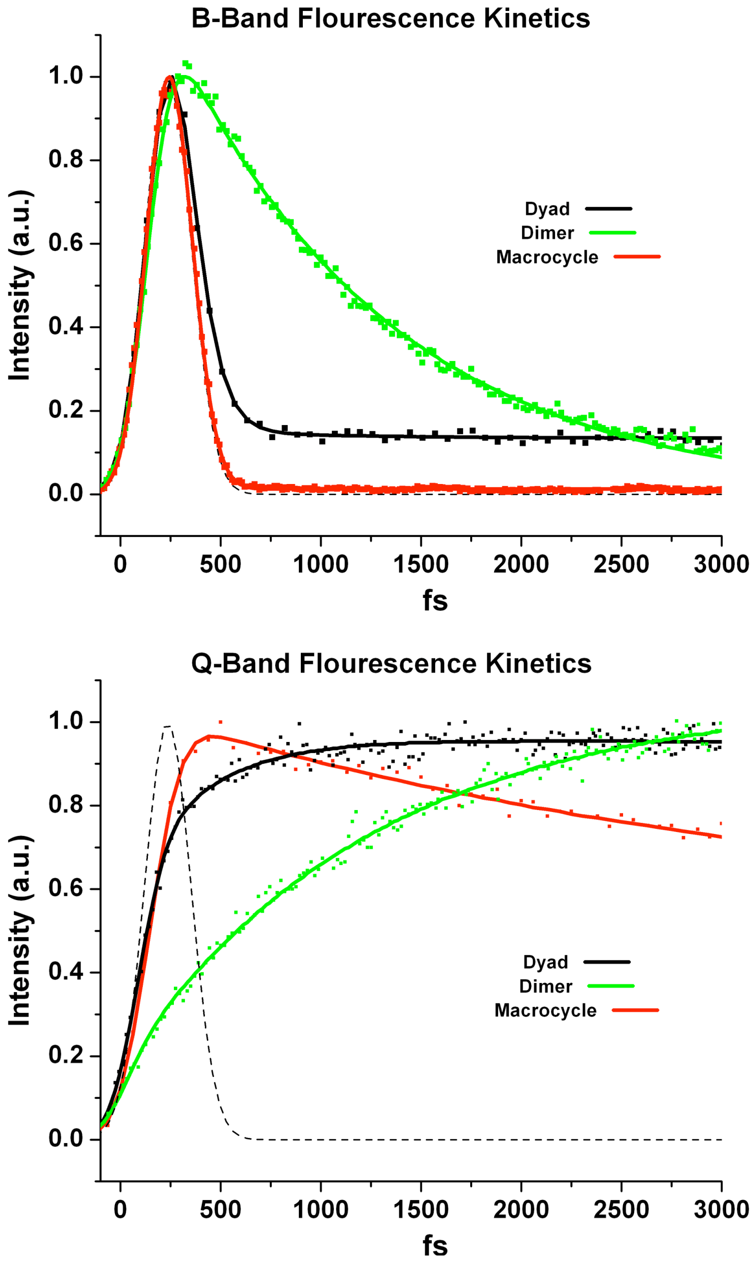

Figure 4-5. Ultrafast Fluorescence Kinetics for the B-band (top) Emission and Q-band (bottom) Emission in the 0-3 ps Regime after 415 nm Excitation

The experimental systems instrument response function is provided (- - - -) for reference.

4-7 Ultrafast Emission Anisotropy Spectroscopy

In order to further elucidate the ultrafast behavior of these systems, fluorescence up-conversion anisotropy spectra were generated for both emission bands for each sample. This is done during the ultrafast emission collection by comparing parallel and perpendicular emission polarizations compared to the excitation polarization. Here, in the first three picoseconds, emission anisotropy can be taken to implicitly indicate the degree of exciton delocalization in a system where $r = 0.4$ indicates emission which has completely localized character and $r = 0$ indicates emission which has been completely delocalized. This is in contrast to longer time scale (ps and ns) anisotropy techniques where the anisotropy signal is a combination of delocalization, longer range conformational changes and molecular rotation.

Observing the B-band emission (figure 6-6) it can be observed that shortly after the initial excitation, all species have an immediate loss of anisotropy. The r_0 values are a good indication of the initial isotropy shortly after excitation in these systems and follow the trend dimer > dyad >> 11-mer macrocycle. The initial B-band anisotropy in the macrocycle, by the end of primary emission, drops to zero and indicates a completely delocalized excited state. The observed residual anisotropy after 500 fs is of only nominal worth for describing the macrocycle behavior, as virtually all B-band excited states have relaxed.

However, when contrasting the dyad and dimer a very strong difference in behavior becomes apparent, especially in light of the emission kinetics discussed earlier. The apparent rise in anisotropy in the B-Band of the dyad and macrocycle is not a formal increase in excited localization, but rather illuminates that the excitons which have delocalized character relax immediately, leaving only the longer lived states (observed as a tail in the emission kinetic plots) to emit. The high anisotropy ($r = 0.33$) of the long lived state is a very clear indicator of a localized excited state which does not span the entire dyad. The dimer, in contrast, displays a more typical anisotropy decay and can be taken to indicate a single exciton type in the B-band with a single relaxation pathway that possesses a fair degree of delocalized character (r ~0.1). This is in keeping with the aforementioned single, short (1 ps) lifetime observed for the dimer. From this it can be taken that B-band delocalization in the dyad system is, taken over the entire duration of S_2 population after excitation, actually lower than the dimer despite the possibility of some ultrafast delocalized states. This finding strongly supports the B-B coupled dimer behavior observed in the fluorescence lifetime spectra.

Q-band anisotropy for all three species remain below 0.1 during the entirety of emission. However, subtle differences in the anisotropy over time reveal several characteristics of these systems. First, the delocalization in the macrocycle emission is uniformly lower that of the dimer and dyad and the anisotropic character of the emission is established earlier than either of the subunit species. This is understandable given the high degree of delocalization of the macrocycle B-band initial emission and the fast rate at which the Q-band populates. Secondly, the Q-band anisotropy in the dyad system also mimics its B-band emission, with anisotropy rising to a maxima once the B-band begins to display localized emission character and the $S_2 \rightarrow S_1$ interconversion is limited to is the relaxation of highly oriented S_2 excitons.

The difference in the anisotropy in both bands after ultrafast relaxation (>700 fs) for the dyad is very large ($\Delta r = 0.26$) and indicates a gross degree of additional delocalized character becoming inherent to the system after transition to S_2. Similar to the delocalization observed in dimer B-band emission, this confirms the assertion that Q-Q coupling, hence Q-band delocalization, is enhanced in the dyad system. A similar assessment regime can be use in evaluating the delocalization observed from Q-band emission when compared to the B-band emission in the dimer. The degree of anisotropy change ($\Delta r = 0.04$) is significantly reduced and displays a limited Q-Q coupling in the dimer configuration.

Taking these findings in total, a picture arises as to the cause of delocalization and rapid relaxation in the macrocycle, one which will later direct our discussion of the ultimate cause for the extraordinary two-photon response in our synthetic light harvesting system. The ultrafast response of the macrocycle should be attributed to the strong transition dipole moment of the B-band (8-15 Debye) [2-

6] being enhanced by a coherent coupling between aligned and adjacent chromophores allowed by the dimer contribution to the response. The moderately weak dipole of the S_1 band (~1 Debye) [2-6] is similarly coupled via the slipped cofacial arrangement contributed by the dyad type component in the response of the macrocycle. These effects are not observed simultaneously in either the dimer or the dyad. Additionally, the change in orientation through the arc of the macrocycle allows for B-Q interactions between both adjacent and distant chromophores and generates faster relaxation (orders of magnitude) and complete delocalization which the individual dimer and dyad subunits cannot provide in isolation. We must then attribute the macrocycle response to a new electronic state spanning multiple dimer units which demands both cofacial interactions and a multiple chromophores conjugation pathway as a result of the combined B-B (dimer), Q-Q (dyad) and B-Q (ring) band interactions.

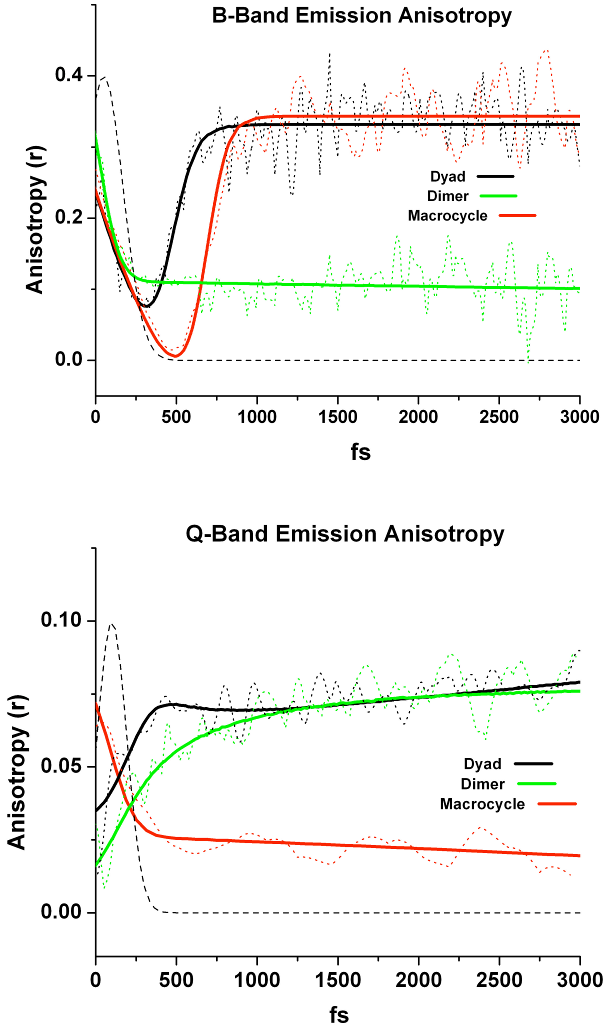

Figure 4-6. Ultrafast Anisotropy Kinetics the B-band (top) Emission and Q-band (bottom) Emission Anisotropies in the 0-3 ps Time Regime After 415 nm Excitation

The experimental systems instrument response function is provided (- - - -) for reference.

4-8 Ultrafast Transient Absorption Spectroscopy

In order to further elucidate the degree to which excited state interconversion from S_2 to S_1 is enhanced by additional dimers in the assembly, a fs-pulsed transient absorption system [14] was used to probe the kinetics of macrocycle complexes of differing sizes. In brief, monochromatic fs-pulses are used to excite a sample, and changes in a fs-pulsed white light probe signal are recorded over time. The primary signal from transient absorption studies is the change in intensity of absorption in the probe pulse as a function of time and wavelength after initial excitation. Typically, this signal is discussed in terms of the photobleach regions, where ΔA is negative, and excited state absorption regions where the signal is positive. Photobleaching is an indication of a denied transition from the ground state to a given excited state, usually overlaps reasonably well with steady state absorption wavelengths, and will be the primary material response of interest for purposes of this discussion. Relaxation in photobleach regions are typically associated with excited state relaxation (e.g. a transition becoming allowed again) while a growth in the photobleach intensity after excitation in a region is typically associated with the "arrival" of electrons from a higher excited state into the band of interest.

The primary bleach regions after 430 nm excitation of two macrocycles of different sizes, a 11 dimer macrocycle and a 17 dimer macrocycle, had maxima at 485 nm and 673 nm for both species, with representative spectra for the 11-mer presented in figure 6-7. Observing first the B-band photobleach region, at 485 nm, the 11-mer displays a significantly slower relaxation (τ_1 = 1 ps) than that observed in the larger 17-mer (τ_1 = 300 fs) species in the ultrafast region (figure 6-8), with significantly higher amplitude for the 17-mer sample. Taken with the ultrafast fluorescence data presented earlier, this points to a gross increase in the degree of S_1-S_1 interactions between dimers and indicates an excited state effected not just by one or two dimer units, but rather the entire ring structure. The second time constant for both macrocycle species is similar, τ_2 = 2.3 ps, and is consistent our emission studies where the majority of relaxation was shown to occur well before this time. This indicates that the architectural effects on dipole coupling in these systems are primarily observed over the first few hundred fs in the B-band.

Further confirmation that the addition of dimers to the cyclic array enhances the degree of S_1-S_2 coupling can be observed in the 673 nm region of the pump-probe kinetics (figure 6-8). Immediately after excitation, excited state absorption can be observed in the Q-band region of both macrocycles. The onset of Q-band excited state absorption prior to B-band depletion indicates that in the first moments of S_2 excitation transitions from S_0 to S_1 become more likely. This again points to a high degree of S_2-S_1 dipole coupling where the S_2 transition dipole is acting on the relatively weak S_1 moment. It also shows that the macrocycle species may be capable of possessing multiple excitons in a single molecule, something which could not be observed from ultrafast emission or steady state results alone. This is a reasonable given the gross number of chromophores per molecule (n= 22 and 34 respectively). The implication of a S_2* coupled S_0-S_1 absorption, when observing the faster onset of excited state absorption in the 17-mer Q-band photobleach region, would be that a greater degree of coupling is present in the larger structure. The increased rate of excited state absorption decay is also indicative of the rapid transition of the delocalized exciton from S_2 to an intermediate state, subsequently leading to the onset of S_1 population. This is observed to occur at a faster time scale and more strongly in the Q-band signal of the 17-mer (130 fs, ΔA_{max}= -0.07), when compared to the 11-mer (170 fs, ΔA_{max}= -0.015), and goes still further towards illuminating the increased $S_2 \rightarrow S_1$ rate of interconversion in the presence of additional dimer units. Again, as in the B-band photobleach region, the longer time scale Q-band kinetics remain unaffected with change in ring size and make clear that the primary effect of enhanced coupling B-Q and Q-Q band interactions are observable only on the fastest time scales. Collectively, these results indicate coherent delocalization which is effected by coupling throughout the entire macrocyclic assembly during excitation with differences observable in the transient absorption and two-photon enhancement for the two macrocycle sizes, and unobservable in the steady state. While this study focuses purely on the first 3 ps of transient response, a representative kinetic scan for both the B-band and Q-band regions are presented in figure 6-9 for the 11-mer species to display kinetics at longer time scales. A summary of the transient absorption kinetics and two-photon response of both macrocycle sizes are presented in table 6-2

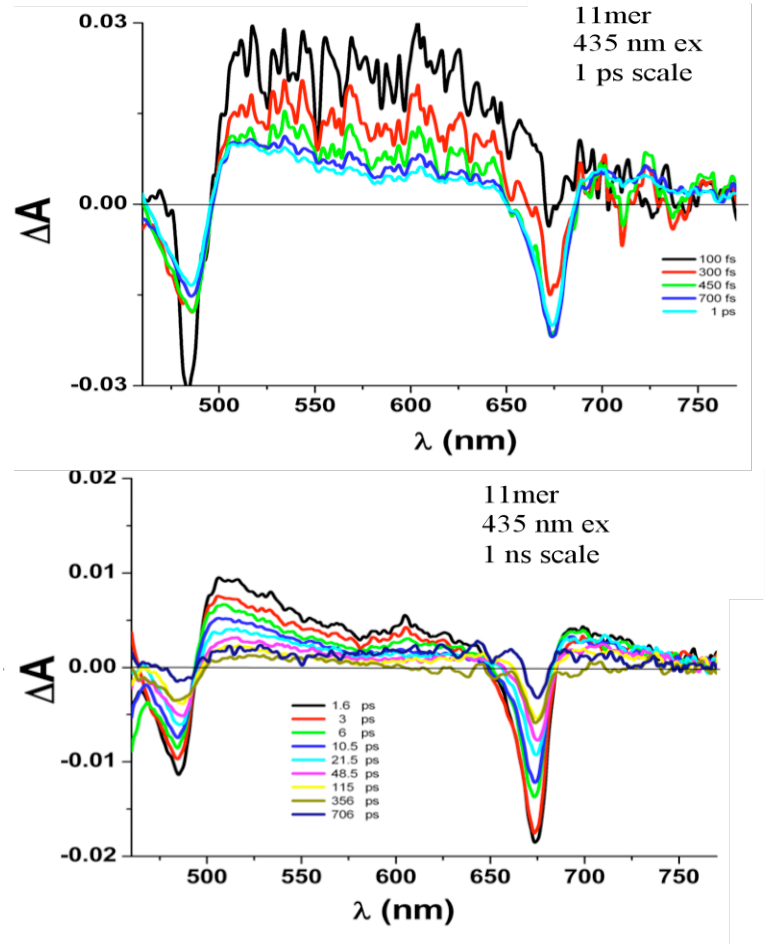

Figure 4-7. Transient Absorption Representative Spectra for the 11-mer Macrocycle for Two Different Kinetic Periods

A 0-1 ps time scale displaying the initial B-band photobleaching growth of the Q-band photobleaching (top) and the 1-700 ps time scale showing relaxation of both photobleach regions (bottom).

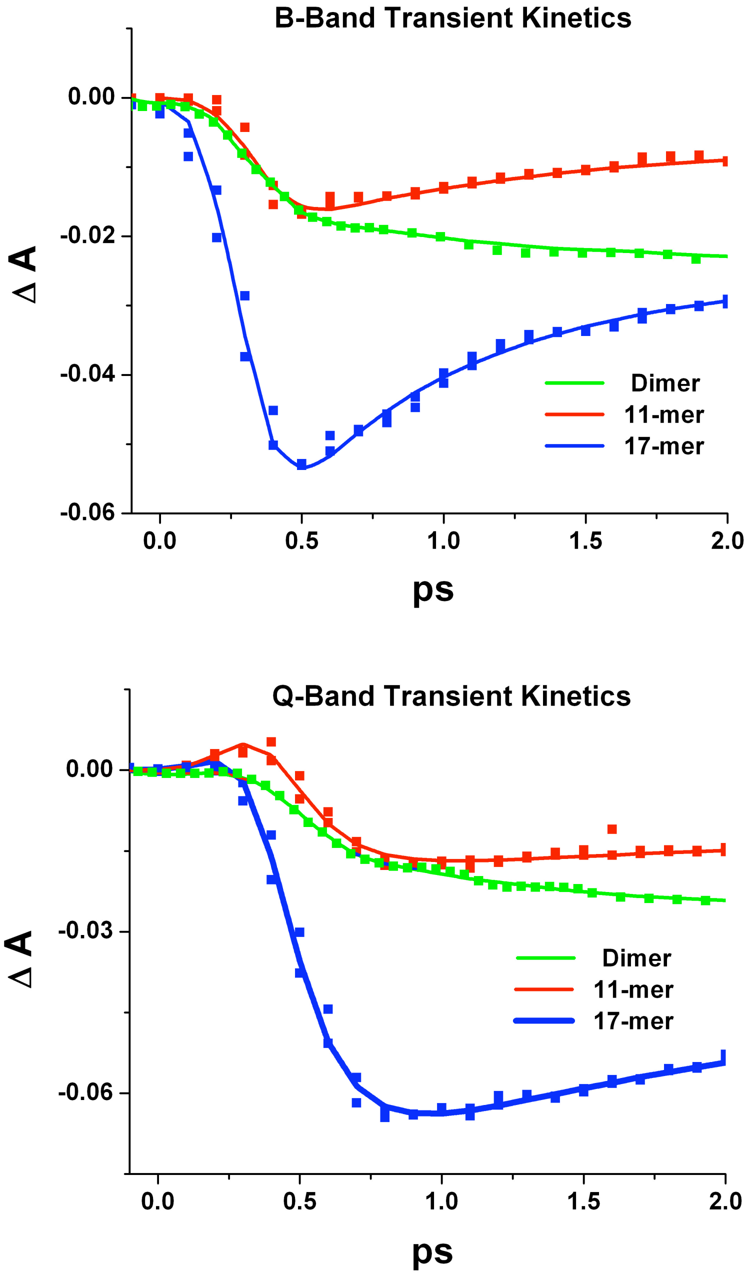

Figure 4-8. Ultrafast Transient Kinetics for the B-band Photobleach Region (top) and the Q-band (bottom) Photobleach Regions for Two Sizes of Macrocycle in the 0-2 ps Regime

The dimer kinetics are provided for comparison.

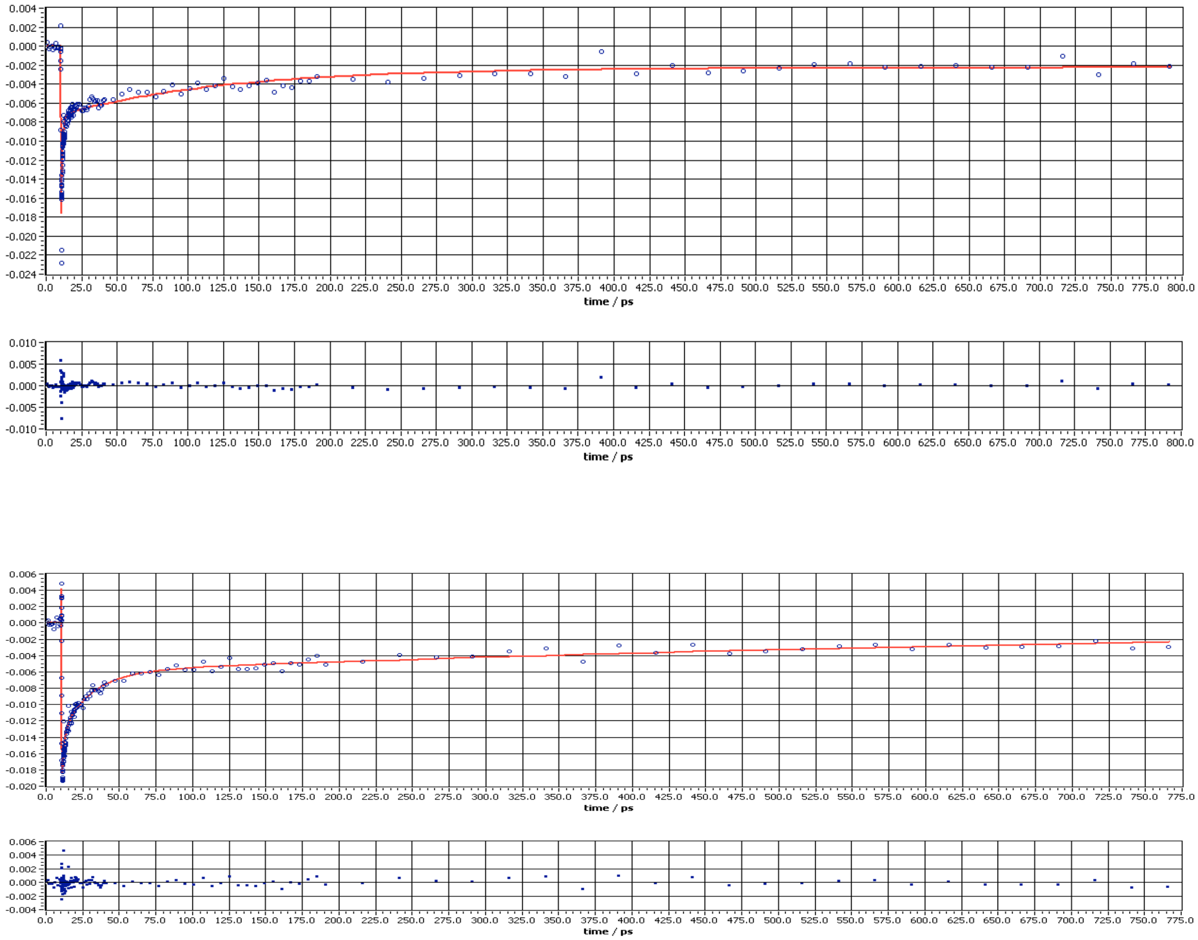

Figure 4-9. Long Time Scale (0-800 ps) Kinetics for the 11-mer Macrocyclic Species

The B-band photobleach region (top) and Q-band photobleach region (bottom) with fitting residuals provided below each.

Table 4-2. Transient Kinetic Time Constants for Both Macrocycle Species

Species	ε_B/dimer	σ_2/dimer	Population Lifetimes (Pump Probe)			
			τ_{1B} (ps)	τ_{2b} (ps)	$\tau_{ESA,Q}$ (fs)	τ_{1Q} (ps)
11-mer (3)	17.1	37000	1	2.3	170	2.4
17-mer (3a)	19.1	40000	0.3	2.3	130	2.2
One photon molar extinction coefficients reported in units of 10^4 $M^{-1}cm^{-1}$, two photon cross sections reported in units of GM						

4-9 Two-Photon Excited State Fluorescence Spectroscopy.

We have reported the two-photon absorption cross-sections (TPACS) for the 11-mer (37000/dimer), 17-mer (40000/dimer) and dimer (572) have been reported [1]. Two-photon cross-sections are reported in units of GM (cm^4/photon-second). For this study, where we probe the cause of this enhancement through excited state studies of the individual interactions (dimer, dyad) as well as ensemble effects (11-mer, 17-mer), it was necessary to determine the two-photon response of the dyad species. Characterization used the TPEF method [1,12]. In this method a two photon emission standard and the sample are excited by a fs-pulsed laser and emission from two photon excitation is collected.

The two-photon absorption maxima for the dyad was found to be 790 nm with a cross-section of 420 GM/dyad determined. The cross-sections of the dyad and dimer were found to be comparable, despite very different modes of chromophore coupling. From the ultrafast studies discussed previously in detail, it is clear that the B-band interaction between chromophores in the dimer species is significantly stronger while the Q-band interactions are enhanced between chromophores in the dyad. By contrasting these TPACS findings with a known porphyrin standard tetraphenylporphyrin (TPP) where the cross-section per porphyrin is ~10 GM, it is clear that both B-B and Q-Q coupling between porphyrin units can play a significant roll in generating a high cross-section species. Transient absorption studies and the 10% TPACS enhancement per dimer observed when comparing the 17-mer to the 11-mer shows that the number of units contributing to the ensemble response are also critical to any discussion of the cause of this enhancement. Combining the steady state absorption, excited state behavior and a diagram of dipole interaction in figure 6-10, it can be illustrated that the combination of dimer and dyad behavior in a single macrocycle results in a strongly coupled system in which delocalization rates, relaxation rates and the density of states are all significantly increased. This informs how the TPA enhancement from ensemble dipole coupling in the cyclic system may be discussed. In figure 6-11 a proposed mode of action for the dyad, dimer, 11-mer, 17-mer and tetraphenylporphyrin (TPP) with regards to increased two-photon cross-section is presented.

Initially considering a non-interacting chromophore, TPP has a TPACS similar to other weak TPA standards (15 GM) [15] and one notices that the intermediate S_1 band (near 500 nm for TPP) has poor energy matching with the two-photon virtual state (TPAVS). Without a near lying state, the TPAVS is not band-stabilized, allowing for no additional TPA enhancement through TPAVS interactions. Additionally, neither B-band nor Q-band splitting is observed to a large degree in TPP, which is in part due to a lack of metallated core, but is also an effect of its single chromophore status. This decreases the number of available states into which a two-photon excited state could be generated and prevents multiple bands from deeply influencing the TPAVS stability. With no inherent interaction between the Q- and B-bands (do to the intrinsic orthogonallity of these states transition dipole moments) even if the Q-band/TPAVS energy matching was better, the similarity of the stabilized state (Q-like) would not necessarily generate a virtual state which promotes readily to a B-band excited state.

Having addressed some the properties which contribute to a nominal two-photon response, it then becomes easier to discuss the moderate enhancement that is observed in the dyad and dimer. At first glance, comparison of the two species TPACS would imply a similar degree of enhancement over a single porphyrin monomer. However, given the differences in band coupling outlined earlier in the ultrafast studies, the type of interactions which generate the sizable TPACSs observed in the two bisporphyrin systems (comparable in terms of magnitude of cross-section increase) are intrinsically different. Specifically, the primary mode of dipole coupling for the dyad system is one in which the Q-band/Q-band interactions between porphyrins are enhanced. This leads to a much stronger Q-band stabilization of the TPAVS, in turn resulting in a TPACS which is larger by more than an order of magnitude than that of two individual TPP molecules.

Regarding dimer TPACS enhancement, a similar discussion can be held concerning B-band coupling and the two-photon excited state. In the ultrafast lifetime measurements we observed strong B-band/B-band interactions between porphyrins in the bridged dimer. This leads to a larger degree of B-band broadening (greater number of states) and generally makes the two-excited state more viable.

While a full investigation into the implicit transition dipole moment strengths of the dyad and dimer are beyond the scope of this study, a general description of these behaviors can be suggested from these observations. First, the typical transition dipole moment strength for Q-band and B-bands in porphyrins are known (~1 dB and ~10 dB respectively) and can be used roughly to approximate the strength of interactions in a general case. From this, we can approximate that the maximum interaction for a Q-Q coupled bisporphyrin system as one order of magnitude weaker than in a closely bound B-B coupled system. By comparing the approximate strength of coupling to the TPA cross-sections observed we find them similar, and can then assert that the ten-fold weaker change in Q-band moment generates only slightly less of an effect than that of the significantly stronger change in B-band moment. This means that, for these systems, the Q-band coupling is roughly 10 times more important to generating a viable two-photon excited transition than B-band coupling when accounting for the differences in dipole moment strength between bands. While in no way rigorous, this qualitative assessment is not a trivial finding, as it will illuminate to a large degree the cause of the extraordinarily large TPACSs observed in the macrocyclic species where both effects are in play. Turning to the 11 dimer and 17 dimer macrocycles, it is reasonable to expect at least the same degree of TPACS enhancement as we observed in either the dyad or the dimer cases. In fact, we find that the cross-section per dimer is actually two orders of magnitude higher for the macrocycles when compared to either the dimer or the dyad, with the 17-mer enhancement being higher than that of the 11-mer.

Given the importance of Q-band coupling to TPACS outlined above, for the macrocycle species we must assume some additional enhancement of the Q-band beyond that provided in Q-Q coupling from adjacent cofacial porphyrins. This points towards some architectural property which allows for B-band (10 times stronger than the Q-band dipole moment) dipole coupling to the Q-band. This is linked to the positioning of additional dimers, beyond a single dimer-dimer interaction, where the configuration orients the spatially separated dimers in such a way as to allow the B-band dipole moment in one dimer to have a direct effect on distant Q-band dipole moments. Therefore it is reasonable to posit a B-Q coupling which is distant, and strong enough to significantly enhance the viability of the TPAVS. This effect need not be as strong as a fully expressed B-Q dipole coupling in order to see a marked increase in TPACS, given the importance of Q-band coupling derived from assessment of the dyad case. This is because of incidental effects that manifest in the system as a result of the B-Q coupling. Namely, one can reasonably assert a degree of increase in the availability of states in the Q-band as supported by steady state absorption band broadening. Additionally, the Q-bands tendency to have “B-band like” electronic properties is increased significantly through such an interaction. In support of this claim, we turn again to the ultrafast kinetics where we have seen clearly that the interconversion rates between B- and Q-bands are significantly impacted by the transition from dyad or dimer type interactions to cyclic species where both interactions are present, and further increased with the addition of more dimers into the macrocycle.

Taken together, the additional enhancement in the TPACS in the macrocycle can be summarized as follows: (1) dyad stacking enhances TPAVS stabilization, (2) bridged dimer character includes a more viable TPA excited state, (3) cyclic architecture provides for B-Q coupling which further enhances TPAVS stabilization, and that (4) this also leads to a TPAVS which, through Q-band stabilization where the Q-band has some B-band character, is much more viable for the generation of a TPA excited state in the B-band.

When comparing this effect in larger macrocycles we have shown that increasing the number of interacting dimers increases all of these effects, resulting in TPA cross-sections in the 17-mer which are ~10% higher per building block when compared to the 11-mer macrocycle. When comparing this effect to our previously reported TPA enhancement maxima in a 19 dimer macrocycle, the enhancement is ~40% higher than in the smaller 11-mer macrocycle. Continued TPACS enhancement with increasing dimer number dictates a delocalization length for the excited state which maps onto the entire macrocycle.

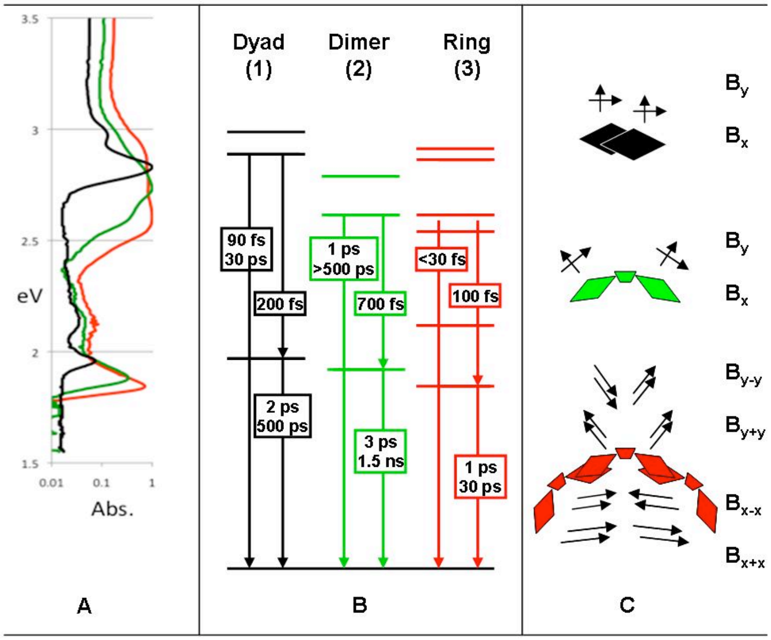

Figure 4-10. Dipole Interactions in Zinc Porphyrin Structures

(A) log scale steady state absorption in eV, (B) band model with fluorescence lifetimes and (C) dipole interactions in the three species observed.

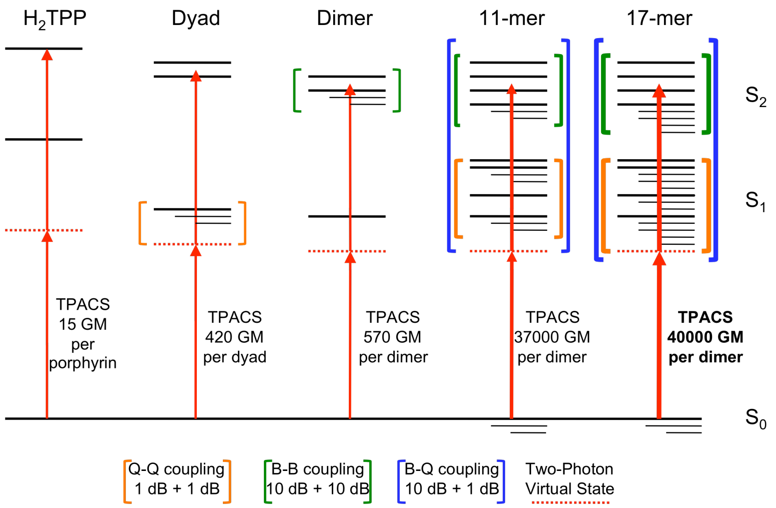

Figure 4-11. Two-Photon Enhancement Through Architecturally Induced Interband and Intraband Coupling in Zinc Porphyrin Systems

Displayed here: a conceptual scheme showing TPP (no enhancement), the dyad (good TPAVS stablization), the dimer (good TPA target state), and the macrocycles (both effects for the 11-mer and further enhancement in the 17-mer).

4-10 Comparison to Natural Light Harvesting Systems

With the motivation for the generation of these macrocycles being fully rooted in an intentional mimicry of naturally occurring light harvesting (LH) complexes, it is appropriate to compare our system to a well known natural system. One of the reasons researchers seek this synthetic mimicry of natural light harvesting systems is the near 100% energy transfer after photoexcitation in LH systems and the extremely rapid rate of delocalization. To this effect, we will discuss the well studied LH1 complex of purple photosynthetic bacteria [16-19]. A typical LH1 complex in this species is a cyclic system in which a large ring of slipped cofacial porphyrins, as part of bacteriochlorophyll molecules, are dimerized and bound to each other through a stabilizing protein scaffold. While some variation between species exists, the typical LH1 complex in purple bacteria average 27 porphyrins per ring. However, in isolation LH complexes are very delicate, easily disassociated and prone to photodamage. In terms of functional materials, this points instead to capturing some of the optoelectronic response observed in these natural systems through an artificial analog where stability can be enhanced. The macrocycles addressed in this study are self assembled from zinc porphyrin dimers into a ring bound by slipped cofacial interactions and further tethered through a ring closing reaction of pendent groups which provide increased stability over the natural system where no covalent binding exists.

The number of porphyrins in the macrocycles presented here are 22 and 34 (11-mer and 17-mer), but we will focus on the 11-mer for purposes of this comparison. Considering the rate at which the primary excitation band transfers energy to other locations, our synthetic system far surpasses the natural system with lifetimes that are well over an order of magnitude faster (<30 fs in the macrocycle compared to 700 fs in LH1) [16]. This indicates that the dimer interaction leads to much more coherent electronic coupling between building blocks in the synthetic system. The Q-band excited state lifetime is also another metric by which to compare these systems, as it is far longer than the B-band lifetime and is the major contributor to the chromophore's overall time spent in the excited state after excitation. For the natural LH1 system, a typical excited state lifetime is 1 ns [17]. The macrocycle is again significantly faster in its energetics, providing a primary lifetime of 30 ps. This two-order of magnitude difference is again indicative of a much more strongly coupled system where a lowest energy state can be rapidly achieved through delocalization over the bulk of the system. The delocalization length of excitons in LH1 is also known, spanning ~9 porphyrin units [18]. In the synthetic system we find total delocalization immediately after excitation and, given the ultrafast and two-photon response observed with the addition of more dimers, we observe that the entire ring of 22 porphyrins is included in the delocalization length. Delocalization findings primarily indicate a greater degree of coherent electronic communication in the synthetic system.

Finally, let us compare the TPACS per ring. The enhanced interband coupling found in the macrocycle species provides an extraordinary increases in cross-section when compared to the natural system. Comparing the per dimer cross-section for each we note 80 GM for the LH1 [19] system and 37,000 per dimer in the 11-mer system. This leads to an enhancement of close to three orders of magnitude per ring when we compare our most TPA active macrocycle to the LH1 system.

4-11 Conclusion

Other species containing bi-acetyl linkages between porphyrins [20-21] have not shown this degree of singlet state coupling, nor have they been observed to provide the two-order of magnitude TPA enhancement on assembly that the macrocycles considered here provide. The contrast lies in the fact that other architectures, while possessing similar slipped cofacial interactions or sp hybridized bridging, lack the orientational requirements which our system possesses, have a limited number of interacting chromophores per cyclic structure or a broken electronic communication pathway between units. This study shows that the acetyl fluorene bridged dimer can be made to provide an ultrafast energy transfer in the presence of properly coupled transition dipole moments, with delocalization and B→Q relaxation rates which surpass those occurring in LH complexes and leading to exceptional two-photon response. This cofacial/pi-bridge structure with many interacting porphyrin units allows for delocalization over the entire structure by way of dyad-type stacking, despite a lack of conventional conjugated linkages between the individual dimer units. Excited state lifetimes for the B-band of these macrocycles are shown to be shorter by an order of magnitude over the lone dimer system with anisotropies less than 0.01, having strong implications for applications such as light harvesting, optical switching and remote sensing. Further probing of the relationship between ring size, two-photon absorption and ultrafast delocalization confirms additional enhancement in structures with more interacting units. In total, these findings lead to more complete picture of what architectural requirements are needed to allow for these strong intraband and interband couplings to promote extraordinary nonlinear optical response and energy delocalization rates.

4-12 Experimental

Steady State Spectroscopy. Absorption spectra of the molecules were measured using an Agilent (Model # 8341) spectrophotometer. Steady state emission spectra were acquired using a Jobin Yvon Spex Fluoromax-2 spectrophotometer.

Ultrafast Fluorescence Up-Conversion Spectroscopy and Anisotropy Measurements The time-resolved fluorescence of the dimer, dyad and 11-mer macrocycle were studied using femtosecond up-conversion spectroscopy. This was achieved using a Spectra-Physics Tsunami laser, frequency doubled to a 415 nm excitation source. A CDP Systems Inc. FOG set up was used to probe emission. Emission intensity was measured by a Hamamatsu R1527P PMT. Analysis was performed using Origin 8 software.

Ultrafast Transient Absorption Spectroscopy. Femtosecond transient absorption investigations have been carried out on the 11-mer and 17-mer macrocycles as well as the dimer species. Excitation was obtained from a Nd:YLF (Evolution) pumped Ti:Sapphire regenerative amplifier (Spectra Physics, Spitfire) with input from a Millennia-pumped Ti:Sapphire oscillator (Spectra Physics, Tsunami). The pump beam was produced by an optical parametric amplifier (OPA-800) at 435 nm. Changes in the white light probe pulse were collected by CCD detector (Ocean Optics). Data acquisition is controlled by software from Ultrafast Systems Inc. Data fitting and deconvolution at less than 10 ps was done using Surface Xplorer software. Data fitting at longer times was performed using Origin 8 software.

Two-Photon Excited State Fluorescence. The two-photon excited fluorescence (TPEF) method involves monitoring the fluorescence intensity as a function of incident intensity and is detailed for both the dimer and macrocyclic species elsewhere [1]. For this study we also report for the first time the dyad TPA cross-section and the method for determination follows in brief. The laser source used in our experiments is a tunable Ti:Saphire laser (Mai-Tai, Spectra Physics). The input intensity can be regulated using a neutral density (ND) filter designed for femtosecond pulses. The fluorescence is measured by a photomultiplier tube (PMT) (R7518P, Hamamatsu). A counting circuit (M8485 counting board, C3866 counting circuit, Hamamatsu) assembly, which is interfaced with a computer, converts the photocurrent from the PMT into an arbitrary number of counts. In this manner, the

TPEF intensity can be quantified. A two-photon excited process is ensured when a logarithmic plot of the TPEF intensity versus input intensity is a straight line with a slope of 2. The absolute two-photon cross-section is reported by comparison to the TPEF standard tetraphenylporphyrin.

Materials and Methods. Concentrations of 2 to 15 uM in a 7:3 solution of spectroscopic grade dichloromethane and pyridine were used for steady state, two-photon and fluorescence up-conversion measurements. For transient absorption measurements, optical densities of 0.1 were used for all samples, irrespective concentration. These measurements were also performed in a 7:3 solution of spectroscopic grade dichloromethane and pyridine.

4-13 Acknowledgement

Funding for this research was provided by the AFRL and NSF.

4-14 References

(1) Raymond, J.E.; Bhaskar, A.; Goodson, T. III; Makiuchi, N.; Ogawa, K.; Kobuke, Y. J. Am. Chem. Soc. 2008, 130, 17212.

(2) Timpmann, K.;, Rätsep, M.; Hunter, C.N.; Freiberg, A. J. Phys. Chem. B 2004, 108, 10581.

(3) D'Souza, F.; Maligaspe, E.; Ohkubo, K.; Zandler, M.; Subbaiyan, N.; Fukuzumi, S. J. Am. Chem. Soc. 2009, 131, 8787

(4) Oliveri, C. J. Am. Chem. Soc. 2006, 128, 16286.

(5) Williams-Harry, M.; Bhaskar, A.; Ramakrishna, G.; Goodson, T., III; Imamura, M.; Mawatari, A.; Nakao, K.; Enozawa, H.; Nichinaga, T.; Iyoda, M. J. Am. Chem. Soc. 2008, 130, 3252.

(6) Ogawa, K.; Zhang, T.; Yoshihara, K.; Kobuke, Y. J. Am. Chem. Soc. 2002, 124, 22.

(7) Raymond, J.E.; Goodson, T. J. Phys. Chem. Lett. 2011, 2, 329.

(8) Chang, M.; Hoffman, M.; Anderson, H.; Herz, L. J. Am. Chem. Soc. 2008, 130, 10171.

(9) Ogawa, K.; Ohashi, A.; Kobuke, Y.; Kamada, K.; Ohta, K. J. Phys. Chem. B 2005, 109, 22003.

(10) Drobizhev, M.; Stepanenko, Y.; Rebane, A.; Wilson, C.; Screen, T.; Anderson, H. J. Am. Chem. Soc. 2006, 128, 12432.

(11) Ahn, T.; Kim, K.; Noh, S.; Aratani, K.; Ikeda, C.; Osuka, A.; Kim, D. J. Am. Chem. Soc. 2006, 128, 1700.

(12) Raymond, J.E.; Ramakrishna, G.; Twieg, B.; Goodson, T. J. Phys. Chem. C. 2008, 112, 7933.

(13) Guo, M.; Varnavski, O.; Narayanan, A.; Mongin, O.; Majoral, J.; Blanchard-Desce, M.; Goodson, T. J. Phys. Chem. A 2009, 113, 4763.

(14) Wang, Y.; He, G.; Prasad, P.; Goodson, T.; J. Am. Chem. Soc. 2005, 127, 10128

(15) Drobizhev, M.; Karotki, A.; Kruk, M.; Rebane, A. Chem. Phys. Lett. 2002, 355, 175.

(16) Jimenez, R.; van Mourik, F.; Yu, J.Y.; Fleming, G.R. J. Phys. Chem. B 1997, 101, 7350.

(17) Freiberg, A.; Jackson, J.A.; Lin, S.; Woodbury, N.W. J. Phys. Chem. A 1998, 102, 4374.

(18) Dahlbom, M.; Pullerits, T.; Mukamel, S.; Sandstrom, V. J. Phys. Chem. B 2001, 105, 5515.

(19) Abe, S. Chem. Phys. 2008, 349, 244.

(20) Park, M.; Yoon, M.; Yoon, Z.; Hori, T.; Peng, X.; Aratani, N.; Hotta, J.; Uji-I, H.; Sliwa, M.; Hofkens, J.; Osuka, A.; Kim, D. J. Am. Chem. Soc. 2007, 129, 3539.

(21) Kochezhenko, A.; Patwardhan, S. Grozema, F.; Anderson, H.; Siebbeles, L. J. Am. Chem. Soc. 2009, 131, 5522

4-15 Biography

Author biographies as submitted.

Figure 4-12. Professor Theodore Goodson III

Theodore Goodson III holds the Richard Barry Collegiate Professorship in Chemistry at the University of Michigan. His research focuses on the nonlinear and ultrafast spectroscopy of novel organic materials. A special interest is given macromolecular assemblies and the quantum effects which govern optoelectronic response in these systems.

Figure 4-13. Jeffery E. Raymond

Jeffery Raymond is a research assistant in the Macromolecular Science and Engineering program at the University of Michigan. His research interests include ensemble effects in biomimetic nanomaterials, near field imaging and multiphoton spectroscopy.

4-16 Supporting Information

Supporting Information as submitted:

Ultrafast Fluorescence Up-Conversion Spectroscopy and Anisotropy Measurements. The time-resolved fluorescence of the dimer, dyad and 11-mer macrocycle were studied using femtosecond up-conversion spectroscopy. The sample solutions were excited with frequency-doubled light from a mode-locked Ti-sapphire laser (Tsunami, Spectra Physics) operated as 830 nm and a repetition rate of 82 MHz. After frequency doubling in a BBO crystal, this produces pulses with a nominal standard deviation of 110 fs at a wavelength of 415 nm. The residual 830 nm beam is routed to a delay line through a 415 nm selective mirror. Our up-conversion apparatus consists of the basic unit of the FOG-100 system (CDP Inc.), in which the 830 nm doubling, excitation, and emission up-conversion occurs. The polarizations of the excitation beam for the anisotropy measurements were controlled with a Berek compensator. The sample cuvette was quartz, 1 mm thick and held in a rotating holder to avoid possible photo-degradation and other accumulative effects. The fluorescence emitted from the samples was upconverted in a non-linear crystal of BBO using the previously mentioned pump beam at 830 nm. This system acts as an optical gate and enables the fluorescence to be resolved temporally via a pump-excitation (830 nm & 415 nm beams) cross-correlation function with a FWHM of 190 fs. The gate step size in this system is 6.25 fs. Spectral resolution is achieved by dispersing the up-converted light in a monochromator and detecting it by use of a photo-multiplier tube (Hamamatsu R1527P). The average excitation power is kept at a level below 3 mW. At these excitation intensities, the fluorescence dynamics were found to be independent of the excitation intensity for all investigated solutions. For this system, B-band (S_2) emission kinetics were observed at 525 nm emission. Q-band (S_1) emission kinetics were observed at 675 nm for the macrocycle and dimer species, and at 650 nm for the dyad species. Anisotropy measurements were obtained from repeating the fluorescence lifetime measurements with parallel excitation and parallel emission (PAR) and again with perpendicular excitation and parallel emission (PER). Anisotropies as a function of time are then presented as a result of the following relationship, comparing the amplitudes of emission at a given time by r=(PAR+2*PER)/(PAR-PER) for each sample. Use of tetraphenylporphyrin as an anisotropy standard provided a G-factor of 1.00, meaning that no correction factor was needed. Data fitting and deconvolution at less than 10 ps was done using Surface Xplorer software. Maximum decovolution time resolution gives a minimum resolution roughly 1/6th of the cross-correlation fuction, or 30 fs. Data fitting at longer times was performed using Origin 8 software. All emission lifetimes are the result of multiexponential decay fitting. When contributions to total emission are presented for a given relaxation lifetime as a percentage, the percentage is given as a ratio of the separated and deconvoluted integrations for the decay, weighted by the fitted amplitude for each decay and compared to total emission.

Ultrafast Transient Absorption Spectroscopy. Femtosecond transient absorption investigations have been carried out using an ultrafast pump–probe spectrometer detecting in the visible region. This system contains 1-mJ, 100-fs pulses at 800 nm with a repetition rate of 1 kHz that were obtained from a Nd:YLF (Evolution) pumped Ti:Sapphire regenerative amplifier (Spectra Physics, Spitfire) with input from a Millennia-pumped Ti:Sapphire oscillator (Spectra Physics, Tsunami). The laser beam was split to generate pump and probe beam pulses with a beam splitter (85% and 15%). The pump beam was produced by an optical parametric amplifier (OPA-800). The pump beam used in the present investigation, 435 nm, was obtained from the fourth harmonic of the idler beam and was focused onto the sample cuvette. The probe beam was delayed with a computer controlled motion controller and then focused into a 2-mm sapphire plate to generate a white light continuum. The white light is then overlapped with the pump beam in a 2-mm quartz cuvette containing the sample, and change in absorbance for the signal is collected by a CCD detector (Ocean Optics). Data acquisition is controlled by software from Ultrafast Systems Inc. The typical energy probe beam is <0.1 μJ, while the pump beam is around ~1–2 μJ per pulse. Magic angle polarization has been maintained between the pump and probe using a wave plate. Pulse duration has been obtained from the nonresonant fitting of the solvent response, which is around 120 fs. The sample is stirred by a rotating magnetic stirrer, and little degradation of the sample was observed during the experiments, as inspected by steady state absorption and emission measurements before and after ultrafast excitation. Data fitting and deconvolution at less than 10 ps was done using Surface Xplorer software. Maximum decovolution time resolution gives a minimum resolution roughly 1/4th of the solvent response, or ~30 fs. Data fitting at longer times was performed using Origin 8 software. All transient lifetimes are the result of multiexponential decay fitting.

Two-Photon Excited State Fluorescence. The two-photon excited fluorescence (TPEF) method involves monitoring the fluorescence intensity as a function of incident intensity and is detailed for both the dimer and macrocyclic species elsewhere[1]. For this study we also report for the first time the dyad TPA cross-section and the method for determination follows in brief. The laser source used in our experiments is a tunable Ti:Saphire laser (Mai-Tai, Spectra Physics). The input intensity can be regulated using a neutral density (ND) filter designed for femtosecond pulses. The fluorescence is measured by a photomultiplier tube (PMT) (R7518P, Hamamatsu). A counting circuit (M8485 counting board, C3866 counting circuit, Hamamatsu) assembly, which is interfaced with a computer, converts the photocurrent from the PMT into an arbitrary number of counts. In this manner, the TPEF intensity can be quantified. A two-photon excited process is ensured when a logarithmic plot of the TPEF intensity versus input intensity is a straight line with a slope of 2. The absolute two-photon cross-section is reported by comparison to the TPEF standard tetraphenylporphyrin.

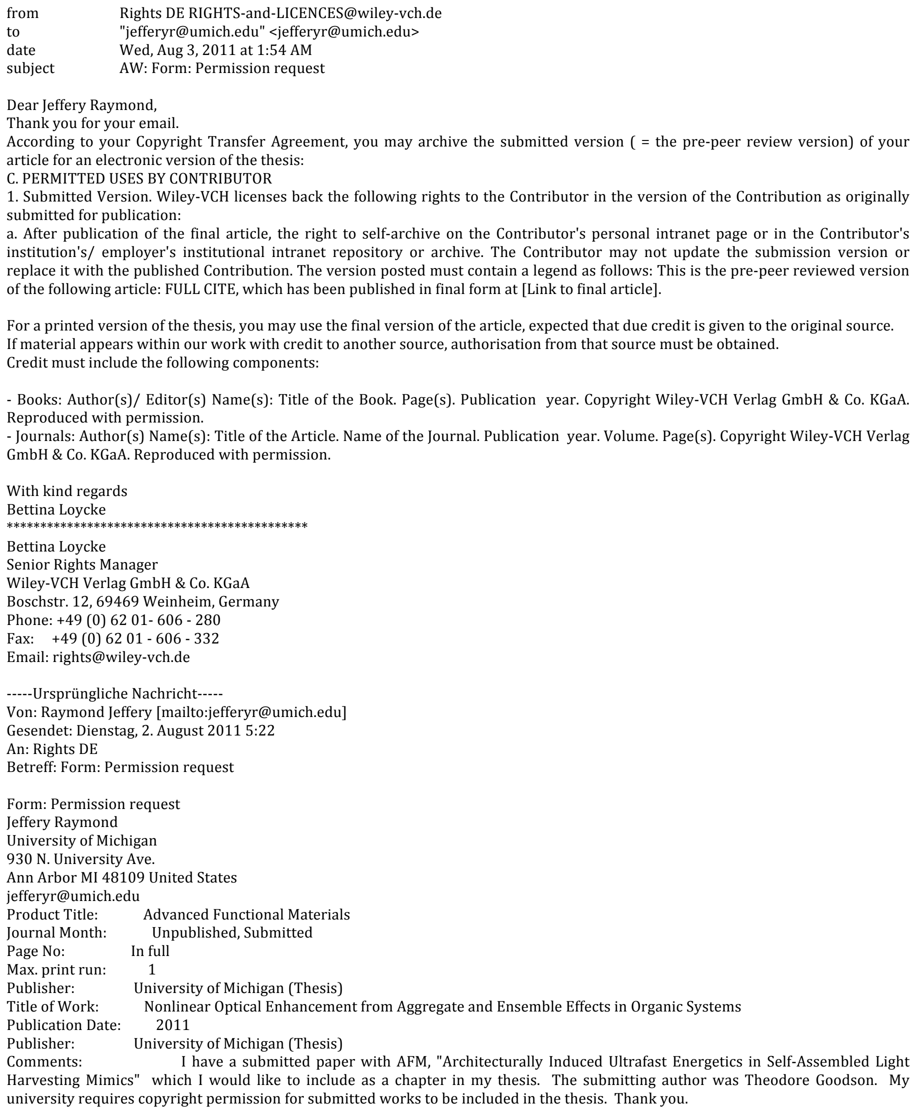

from Rights DE RIGHTS-and-LICENCES@wiley-vch.de
to "jefferyr@umich.edu" <jefferyr@umich.edu>
date Wed, Aug 3, 2011 at 1:54 AM
subject AW: Form: Permission request

Dear Jeffery Raymond,
Thank you for your email.
According to your Copyright Transfer Agreement, you may archive the submitted version (= the pre-peer review version) of your article for an electronic version of the thesis:
C. PERMITTED USES BY CONTRIBUTOR
1. Submitted Version. Wiley-VCH licenses back the following rights to the Contributor in the version of the Contribution as originally submitted for publication:
a. After publication of the final article, the right to self-archive on the Contributor's personal intranet page or in the Contributor's institution's/ employer's institutional intranet repository or archive. The Contributor may not update the submission version or replace it with the published Contribution. The version posted must contain a legend as follows: This is the pre-peer reviewed version of the following article: FULL CITE, which has been published in final form at [Link to final article].

For a printed version of the thesis, you may use the final version of the article, expected that due credit is given to the original source.
If material appears within our work with credit to another source, authorisation from that source must be obtained.
Credit must include the following components:

- Books: Author(s)/ Editor(s) Name(s): Title of the Book. Page(s). Publication year. Copyright Wiley-VCH Verlag GmbH & Co. KGaA. Reproduced with permission.
- Journals: Author(s) Name(s): Title of the Article. Name of the Journal. Publication year. Volume. Page(s). Copyright Wiley-VCH Verlag GmbH & Co. KGaA. Reproduced with permission.

With kind regards
Bettina Loycke
****
Bettina Loycke
Senior Rights Manager
Wiley-VCH Verlag GmbH & Co. KGaA
Boschstr. 12, 69469 Weinheim, Germany
Phone: +49 (0) 62 01- 606 - 280
Fax: +49 (0) 62 01 - 606 - 332
Email: rights@wiley-vch.de

-----Ursprüngliche Nachricht-----
Von: Raymond Jeffery [mailto:jefferyr@umich.edu]
Gesendet: Dienstag, 2. August 2011 5:22
An: Rights DE
Betreff: Form: Permission request

Form: Permission request
Jeffery Raymond
University of Michigan
930 N. University Ave.
Ann Arbor MI 48109 United States
jefferyr@umich.edu
Product Title: Advanced Functional Materials
Journal Month: Unpublished, Submitted
Page No: In full
Max. print run: 1
Publisher: University of Michigan (Thesis)
Title of Work: Nonlinear Optical Enhancement from Aggregate and Ensemble Effects in Organic Systems
Publication Date: 2011
Publisher: University of Michigan (Thesis)
Comments: I have a submitted paper with AFM, "Architecturally Induced Ultrafast Energetics in Self-Assembled Light Harvesting Mimics" which I would like to include as a chapter in my thesis. The submitting author was Theodore Goodson. My university requires copyright permission for submitted works to be included in the thesis. Thank you.

Figure 4-14. Email Transcript of Wiley-VCH Publishing Permission Granted to Publish in Thesis

Chapter 5

Building a Smaller Two-Photon Biomimic: Synthesis and Optoelectronic Enhancement of a Self-Assembled Porphyrin Macrocycle

5-1 Original Publication Information

This chapter has been submitted for publication as the following document:

> "Building a Smaller Two-Photon Biomimic: Synthesis and Optoelectronic Enhancement of a Self-Assembled Porphyrin Macrocycle"
>
> Jeffery E. Raymond, Zin Seok Yoon, Takefumi Yotsutuji, Kazuya Ogawa, Yoshiaki Kobuke, Theodore Goodson III
>
> *The Journal of Physical Chemistry Letters*, as submitted in Q3 of 2011

Modifications to the original document are cosmetic and used only to conform the format of this document or provide uniformity of enumeration.

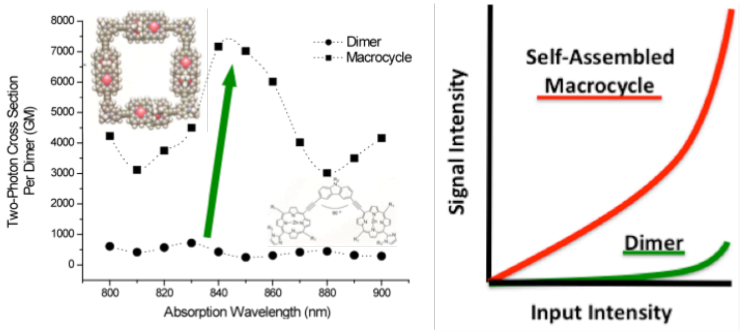

10x TPACS Enhancement Through Self Assembly

Figure 5-1. Table of Contents Figure as Submitted

5-2 Qualifying Statement

This chapter is a follow up to chapters 3 & 4 where a smaller, brighter two-photon material is sought. This material is still the result of porphyrin dimer self assembly, but is now using a 90 deg. bridge resulting in a single product, 4 dimer square with exceptional two photon fluorescence enhancement. No new techniques are introduced in this chapter.

5-3 Abstract

In this study we present the synthesis of a carbazole bridged porphyrin dimer system which possesses a 90° orientation change between porphyrin units and the single-product four dimer macrocycle formed on self-assembly of the dimer. Subsequent characterization of the two-photon absorption and ultrafast emission lifetimes of these systems indicates a very strong coupling between the Soret and Q bands in the assembled macrocycle structure. These interactions lead to a red-shifted two-photon response and a full order of magnitude increase in the absorption cross-section per building block with respect to the lone dimer. This points to the use of our small light harvesting mimic for nonlinear optical applications where aggregation effects have previously stymied development.

5-4 Introduction

Organic nanomaterials for advanced optoelectronic applications with high tunability, extraordinary response or novel chemistries are in high demand [1]. As we force the materials requirements of a new generation of technology on a somewhat aged semiconducter industry, it is clear that the capabilities and advantages of organic and composite materials will be critical to meeting the needs of future device design [2]. The high cost of Si refinement, the exotic and hazardous chemicals necessary for high purity manufacturing, size restrictions from top-down processing and the shear energy requirements for generating the highest quality semiconductor devices are all limitations to which organic materials offer solutions [3]. Specifically, the 'beaker manufacturing' that organic self-assembling materials provide offers a decreased cost, smaller manufacturing infrastructure and the potential for improved performance. Two types of material which have immediate applications are those showing a high degree of optical nonlinearity and those materials which can rapidly be self-assembled to alter their optical properties based on application need. Meeting both criteria are highly ordered organic systems, including synthetic light harvesting mimics, in which controlled ensemble interactions are capable of providing extraordinary increases in the two-photon absorption (TPA) of a material. These materials are known to be viable candidates for optical limiting, 3-D data storage, quantum optical applications and remote sensing [4-8].

It has been shown that large macrocycles, similar in size to LH complexes, can offer significant advantages over other structures for multiphoton applications [8-11]. For processes in which the solubility and the size of the assembly are a limiting factor to device design, obtaining TPA cross-section (σ_2) enhancement with the minimum architectural size is of great importance. To address these concerns, we offer here the synthesis, two-photon and ultrafast emission characterization of a porphyrin dimer. On self-assembly, it forms a square macrocycle which provides a ten-fold σ_2 enhancement and can be covalently bound to provide a robust architecture viable in multiple environments. Unlike species in which self-assembly generates a broad range of sizes [8-9], only a single macrocycle species is obtainable with the carefully selected 90° carbazole bridge (figure 7-2).

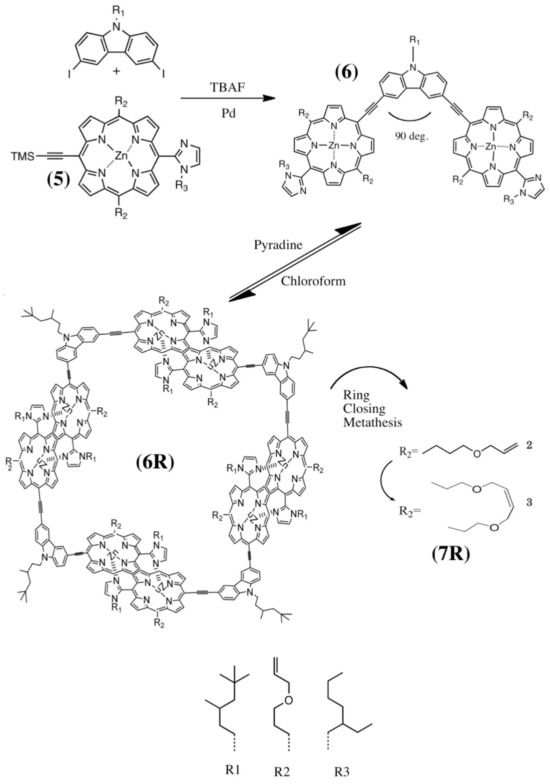

Figure 5-2. Synthesis of a Carbazole Bridged Zn Porphyrin Dimer and Subsequent Self Assembly

5-5 Synthesis

The porphyrin dimer (**6**) was synthesized from ethynylimidazolylporphyrin (**5**) and 3,6-Iodo-9-(3,5,5-trimethyl)hexylcarbazole (**2**) using a $Pd_2(dba)_3/AsPh_3$ catalytic system (SI). The resultant dimer was isolated using preparative GPC with pyridine elution in 30% yield. The cyclic four unit system (**6R**) was allowed to self-assemble over time [8,12]. This was accomplished with a solution of 113 μM of **6** in 30 ml of chloroform/methanol (7:3, v/v) which was subsequently allowed to age for 24 hours at room tempurature without exposure to light. The solution was evaporated and subjected to preparative GPC with chloroform elution to give pure **6R** (58%). To determine the exact molecular weights of the cyclic tetramer by mass measurement, we fixed the coordination structure via a ring-closing metathesis reaction of meso-substituents to produce **7R**. After the reaction, GPC separation was performed again. MALDI-TOF spectra of the main fraction showed a sharp ion peak at 7096.48 corresponding to the molecular weight of the four dimer macrocycle. Full synthesis and characterization can be found in supporting information.

5-6 Steady State Spectra

Steady state spectra (table 7-1) indicate a red shift in absorption for the macrocycle species when compared to the dimer. The observed shift (485 cm^{-1}) is consistent with J-aggregation [13]. This can be attributed to the strong zinc-nitrogen interactions provided by the pendant imidazolyl at the terminus of each porphyrin and may also contribute to the retention of a relatively high fluorescence quantum yield despite aggregation. The imidizolyl-zinc interaction forces a slipped cofacial arrangement, which has been shown to provide strong coupling between the Soret (B/S_2) and Q (S_1) bands in adjacent porphyrins [8,12,14]. The emission of the dimer shows a distinct splitting of the primary emission band, which can be attributed to the pendant groups (R_1 and R_2) preferentially providing two configurations in solution through steric/solvent interactions. This is typical of some dimers in which there is a dynamic mix of two emissive species; one in which the chromophores are coplanar (red shift) and one in which they are non-coplanar (blue shift) [12,14]. This effect is lost on transition to the macrocyclic species, in which the porphyrins becomed locked into a relatively constant position with respect to adjacent porphyrins and positioned similarly throughout the structure. The macrocycle emission is consistant with a coplanar configuration.

Table 5-1. Summary of Steady State, Two Photon and Fluorescence Lifetime Measurements

Species	Abs λ_{max}	PL λ_{max}	Φ_{PL}	δ_2	δ_2/dimer	S_2 Kinetics/Anisotropy				S_1 Kinetics/Anisotropy			
						τ_1	τ_2	r_0	r_{res}	τ_1	τ_2	τ_{rise}	r_{res}
Dimer (6)	450, 652	649, 673, 717(s)	0.15	720	720	0.3	50	0.22	0.4	5	>50	0.36	0.02
Macrocycle (7R)	460, 660	667, 723(s)	0.14	28680	7170	0.18	17	0.15	0.23	1.2	33	0.22	0.04

Two photon cross sections reported in units of GM, wavelengths reported in units of nm and kinetics reported in units of ps.

5-7 Two Photon Spectroscopy

Two-photon enhancement has been shown in assemblies possessing strong transition dipole interactions, a high degree of molecular symmetry and a tendency towards excited state delocalization [15-16]. A summary of the TPA of the **6** and **7R** can be found in table 7-1 with spectra depicted in figure 7-3. These results were obtained through the two-photon excited fluorescence (TPEF) method using a 100 fs pulsed Spectra-Physics Mai Tai laser, and have been outlined elsewhere in detail [4-6]. The dimer in this system offers only moderate TPA response, when considered in isolation, and is comparable to that observed from other π-bridged Zn-porphyrin dimers [8]. However, upon assembly to the four dimer macrocycle, a σ_2/dimer which is an impressive 10 times larger per dimer is observed.

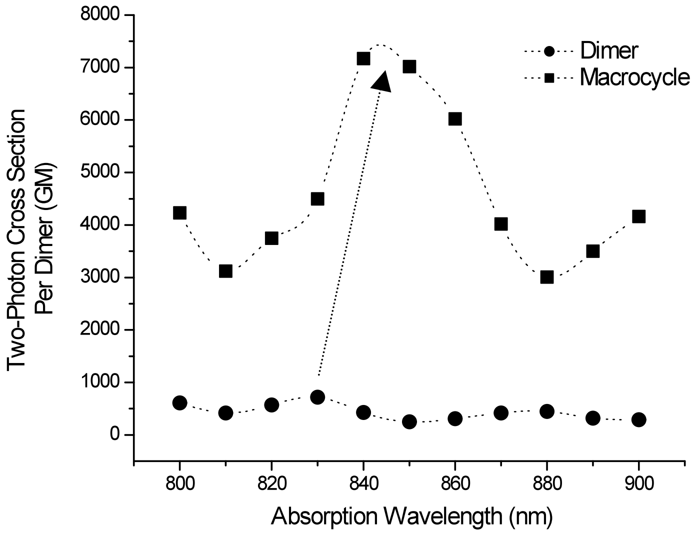

Figure 5-3. Two-Photon Cross-Section of 6 and 7R per Dimer

5-8 Ultrafast Fluorescence Up-Conversion Spectroscopy

To further address how the excited state behavior may relate to the σ_2 enhancement, fluorescence up-conversion measurements were performed at 430 nm excitation [17]. Fluorescence lifetime spectra for both of the primary emission bands of the two systems are presented in figure 7-4. The increased rate at which the S_2 excited state interconverts to the S_1 state in the macrocycle over the dimer indicates a stronger interaction between the S_2 and S_1 bands and can be observed in the τ_1 of S_2 and the τ_{rise} of S_1. For all emissions the time components are significantly shorter for the macrocycle when compared to the dimer. The shorter excited state lifetimes in the macrocycle, coupled with a similar fluorescence quantum yield, shows a much more efficient interconversion from S_2 to S_1 than that observed in the dimer. This finding also implies a greater density of states between emission bands [18].

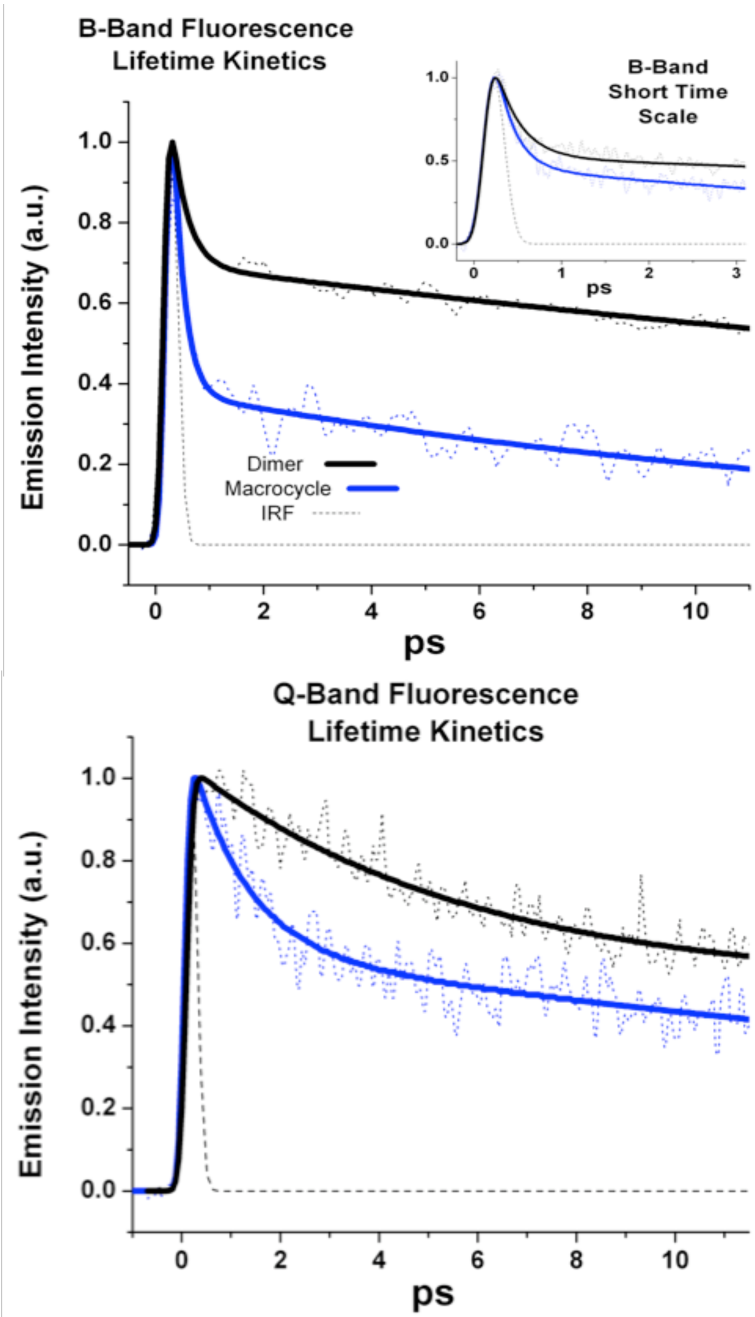

Figure 5-4. Fluorescence Lifetime Kinetics

B-band (S2) emission from 525 nm. Shorter time scale shown as inset. Q-band (S1) emission from 673 nm. Both provide dimer (black) and cyclic (blue) spectra.

5-9 Ultrafast Emission Anisotropy Spectroscopy

Anisotropy measurements, provided in figure 7-5, confirm strong B-Q interactions with a greater degree of initial and residual delocalization of S_2 for **7R** ($r_{S2(0)}$ 0.15, $r_{S2(res)}$ 0.23) when compared with **6** ($r_{S2(0)}$ 0.22, $r_{S2(res)}$ 0.4). Residual anisotropy in the S_1 band, also an indicator of strong S_n to S_{n-1} coupling in systems where excitation occurs at S_n, is twice as high in the macrocycle. It should be noted that the apparent rise in anisotropy in both the dimer and the macrocyce after the first ~200 fs in the S_2 band emission is not indicative of a formal increase in localization of the excited state. Rather, it should be taken that those excitons possessing the greatest degree of delocalized character have rapidly relaxed into the S_1 band and the region of increased localized character can be related to the signal provided by excited states which are localized, trapped or otherwise less strongly coupled to the Q-band.

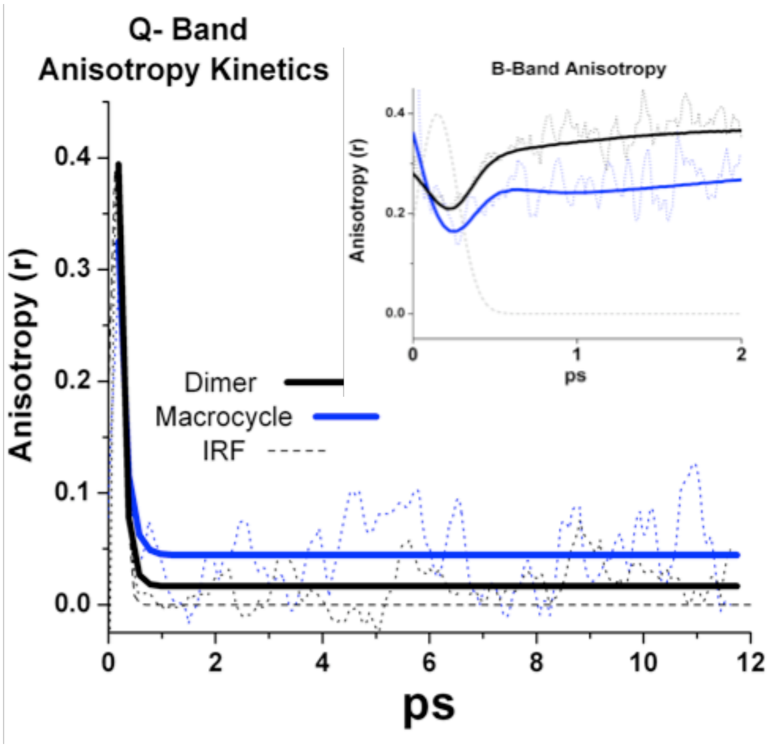

Figure 5-5. Fluorescence Anisotropy Kinetics

Q-band (S1) and B-band (S2) as inset.

5-10 Inter- and Intraband Coupling

It is known that strongly interacting transition dipoles in organic systems can provide enhanced two-photon response, specifically when the effect is delocalized over a highly symmetric system [10,14]. This enhancement can be discussed in terms of the two types of dipole coupling which occur in the **7R**. The first is the conjugated bridge between the porphyrin arms of the dimer. Unlike J-aggregation in linear assemblies, the primary dipole moment of the covalently bound porphyrins are orthogonal to one another in the dimer and directed towards the bridging carbazole. This leads to an environment where B-B transition dipole coupling, as well as a less pronounced Q-Q coupling, will be minimized. Instead, we propose that the transition dipole interactions involved occur from B-Q coupling and can lead to a greater rate of the $S_2 \rightarrow S_1 \rightarrow S_0$ emission process [19-20]. This effect exists in both dimer and macrocycle species and provides, in conjunction with the steady state results, an additional cause for the retention of high fluorescence in **7R**. Howerver, unlike the dimer, the slipped cofacial interaction in **7R** provides B-B and Q-Q coupling typified in other linear J-aggregates, despite a square-like archetecture [14,19]. The combination of both types of interactions in a single, small, covalently bound macrocycle strongly suggests an environment which allows for a significantly larger degree of intraband dipole coupling beteen dimers within the macrocycle.

5-11 Conclusion

In this study we have presented the total sysnthesis of a zinc porphyrin dimer capable of selective self-assembly into four unit macrocycles. For the lone dimer in solution, we report a δ_2 = 720 GM/dimer. On assembly to the macrocycle species, a full order of magnitude two-photon absorption enhancement is observed providing a δ_2 = 7120 GM/dimer. Ultrafast lifetime and anisotropy studies confirm that this enhancement corresponds to a significantly greater degree transition dipole interaction between porphyrins. This includes B-B, Q-Q and B-Q interactions dependent largely on the self-assembled architecture, a response only partially observed in the dimer. This synthesis and spectroscopic study presents an architecturally driven method by which the rapid generation of organic two-photon enhanced materials can be achieved, a property critical to next generation nonlinear and quantum optical materials applications.

5-12 Acknowledgement

This project was supported by Air Force Office of Scientific Research (Chemistry).

5-13 References

(1) Brunetti, F.; Kumar, R.; Wudl, F. J. Organic Electronics from Perylene to Organic Photovoltaics: Painting a Brief History with a Broad Brush. Mater. Chem., 2010, 20, 2934.

(2) Whitesides, G.; Lipomi, D. Soft Nanotechnology: "Structure" vs. "Function". Faraday Discussions, 2009, 143, 373.

(3) Yoon, M; Facchetti A.; Stern C., Marks, T. Fluorocarbon-Modified Organic Semiconductors: Molecular Architecture, Electronic, and Crystal Structure Tuning of Arene- versus Fluoroarene-Thiophene Oligomer Thin-Film Properties. J. Am. Chem. Soc., 2006, 128, 5792.

(4) Bhaskar, A.; Ramakrishna, G.; Lu, Z.; Twieg, R.; Hales, J.; Hagan, D.; Stryland, E.; Goodson, T. Investigation of Two-Photon Absorption Properties in Branched Alkene and Alkyne Chromophores. J. Am. Chem. Soc., 2006, 128, 11840.

(5) Chang, M.; Hoffman, M.; Anderson, H.; Herz, L. Dynamics of Excited-State Conformational Relaxation and Electronic Delocalization in Conjugated Porphyrin Oligomers. J. Am. Chem. Soc. 2008, 130, 10171.

(6) Raymond, J.E.; Ramakrishna, G.; Twieg, R.J.; Goodson, T. Two-Photon Enhancement in Organic Nanorods J. Phys. Chem. C. 2008, 112, 7913.

(7) Narayanan, A.; Varnavski, O.; Swager, T.; Goodson, T. Multiphoton Fluorescence Quenching of Conjugated Polymers for TNT Detection. J. Phys. Chem. C 2008, 112, 881.

(8) Raymond, J. E.; Bhaskar, A.; Goodson, T., III; Makiuchi, N.; Ogawa, K.; Kobuke, Y. Synthesis and Two-Photon Absorption Enhancement of Porphyrin Macrocycles. J. Am. Chem. Soc. 2008, 130, 17212.

(9) Raymond, J.E.; Goodson, T. Single-Particle Two-Photon Absorption Imaging and Enhancement Determination for Organic Nanoparticles. J. Phys. Chem. Lett. 2011, 2, 329.

(10) Williams-Harry, M.; Bhaskar, A.; Ramakrishna, G.; Goodson, T., III; Imamura, M.; Mawatari, A.; Nakao, K.; Enozawa, H.; Nichinaga, T.; Iyoda, M. Giant Thienylene-Acetylene-Ethylene Macrocycles with Large Two-

Photon Absorption Cross Section and Semishape-Persistence. J. Am. Chem. Soc. 2008, 130, 3252.

(11) Bhaskar, A.; Ramakrishna, G.; Hagedorn, K.; Varnavski, O.; Mena-Osteritz, E.; Bauerle, P.; Goodson, T. Enhancement of Two-Photon Absorption Cross-Section in Macrocyclic Thiophenes with Cavities in the Nanometer Regime J. Phys. Chem. B 2007, 111, 946.

(12) Ikeda, C.; Satake, A.; Kobuke, Y. Proofs of Macrocyclization of Gable Porphyrins as Mimics of Photosynthetic Light-Harvesting Complexes Org. Lett. 2003, 5, 4935.

(13) Verma, S.; Ghosh, A; Das, A.; Ghosh, H. Ultrafast Exciton Dynamics of J- and H-Aggregates of the Porphyrin-Catechol in Aqueous Solution. J. Phys. Chem. B 2010, 114, 8327.

(14) D'Souza, F.; Maligaspe, E.; Ohkubo, K.; Zandler, M.; Subbaiyan, N.; Fukuzumi, S. Photosynthetic Reaction Center Mimicry: Low Reorganization Energy Driven Charge Stabilization in Self-Assembled Cofacial Zinc Phthalocyanine Dimer–Fullerene Conjugate. J. Am. Chem. Soc. 2009, 131, 8787.

(15) Katan, C.; Terenziani, F.; Mongin, O.; Werts, M.; Porres, L.; Pons, T.; Mertz, J.; Tretiak S.; Blanchard-Desce, M. Effects of (Multi)branching of Dipolar Chromophores on Photophysical Properties and Two-Photon Absorption. J. Phys. Chem A 2005, 109, 3024.

(16) Arnbjerg, J.; Jimenez-Banzo, A.; Paterson, M.; Nonell, S.; Borrell, J.; Christiansen, O.; Ogilby, P. Two-Photon Absorption in Tetraphenylporphycenes: Are Porphycenes Better Candidates than Porphyrins for Providing Optimal Optical Properties for Two-Photon Photodynamic Therapy? J. Am. Chem. Soc. 2007, 129, 5188.

(17) Flynn, D.; Ramakrishna, G.; Yang, H.; Northorop, B.; Stang, P.; Goodson, T. Ultrafast Optical Excitations In Supramolecular Metallacycles with Charge Transfer Properties. J. Am. Chem. Soc. 2010, 132, 1348.

(18) Lakowicz, J. Principles of Fluorescence Spectroscopy, 4th Ed., Springer Inc., 2006, pp 1-25, 272-327.

(19) Drobizhev, M.; Stepanenko, Y.; Rebane, A.; Wilson, C.; Screen, T.; Andersen, H. Strong Cooperative Enhancement of Two-Photon Absorption in Double-Strand Conjugated Porphyrin Ladder Arrays. J. Am. Chem. Soc. 2006, 128, 12432.

(20) Davis, W.B.; Ratner, M.A.; Wasielewski, M. Conformational Gating of Long Distance Electron Transfer through Wire-like Bridges in Donor–Bridge–Acceptor Molecules. J. Am. Chem. Soc. 2001, 123, 7877.

5-14 Supplemental Information

Supplemental information as submitted for web publication.

General. ^{1}H NMR spectra were obtained in $CDCl_3$ with Me_4Si as the internal standard (δ 0 ppm) and recorded on either JEOL JNM EX270 or JEOL ECP600. UV-vis spectra were obtained on either Shimadzu UV-1650PC or UV-3100PC. MALDI-TOF mass spectra were obtained on Perseptive Biosystems Voyager DE-STR or Shimadzu/KRATOS Axima-CFR Kompact MALDI with dithranol (Aldrich) the matrix. Reactions were monitored on silica gel 60 F254 TLC plates (Merck). The silica gel utilized for column chromatography was purchased from Kanto Chemical Co. Inc.: Silica Gel 60N (Spherical, Neutral) 60-210 mm and 40-50 mm (Flash). The alumina used for column chromatography was purchased from Merck: Aluminum oxide 90 active basic. Analytical GPC measurements were performed on a HEWLETT PACKARD 1100 SERIES with a JAIGEL 3H-A column for chloroform eluent.

3,6-Iodo-9-(3,5,5-trimethyl)hexylcarbazole (2) [S1]. This compound was prepared according to the literature [S1] in a 91% yield. ^{1}H NMR (270 MHz, $CDCl_3$) δ 8.27 (d, 2H, *J* = 1.7 Hz), 7.68 (dd, 2H, *J* = 8.6,1.7 Hz), 7.13 (d, 2H, *J* = 8.6 Hz), 4.16-4.22 (m, 2H), 1.73-1.86 (m, 1H), 1.51-1.63 (m, 2H), 1.01-1.30 (m, 2H), 0.87 (s, 12H).

9-(3,5,5-Trimethyl)hexylcarbazole (1). Carbazole (0.270 g, 1.61 mmol), 1-bromo-3,5,5-trimethyl hexane [S2] (0.500 g、 2.41 mmol), and potassium carbonate (0.67 g, 4.82 mmol) were added in 2.7 ml of DMF. The reaction solution was stirred at 90 ºC for 44 hours. Then, 27 ml of water was added and extracted with chloroform. The organic layer was evaporated and crude was purified with silica gel column chromatography using hexane as an eluent (85%). ^{1}H NMR (270 MHz, $CDCl_3$) δ 8.10 (d, 2H, *J* = 7.8 Hz), 7.44-7.47 (m, 4H), 7.21 (d, 2H, *J* = 7.8 Hz), 4.26-4.32 (m, 2H), 1.81-1.91 (m, 1Hg), 1.62-1.73 (m, 2H), 1.10-1.36 (m, 5H), 0.90 (s, 9H) .

1-(2-Ethylhexyl)imidazole (3). Under nitrogene atmosphere, NaH (2.40 g, 60% in oil) was suspended in 50 ml of dry THF and imidazole (3.40 g, 50.0 mmol) was slowly added at 0 ºC. Then, 1-bromo-2-ethylhexane (11.0 ml, 60.0 mmol) and KI (1.66 g, 10.0 mmol) were added at room temperature and refluxed for 8 hours. Water was added and extracted with AcOEt. The crude was extracted with diluted hydrochloric acid (pH 1). pH of water layer was adjusted to 9 with K_2CO_3 and extracted again with AcOEt. The crude was purified by vacuum distillation (100 Pa, 140 ºC) in a 79% yield. ^{1}H NMR (270 MHz, $CDCl_3$) δ 7.43 (s, 1H), 7.05 (s, 1H), 6.87 (s, 1H), 3.82 (d, *J* = 6.9 Hz , 2H), 1.64-1.74 (m, 1H), 1.21-1.29 (m, 8H), 0.84-0.92 (m, 4H).

1-(2-Ethylhexyl)imidazole-2-carbaldhyde (4) [S2]. This compound was synthesized according to the literature [S2] in a 41% yield. ^{1}H NMR (270 MHz, $CDCl_3$) δ 9.81 (d, 1H, *J* = 0.8 Hz), 7.28 (d, 1H, *J*= 1.0 Hz), 7.13 (s, 1H), 4.29 (d, 2H, *J*= 7.4 Hz), 1.78 (m, 1H), 1.17-1.34 (m, 8H), 0.87-0.89 (m, 6H).

5,15- Bis -(3-allyloxypropyl) -10- (trimethylsilylethynyl) -20- [1-(2-ethylhexyl) imidazol -2-yl] porphyrinatozinc(II) (5). This compound was synthesized using **4** according to the literature [S3] in a 6.7% yield. ^{1}H NMR (600 MHz, $CDCl_3$) δ 9.90 (d, 2H, *J* = 4.2 Hz), 9.69 (m, 2H), 8.85 (m, 2H), 6.19-6.20 (m, 2H), 5.53 (d, 2H, *J* = 17.4 Hz), 5.49 (s, 1H), 5.35-5.39 (m, 4H), 5.18-5.21 (m, 4H), 4.23-4.28 (m, 4H), 3.91-3.94 (m, 4H), 2.97-3.08 (m, 4H), 2.01 (s, 1H), 1.74 (s, 2H), 0.74 (s, 9H), -0.53- 0.04 (m, 15H). MALDI-TOF mass (dithranol) m/z 843.38 $(M + H)^+$, calcd for $C_{48}H_{58}N_6O_2SiZn$ 843.376 $(M + H)^+$.

Species 6. Under an argon atmosphere, **5** (41 mg, 49 μmol) was dissolved in 20 ml of dry THF. Then, tetrabutylammonium fluoride in THF (98 μl, 98 μmol) was added. After 30 minutes, triethylamine (3.6 ml), $Pd_2(dba)_3$ (11.6 mg, 11.2 μmol), **2** (12.2 mg, 22.3 μmol) and $AsPh_3$ (13.7 mg, 44.6 μmol) were added and degassed by a frozen-thaw method. After stirring for 7 hours at room temperature, the reaction solution was evaporated. The residue was dissolved in chloroform and washed with water. The crude was purified by preparative GPC (Tosoh G2500H_{HR}, pyridine elution) to give **6** (12 mg, 30%). The cyclic tetramer **6R** was prepared by reorganization as below [S1]. A solution of 113 μM of **6** in 30 ml of chloroform/methanol (7:3, v/v) was allowed for 24 hours under dark at room temperature. The solution was evaporated and separated by preparative GPC (JAIGEL 3H, chloroform elution) to give the title compound (58%). ^{1}H NMR (600 MHz, $CDCl_3$) δ10.3 (d, 16H, *J* = 3.6 Hz), 9.88 (s, 16H), 9.31 (s, 8H), 8.97 (m, 16H), 8.49 (d, 8H, *J* = 7.8 Hz), 7.86 (d, 8H, *J* = 7.8 Hz), 6.30 (m, 16H), 5.61-5.65 (m, 24H), 5.43-5.53 (m, 32H), 5.32 (s (br), 32H), 4.66 (s(br), 8H), 4.32-4.34 (m, 32H), 4.01 (m, 32H), 3.11-3.22 (m, 32H), 2.28 (d, *J* = 3.0 Hz, 8H), 1.86 (m, 16H), 0.86-2.28 (m, 68H), -0.48-0.15 (m, 15H). MALDI-TOF mass (dithranol) m/z 1830.51 $(M + H)^+$ (detected as monomer **6**), calcd for $C_{111}H_{123}N_{13}O_4Zn_2$ 1830.84 $(M + H)^+$.

Species 7R. To confirm molecular weight of **6R** by MALDI-TOF mass, the cyclic structure was fixed by a ring closing metathesis reaction. **6R** (2.1 mg, 1.2 μmol) was dissolved in 4 ml of dichloromethane. Under a nitrogen atmosphere, Grubbs catalysis $RuCl_2(=CH\text{-}p\text{-}C_6H_5)(PCy_3)_2$ [S4] (0.95 mg, 1.15 μmol) was added into the solution and stirred for 2 hours at room temperature. The solution was diluted with chloroform and washed with water. The crude was purified by preparative GPC (JAIGEL 3H, chloroform elution). MALDI-TOF mass (dithranol) m/z 7096.48 $(M + H)^+$, calcd for $C_{428}H_{460}N_{52}O_{16}Zn_8$ 7096.11 $(M + H)^+$.

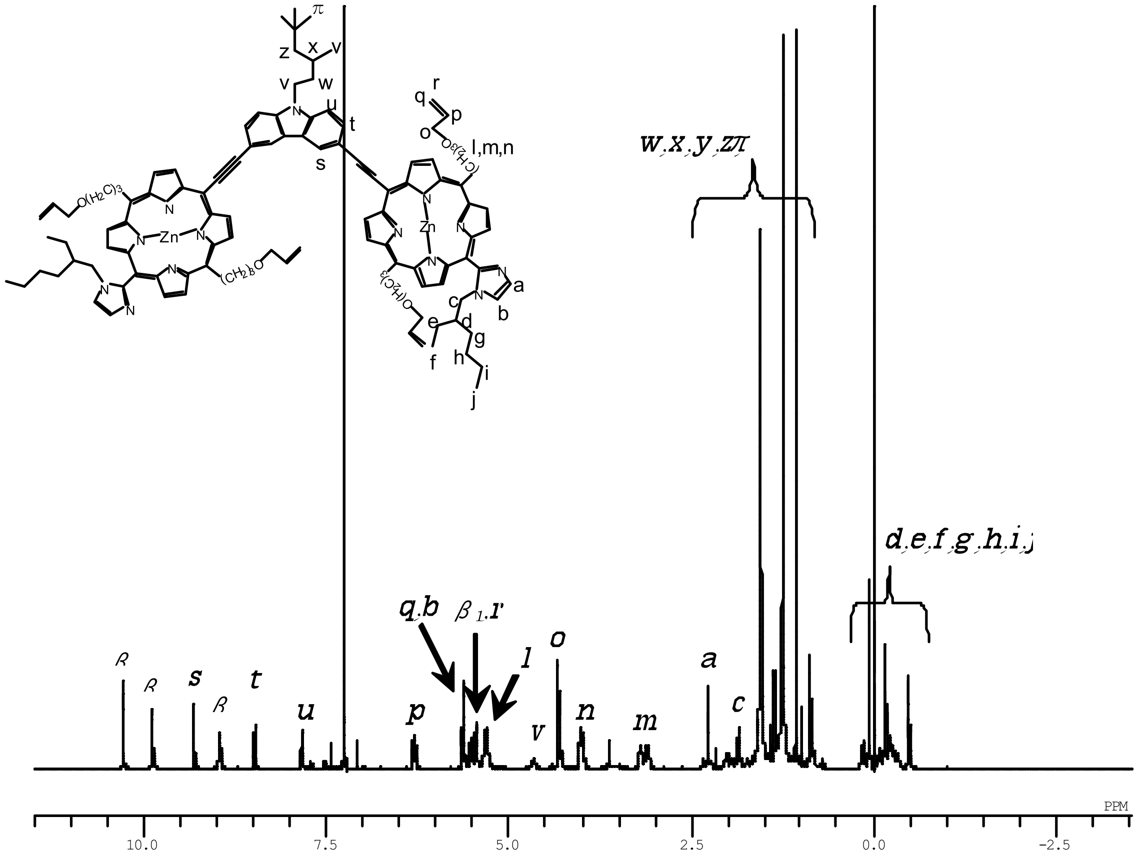

Figure 5-6. 600 MHz ^1H NMR spectrum of 6R in $CDCl_3$

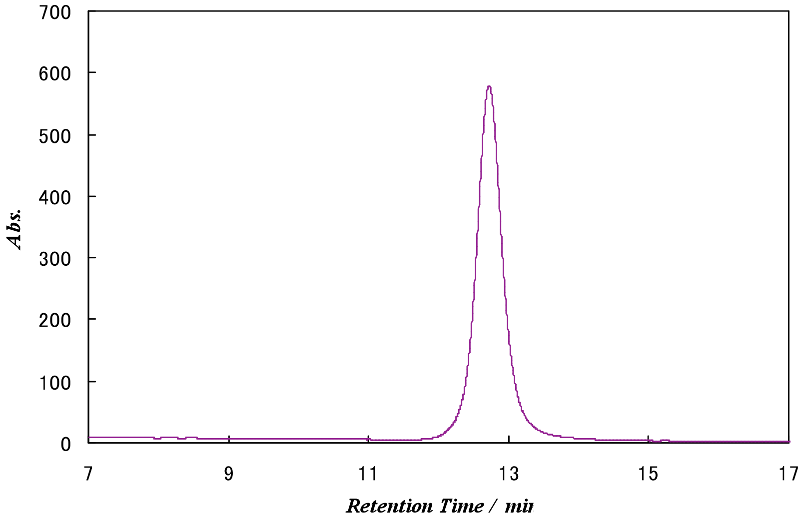

Figure 5-7. Analytical GPC Chart of 6R after the Reorganization

Column: JAIGEL 3H-A (exclusion limit is 70,000 Da at the retention time of 7 min), Eluent: CHCl$_3$ *monitored at 450 nm.*

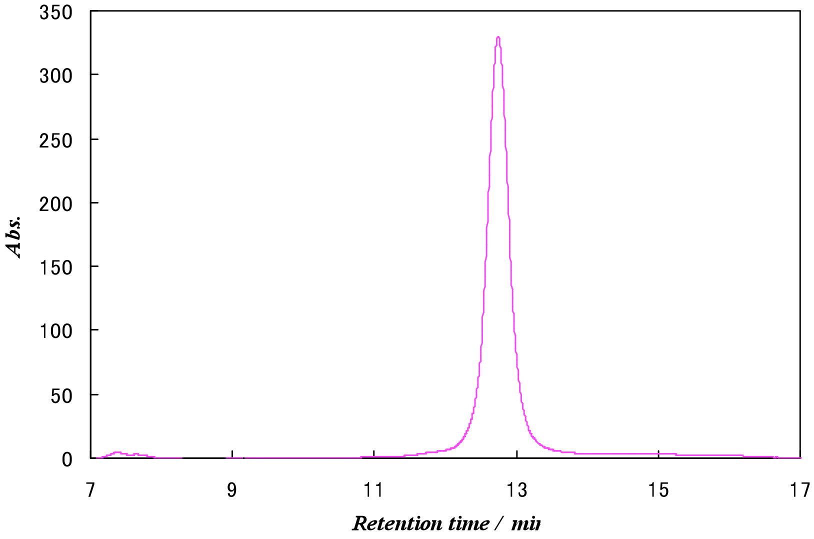

Figure 5-8. Analytical GPC of 7R after Preparative GPC Separation

Column: JAIGEL 3H-A, eluent: CHCl$_3$*.*

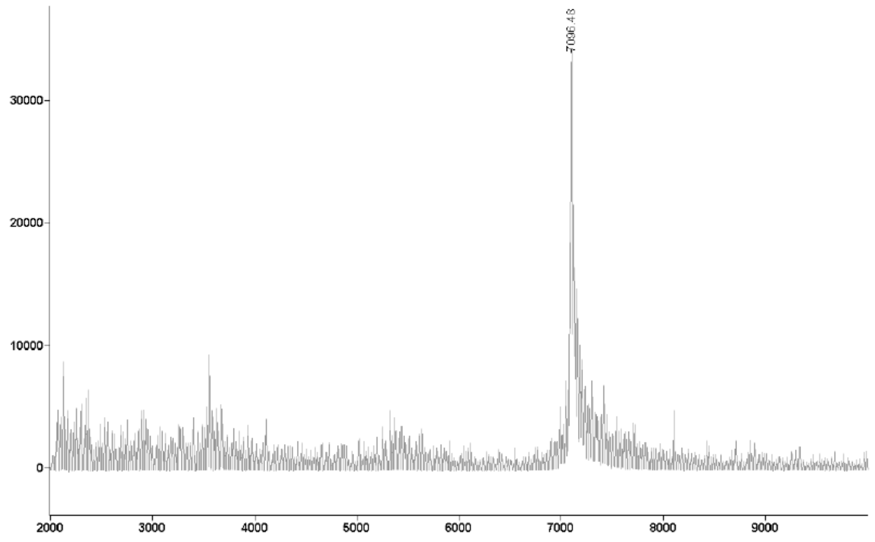

Figure 5-9. MALDI-TOF mass spectra of 7R after the GPC separation

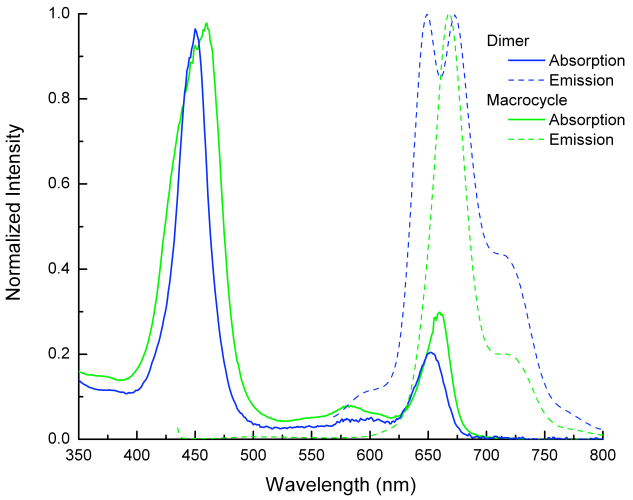

Figure 5-10. Steady State Spectra for Dimer (6) and Bound Macrocycle (7R)

Fluorescence Up-Conversion. Ultrafast fluorescence lifetime and anisotropy measurements were obtained using a Tsunami laser (Spectra-Physics) operating at 830 nm (80 MHz) and with 110 fs pulses. For excitation of the B band, the 830 nm source was energy doubled via a BBO crystal to 415 nm. Collection was performed using a FOG 100 (CDP Inc.) optics and collection set. Data collection was performed at very short (0-2 ps @ 12.5 fs) steps and longer (0-13 ps@125 fs) steps. Emission was observed at 525 nm (S_2 Band) and 670 nm (S_1 Band). Fitting and deconvolution were performed using Surface Xplorer and Origin software packages.

Two-Photon Fluorescence. Excitation was provided by a Mai-Tai (Spectra-Physics) laser source, tunable from 690-1020 nm and operating at 80 MHz with 110 fs pulses. Data collection was performed using a Oriel Cornerstone (Newport) monochromoter and Hamamatsu C9744 photocounting unit. Rhodamine B in methanol (10 uM) was used as the standard.

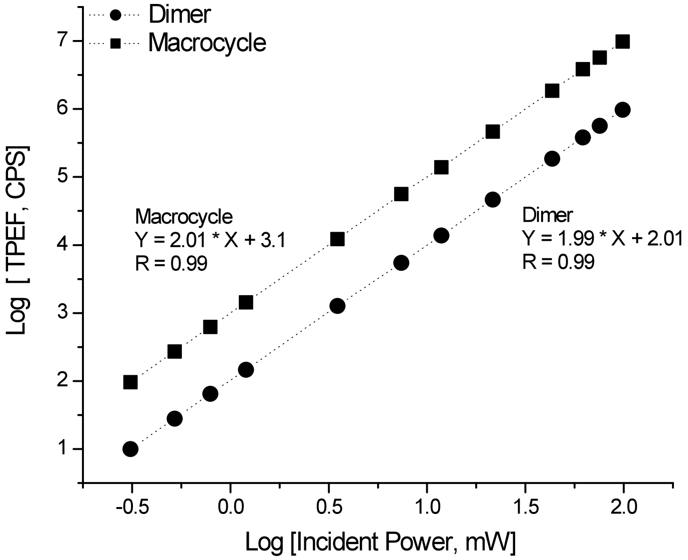

Figure 5-11. Log-Log Plot of Two-Photon Emission v. Excitation Power

The slope of two is indicative of two photon response. Data presented is from 830 nm excitation.

5-15 Supplemental Information References

(S1) Raymond, J. E.; Bhaskar, A.; Goodson, T., III; Makiuchi, N.; Ogawa, K.; Kobuke, Y. J. Am. Chem. Soc., 2008, 130, 17212.

(S2) Milgrom, L. R.; Dempsey, P. J. F.; Yahioglu, G. Tetrahedron, 1996, 52, 9877.

(S3) Hajjaj, F.; Yoon, Z. S.; Yoon, M.-C.; Park, J.; Satake, A.; Kim, D.; Kobuke, Y. J. Am. Chem. Soc. 2006, 128, 4612

(S4) Schwab, P.; Grubbs, R. H.; Ziller, J. W. J. Am. Chem. Soc., 1996, 118, 100.

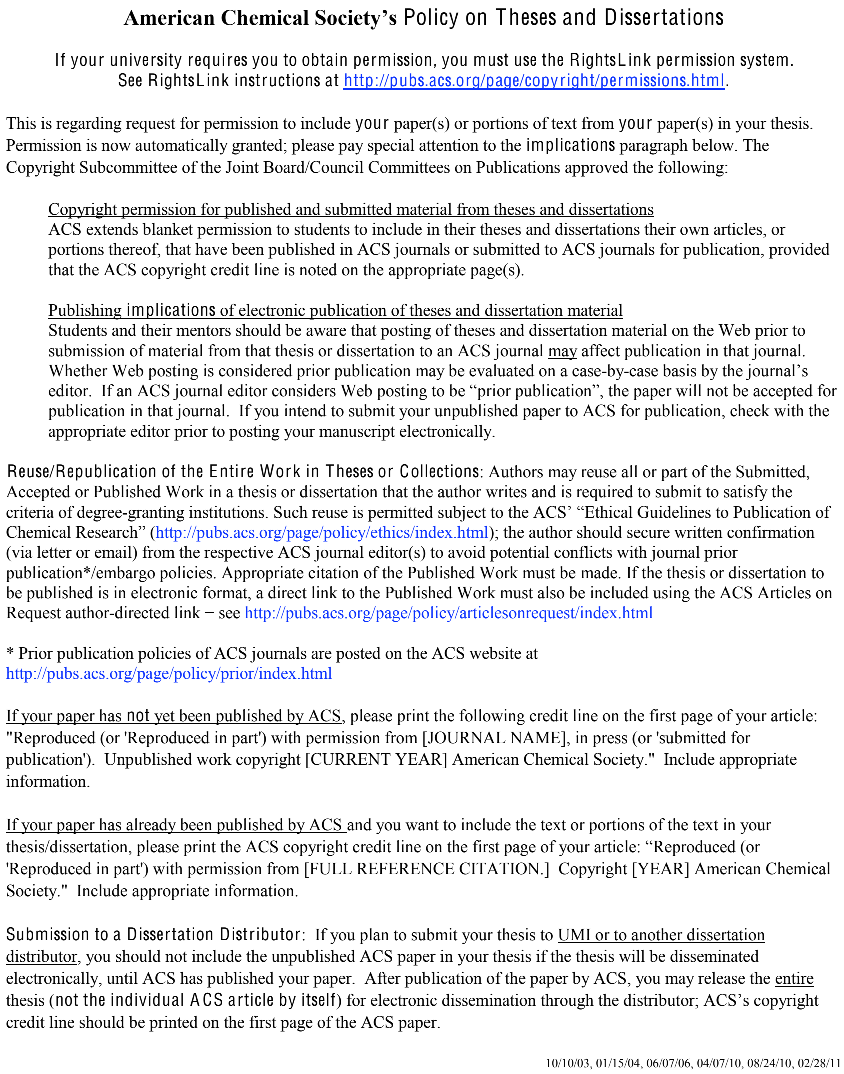

American Chemical Society's Policy on Theses and Dissertations

If your university requires you to obtain permission, you must use the RightsLink permission system.
See RightsLink instructions at http://pubs.acs.org/page/copyright/permissions.html.

This is regarding request for permission to include your paper(s) or portions of text from your paper(s) in your thesis. Permission is now automatically granted; please pay special attention to the implications paragraph below. The Copyright Subcommittee of the Joint Board/Council Committees on Publications approved the following:

> Copyright permission for published and submitted material from theses and dissertations
> ACS extends blanket permission to students to include in their theses and dissertations their own articles, or portions thereof, that have been published in ACS journals or submitted to ACS journals for publication, provided that the ACS copyright credit line is noted on the appropriate page(s).
>
> Publishing implications of electronic publication of theses and dissertation material
> Students and their mentors should be aware that posting of theses and dissertation material on the Web prior to submission of material from that thesis or dissertation to an ACS journal may affect publication in that journal. Whether Web posting is considered prior publication may be evaluated on a case-by-case basis by the journal's editor. If an ACS journal editor considers Web posting to be "prior publication", the paper will not be accepted for publication in that journal. If you intend to submit your unpublished paper to ACS for publication, check with the appropriate editor prior to posting your manuscript electronically.

Reuse/Republication of the Entire Work in Theses or Collections: Authors may reuse all or part of the Submitted, Accepted or Published Work in a thesis or dissertation that the author writes and is required to submit to satisfy the criteria of degree-granting institutions. Such reuse is permitted subject to the ACS' "Ethical Guidelines to Publication of Chemical Research" (http://pubs.acs.org/page/policy/ethics/index.html); the author should secure written confirmation (via letter or email) from the respective ACS journal editor(s) to avoid potential conflicts with journal prior publication*/embargo policies. Appropriate citation of the Published Work must be made. If the thesis or dissertation to be published is in electronic format, a direct link to the Published Work must also be included using the ACS Articles on Request author-directed link – see http://pubs.acs.org/page/policy/articlesonrequest/index.html

* Prior publication policies of ACS journals are posted on the ACS website at
http://pubs.acs.org/page/policy/prior/index.html

If your paper has not yet been published by ACS, please print the following credit line on the first page of your article: "Reproduced (or 'Reproduced in part') with permission from [JOURNAL NAME], in press (or 'submitted for publication'). Unpublished work copyright [CURRENT YEAR] American Chemical Society." Include appropriate information.

If your paper has already been published by ACS and you want to include the text or portions of the text in your thesis/dissertation, please print the ACS copyright credit line on the first page of your article: "Reproduced (or 'Reproduced in part') with permission from [FULL REFERENCE CITATION.] Copyright [YEAR] American Chemical Society." Include appropriate information.

Submission to a Dissertation Distributor: If you plan to submit your thesis to UMI or to another dissertation distributor, you should not include the unpublished ACS paper in your thesis if the thesis will be disseminated electronically, until ACS has published your paper. After publication of the paper by ACS, you may release the entire thesis (not the individual ACS article by itself) for electronic dissemination through the distributor; ACS's copyright credit line should be printed on the first page of the ACS paper.

10/10/03, 01/15/04, 06/07/06, 04/07/10, 08/24/10, 02/28/11

Figure 5-12. General American Chemical Society Guideline on In-Press Usage and Author Publication in Thesis

Chapter 6

Single-Particle Two-Photon Absorption Imaging and Enhancement Determination for Organic Nanoparticles

6-1 Original Publication Information

This chapter was originally published as the following document:

> "Single-Particle Two-Photon Absorption Imaging and Enhancement Determination for Organic Nanoparticles"
> Jeffery E. Raymond, Theodore Goodson III
> *Journal of Physical Chemistry Letter*, **2011**, *volume 2,* issue 4, pp 329-333

Modifications to the original document are cosmetic and used only to conform the format of this document or provide uniformity of enumeration.

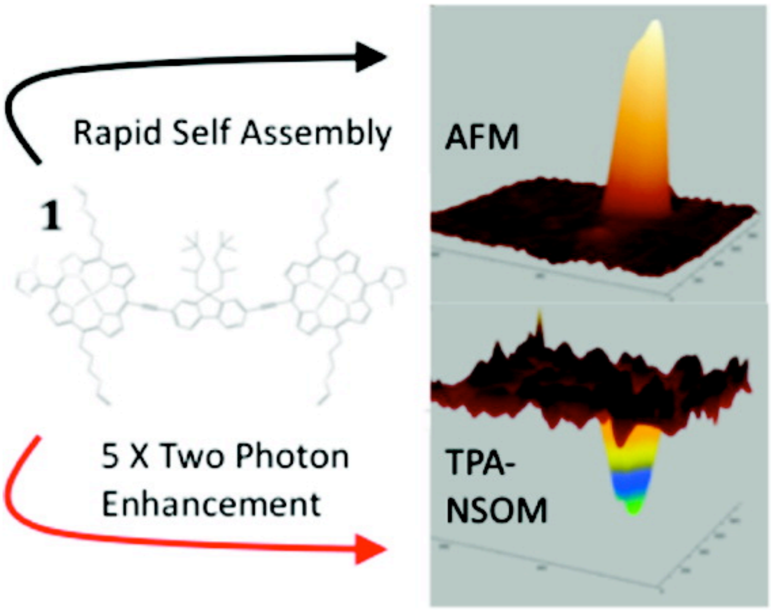

Direct two photon characterization of individual non-emissive organic nanoparticles

Figure 6-1. Table of Contents Image as Published

6-2 Qualifying Statement

In this chapter, the cause of the TPA enhancement discovered in chapter 4 motivates the generation of porphyrin nanoparticles in order to make dispersible solid state materials which have built in TPA enhancement. This study is centered entirely around TPA NSOM and its application. A five-fold enhancement in the particles are observed.

6-3 Abstract

The lack of characterization regimes available for the rapid single-particle assessment of two-photon (TPA) response in nanomaterials remains a critical barrier to nonlinear optical device development. This is particularly true of nonemissive species whose TPA must often be characterized in the bulk. In this study, self-assembly is used to produce uniform nanoparticles from a novel

porphyrin dimer, which is known to exhibit both severe fluorescence quenching and two-photon cross section (TPACS) enhancement when assembled into macromolecules. We present here the first reported use of fiber aperture near-field optical microscopy (NSOM) for the purpose of characterizing directly the TPA of nonemissive nanoparticles, observing directly a 5-fold enhancement in TPA response. This assembly/characterization regime provides a fast and fully actualized method for the generation of low-scatter optical-limiting organic nanomaterials where domain size, morphology control, and TPA enhancement are all critical to application viability and unobservable via bulk measurements.

6-4 Introduction

As attempts to develop functional condensed-phase nanomaterials for nonlinear optical (NLO) applications grow more sophisticated, it is critical that methods for directly probing the NLO structure−function relationship of assemblies be actualized. This is a particularly poignant concern for developing next-generation organic nanomaterials for applications like remote sensing, light harvesting, and optical limiting [1-3].

Directly probing the NLO character of individual nanoscale assemblies is critical to determine how subtle changes in size, morphology, and environment may enhance the response of a system. This is necessary for applications where optical-limiting or light-harvesting materials must coat or surface treat another functional device such as a CCD, remote sensor, or inorganic solar array. In these instances, it is uniformly required that the optically active coating diffract or scatter the nonabsorbed light as little as possible and generate little or no fluorescence. This can be achieved readily by using organic nanomaterials which self-assemble and have well-characterized optoelectronic properties at the interface of the particles. The viability of using two-photon excited fluorescence microscopy for probing directly the third-order nonlinear two-photon response of individual self-assembled nanomaterials has been displayed [4-8]. However, if a species experiences large quenching effects on assembly, quantitative two-photon fluorescence imaging poses a difficult prospect. This points instead to direct imaging of the multiphoton absorption. The possibility of true absorption imaging by NSOM has been displayed [9-10], but little has been done to investigate two-photon absorption near-field imaging (TPA NSOM) as a viable method for the quantitative inspection of nonfluorescing nanoscale materials.

6-5 Molecular Structure

Organic nanoassemblies in a variety of configurations, such as rods, macrocycles, molecular wires, ladders, and dendrimers [4, 11-14], have been shown to display enhanced NLO properties in ensemble over the individual building blocks. Previously, we have characterized an imidizoyl-terminated porphyrin dimer (figure 5-2), which has be been shown to possess a TPA cross-section enhancement factor of 90 when self-assembled into a slipped cofacial macrocycle [11]. It is reasonable to assume that it is possible to assemble different architectures that capture at least some of this ensemble enhancement, even if assembly is largely with random or uncontrolled orientation.

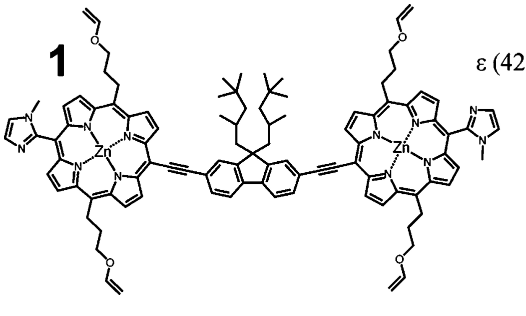

Solution (DMF)
ε (420 nm): $28.8 \cdot 10^4$ $M^{-1}cm^{-1}$
σ_2 (830 nm): 570 GM
Φ_F : 0.1

Particle
Φ_F : $<10^{-5}$
σ_2 (830 nm): 2800 GM

Figure 6-2. Porphyrin Dimer (1) and Optical Response Per Molecule

6-6 Two Photon Absorption NSOM

FM scans of the assembled nanoparticles on a mica substrate (figure 5-3) show uniform porphyrin particles. The features observed in the simultaneously collected NSOM image show a decrease in counts typically associated with absorption or scattering in most systems and can be imaged below an edge resolution of 15 nm. For NSOM scattering images [15-17], this is typical of other systems with similar illumination and collection but is one of the highest reported resolutions for optical absorption images [18, 19]. From peak averaging at a high incident flux, the majority contribution for this signal appears as two-photon absorption in the nanostructure and is indicated in the extracted quadratic TPA signal given in figure 5-4. Quantitative polynomial extraction can be performed on the observed intensity such that

$$\iint I(x,y,i)dxdy = \iint s(x,y,z)I(x,y,i)dxdy + \iint t(x,y,z)I(x,y,i)^2 dxdy \qquad \text{(I.)}$$

and in a pixilated environment with constant z (AFM value) and i (incident intensity), it becomes

$$\Delta I = s_z \sum_{x,y} I_{i,j} + t_z \sum_{x,y} I_{i,j}^2 \qquad \text{(II.)}$$

This is with s as the cofactor for scattering, t as the cofactor for TPA (linearly related to σ_2), and both s and t determined from polynomial fitting from equation 5-2 and shown in figure 5-4.

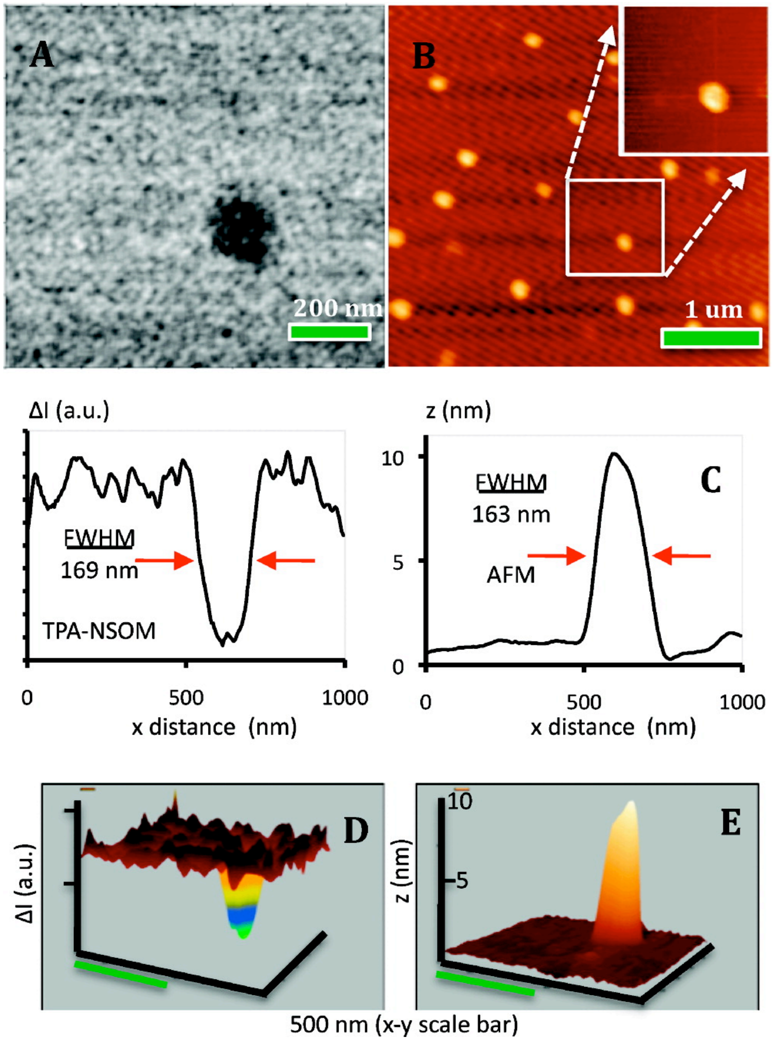

Figure 6-3. Topographic and Near-field Optical Characterization of the Porphyrin Nanoparticle

(A) TPA NSOM of a single particle with the contrast adjusted for maximum feature visibility using raw image data. (B) AFM of uniform particles. Single-particle image as the inset. (C) X line selections displaying feature resolution. 3D rendering of TPA NSOM (D) and AFM (E) for a single particle. Panels C–E all use false pixel doubling and second-nearest-neighbor averaging of raw image data.

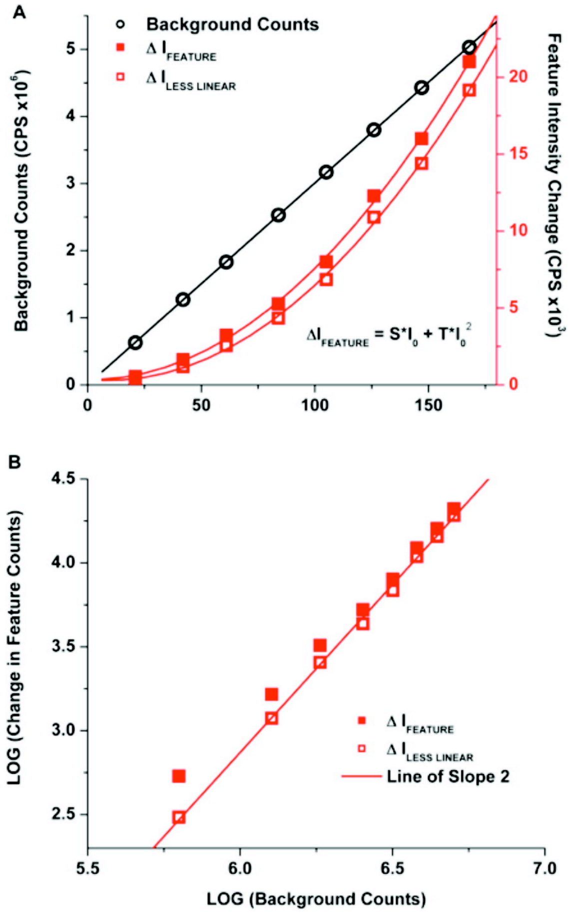

Figure 6-4. Power Dependence Determination of TPA and Scattering/Linear Components of Nanoparticle Images

(A) Intensity dependence of image features including nonfeature background counts (left axis) and the change in intensity at the center of for the particle and the change in intensity without linear contributions (right axis). (B) Log–log plot confirming the I2 dependence of the TPA contribution to ΔI by way of a slope of 2 after linear/scattering signal removal.

Several scans of an individual nanoparticle were made from 21 to 168 mW of incident power on the NSOM fiber optics, having relative intensities ranging from 1 to 8 (figure 5-5). Observation of the coupling efficiency for our system, through a pinhole with the probe 1 μm above contact, gives a 1.5% throughput at the probe tip due to the extremely high optical bleed at the onset of taper and spot size/rejection at the fiber coupling point. The collection efficiency for absorption imaging is presumed near 100%. Correcting for scatter, the PMT sensitivity at 830 nm, and the chromophore density, a TPACS of 2800 ± 600 GM (1 GM = 10^{-50} cm^4–s/photon) was determined for the porphyrin dimer using the following relationship, given constant incident intensity

$$\frac{(1-s)\iint I(x,y)dxdy}{\iint \frac{\rho}{\mathrm{M}} N_A z(x,y)dxdy} = \sigma_2 / molecule \qquad \text{(III.)}$$

This is with ρ being an assumed density of 1.2 g/mL [20, 21] and M the molar mass. The TPACS reported here is the average of three particles. From AFM, relatively uniform particle sizes were determined for this assembly method, providing heights of 9.1 ± 2 nm and diameters of 180 ± 40 nm, giving a TPACS/particle of 3.8×10^8 GM. The extremely large cross section per particle allows for greater ease of detection in contrast to comparable TPA far-field detection of single molecules like rhodamine, where cross sections are 7−8 orders of magnitude lower. The uniform intensity assumption at the sample in this calculation may lead to some error; however, due to the near-field constraint of the fiber optic aperture, any distortion is assumed to be minimal.

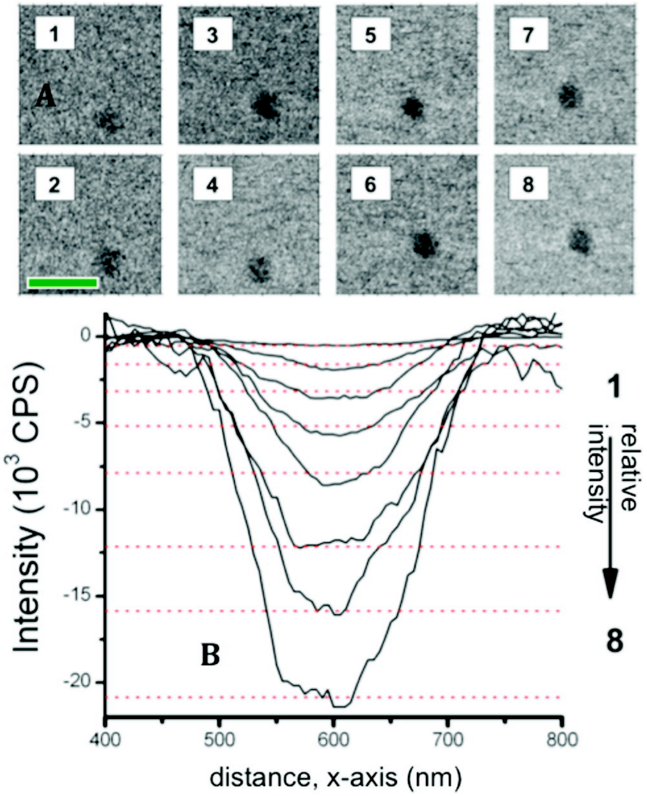

Figure 6-5. Power-Dependent TPA NSOM of a Single Porphyrin Nanoparticle

(A) TP -NSOM, relative intensities from 1 to 8. Image contrast adjusted to enhance feature visibility using raw image data. The scale bar denotes 500 nm. (B) X-axis line plots adjusted to zero background in order to provide a clear contrast of ΔI at various intensities. Red dotted lines indicate the expected change in intensity based on the signal polynomial from the fitting (equation 5-2) given with linear and nonlinear two-photon components.

In solution, this dimer possesses a TPACS of 570 GM. As a self-assembled macrocycle with 19 dimer units, the TPACS per dimer was found to be 2 orders of magnitude higher. In the macrocycle, the principle mode of enhancement was found to be related to a slipped cofacial imidizoyl–Zn association in conjunction with additional locally coordinated dimers, resulting in a greatly enhanced transition dipole coupling in the system. It is reasonable to assume, even given a random configuration, that some of the chromophores will find themselves in this or a similar environment. This leads to a more than modest particle ensemble TPACS enhancement factor of 5 for this assembly method as measured by our TPA-NSOM system.

The scattering signal appears low for this system, with S/N remaining constant at 0.2. This is specifically true when compared to other NSOM techniques in which scattering is the primary method for imaging from far-field illumination. Several components of the system, including the apertured top-down illumination, may contribute to this low observed scattering and the 830 nm wavelength. The proximity of the excitation source, low aperture diameter, <5 μm thickness of the mica substrate, and the close proximity of the collection aperture all may result in a low observed scattering, unlike other NSOM methods in which far-field excitation and near-field collection occur and other systems where the collection is not in the direction of excitation. Additionally, far-field diffraction-type rings at λ/2 from the center of the object mass appear nominal, with intensities beginning below 1/10 of the noise level in the majority of line plots, further confirming that the majority of signal is related to near-field excitation. These features of the system lead to a series of power-dependent images by which scattering can be extracted via polynomial fitting and the two-photon character determined from the nonlinear component. Shown in figure 5-5 and table 5-1 are the NSOM transmission results for the study. It can be shown that the polynomial model used to determine scattering and TPA contributions reasonably matches the line scan maxima observed in figure 5-5b.

Table 6-1. Summary of Experimental Results for Quantitative TPA NSOM

I_{input} (mW)	Relative Power	I_{obs} (10^6 cps)	N (10^3 cps)	ΔI (cps)	S/N
168	8	5.03	4.53	19166	4.23
147	7	4.43	4.51	14389	3.19
126	6	3.8	3.95	10896	2.76
105	5	3.17	3.62	6846	1.89
84	4	2.53	2.34	4339	1.86
61	3	1.83	1.86	2553	1.38
42	2	1.27	1.59	1185	0.74
21	1	0.63	1.15	305	0.26

I_{input}= incident intensity coupled into fiber; I_{obs}, median nonfeature counts; N, xtandard deviation of nonfeature counts; ΔI, median change in intensity at the feature less the scattering/linear contribution to the counts.

6-7 Conclusion

Shown here for the first time is the viability of using TPA NSOM for the observation of low-scatter systems in order to determine the exact TPA response of a nonfluorescing organic nanostructure. Through a straightforward assembly method of a known TPA material, exact per particle assessment of the NLO character can be extracted with an optical edge resolution of less than 15 nm. TPA-NSOM makes possible a high-throughput analysis of the per particle TPA for materials and their morphologies under ambient conditions even when a material's nanoscale fluorescence is difficult to observe. Through a similar, empirically rigorous regime, it can be assumed that other organic material/assembly paradigms can be investigated for low-scatter composite optical devices in the future.

Additionally, in samples that do exhibit fluorescence, it may be possible to compare other TPEF analogue fluorescence imaging techniques [12-13] to the Z-scan analogue TPA-NSOM power dependency images, thereby clarifying discrepancies in the TPA cross sections periodically observed by comparing the two methods for solid-state materials.

6-8 Experimental Section

A femtosecond excitation source is used (Spectra-Physics Mai Tai) for this study, operated at 830 nm, 80 MHz, and a pulse fwhm of 110 fs. Intensity is regulated using a variable neutral density filter. The excitation is coupled into a CDP-NSOM multiscope with shear force AFM, absorption, and fluorescence detection capabilities. The probes use a single-mode fiber optic cable (F-SF Newport for 820 nm signaling). The probes are pretreated with weak acid to hydrolyze and soften the cladding (0.1 M HCl) and are pulled using a Sutter P-2000 CO2 capillary puller optimized for a 13° initial taper and low-impact drawing. Tips are immediately submerged into a methanol ice bath to restrict cladding relaxation. The nominal aperture diameter is 30 nm from a nonmetalated probe, as determined from a fluorescent standard [22]. The nontrivial far- and near-field scattering signal inherent to a nonmetalated probe, which is linearly dependent on incident intensity, is removed after fitting from the nonlinear component of the feature signals. Collection is done with a 2.5 nm pixel size. False doubling to 1.25 nm and subsequent three-pixel nearest-neighbor averaging is performed on AFM and TPA-NSOM images using Nanoscope software. A 98 μM porphyrin dimer solution in 9:1 DMF/pyridine is added to Millipore purified water at a 1:20 ratio and shaken vigorously for 10 s. The resultant suspension is then vented for 30 s under a nitrogen flow and drop-deposited on cleaved mica and vacuum-dried for 30 min. Pixel size, averaging, and probe dither give a 2.5 nm uncertainty in the AFM signal (x–y) and result in a nominal edge resolution in the TPA NSOM image (5 nm) of <15 nm.

6-9 Acknowledgement

The authors thank Yoshiaki Kobuke et al. at the Nara Institute for supplying the porphyrin dimer.

6-10 References

(1) Davis, D.; Hamilton, A.; Yang, J.; Cremar, L.; Van Gough, D.;Potisek, S.; Ong, M.; Braun, P.;Martinez, T.; White, S.;Moore, J.;Sottos, N. Polymeric Materials. Nature 2009, 459, 68–73.
(2) Hardin, B.; Hote, E.; Armstrong, P.; Yum, J.; Comte, P.; Torres, T.; Frechet, J.; Nazeeruddin, M.; Gratzel, M.; McGehee, M. Nat. Photonics 2009, 3, 406–410.
(3) Dini, D; Calvete, M.; Hanack, M.; Amendola, V.; Meneghetti, M. J. Am. Chem. Soc. 2008, 130, 12290–12298.
(4) Raymond, J. E.; Ramakrishna, G.; Twieg, R.; Goodson, T. J. Phys. Chem. C 2008, 112, 7913–7921.
(5) Hayazawa, N.; Furusawa, K.; Taguchi, A.; Kawata, S.; Abe, H. Appl. Phys. Lett. 2009, 94, 193112–193114.
(6) Raymond, J. E.; Goodson, T. Proc. SPIE 2009, 74130Y, 1–7.
(7) Folling, J.; Bossi, M.; Bock, H.; Medda, R.;Wurm, C.; Hein, B.;Jakobs, S.; Eggeling, C.; Hell, S. Nat. Methods 2008, 5, 943–945.
(8) Hell, S. Nat. Methods 2009, 6, 24–32.
(9) Knoll, B.; Keilmann, F. Nature 1999, 399, 134–137.
(10) de Paula, A.; Chaves, C.; Silva, H.; Weber, G. Appl. Opt. 2003, 42, 3005–3008.
(11) Raymond, J. E.; Bhaskar, A.; Makiuchi, N.; Ogawa, K.; Kobuke, Y.; Goodson, T J. Am. Chem. Soc. 2008, 130, 17212–17213.
(12) Ahn, T.; Kim, K.; Kim, D.; Noh, S.; Aratani, N.; Ikeda, C.;Osuka, A.; Kim, D. J. Am. Chem. Soc. 2006, 128,1700–1704.
(13) Zheng, Q.; Gupta, S.; He, G.; Tan, L.; Prasad, P. Adv. Funct. Mater. 2008, 18, 2770-2779.
(14) Narayanan, A.; Varnavski, O.; Swager, T.; Goodson, T. J. Phys. Chem. C 2008, 112, 881–884.
(15) Huang, B.; Wang, W.; Bates, M.; Zhuang, X. Science 2008, 319, 810–813.
(16) Bailo, E.; Deckert, V. Chem. Soc. Rev. 2008, 37, 921–930.
(17) McFarland, A.; Van Duyne, R. Nano Lett. 2003, 3, 1057–1062.
(18) Pomraenke, R.; Ropers, C.; Renard, J.; Lienau, C.; Lur, L.; Polli, D.; Cerullo, G. J. Microsc. 2008, 229, 197–202.
(19) Li, L.; Gattaas, R.; Gershgoren, E.; Hwang, H.; Fourkas, J. Science 2009, 324, 910–913.
(20) Schauer, C.; Anderson, O.; Eaton, S.; Eaton, G. Inorg. Chem. 1985, 24, 4082–4086.

(21) LeCours, S.; DiMagno, S.; Therien, M. J. Am. Chem. Soc. 1996, 118, 11854–11864.
(22) Kim, J.; Kim, D. C.; Nakajima, K.; Mitsui, T.; Aoki, H. J. Korean Phys. Soc. 2010, 56, 1748–1753.

Rightslink® by Copyright Clearance Center 8/2/11 11:08 AM

Copyright Clearance Center RightsLink®

ACS Publications
High quality. High impact.

Title: Single-Particle Two-Photon Absorption Imaging and Enhancement Determination for Organic Nanoparticles
Author: Jeffery E. Raymond et al.
Publication: Journal of Physical Chemistry Letters
Publisher: American Chemical Society
Date: Feb 1, 2011
Copyright © 2011, American Chemical Society

Forgot Password/User ID?

If you're a copyright.com user, you can login to Rightslink using your copyright.com credentials. Already **a Rightslink user** or want to learn more?

No charge permission and attribution

Permission for this particular request is granted for print and electronic formats at no charge. Figures and tables may be modified. Appropriate credit should be given. Please print this page for your records and provide a copy to your publisher. Requests for up to 4 figures require only this record. Five or more figures will generate a printout of additional terms and conditions. Appropriate credit should read: "Reprinted with permission from {COMPLETE REFERENCE CITATION}. Copyright {YEAR} American Chemical Society." Insert appropriate information in place of the capitalized words.

Copyright © 2011 Copyright Clearance Center, Inc. All Rights Reserved. Privacy statement.
Comments? We would like to hear from you. E-mail us at customercare@copyright.com

https://s100.copyright.com/AppDispatchServlet Page 1 of 1

Figure 6-6. American Chemical Society Permission to Publish in Thesis

Chapter 7

Quantitative Non-Linear Optical Imaging in the Nano-Regime

7-1 Original Publication Information

This chapter was originally published as the following document:

"Quantitative Non-Linear Optical Imaging in the Nano-Regime"
Jeffery E. Raymond, Theodore Goodson
Proceedings of the International Society of Optics and Photonics (SPIE),
2009, *volume 7413,* issue 0Y, pp 1-14.

Modifications to the original document are cosmetic and used only to conform the format of this document or provide uniformity of enumeration.

7-2 Qualifying Statement

This chapter is exclusively focused on the generation of standards and standard practices in TPA NSOM. No additional techniques are introduced.

7-3 Abstract

The development of functional solid state non-linear optical (NLO) systems for device applications is critical to several fields. Optical computing, laser hardening, 3-dimensional data storage and remote sensing are just a few of the areas advanced by the characterization of new NLO systems. One promising venue for the development of these technologies is the nano-/meso-scale self assembly of viable chromophores into tunable aggregates. Here we present a method by which individual aggregates can be uantitatively imaged by two photon fluorescence near field scanning optical microscopy (TPA NSOM).

7-4 Background

NSOM imaging using a single mode fiber optic cable allows for the use of a femptosecond pulsed excitation source, provided that the probe is not metalized [1]. The transition to near-field imaging is needed when attempting to optically resolve features below the Bragg diffraction limit. The resolution for near field optical imaging is related to several factors, including the probe coating, atmospheric conditions, illumination source proximity and the aperture size of the illuminating source. This resolution for a given probe can vary from the aperture size (D) to as small as D/4 and is applicable when the aperture proximity to a feature is within the Fraunhofer Distance (equation 4-1).

$$d = 2D^2 / \lambda \qquad \text{[I.]}$$

This is with d as distance between feature and aperture, D as aperture diameter, λ as wavelength of the illumination.

Two photon excited state fluorescence (TPEF) is a potential NSOM imaging mode. In this mode, illumination is provided from a pulsed laser system at a wavelength that is within the two photon absorption (TPA) spectra of the sample. The illumination is delivered to the sample from the probe and collected in the far field from the sample, along with the TPEF of the sample. The illumination is removed from the TPEF signal and a near-field fluorescence image is generated. This image will have enhanced resolution over a similar luminescence from a one photon process. This is due to the quadratic relationship the third order TPA process has to the incident flux and the uneven intensity distribution at the aperture. Typical TPEF measurements are taken using a standard reference material (equation 4-22) [2].

$$\delta = \delta_0 \bullet (PL / PL_0) \bullet ([C] / [C_0]) \bullet (\eta / \eta_0) \qquad \text{[II.]}$$

The use of TPA NSOM to obtain TPA images of organic nanorods has been shown elsewhere [1]. This imaging technique allows comparison of individual nanoscale aggregates in order to correlate TPEF response to both morphology and size of the sample. Comparing the volume of a given feature, as determined by the AFM image, provides relative TPEF response within a given image frame.

7-5 Experimental

The TPA cross sections and fluorescence were obtained by the TPEF method [2-4]. The 840 nm excitation source was obtained from a Spectra-Physics Mai Tai unit. The 1100 nm excitation source was obtained from the Mai Tai unit coupled into a Spectra-Physics OPAL temperature tunable optical parametric amplifier. The intensity was monitored by a Thor Labs DET 100A photo-voltmeter. Fluorescence was collected using a Hamamatsu R7518P PMT. AFM and TPA NSOM images were obtained from a CDP-MoScan Near-Field Multiscope [figure 4-1]. Probes were made using S-FS single mode optical fiber from Newport Corp. Rhodamine B dye was obtained from Ciba Chemicals. Rhodamine B impregnated polystyrene spheres were obtained from Melorium Inc. and have a 0.5% wt loading. Slide deposition is done with and aspirator on freshly hewn mica slides.

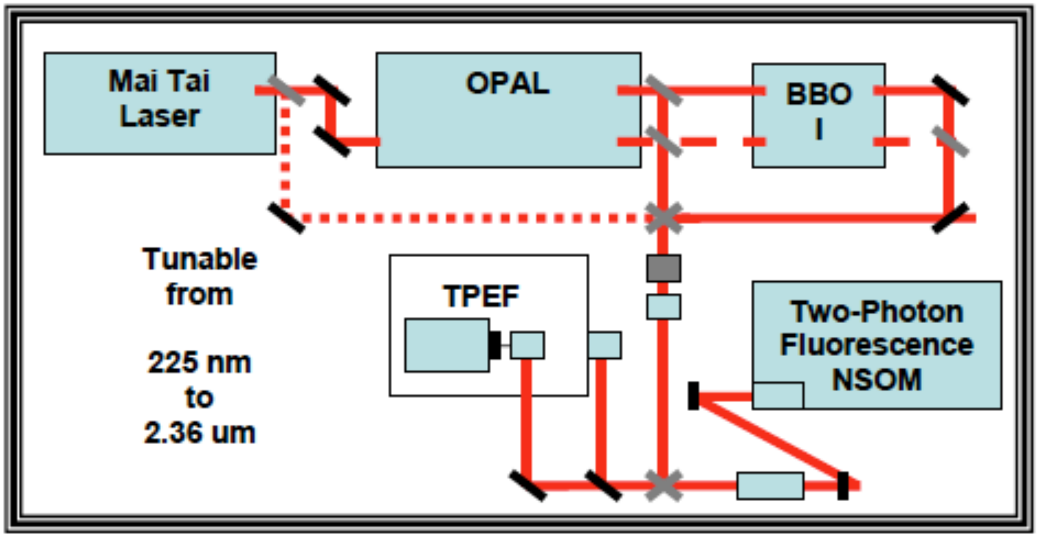

Figure 7-1. Experimental Set-Up for Bulk TPEF and TPA NSOM Measurements

7-6 Results and Discussion

There is a need to develop a method of TPA NSOM imaging that allows for quantitative imaging. Current imaging techniques allow a relative comparison between features on a single sample slide. However, this method does not readily allow for comparison when samples, experimental conditions, or probe type differ. In order to perform quantitative TPEF measurements by NSOM, there are two avenues that can be taken. The first avenue is a determination of the true plane wave/pulse shape, flux profile, probe aperture shape, and the G-factor at the sample. A second, more functionally elegant method is to have a known standard in the field of view for the wavelength at which imaging will occur. As there are no standards for quantitative TPA NSOM, a standard need first be developed. There are several properties that should be targeted while attempting to develop a standard for quantitative TPA NSOM.

a. Well characterized TPA spectra at the wavelengths of interest.
b. Encapsulation of the signaling species to give environmental robustness.
c. Viable for bulk TPEF or TPA z-scan measurements in suspension.
d. Only trivial spectral changes on transition to solid-state.
e. A commercially available product with a known formulation.
f. A variety of available sizes, application selectable for specific feature sizes.

An appropriate dye at the wavelengths of 840 nm and 1100 nm is rhodamine B. It has been used extensively in other TPA standard studies [2,5], is readily commercially available and has a readily observable TPA cross section over a broad (300+ nm) range of the Vis-NIR spectrum. Rhodamine B also is used in two photon laser scanning confocal microscopy to good effect, though not with the resolution possible by NSOM. A dye impregnated polystyrene sphere was chosen over a dye surface labeled system to give uniform signal across the depth of the feature and to ensure that the dye would not significantly change its behavior on transition from suspension to solid state. Dye loading of 0.5% was chosen to maintain a penetration depth in excess of 1 um. Results for the TPA cross section are given in table 4-1, as well as the results from two other TPA standard studies [2,5].

Table 7-1. TPEF Measured Cross Sections and Standards for Rhodamine B Systems

Wavelength	Rh B Spheres per 600 nm sphere	Rh B Sphere per molecule	Rh B Doped PMMA Film	Rh B in Methanol (2)	RhB in Methanol (5)
840 nm	6.6×10^8	160	173	165	180
1100 nm	8.6×10^6	21	23	28	24
Reported in Units of GM = 10^{-50} cm^4/photon-second					

These measurements confirm the findings in other TPEF standard studies and provide confidence that the polymer impregnated species varies little from the solution phase dye. Determining the full sphere cross section provides a value to attribute to the total integrated value of the TPEF image of a feature. The TPEF NSOM imaging was done intentionally without monitoring the absolute throughput of the incident beam from the probe, which is both time consuming and system-destabilizing. Instead, by locating the probe over a region without a TPEF responsive feature, it can be shown that incident intensity (mW) correlates directly with counts when the incident beam is not fully filtered (figure 4-2).

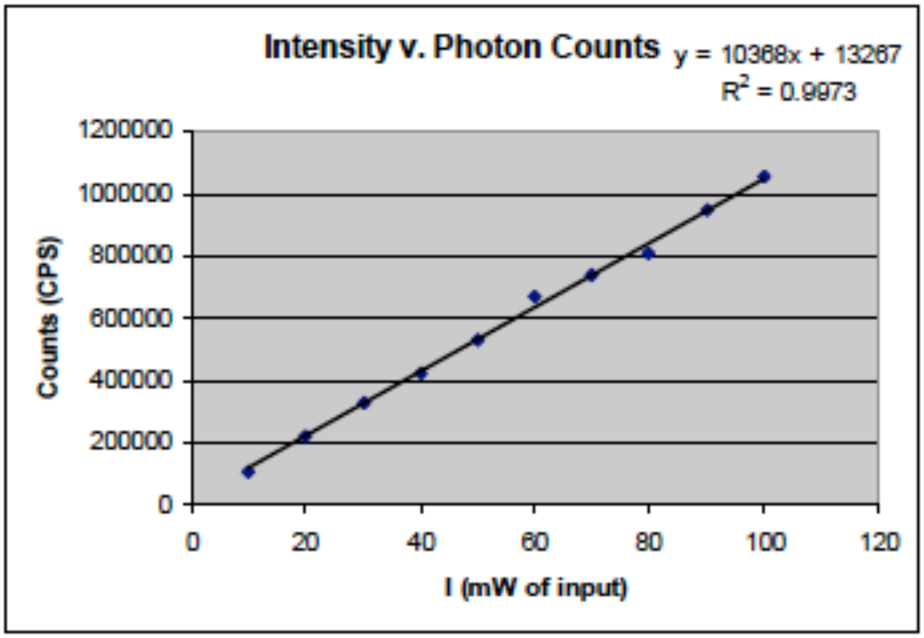

Figure 7-2. Confirmation of Linear Relationship Between Input Intensity and PMT Response

Once the linearity of the probe throughput was confirmed, TPA NSOM images were obtained using input intensities over the range measured. Figure 4-3 provides a comparison of a TPEF image to the simultaneously obtained AFM image, while figure 4-4 presents the intensity study images performed at 840 nm. All fields of view are 5 um x 5 um at a resolution of 20 nm.

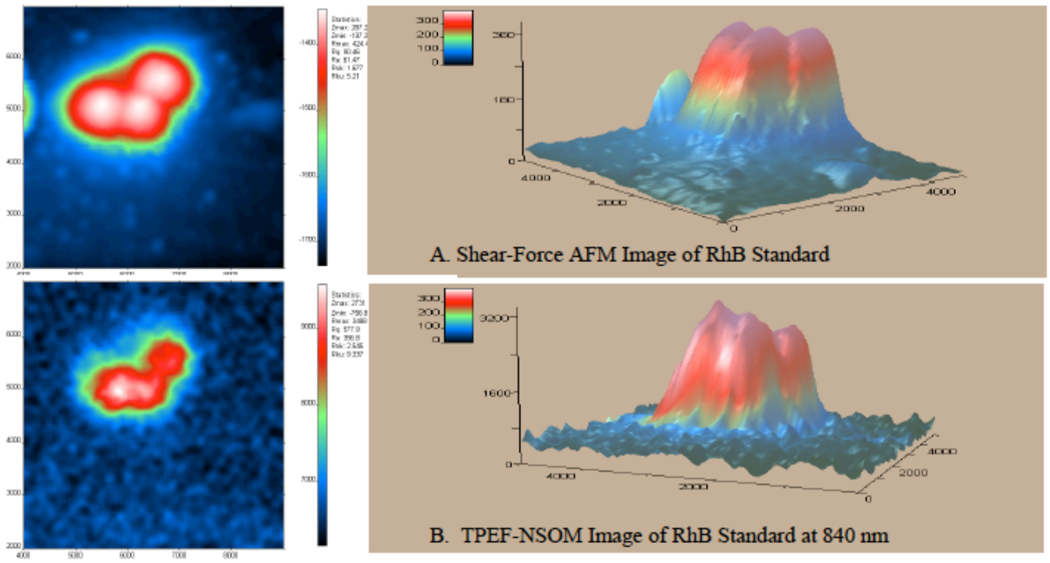

Figure 7-3. Representative Images of RhB Standard (2d and 3d Renderings)

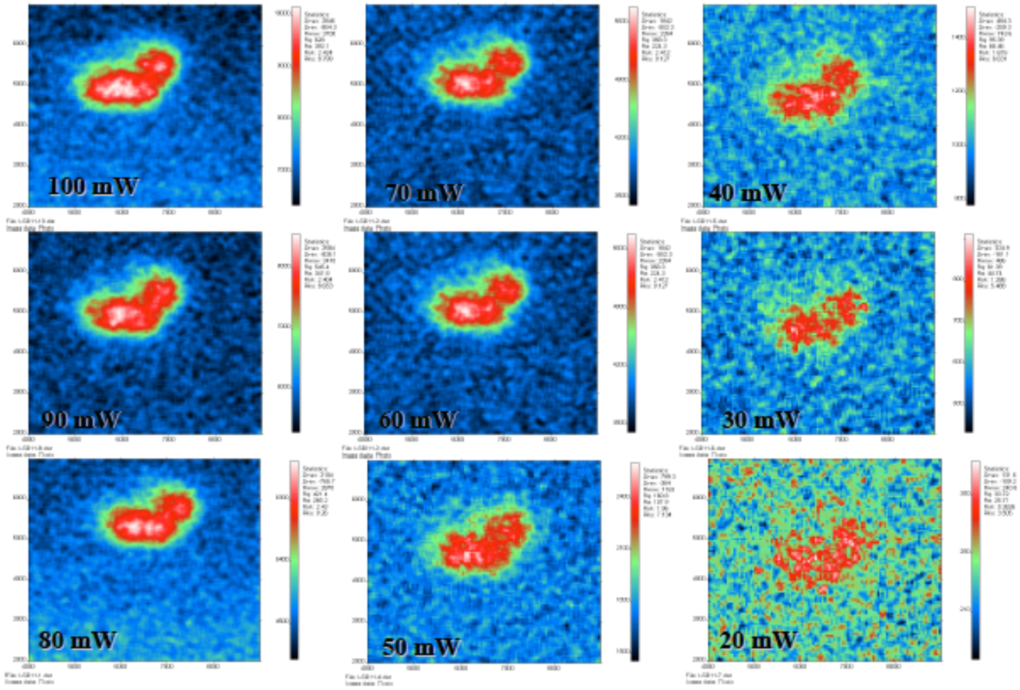

Figure 7-4. TPA NSOM Images of RhB Standard Spheres with Intensity Change

In order to confirm the intensity-squared dependence of the features observed, it is necessary to remove the background counts of the non-feature region from the entire image and then integrate the counts in both x and y. The log-log plot of input power (mW) and counts (CPS), conventionally used to confirm TPA response, gives a slope very close to two (figure 4-5) which confirms the viability of this method for quantitative imaging.

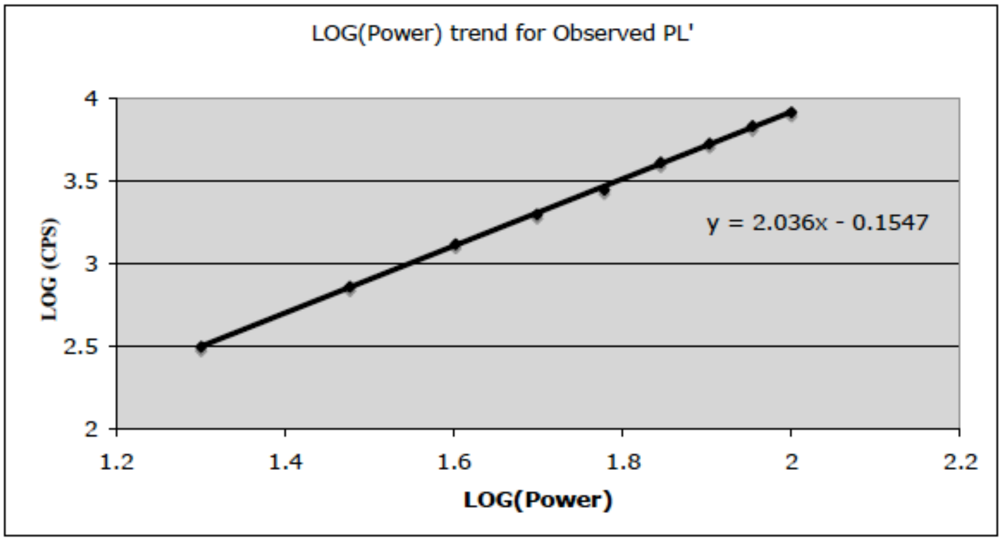

Figure 7-5. Log(mW) v. Log(CPS) for TPA NSOM RhB Spheres Study

Additionally, a height dependence study was initiated. A gradual progression from full contact mode to a non-contact mode height of ~1.5 um in ~100 nm steps is presented in figure 4-6. Though not calculated implicitly, whole feature CPS integration and broadening in the TPEF-NSOM image feature should give effective point source height and focal length. This may be useful for better defining a near field system that normally obfuscates these typical far field descriptions. Lack of peak intensity degradation during probe height changes provides an empirical display of effective penetration depth. Differing non-linearity in the feature signal and background signal allows for accurate image correction to account for intrinsic systemic NLO response within the field of view, should one be observed.

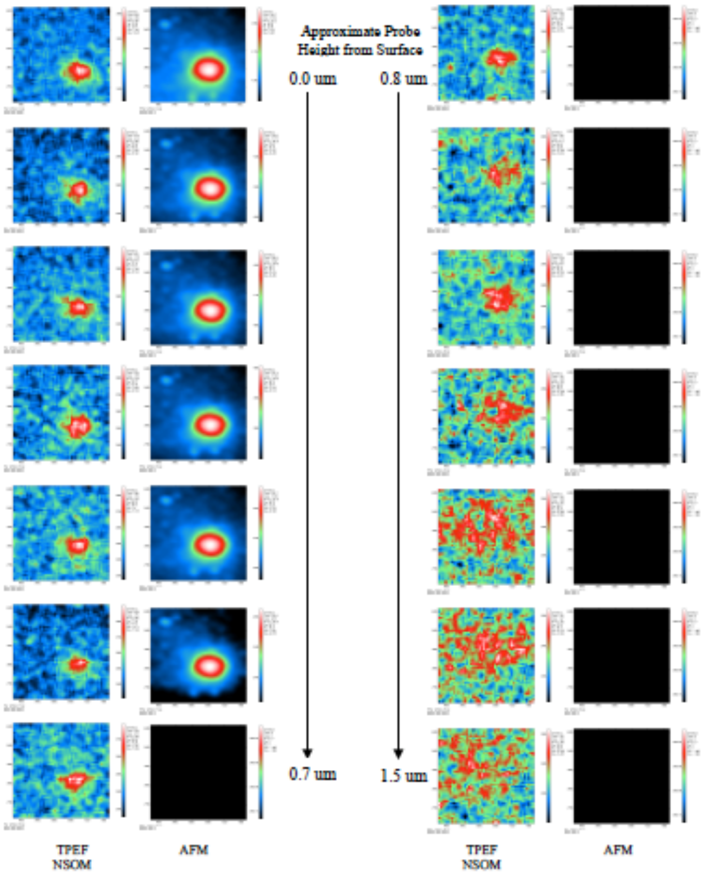

Figure 7-6. Height Study of RhB Spheres by TPEF NSOM with 820 nm Excitation (FOV 3.5 um)

7-7 Conclusions

Despite the many complications that arise from attempting an absolute TPA cross section measurement via NSOM, a referential method has been displayed here. A reference material is characterized for two NIR wavelengths and is confirmed to provide a quantitative NLO response. The ease of calculation and relatively fast processing time of this method should provide a fast and elegant method by which to compare nanoscale aggregates. The robustness of the system provides the possibility of imaging second harmonic generation and non-linear Ramen response in nanoscale materials.

7-8 References

(1) Raymond, J.E.; Guda, R.; Twieg, R.J; Goodson, T., III; “Two Photon Enhancement in Organic Nanorods”, J. Phys. Chem. C, 112 (21), 7913–7921, (2008)

(2) Xu, C.; Webb, W.W.; “Measurement of two-photon excitation cross sections of molecular fluorophores with data from 690 to 1050 nm”, J. Opt. Soc. Am. B, 13(3), 481-492, (1996)

(3) Raymond, J.E.; Bhaskar, A., Goodson, T. III; Makiuchi, N.; Ogawa, K.; Kobuke, Y.; “Synthesis and Two-Photon Absorption Enhancement of Porphyrin Macrocycles”, J. Am. Chem. Soc., 130 (51), 17212–17213, (2008)

(4) Bhaskar, A.; Guda, R.; Haley, M.M.; Goodson, T., III; “Building Symmetric Two-Dimensional Two-Photon Materials”, J. Am. Chem. Soc., 128(43), 13972-13973, (2006)

(5) Makarov, N.S.; Drobizhev, M.; Rebane, A.; “Two-photon absorption standards in the 550-1600 nm excitation wavelength range”, Opt. Express, 16(6), 4029-4047, (2008)

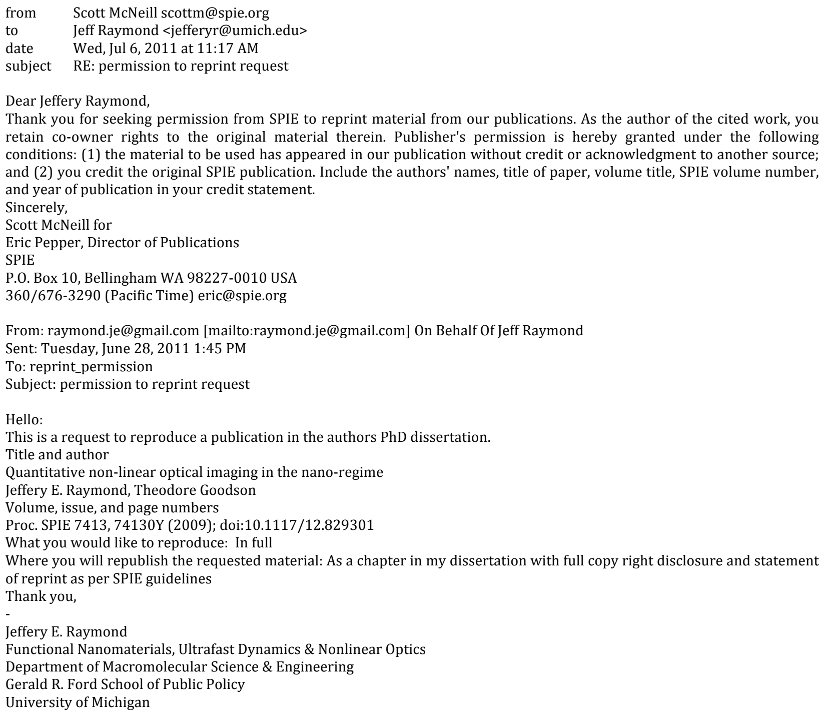

from Scott McNeill scottm@spie.org
to Jeff Raymond <jefferyr@umich.edu>
date Wed, Jul 6, 2011 at 11:17 AM
subject RE: permission to reprint request

Dear Jeffery Raymond,
Thank you for seeking permission from SPIE to reprint material from our publications. As the author of the cited work, you retain co-owner rights to the original material therein. Publisher's permission is hereby granted under the following conditions: (1) the material to be used has appeared in our publication without credit or acknowledgment to another source; and (2) you credit the original SPIE publication. Include the authors' names, title of paper, volume title, SPIE volume number, and year of publication in your credit statement.
Sincerely,
Scott McNeill for
Eric Pepper, Director of Publications
SPIE
P.O. Box 10, Bellingham WA 98227-0010 USA
360/676-3290 (Pacific Time) eric@spie.org

From: raymond.je@gmail.com [mailto:raymond.je@gmail.com] On Behalf Of Jeff Raymond
Sent: Tuesday, June 28, 2011 1:45 PM
To: reprint_permission
Subject: permission to reprint request

Hello:
This is a request to reproduce a publication in the authors PhD dissertation.
Title and author
Quantitative non-linear optical imaging in the nano-regime
Jeffery E. Raymond, Theodore Goodson
Volume, issue, and page numbers
Proc. SPIE 7413, 74130Y (2009); doi:10.1117/12.829301
What you would like to reproduce: In full
Where you will republish the requested material: As a chapter in my dissertation with full copy right disclosure and statement of reprint as per SPIE guidelines
Thank you,
-
Jeffery E. Raymond
Functional Nanomaterials, Ultrafast Dynamics & Nonlinear Optics
Department of Macromolecular Science & Engineering
Gerald R. Ford School of Public Policy
University of Michigan

Figure 7-7. Email Transcript of SPIE Permission Granted to Publish in Thesis

Chapter 8

In-Press NSOM and TPA NSOM Studies

8-1 Introduction

In this chapter, those components of this body of work which are not complete enough studies to warrant publication at this time are presented. All of these works focus primarily on one and two photon NSOM investigation of novel nanomaterials. No information beyond sample descriptions, findings and experimental conditions will be presented as the methods involved are well detailed in previous chapters.

8-2 Qualifying Statement

A variety of studies are put forward in this chapter of unpublished work. Several concepts, including other multiphoton processes are introduced. A focus is placed on NSOM applications.

Other Coherent Multiphoton Processes Besides TPA. Another coherent multiphoton process discussed in chapter 8 is that of three photon absorption. This is similar to two photon absorption but involves an initial virtual energy level, a second virtual energy level and a final transition to a real excited state. Units for three photon cross section are reported in $cm^6s^2/photon^2$ and have typical magnitudes of 10^{-87}. A final multiphoton process referred to in the silver aggregate section of the conclusion is one that occurs in metal oxide and semiconductor crystals, as well as a small number of well ordered organometallic species, and is known as second harmonic generation (SHG). SHG is an instantaneous process in which a large flux is focused in SHG crystal where two lower energy photons are spontaneously interconverted to a single photon of higher energy. This process is often intrinsic to lasing operations where wavelength tunability is needed.

However, in nanocrystalline materials SHG signal may obscure TPEF emission as they are both I^2 processes. As SHG is an instantaneous process which has a narrow band width and is exactly matching twice the excitation energy, it can often be deconvoluted from a spectrum once identified. If this is not possible, then emission lifetime measurements will reveal the SHG process with a signal lifetime profile which will match the excitation source (i.e. $\tau_F = 0$).

8-3 NSOM Operations and Training

During the summer of 2009, the author worked at the Air Force Research Laboratory as a summer research assistant. Working under Augustine Urbas and Thomas Cooper of the Optical Limiting group in the Materials and Manufacturing Directorate, a non-functional and disassembled Aurora 3 NSOM microscope was redeployed. The author rebuilt, repaired, calibrated and subsequently trained the staff on use of the instrument. The following is the standard operating manual that was generated at that time.

Aurora 3
Near Field Scanning Optical Microscope (NSOM)

Standard Operating Procedure

Created By: Jeffery Raymond

Created On: July 10 2009

Updated By: Jeffery Raymond

Updated On: August 20 2009

Powering on the Aurora 3 System

- Turn on control box (under table)
- Turn on CPU
- Turn on CPU and video monitor
- Turn on laser to be used
- Open the SPM software

Software Preparation

- Open the SLP software on the Desktop
- Click on the AFM cantilever button
- Click [OK] and [Engage]
- [Setup]→[Acquire]→select topography, internal sensor and PMT (all forward)
- Set initial parameters in the acquisition panel
    - Set Point: -64 nA
    - Scan Range: 5 um
    - Scan Rate: 2.5 um
    - Resolution: 200
    - Proportional: 1
    - Integral: 0.05
    - Derivative: 0

Probe Approach

- [Setup] → [Video] : turn on the light, camera and toggle to the reflection image CCD
- Confirm that the probe is significantly distant from the sample surface.

- Adjust the x and y head positioning dials so that the probe point is centered on the monitor
- Confirm that the probe is in the field of view by toggling to the transmission image CCD and focusing until you see the probe
- Return to reflection CCD
- Manually lower the head so that the probe and its reflection are both in the field of view using the hand knobs.
- IF you have not already coupled the probe adequately, perform probe coupling now.
- Use the probe down button to approach the surface as closely as possible.
- IF you have not already determined the probe resonance set points, determine them now.
- Below the acquisition panel press [>>] or [<<] until 'Prescan' shows
- BEFORE pressing the Tip Approach button, ensure that the Set Point is at -64 nA.
- Press [Tip Approach]
- Note the tips retraction from the surface on the CCD monitor.
- Observe the internal sensor on the oscilloscope in [Scope] mode.
- This should read between -35 and -25 nA
- Set the Set Point to ~5 nA more negative than the reading.
- Observe the Peizo voltage in the lower half of the oscilloscope, which should read -210 V
- Adjust the Set Point positive until you see the voltage jump up off the -210 V baseline (should be close to the Internal sensor value)
- Slowly increase the set point further until the voltage begins a regular rise.
- Eventually the voltage will spike and then settle. At this point take the set point to 0.1 higher.
- If the voltage goes to +210 V, raise tip and try again.
- If the voltage begins descending to -210 V, raise the set point until contact is found again.

<u>Determination of Probe Resonance</u>

- In the Non-contact Control Window, set the mode to Amplitude
- Set Amplitude to 0.1 V and the Gain to 8.
- [Full Spectrum]
- [Zoom in] to the region from 90-100
- Look for a sharp peak.
- Adjust voltage and gain until the peak is ~5 V (voltage should not go above 1.15 V)
- Ideally you want as low of a voltage as possible without making the curve rough.
- Select the peak of the curve
- Switch to Phase mode
- [Auto Phase] → [+90] → [+90] → [+90]

- Confirm in the Oscilloscope (in scope mode) that the internal sensor signal is close to -30 nA.
- Minimize the Non-contact Control Window

Fiber Coupling and Signal Maximization

- Turn on laser
- Choose wavelength
- Allow appropriate time for laser stabilization
- Set fiber optic cable into the fiber chuck if not already set
- Bring fiber end to ~1/4 inches from objective
- Using software, bring the probe close to the surface, but not in contact.
- Turn off CCD light
- Adjust chuck x/y until the reflected probe light is visible in the CCD
- [Set-Up] → [PMT] → turn on
- Adjust voltage until signal voltage for the PMT in the oscilloscope is ~2V
- Align the system using the PMT as a judge of alignment
- Suggested method
    - Distance control
    - Chuck x adjust
    - Chuck y adjust
    - Lens x adjust
    - Lens y adjust
    - Laser wavelength
    - Laser cavity adjust
- If the voltage signal raises above 5 V, decrease the PMT input voltage until the signal is closer to 2 V.
- Execute the alignment sequence until maximum alignment is found.
- Decrease PMT voltage until the base line signal voltage is ~1 V

Imaging Guidelines

- Be sure contact has been made and the Peizo voltage has stabilized
- Begin with initial set points outlined in Software preparation
- Switch to line scan on the oscilloscope.
- Change the line scanned until a viable feature is seen
- Change the range, rate and resolution to accommodate features.
- Slowly raise integral and lower proportional until a features become symmetric
- Proportional should remain > 0.5 and integral should remain < 0.3
- Initiate scan

Probe Replacement

- Block beam or turn off laser
- Remove fiber chuck from coupling mount

- Remove fiber from chuck
- Unplug head from the NSOM
- Remove head in the X-Y-Z fashion
- Secure the head and locate the replacement probe
- Remove the current probe and place it in a safe location
- Ready the replacement by unrolling fiber, removing tape and pressing foam aside
- Place probe under tines on the head, being careful to not snap the fiber
- Store and label previous probe
- Raise the X and Y mounts so that the probe is obviously (by eye) above the contact plane.
- Replace head in the Z-Y-X fashion, observing it during placement
- Plug the head in to the NSOM (may be done before head placement if more light is desired)
- Secure the fiber into the chuck and the chuck into the coupler
- Probe approach and fiber coupling as above

8-4 NSOM Investigation of Chromophore Labelled Gold Nanoparticles

The following research was performed at the Air Force Research Laboratory.

One method of photonic enhancement is the use of plasmonic nanoparticles. In brief, a plasmonic nanoparticle is often a metal (here gold) where the interaction with an oscillating E-M field can induce a electronic oscillation in the material. The presence of this electronic oscillation can grossly enhance the dipole moments of nearby materials and result in strong enhancement of opto-electronic processes. This can result in effects like enhanced absorption, Raman signal, two photon absorption, and fluorescence.

Gold nanoparticles of ~50 nm diamater where surface stabilized through covalently bound azide molecules with a coating thickness ~20 nm. Azide has a sharp absorption band at 400 nm with emission near 550 nm. The gold plasmon peak for these particles was found to be near 530 nm. Using 532 nm excitation to directly excite the gold emission band, pure emission from the Azide was observed with a full order of magnitude of enhancement in fluorescence quantum yield, clearly showing plasmonic enhancement. This leads to the question of whether the external surface of the coating, the 'bulk' coating material or the M-L interface was emitting. The author's contribution to this project was to use the Aurora 3 NSOM to directly observe individual particles or particle aggregates to directly observe the source of this enhanced emission (figure 11-1).

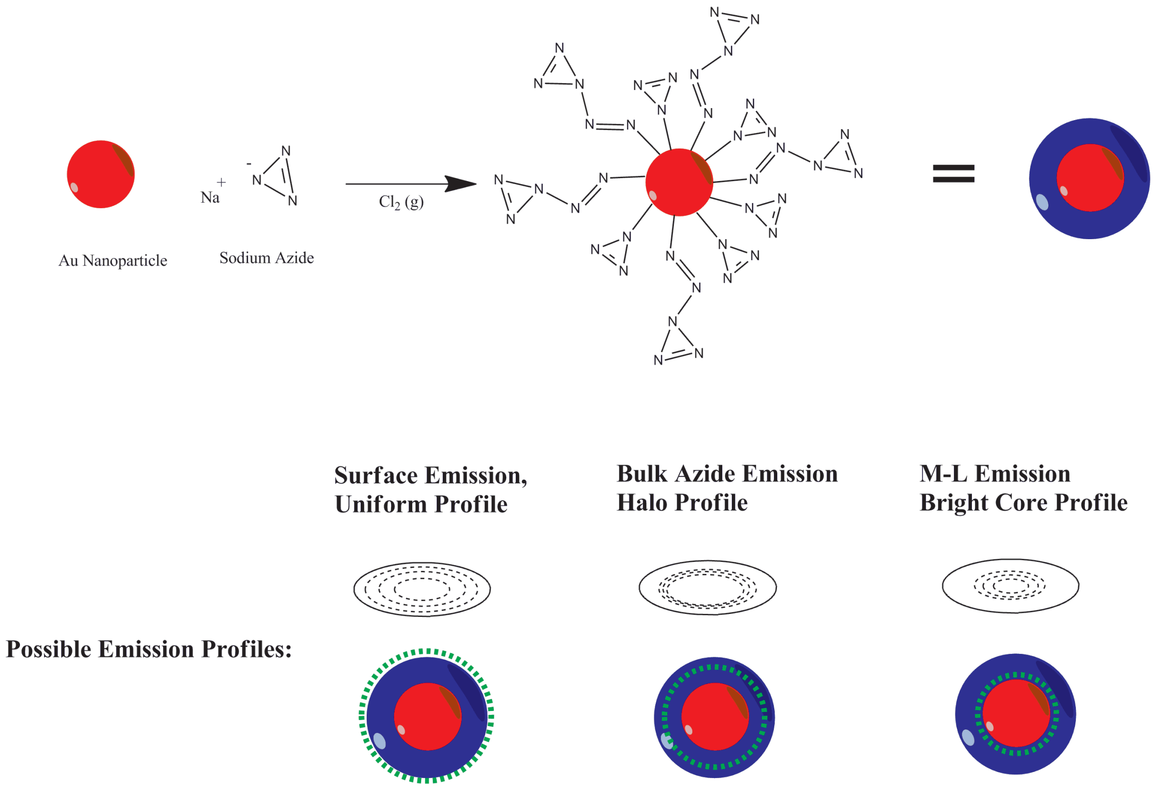

Figure 8-1. Formation of Gold-Azide Nanoparticles and Anticipated Emission Profiles Based on Emission Source

For this work, the results were conclusive: The nanoparticle emission was coming from the outer surface of the particle (figure 11-2). In the overlayed image, where emission is green/yellow and AFM is brown/red, it is clear that the particles prefer to dimerise or trimerize in the solid state, and that surface to surface contact between particles appears to not have a quenching effect.

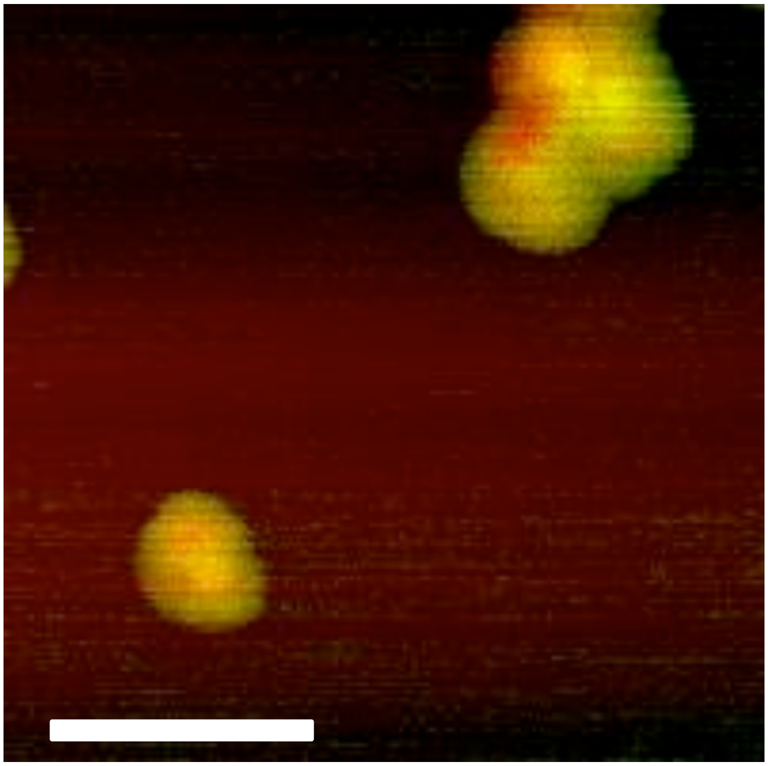

Figure 8-2. Fluorescence NSOM of Gold Azide Nanoparticles

Red-brown is for AFM, yellow-green is overlaid emission. Scale bar is 200 nm.

8-5 NSOM Investigation of Chromophore Labelled Silver Nanoparticles

This project was performed at the Air Force Research Laboratory.

Similar to the plasmon enhanced azide emission in the gold system, larger silver particles were used with a different fluorophore, stilbene (figure 11-3). The silver nanoparticles had average sizes of 150 nm with an outer stilbene layer of ~100 nm.

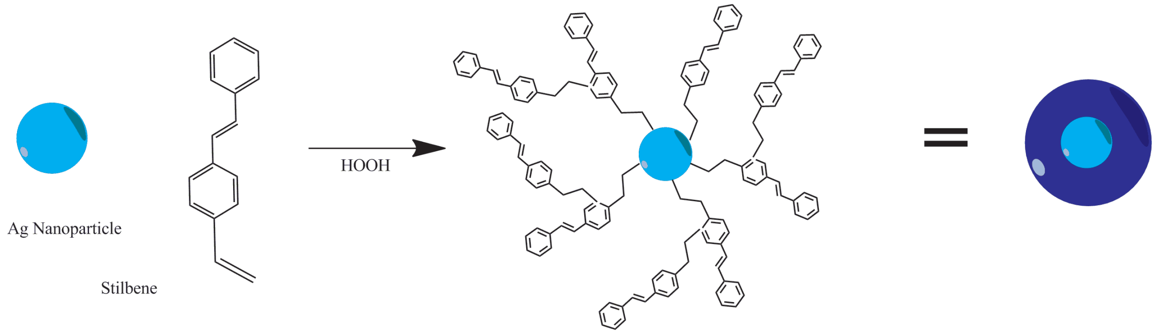

Figure 8-3. Stilbene Ag Nanoparticle

In this study, using 532 nm excitation to target a nearby plasmon band in the silver (~550 nm), fluorescence NSOM was again able to rapidly resolve the emission location for this system (figure 11-4). Specifically, it can be seen that only the regions near the silver core are able to generate significant emission. Also a tendency to dimerize or trimerize can be observed.

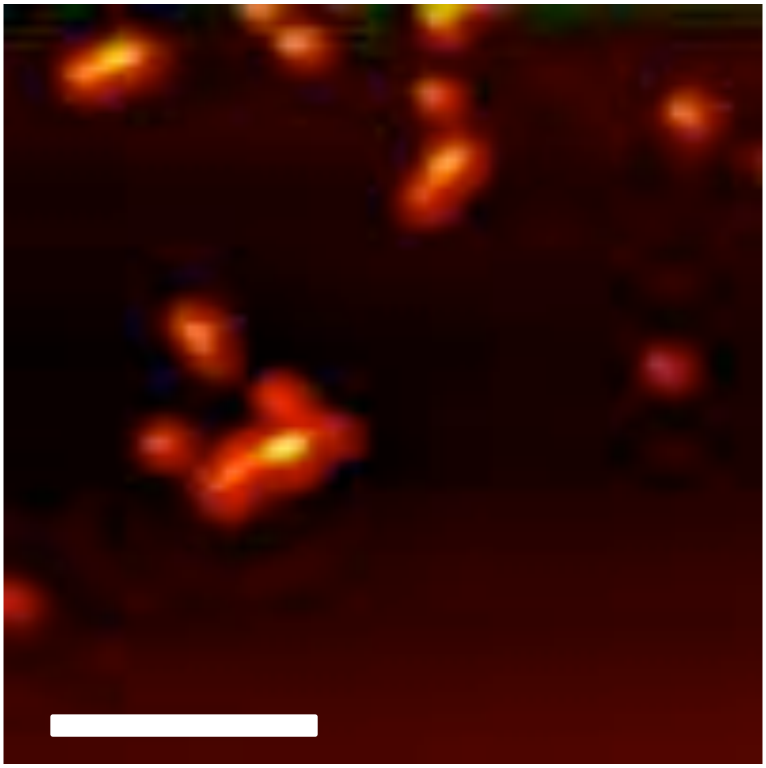

Figure 8-4. Fluorescence NSOM of Silver-Stilbene Nanoparticles and Aggregates

Red-Brown is AFM signal, yellow-green is NSOM emission signal. Scale bar is 2 um.

8-6 NSOM Investigation of Pt Core Liquid Crystal Self Assembly

This project was undertaken at the Air Force Research Laboratory.

In an attempt to generate good TPA enhancement and excellent excited state absorption, the synthesis group at the AFRL attempted to use molecular characteristics based on the liquid crystal nanorods presented in chapter 2. This led to the synthesis to a platinum acytilide compound with donor and acceptor groups exactly like those in found in chapter 2 (figure 11-5).

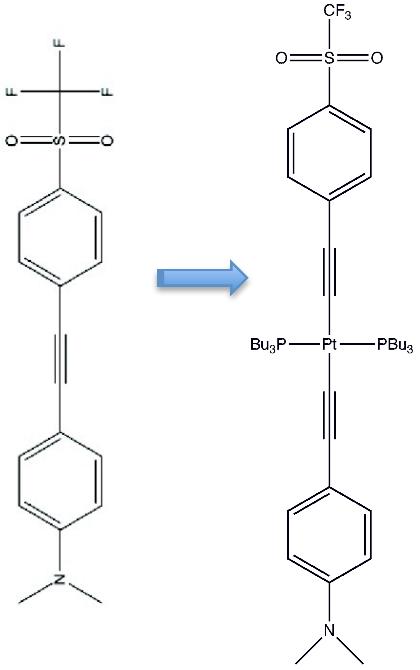

Figure 8-5. Pt-Liquid Crystal Based on NLO Liquid Crystal that Self Assembles into Nanorods

Platinum acytilide complexes are exceptional excited state absorbers after continued excitation because of a series of high cross section triplet-triplet transitions available to them. The intent for building this system was threefold: (1) to use aggregation to limit emission, (2) use self assembly to obtain the TPA enhancement this donor acceptor group has shown, and (3) use the long lived triple state after TPA excitation to absorb continuous wave excitation. Ideally, this material should be capable of optically limiting both pulsed and non-pulsed excitation sources.

Bulk solution phase measurements showed a very high nonlinear response with absorption being a function of $I^{2.6}$, notable as exponents above two and below three usually mean a combined TPA/ESA process. However, where most Pt-acytilide systems are non-emissive, some emission was observed.

Different solvent regimes were used to try to generate aggregates which did not emit. A water/acetonitrile mix eventually resulted in a nonemissive species which was subsequently imaged by NSOM with 580 nm excitation (figure 11-6) and compared to a disordered film of aggregate (figure 11-7). In figure 11-6 it can be seen that the resulting species was a nanowire with an exceptionally high aspect ratio. In this figure, AFM is rendered as red while the signal from the NSOM excitation is in green. The image shows clearly an enhanced absorption in the nanowire. No emission NSOM was recorded as no emission signal was observed.

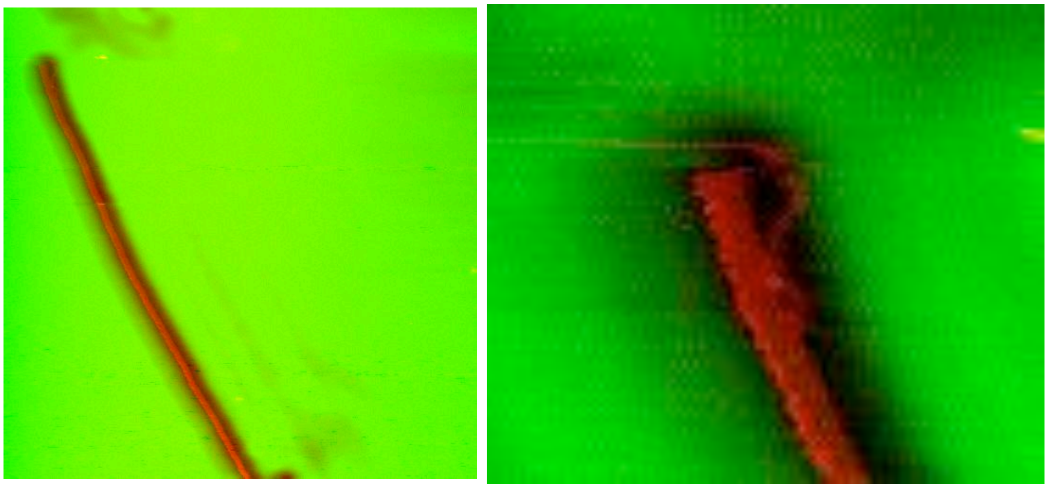

Figure 8-6. Absorption NSOM of an Organometallic Nanowire made from a Pt-bridged Liquid Crystal

Field of view on the left is 5 um x 5 um, on the right it is 0.8 um x 1 um.

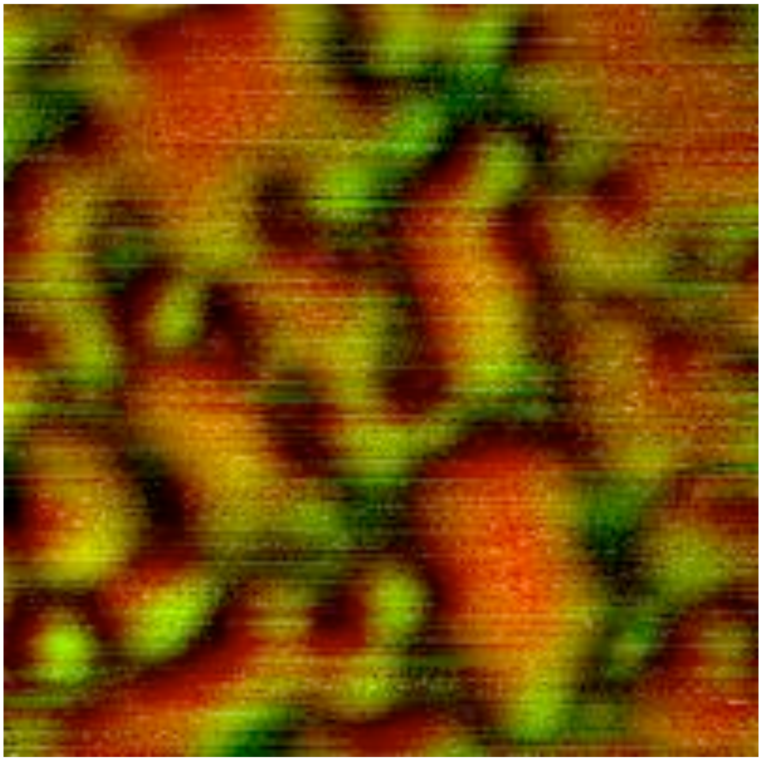

Figure 8-7. Fluorescence NSOM of Amorphous Pt-bridged Liquid Crystal Aggregates

Emission rendered in green, AFM in red, field of view is 5 um x 5 um

When the wire image is compared to figure 11-7, it is clear that the NSOM images indicate that aggregation and high concentrations are not sufficient to quench emission and that nanoscale ordering can dictate the response of this liquid crystal system. This is an important finding as optical limiting materials must have virtually undetectable emission if the instrument being protected is sensitive to the emission wavelength.

8-7 Two Photon NSOM of Synthetic Peptide Aggregates

There is a large interest in understanding the precise mechanism by which peptides transition from alpha helices to beta sheets to fibrils to plaques. This is due to strong correlations between diseases such as Alzheimer's and Parkinson's and the amount of certain peptide plaques found in the brain. One method that has been attempted in the study of these phase change processes is the generation of synthetic peptides with strongly emissive groups within them. These systems, through quenching and other photophysical processes, allow us to study basic structure change kinetics in an unambiguous way.

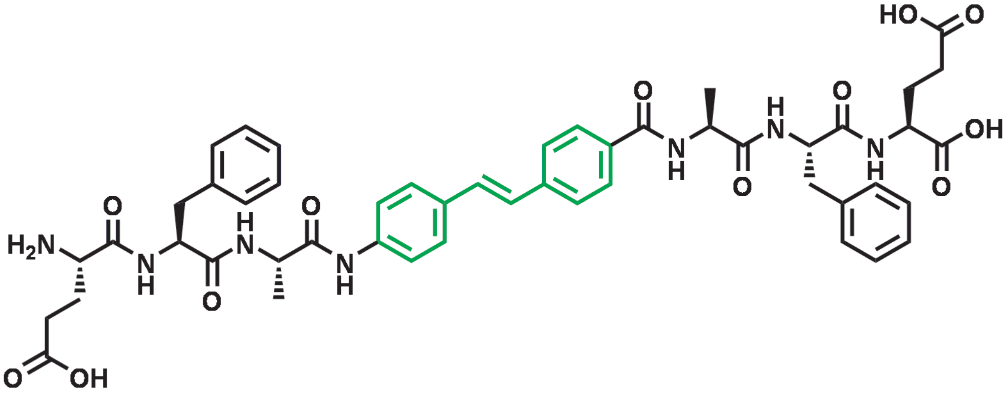

Figure 8-8. Stilbene Core Synthetic Peptide

To this extent, a stilbene core peptide was sysnthesized (figure 11-8) where changes in both one and two photon response can be observed readily. These changes in emission were largely investigated based on pH induced aggregation. Specifically, when investigating the resulting aggregates via TPA-NSOM, two different pH's were used, both generating aggregates when deposited onto a glass substrate.

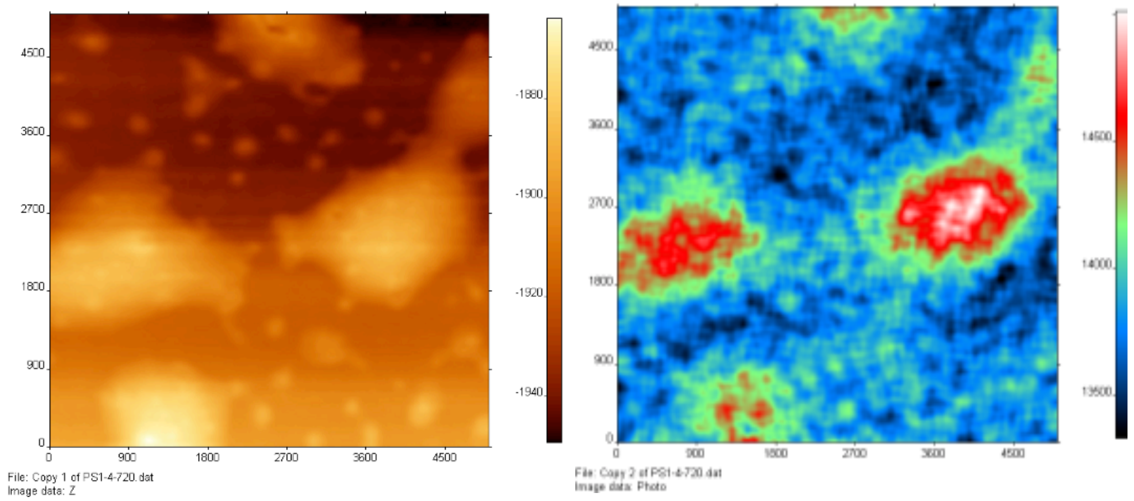

Figure 8-9. High Two Photon Emission Plaques from pH 11

TPA emission is ~15% above background with 2 mW incident power.

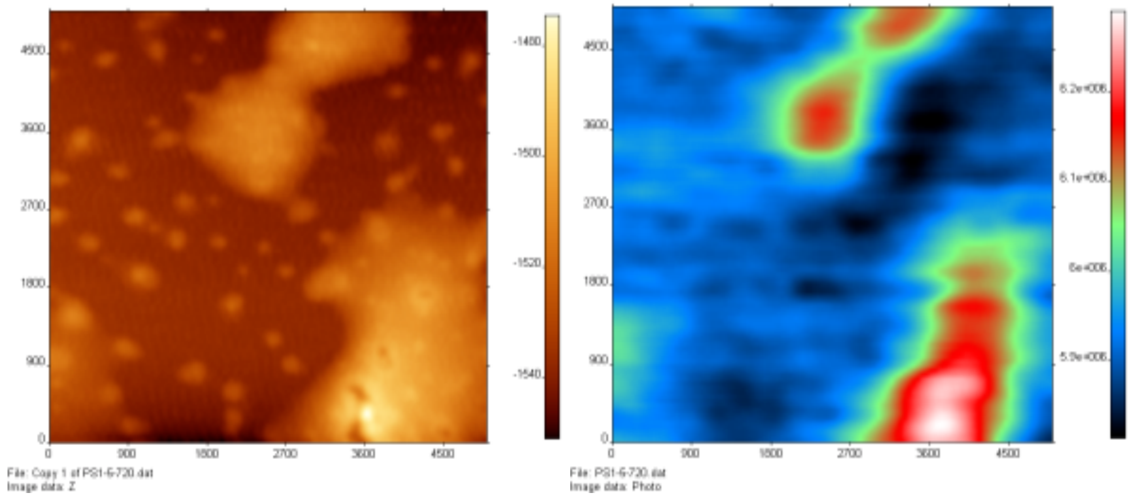

Figure 8-10. Low Two Photon Emission Plaques from pH 8

TPA emission is ~15% above background with 180 mW incident power.

From these preliminary results, it appears that the more basic aggregates appear to emit much more than similar volumes of the more acidic aggregate. This may imply that the basic aggregates have less stilbene-stilbene interactions or are generally less densely packed. Regardless of cause, this study demonstrates the ability of two photon NSOM to quickly distinguish between two biomimicking plaques despite very similar sizes, identical building blocks and indistinguishable morphologies.

8-8 Two Photon NSOM of Defects in Gold Plasmonic Films

This study was performed in collaboration with Julie Biteen (University of Michigan).

Plasmon enhanced imaging is becoming an ever more popular form of bioimaging. Of particular interest are plasmonic 'hot spots' where multiple plasmonic fields are felt in a single region, leading to a multiple order of magnitude enhancement of emission for some configurations. One method for the generation of these hot spots is to sputter a thin layer of amorphous gold onto a substrate and then anneal the sample. The result desired is one in which the metastable amorphous gold becomes free to phase transition into more stable nanoislands with low temperature annealing. The results of one such attempt are displayed in figure 11-11. This AFM and the resulting line scans show a gold layer much thicker than anticipated and only some 'island" formation is evident. It is immediately clear that the system is also riddled with holes ranging from 50 to 700 nm in size. These holes provide a reliable measure of actual film thickness (~16 nm) as substrate can be found within them.

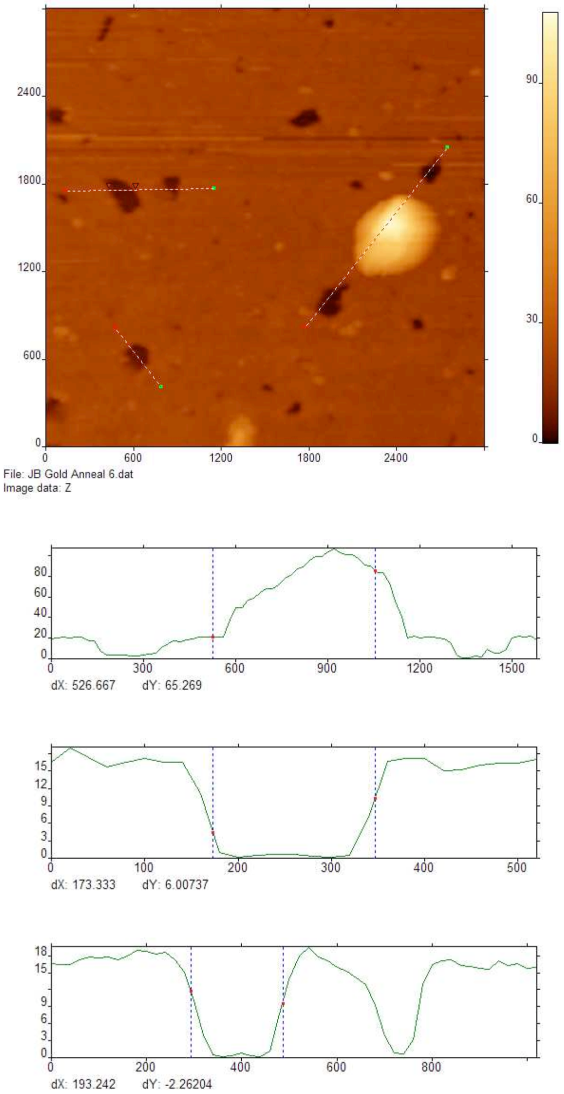

Figure 8-11. AFM of a 16 nm Gold Film and Nanodefects After Annealing

The top line scan is of the large particle, the second is of the individual hole in the third quadrant of the AFM image and the third displays two smaller holes on the left side of the image.

Gold nanoparticles are capable of some degree of emission. It is not then a far stretch to suggest a two photon response from this film. To investigate, TPA NSOM was used with an excitation wavelength of 800 nm and a coupling intensity of 50 mW. The results are displayed in figure 11-12.

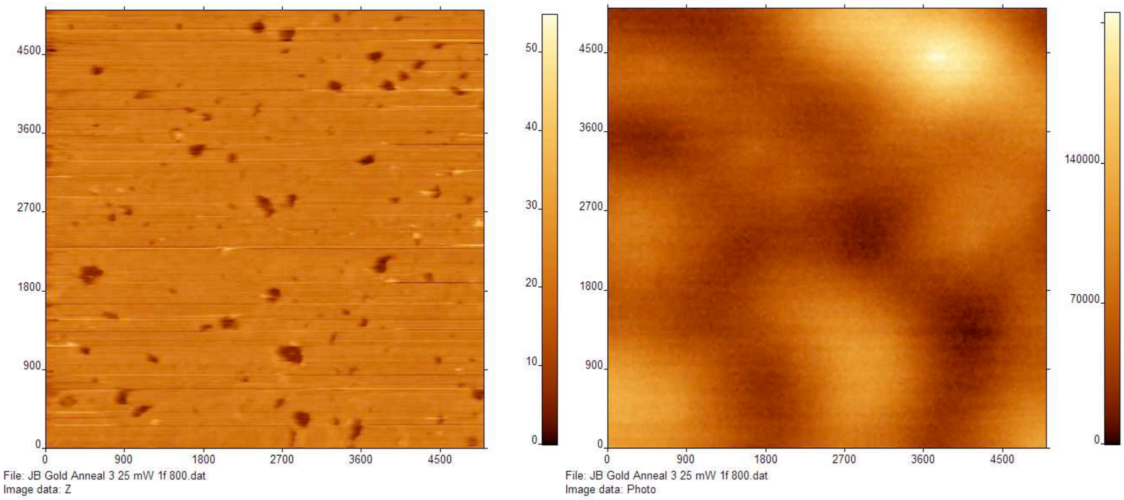

Figure 8-12. TPA NSOM of a High Defect Film

Regions with large holes/hole density show high signal, implying that all signal comes from absorption contrast.

The contrast observed in the NSOM of the gold film appears to correspond only to those regions where there is a high hole density and the holes present are large. This implies that either the hole edges are capable of emission or the contrast observed is strictly due to absorption of the excitation source by the substrate. Absorption by a thin metal film seems most reasonable, but emission should be discounted before one can be certain.

Two methods were employed to confirm that the images taken are in fact two photon absorption images (and not emission) were far field excitation of the film and top-down collection of NSOM signal. First, the film was placed in a sample holder and illuminated by a focused 800 nm fs pulsed light source and intensity was increased until the film burned. An Ocean Optics CCD was used to collect emission from 400-700 nm. No emission was observed. Additionally, a power meter was moved behind the film and the transmission intensity was observed from different areas of the sample. With a 0.1 mW beam, the transmission ranged from 5 uW to 50 uW just from repositioning alone. When the film was held constant and transmission was observed based on power changes, an I^2 relationship to the change in I was observed. This suggests strongly that two photon absorption is limiting the throughput in areas where undamaged film exists and allowing transmission in regions with more holes.

The second method used to confirm TPA absorption top-down collection in TPA NSOM. TPA NSOM was deployed to confirm this finding, but a different collection regime was implemented. A high power objective above the NSOM stage was focused just below the NSOM probe and the PMT was coupled to the objective. Scanning occurred as normal, but only photons cast back at the objective are collected. This signal then includes be a combination of emission (if any) and any reflected/scattered light. Figure 11-13 depicts the results of this experiment. Note that the TPA NSOM signal is fairly uniform over the majority of the film, however a slight increase in counts can be seen over the one particle in the field of view (increased scatter) and a gross loss of signal occurs near the hole. While the hole feature in TPA NSOM is not perfectly resolved, clearly it is not surrounded by a halo of illumination as one would expect from an edge emission process. This final image fully supports the theory that the hole laden film can be imaged by two photon absorption NSOM and that the hole edges do not meaningfully emit under two photon excitation. In terms of generating gold nanoislands this study was unsuccessful. However, it does show the versatility and effectiveness of TPA NSOM absorption imaging in the assessment of metallic films and nanostructures and was the motivation for the final study presented in this chapter.

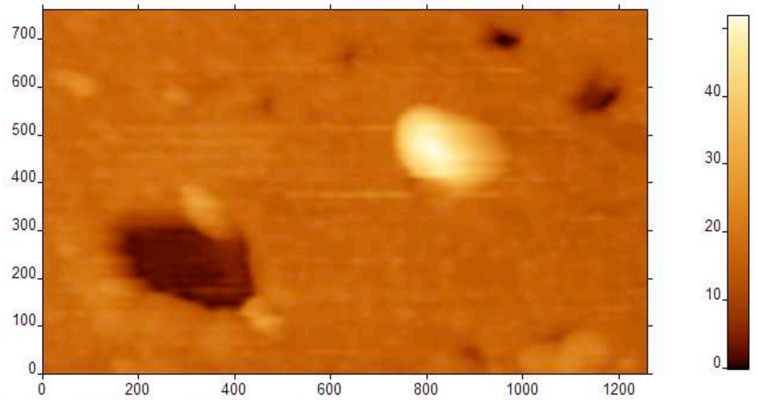

File: Copy 1 of JB Gold Anneal 4 1f 800 TOP
Image data: Z

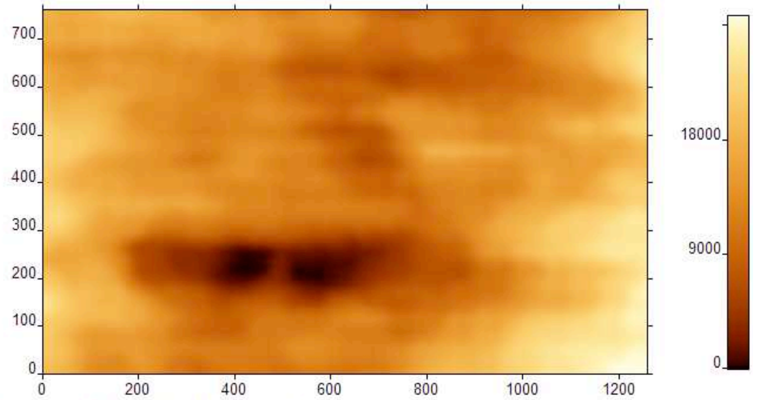

File: Copy 2 of JB Gold Anneal 4 1f 800 TOP
Image data: Photo

Figure 8-13. Reflection Mode Collection for TPA NSOM of a Gold Film

8-9 Plasmon Enhanced Two Photon NSOM of Self Assembled Silver Dendritic Crystals

This project was performed in collaboration with Raoul Kopelman (University of Michigan).

The previous gold study did not result in particles which would be appropriate for plasmonic enhancement. However, with the viability of absorption imaging of metallic nanostructures by TPA NSOM proven, it stands that other avenues to plasmonic structures may still be readily investigated by this technique. To this extent, carboxylate stabilized silver nanoparticles with diameters in the 10-20 nm range were obtained. The absorption spectra of the particles in solution showed a maximum at 400 nm. Allowing the particles to age, surface oxidize and partially aggregate to average sizes of 200 nm led to the growth of a plasmon band in the absorption spectra at 600 nm. Origanlly, the research was to include deposition of the 200 nm silver onto a substrate with TPA NSOM being done on the raw particles. After, the application of a small amount of chromophore to the substrate was to occur. An accompanying TPA NSOM study being done to identify 'hot spot' locations and how that related to particle density and orientation. Initial TPA NSOM can be seen in figure 11-14.

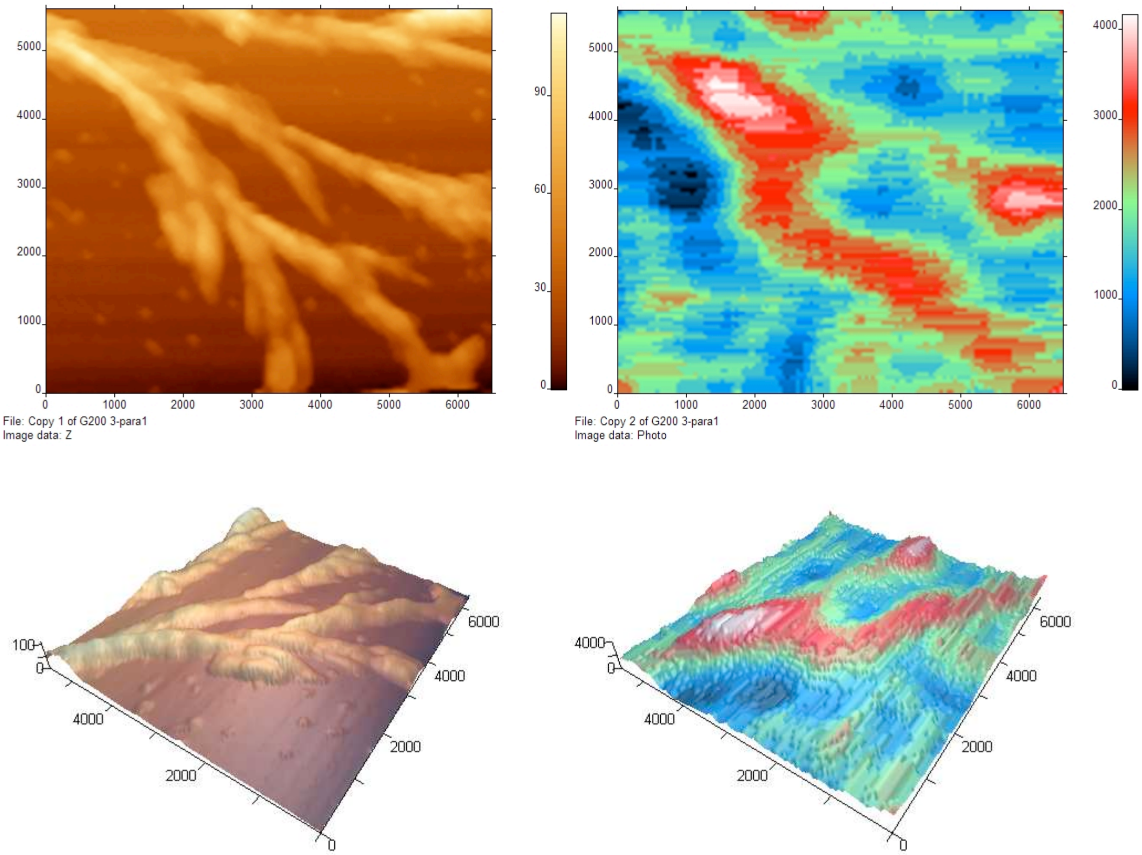

Figure 8-14. TPA NSOM of Silver Dendritic Microstructures

2D and 3D profiles. AFM on the left, two photon emission on the right.

From this image it is clear that the majority of the silver has aggregated into a dendritic polycrystalline structure and that regions of this structure are clearly more emissive than others. However, the reason for this crystallization and the source of emission was not immediately clear. In order to confirm this finding, a larger scan was performed at extremely slow scan rates. This result is found in figures 11-15 and 11-16.

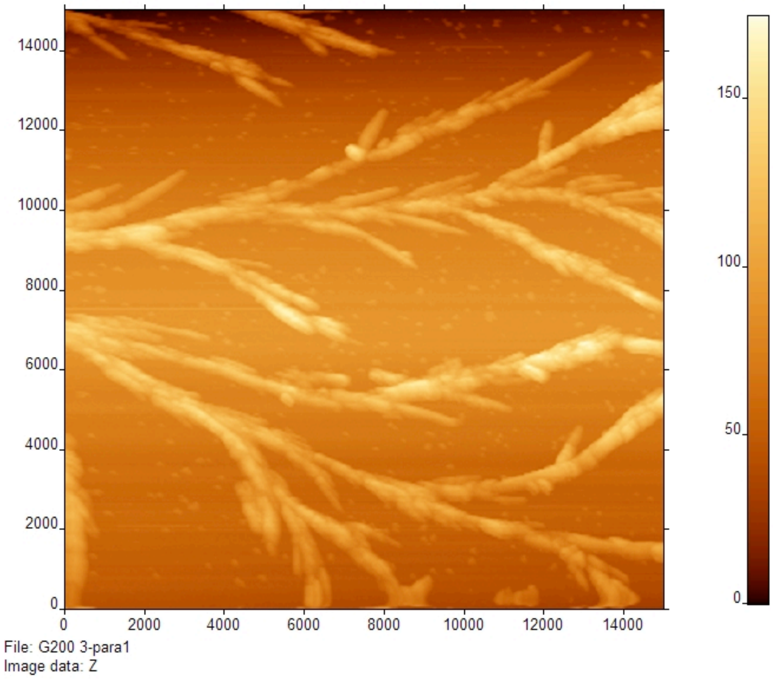

Figure 8-15. 15 um x 15 um AFM of a Silver Dendritic Nanostructure

Regarding the physical dimensions of this structure, it is clear that surface coverage (ie a high surface energy substrate) dominated the crystal formation. The average height of each branch is 100 nm, while widths range from 400 nm to 1um. This indicates that some process has destabilized the silver and forced a substrate mediated crystallization. It can also be seen that some of the particles remain on the substrate in small aggregates, but this is less than 0.1 % of the total volume in this field of view and can most likely be discounted in terms of contribution to emission.

Simultaneous TPA emission was taken by NSOM of the region and is presented in figure 11-16 where it can be seen that emission signal clearly correlates to the AFM features, with some regions having a disproportionate amount of emission based purely on the volume of crystal in the region.

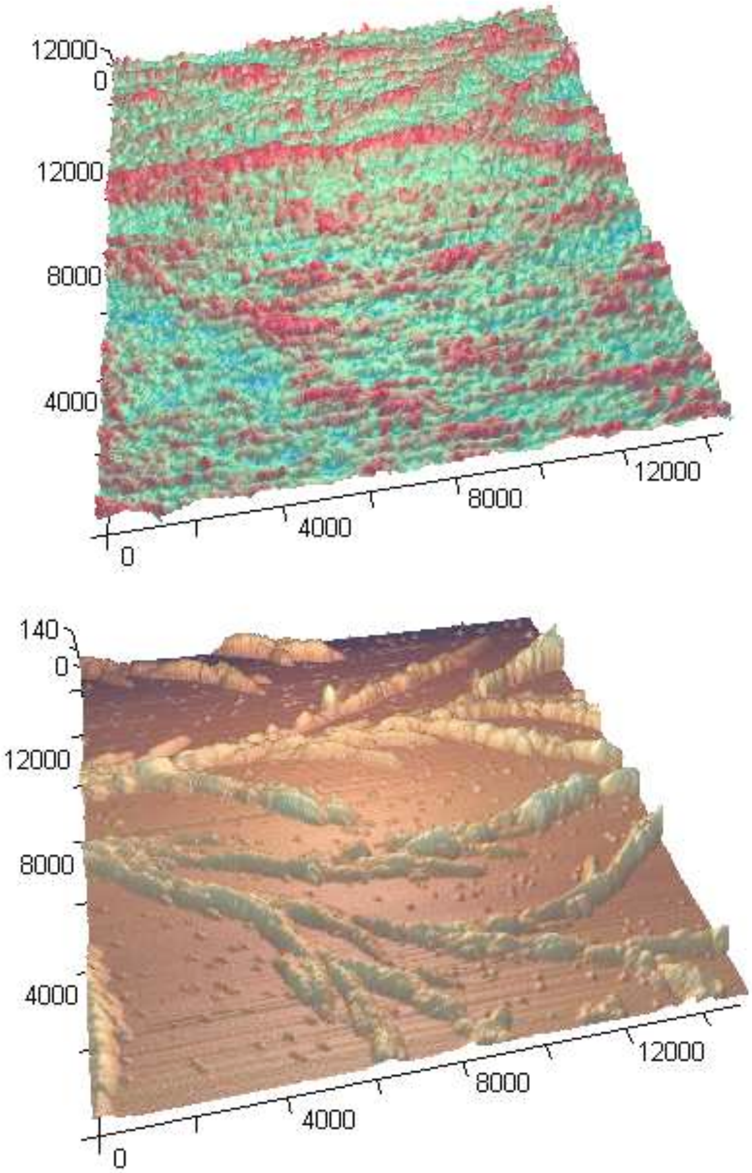

Figure 8-16. TPA NSOM (top) and AFM (bottom)

TPA NSOM emission scan shows the majority of the major AFM features. While most of those features are aligned left to right, some are not and still emit. Also some left to right growth does not emit at all. This suggests that the on and off regions are do to the microstructure, and not do to orientation of the excitation polarization.

From figure 11-16 it could be taken that a majority of the microstructure is generating emission from two photon excitation, however scattering and stimilulated emission remain possibilities. To confirm this response is from a two photon process, excitation coupling power was reduced from 50 mW to 40 mW and TPA NSOM was performed on a smaller region (5 um x 5 um), presented in figure 11-17. Feature clarity was sharply impacted and maximum feature emission dropped from 12,000 CPS to 8000 CPS, in keeping with a response related to I^2.

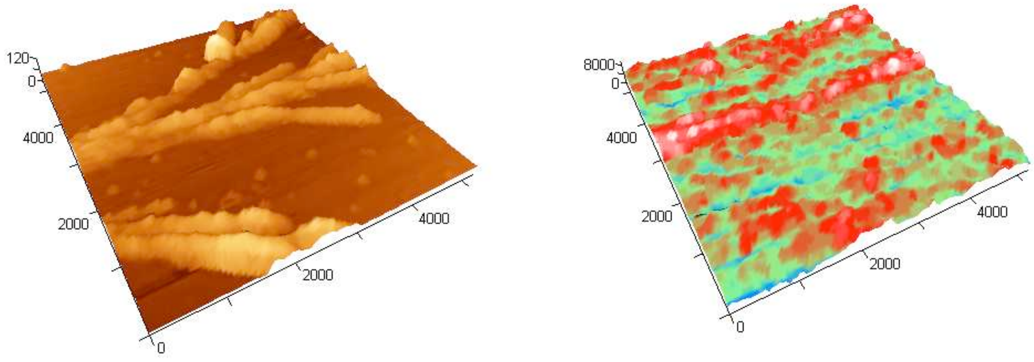

Figure 8-17. Lower Power AFM (left) and TPA NSOM (right) of Silver Dendritic Structure

Through TPA NSOM several things are now well known about this sample:

1. 99.9+ % of the silver was converted from nanoparticles to dendritic microstructure.
2. Regions of the microstructure display emission under pulsed NIR excitation.
3. This emission does not always correlate to the amount of material present at the feature.
4. This emission is due to two photon excitation fluorescence.
5. Crystal growth is mediated at least as much by the surface energy of the substrate as any instability in the nanoparticulate silver.

The authors preliminary thoughts on the crystal formation largely involve the substrate used and the surface stabilizing carboxylate.

These features of the system still do not answer the pivotal question: What is emitting a why? To address this, a bulk suspension study was performed on the pure silver particles, on 200 nm aggregates and on 700 nm aggregates. The emission results for this are shown in figure 11-18 for all samples under two excitation powers, 200 mW and 400 mW. All spectra are taken from 830 nm excitation with 100 fs pulses.

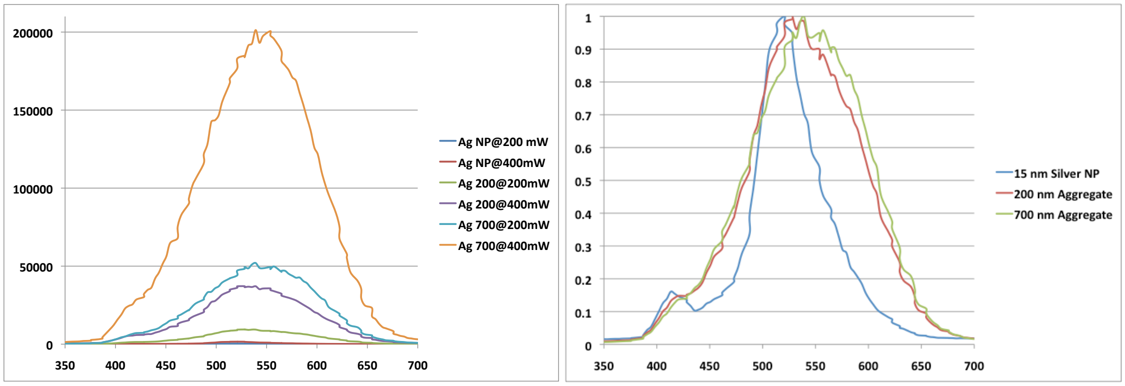

Figure 8-18. Bulk TPA Emission from Silver Nanoparticles, 200 nm Aggregates and 700 nm Aggregates

Solution densities are the same by mass, with 10 ug per mL. Corrected for PMT sensitivity and background scatter. Left, raw emission spectra from 200 mW and 400 mW excitation. Right, normalized emission to show differences in spectra.

The bulk TPA findings are consistent with increased TPA emission from the 700 nm aggregate sample, which has at least one dimension in common with bulk crystals. The peak location at 545 nm for the 700 nm aggregated samples is consistent with the emission profile of silver oxide (AgO). The pure sample, significantly less responsive, shows a blue shift and a narrowing of emission. This should not be taken formally as a change in emission properties of the AgO. Rather, the silver is most likely reabsorbing on either side of the emission peak, with the 400 nm absorption band taking from the blue edge and the plamon band estracting from the red edge. This is typical of systems where absorption is significantly stronger than emission process. Another feature of the pure silver sample is a 415 nm peak, which should be taken as a small amount of SHG from the 830 nm excitation. The 200 nm aggregate shows a mix of both behaviors.

However, AgO is an abysmal emitter with estimated quantum yields of less than 10^{-10} and only a nominal two photon absorber. Despite this, emission is clearly observed from the samples, indicating three things: a component of the surface stabilization of the for these particles is the formation of AgO, that the AgO content of the larger structures is higher and that the AgO and that TPA emission is enhanced by the pure silver beneath the AgO surface.

To support these findings, a small amount of water was added to the substrate and then pipetted off and allowed to dry in a desiccator for 30 minutes. This was done to generate further oxidation on the microcrystal surface. Afterward the sample was imaged by TPA NSOM. The results of these measurements are displayed in figures 11-19 and 11-20.

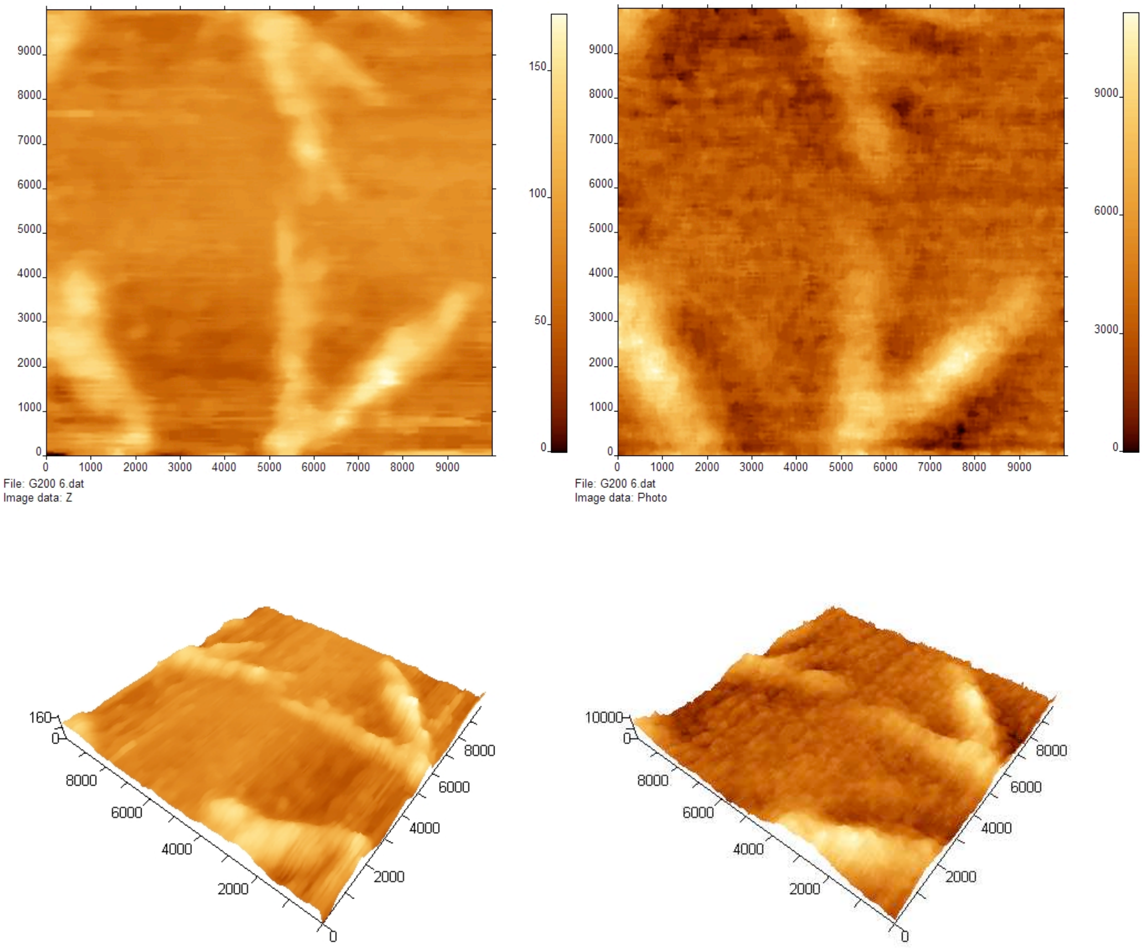

Figure 8-19. AFM (left) and TPA NSOM (right) of the Washed Silver Dendrimer

Excitation of 800 nm and 50 mW coupling intensity.

While the AFM resolution in figure 11-19 suffers, this was an expected consequence of residual moisture on the film as shear force AFM suffers greatly from even small amounts of moisture. However, the TPA NSOM is conclusive: All microcyrstalline features are now resolved with emission, with no breaks or poor emission regions. This strongly supports two earlier assertions: that the polarization dependence was not the major contributor to TPA NSOM detection and that some microfeature was responsible and that AgO on the surface of these materials is the major contributer to emission. Figure 11-20 observes the tip region of a microstructure branch. Before the wetting/oxidizing process, the tip regions seemed to have a lower emissivity than the branching nodes, perhaps due to greater AgO at the nodes originally. However, after washing, the tip region now shows very bright emission, confirming that the initial AgO locations in the sample were different for different regions and that with forced oxidation the entire dendrimer can be made into a plasmonically enhanced two photon emitter.

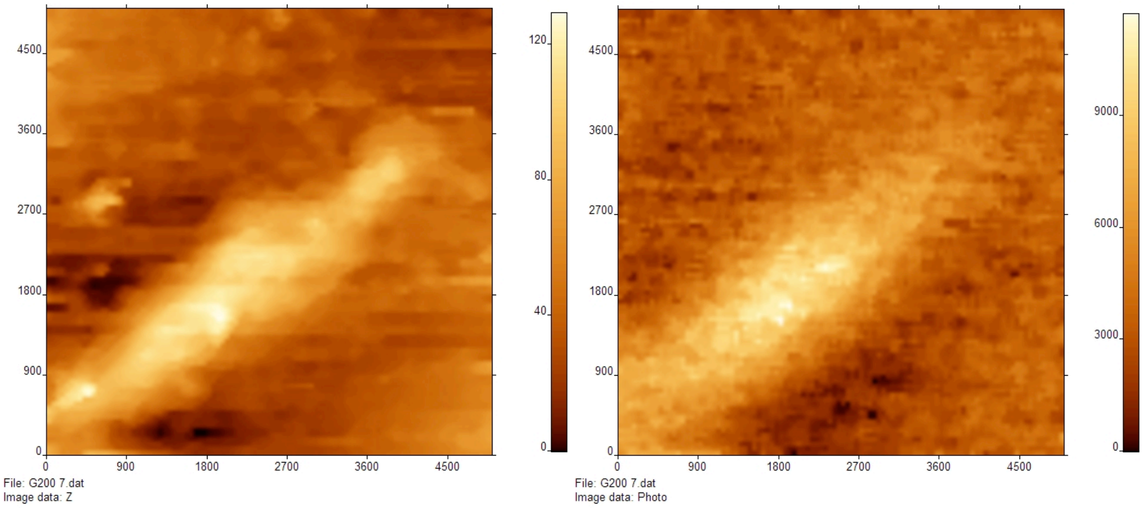

Figure 8-20. AgO Coated Silver Dendrite Tip and TPA NSOM of the Region

AFM (right) and TPA NSOM (left).

These are preliminary results, but relatively conclusive. The next step in this study will to see how dendrite shape and size can be modified based on different deposition methods. In order to fully characterize the plasmonic enhancement of this structure, it will be useful to use a species which is significantly more easily detected and characterized that AgO (a poor TPA emitter). The author has recommended the use of Rhodamine B, a well characterized TPA standard, be applied to the silver sample both pre- and post-deposition.

Chapter 9

Two-Photon Mediated Three-Photon Fluorescence: Lessons from a Quinoidal Oligothiophene Dimer

9-1 Original Publication Information

This chapter has been accepted for publication as the following document:

> "Two-Photon Mediated Three-Photon Fluorescence: Lessons from a Quinoidal Oligothiophene Dimer"
> Jeffery E. Raymond, Zin Seok Yoon, Juan Casado, Theodore Goodson III
> *The Journal of Physical Chemistry Letters*, accepted for publication 2011

Modifications to the original document are cosmetic and used only to conform the format of this document or provide uniformity of enumeration.

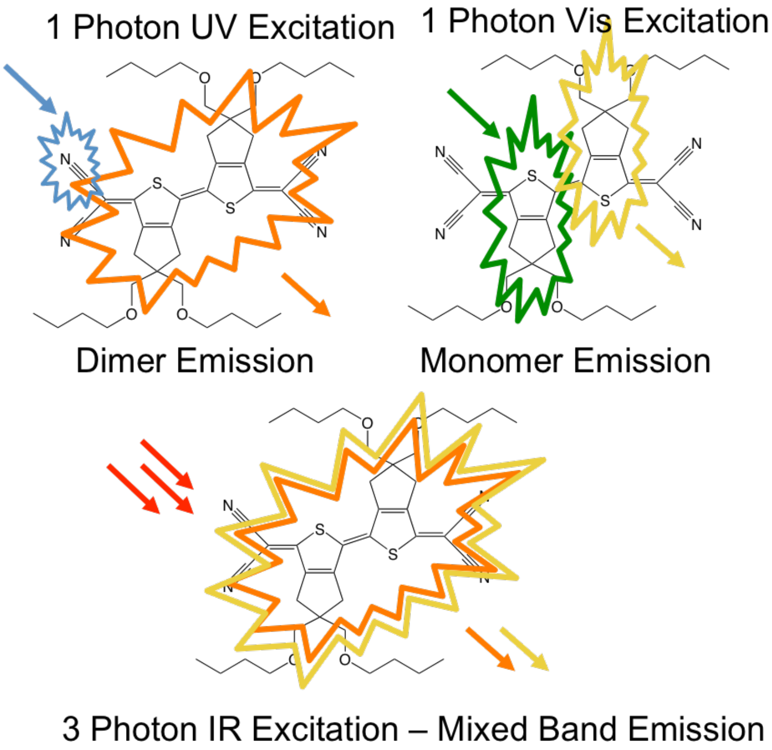

Figure 9-1. Table of Contents Figure as Submitted

9-2 Qualifying Statement

In this chapter, three photon fluorescence will be observed. The cause will be revealed to be virtual state stabilization, similar to that observed in the macrocycles in chapters 3, 4 and 5. Excitation spectroscopy, a steady state technique, will be introduced.

Excitation Spectroscopy. Excitation spectroscopy is another fluorescence technique and is performed by selecting a given wavelength at the photodiode while scanning through excitation wavelengths. This provides an excitation spectrum and depicts which energies of excitation result in fluorescence from the emission band monitored. While excitation scans can often overlap seamlessly with absorption spectra, sometimes critical information is revealed about internal electronic processes in a species that could be missed otherwise. It is this authors opinion that excitation spectroscopy is a grossly underutilized technique by spectroscopists, chemists and biologists as the likelihood of misinterpreting other spectroscopic data is decreased while the technique itself is not time consuming or labor intensive. A few things which excitation spectroscopy can reveal or at least correlate are: impurities, trapped states, intersystem crossing, multiple relaxation processes, breaks in π-conjugation in multichromophore systems and it can also be used to generate a spectrum of quantum yields for all UV-vis wavelengths. Typically, excitation spectra is measured in a voltage of some magnitude and presented as arbitrary units.

9-3 Abstract

Detailed here is the use of NIR femtosecond pulsed excitation to drive three-photon absorption (3PA) in a cyano- terminated quinoidal oligothiophene (QOT) dimer to the exclusion of all other fluorescing processes, resulting in 3PA emission bright enough to be visible by eye. Through steady state, multiphoton and ultrafast transient spectroscopy it is shown that dispite competing nonlinear optical processes, such as an available two-photon transition (2PA) and excited state absorption (ESA), emission characteristics remain an I^3 process explicitly due to 3PA. Specifically, we will show the viability of a two photon transition at the pump wavelength, strong excited state absorption, and display neither occurs to a significant degree in this QOT system when pump energies match both a virtual state near resonant with a viable 2PA state and a higher lying 3PA energy level. This study provides a clear method for evaluating multiband 3PA emitters which bypasses much of the ambiguity observed in purely absorption based studies where 2PA, ESA and 3PA may all contribute to signal and are difficult to distinquish. Additionally, this study introduces a rigid, molecular wire-like thiophene oligomer as a strong nonlinear optical responsive material with gross response changes based on small changes in IR excitation.

9-4 Introduction

Nonlinear multiphoton processes such as two-photon absorption (2PA), second harmonic generation (SHG), and excited state absorption (ESA) play a critical role in applications like in situ bio-imaging [1], optical limiting [2] and fiber lasing [3]. Recent developments have also shown these processes to be often uniquely appropriate for the investigation of quantum optic systems [4] in which events such as sub-diffraction photoswitching [5] and entangled photon interactions [6] are of interest. A variety of structures have been shown to possess enhanced multiphoton response from architecturally induced ensemble effects in which a multichromophore extended π network provides cross-sections far in excess of the individual constituents [7]. When assessing this enhancement effect in an array, it is reasonable to perform initial investigations on a dimeric system where electronic processes are as closely tied to the individual building block as possible. One family of macromolecules, oligothiophenes (OT), have shown exceptional promise in many guises, to include macrocycles [8], molecular wires [9] and dendrimers [10], archetectures which have all shown enhanced multiphoton response. Related, quinoidal oligothiophenes [11] (QOT) possess positionally locked double bonding between repeat units, giving a forced degree of π-overlap and rigidity lacking in traditional oligothiophene materials. Known to possess excited states very different electronically than the ground, QOT samples have shown incredible ensemble changes in energetics for one-photon events [12]. The focus of this study is the multiphoton absorption of a CN- terminated QOT dimer species (QOT2).

Two-photon absorption and fluorescence, a χ_3 process dependant on the incident flux squared (Φ^2), has been studied extensively in single and multichromophoric organic systems [13]. In these studies, it has been shown that the presence of an intermediate state between the ground state and the two-photon excited state can greatly enhance the likelihood of a two-photon transition occurring [13]. Three-photon absorption has also been investigated in some organic systems [14] however, in part due to the extremely high intensities required to observe the Φ^3 response, it remains one of the least observed multiphoton processes in organics materials. While the selection rules which dictate an allowed three-photon transition in a material resembles one-photon absorption much more strongly than 2PA [14], 3PA materials have been shown to have cross-sections ~35 orders of magnitude lower than comparable 2PA processes [15]. For instances where both 2PA and 3PA processes are promotion possibilities to a specific energy level at a given excitation wavelength, 2PA excitation events can be presumed to dominate. In order to probe the viability of 3PA materials for multiphoton applications, it remains critical to find molecular architectures and viable excitation regimes in which strict 3PA can be observed independently from competing, often obscuring, events. One possible strategy, using knowledge of intermediate state enhancement of 2PA as a guide, for observation of 3PA response is the targeting of materials which possess 2PA near resonance to the second three-photon virtual state and will be discussed in detail throughout this study.

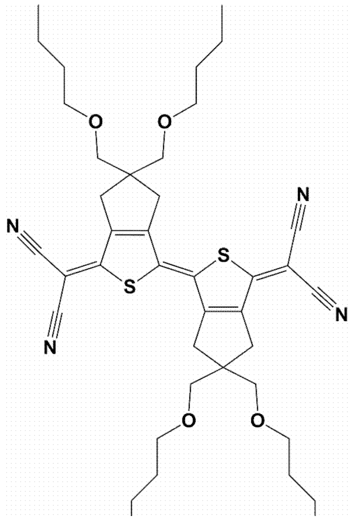

QOT2

Absorption
$\varepsilon = 10^5\ \mathrm{M}^{-1}\ \mathrm{cm}^{-1}$
$\lambda_{max} = 550$ nm

"Dimeric" Emission
$\lambda_{em} = 600$ nm
$\lambda_{ex} = 265$ nm

"Monomeric" Emission
$\lambda_{em} = 415$ nm
$\lambda_{ex} = 470$ nm

Figure 9-2. Structure of QOT2 Quinoidal Oligothiophene Dimer and a Summary of the Steady State Absorption, Emission and Excitation Maxima

The quinoidal oligothiophene dimer (QOT2) under investigation is depicted in figure 8-2 along with a summary of the steady state results discussed in this section. The synthesis and characterization of QOT2 are described elsewhere [12], and all work was performed in spectroscopic grade THF. Details regarding confirmation of sample and solvent purity can found in the supporting information. The absorption, emission and excitation spectra are provided in figure 8-3. They depict two excitation and emission regimes which appear to have virtually no energy transfer between states. The first excitation/emission regime shows a phenomenal stokes shift of 2.6 eV from 265 nm excitation and 600 nm emission. The excitation band agrees reasonably well with the UV region of the absorption spectra and resultant emission is surprisingly close to the energy one might expect for emission from the primary absorption peak at 550 nm. It should be noted that direct excitation at the absorption maxima gives an extremely weak emission in the 600 nm region, barely observable at largest exposure, and is estimated to have Φ_F $<10^{-7}$. While implicit determination of the relaxation process(es) related to this large shift are beyond the scope of this study, it is our initial proposal that the large stokes shift may be an indication of several dark bands unobserved in steady state measurements, an excited state conformational requirement precluding alternate relaxation pathways, or excited state intermolecular proton transfer (ESIPT). The second excitation/emission regime provides a 415 nm excitation and 470 nm emission, neither of which correspond to observed bands in the absorption spectra and can indicate a classically disallowed transition from the ground state. This dark state response is often an indication of a two-photon allowed process [16].

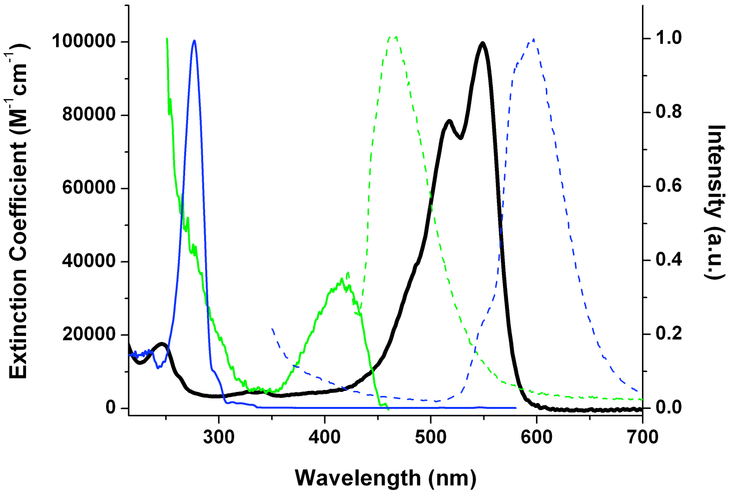

Figure 9-3. Steady State Absorption (Black) and Emission/Excitation Spectra

The monomer-like excitation (solid green) and emission regime (dashed green) as well as the dimer-like excitation (solid blue) and emission (dashed blue) are given on the right axis.

9-5 Excitation and Emission of Different Molecular Regions

Quinoidal oligothiophenes have been shown to possess bi-radical type photoexcited states from visible and NIR one photon excitation. While the implicit location of the radical character and resultant single bond character cannot be determined here, we propose a dimer-type (non-radical) and monomer-type (bi-radical) relaxation regime for two different excited states based on the energetic levels of the events observed and some understanding of localized R-CN excitation in organic systems. The absorption and excitation bands near 260 nm are similar to those observed in longer –CN terminated QOT oligomers and typical of excitation bands found in other R-CN structures and M^+ CN^- salts [17]. This indicates a localized excitation at the CN-terminus of the dimer. Presuming that the 550 nm absorption maxima is indicative of a $S_0 \rightarrow S_1$ promotion to a molecular orbital which spans the entire π-conjugated length (dimer-like), the 600 nm emission can reasonably be attributed to a $S_1 \rightarrow S_0$ type relaxation, with a dimer-like behavior involving the entire molecules conjugation pathway. In the second excitation/emission regime, we observe fluorescence from a dark state unobserved in our absorption spectra and from higher energy than the one-photon absorption maxima. This implies a much more localized excited state that cannot freely interconvert to the dimer-type emission regime and is not a classically allowed one-photon transition. Previous studies of QOT monomer species shows primary absorption in the 400-450 nm region [12], consistant with the primary excitation band from which the 470 nm emission is observed. This strongly implies an excited state localized on one half of the dimer, giving rise to monomer-like emission. The known bi-radical character of this QOT species, obtained from visible wavelength excitation, makes it possible to propose a radical isolated excited state that results in conformational changes and/or a reduction in bond order between units.

9-6 Multiphoton Excitation Fluorescence Spectroscopy

Multiphoton excitation emission spectra for QOT2 are presented in figure 8-4 at various excitation intensities, providing a primary emission peak at 470 nm and a

570 nm shoulder, with energies similar to the monomeric and dimeric type emissions observed in the steady state data. Excitation occurs from an 800 nm femtosecond pulsed laser source and is described in detail elsewhere [18]. It can be readily observed that the emission spectra does not change qualitatively with intensity of excitation, but rather scales in intensity non-linearly. Polynomial fitting of the fluorescence intensities for both features and integrated peak intensity are presented in figure 8-6. Also shown is the LOG(I_F)-LOG(I_0) plot depicting a slope of three with increasing excitation power, indicating a I^3 dependence typical of three-photon excitation. While it is possible that at lower intensities 2PA and linear-scattering may play a more significant role, the observed onset of multiphoton excited fluorescence shows that 3PA emission quickly dominates all other signals. Unlike other systems where 3PA signal is obscured by other events at high intensity such as scattering, self-focusing, ESA and 2PA, it can be seen that 3PA emission is clear and unconvoluted in this system. An approximation for the 3PA cross-section can be made based on a typeical two photon cross-sections for dye molecules of this size (~10^{-49} cm^4/photon-s). Given that 3PA is the dominant process, and assuming that the coherent transition from the second virtual state to the 3PA excited state is at least as probable as half of a two photon process, a 3PA cross-section somewhere near an order of 10^{-74} cm^6/$photon^2$-s^2.

As mentioned previously, enhanced 2PA processes have been observed in multiband oligomeric systems where the presence of an intermediate state near the induced virtual state provides resonance energy matching and leads to a greatly enhanced cross-section when compared to similar systems without a mediating state [12]. We propose that the presence of a relatively pure 3PA emission signal, despite the strong possibility of a highly responsive two-photon band at 415 nm, can be explained by a regime similar to the intermediate band stabilization in a two-photon process. By choosing an excitation regime which provides two-photon energy matching to the 415 nm excitation band and one-photon energy matching to the 415 nm → 265 nm transition, 3PA to the 265 nm band can be achieved by a near resonant two-photon virtual state being promoted to the 3PA state in the presence of a strong 800 nm flux. We compare this to our one-photon excitation regime in figure 8-5. It is important to note that the strong coupling of the ⅔ ΔE virtual state to the 415 nm band provides a different regime for multiphoton emission than that observed in 1PA emission. We propose that the virtual state coupling to an excited state having bi-radical character allows for a degree of bi-radical character in the 3PA state, very different from the 1P case. This is supported by a normalized polynomial that shows in figure 8-6 the same power dependence for all emission features, indicating that both emission features derive from the same 3PA excited state despite differing relaxation pathways. Excitation at energies which did not target both the 3PA enhancing 425 nm energy level and the 265 nm target state (off resonance excitation) showed only a single emission type and quadradic power dependence (supp. info.).

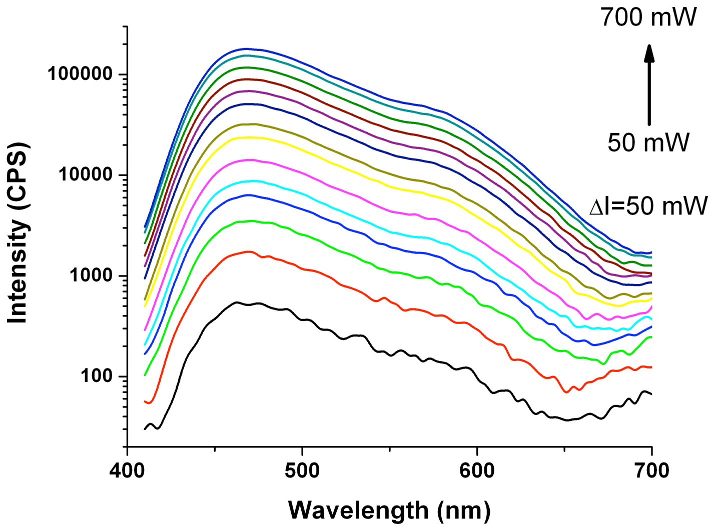

Figure 9-4. Three-Photon Excited Fluorescence Spectra for Incident Intensities Ranging from 50 to 700 mW @ 800 nm Excitation

Log scale for intensity is provided for clarity of features from all excitation powers. From the highest intensity emission spectra to the lowest, excitaton powers are 700, 650, 600, 550, 500, 450, 400, 350, 300, 250, 200, 150, 100 and 50 mW.

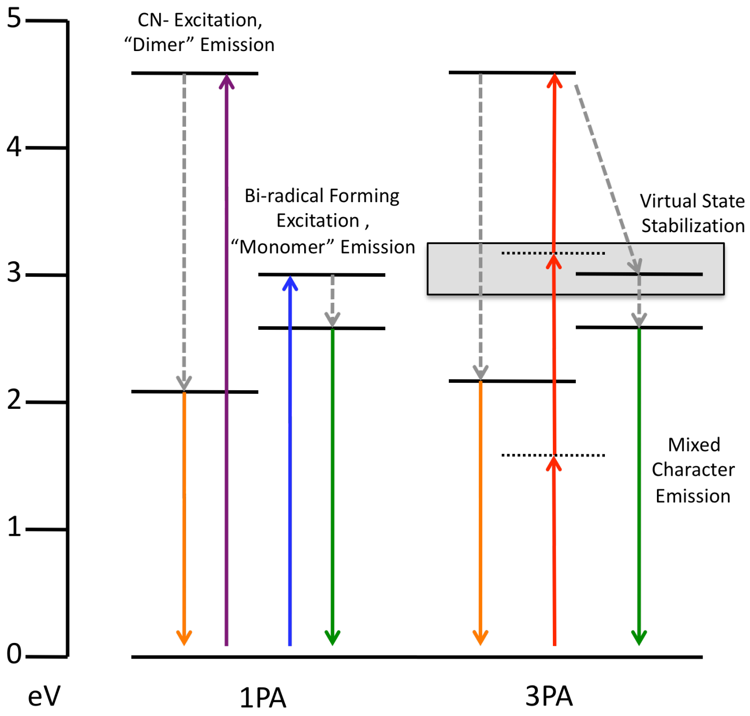

Figure 9-5. One- and Three-Photon Energy Diagrams Depicting 2PA Mediated 3PA and Subsequent State-Mixed Emission

The gray area indicated the on-resonance enhancement of a coherent 3PA process through energy matching of the second virtual state to a nearby energy level.

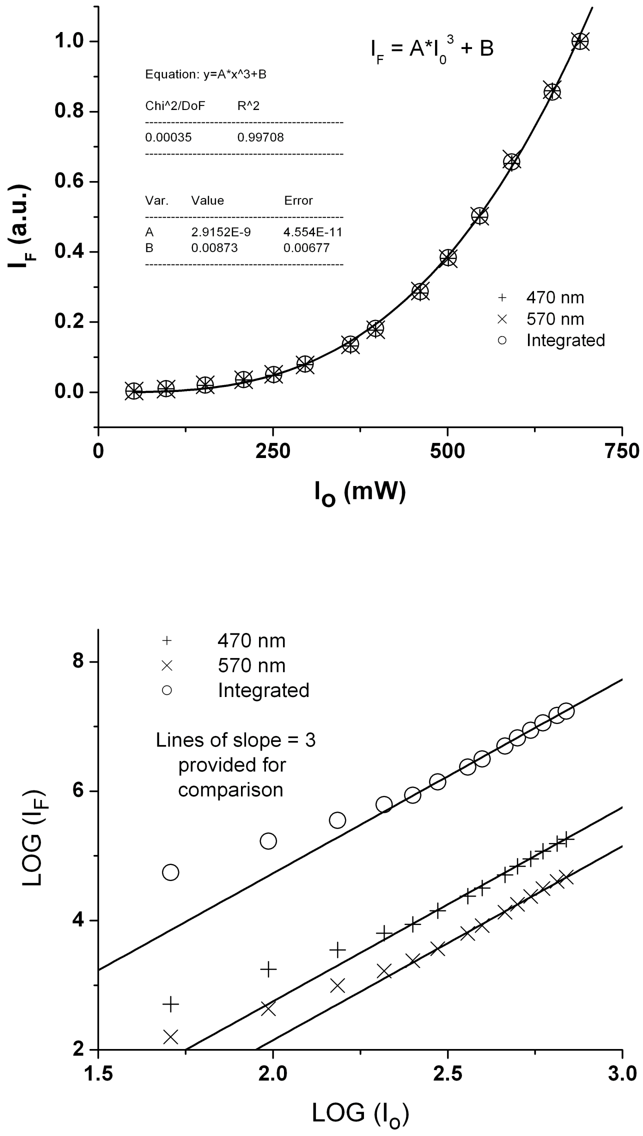

Figure 9-6. Uncorrected Power Dependence of Emission Shown on Linear (top) and LOG-LOG (bottom) Axis's

Note that data (top) are successfully fitted to I^3 *and is confirmed at higher intensities (bottom) where data is shown next to slope three lines for context.* I^3 *processes dominate shortly after background counts become insignificant to signal, and well within an order of magnitude of observable emission onset.*

9-7 Ultrafast Transient Absorption Spectroscopy.

In order to confirm the viability of the proposed transition from a two-photon mediated state to a three-photon excited state, we preformed ultrafast transient absorption on the QOT2 sample. A special focus is placed on excited state absorption (ESA) which results in a 265 nm excited state. Figure 8-7 contains both representative spectra and kinetic fitting for this component of the study. Transient spectra show photobleaching (PB) with a 580 nm maxima and primary ESA occurring broadly with a maxima near 600 nm shortly after excitation. In order to confirm that PB and ESA spectral features have intrinsic kinetic and event ratio dependence, kinetic fitting and peak integration were performed. ESA and PB wavelengths (620 & 470 nm) with sum energies equal to the 265 nm energy level (not near the isosbestic point) were selected for fitting in order to avoid any ambiguities from ESA/PB signal overlap. Kinetic traces (figure 8-7) show 2 ps lifetimes from both regions, with comparable amplitudes and long time scale residuals. Comparing the ratio of peak integrations, $\int (ESA)deV / \int (PB)deV$, gives similarly high ratios during the primary kinetic lifetime (0.61 at 150 fs) and after the majority of relaxation (0.58 at 5 ps) which is an indication of ESA intrinsicly linked to PB population density. Without implicitly determining the ESA cross-section, these results display clear ESA to the 265 nm energy level in our QOT2 system after excitation while integration provides additional confirmation of an extremely high rate of ESA which remains during the entirety of the excited state lifetime. The experimental details for our transient absorption set-up, preformed at 515 nm excitation in this study, are provided elsewhere in detail [19]. While this study illuminates the types of interconversion that are allowed in our QOT system, it is critical to note that the observed 3PA cannot be a formal 2PA process followed immediately by ESA. At the intensities observed during the pulse (~5 nJ focused onto a diffraction limited point), where all light is at a wavelength appropriate for ESA to occur, $<P_{ESA}>$ approaches unity and the resultant fluorescence signal would be a function of I^2. Additionally, at lower excitation intensities below the threshold of observable 3PA emission, a formal 2PA excited state would have emission characteristics which mimic those observed in the 1PA 415 nm excitation regime and is also unobserved. These findings also provide a good argument for the use of 3PEF (three photon excited fluorescence) as and appropriate technique for materials investigations where absorption studies alone would have a large degree of ambiguity regarding the source of observed nonlinearities.

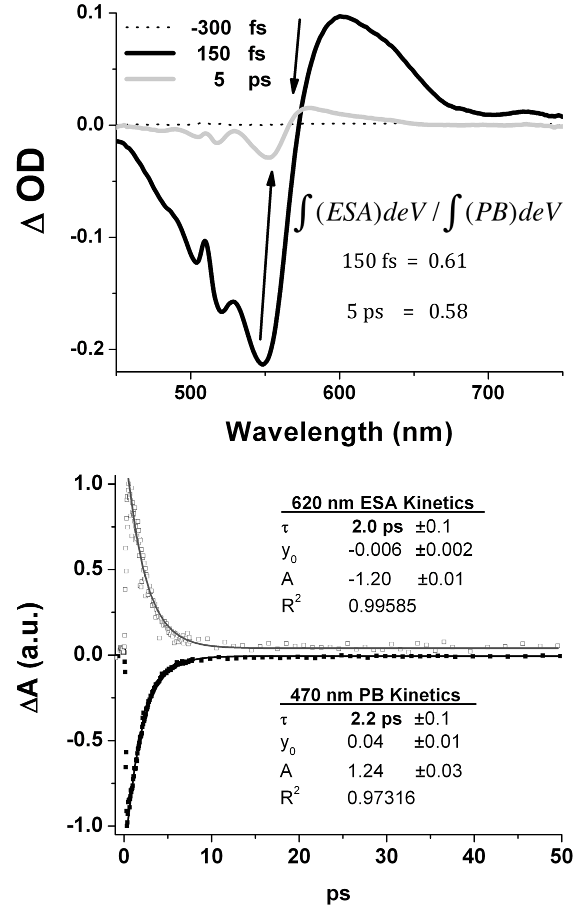

Figure 9-7. Representative Spectra(top) and Kinetic Traces (bottom) for Transient Absorption in the QOT Dimer

9-8 Conclusions

This study provides a full assessment of 3PA emission observed from a quinoidal oligothiophene dimer. While several interesting attributes of this system beg additional investigation, such as the enormous Stokes shift and isolation of 1P emission regimes, this investigation clearly shows a functional approach to obtaining 3PA emission, exclusively. Using steady state, multiphoton and ultrafast spectroscopic techniques on a QOT dimer we have clearly outlined the four material/excitation requirements needed to observe this type of isolated 3P signaling: (1) A high lying 1PA accessible energy level at ΔE, (2) a 2PA responsive intermediate state near ⅔ ΔE of the 1PA band, (3) proven ESA for excitation to the high lying 1PA state from lower energy levels, and (4) an excitation source at wavelengths near ⅓ ΔE and with peak intensities sufficient to drive 3PA processes. These first three attributes, taken collectively, are not likely to be common to many families of organic chromophores. However, this study provides a new frame of reference to systematically assess known systems and selectively target new molecular architectures which will be expressly functional 3PA materials. While certainly there are other potential avenues for targeting I^3 based emission, this work provides a clear route to approach the relatively untouched realm of explicit three-photon applications.

9-9 Acknowledgement

This project was supported by Air Force Office of Scientific Research (Chemistry) and the Army Research Office (Materials).

9-10 References

(1) Smith, A.; Smoligovets, A.; Groves, J.; Patterned Two-Photon Photoactivation Illuminates Spacial Reorganization in Live Cells. J. Phys. Chem. A 2011, 115, 3867-3897.
(2) Ramakrishna, G.; Rogers-Haley, J.; Cooper, T.; McLean, M.; Urbas, A.; Goodson, T. Ultrafast Intersystem Crossing: Excited State Dynamics of Platinum Acetylide Complexes. J. Phys. Chem. C 2009, 113, 1060-1066.

(3) Quochi, F.; Codella, F.; Mura, A.; Bongiovanni, G.; Balzer, F.; Rubahn, H. One Dimensional Random Lasing in a Single Organic Nanofiber. J. Phys. Chem. B 2005, 109, 21690-21693.

(4) Guzman, A.; Harpham, M.; Suzer, O.; Haley, M.; Goodson, T. Spatial Control of Entangled Two-Photon Absorption with Organic Chromophores. J. Am. Chem. Soc. 2010, 132, 7840.

(5) Zhu, M.; Zhang, G.; Li, C.; Aldred, M.; Change, E.; Drezak, R.; Li, A. Reversible Two-Photon Photoswitching and Two-Photon Imaging of Immunofuctionalized Nanoparticles Targeted to Cancer Cells. J. Am. Chem. Soc. 2011, 133, 365-372.

(6) Harpham, M.; Suzer, O.; Ma, C.; Bauerle, P.; Goodson, T Thiophene Dendrimers as Entangled Photon Sensor Materials. J. Am. Chem. Soc. 2009, 131, 973-979.

(7) Raymond, J.; Bhaskar, A; Makiuchi, N. Ogawa, K.; Kobuke, Y; Goodson, T. Synthesis and Two-Photon Absorption Enhancement of Porphyrin Macrocycles. J. Am. Chem. Soc. 2008, 130, 17212-17213.

(8) Williams-Harry, M.; Bhaskar, A.; Ramakrishna, G.; Imamura, M.; Mawatari, A.; Nakao, K.; Enozawa, H.; Nishinaga, T.; Iyoda, M.; Goodson, T. Giant Thienylene-acetylene-ethylene Macrocycles with Large Two-Photon Absorption Cross Section and Semishape-Persistence. J. Am. Chem. Soc. 2008, 130, 3252-3253.

(9) Pina, J; de Melo, J. A Comprehensive Investigation of the Electronic Spectral and Photophysical Properties of Conjugated Naphtalene-Thiophene Oligomers. PhysChemChemPhys 2009, 11, 8706-8713.

(10) Ramakrishna, G.; Bhaskar, A.; Bauerle, P.; Goodson, T. Oligothiophene Dendrimers as New Building Blocks for Optical Applications. J. Phys. Chem. A 2008, 112, 2018-2026.

(11) Fazzi, D.; Canesi, E.; Negri, F.; Bertarelli, C.; Castiglioni, C. Biradicaloid Character of Thiophene-Based Heterophenoquinones: The Role of Electron-Phonon Coupling. ChemPhysChem 2010, 11, 3685-3695.

(12) Pappenfus, T. Shneiderman, D.; Casado, J.; Navarrete, J.; Delgado, M.; Zotti, G.; Vercelli, B.; Lovander, M.; Hinkle, L.; Bohnsack, J.; et. al.; Oligothiophene Tetracyanobutadienes: Alternative Donar-Acceptor Archetectures for Molecular and Polymeric Materials. Chem. Mater. 2011, 23, 823-831.

(13) Raymond, J.E.; Ramakrishna, G.; Twieg, R.; Goodson, T. Two-Photon Enhancement in Organic Nanorods. J. Phys. Chem. C 2008, 112, 7913-7921.

(14) Drobizhev, M.; Rebane, A.; Suo, Z.; Spangler, C. One-, Two- and Three-photon Spectoscopy of Pi-conjugated Dendrimers: Cooperative Enhancement and Coherenent Domains. J. Lumin. 2005, 111, 291-305.

(15) Lin, N.; Ferrighi, L.; Zhao, X.; Ruud, K.; Rizzo, A.; Luo, Y. Solvent Effects on the Three-Photon Absorption of a Symmetric Charge-Transfer Molecule. J. Phys. Chem. B 2008, 112, 4703-4710.

(16) Wehling, A.; Walla, P Time-Resolved Two-Photon Spectroscopy of Photosystem I Determines Hidden Carotenoid Dark-State Dynamics. J. Phys. Chem. B. 2005, 109, 24510-24516.

(17) Gutowski, K.; Holbery, J.; Rogers, R.; Dixon, D.; Prediction of the Formation and Stabilities of Energetic Salts and Ionic Liquids on Ab Inition Electronic Structure Calculations. J. Phys. Chem. B 2005, 109, 23196-23208.

(18) Narayanan, A.; Varnavski, O.; Mongin, O.; Majoral, J.; Blanchard-Desce, M.; Goodson, T. Detection of TNT Using a Sensitive Two-Photon Organic Dendrimer for Remote Sensing. Nanotechnology 2008, 19, 115502.

(19) Transient Abs. Method: Flynn, D.; Ramakrishna, G.; Yang, H.; Northrop, B.; Stang, P.; Goodson, T. Ultrafast Optical Excitations In Supramolecular Metallacycles with Charge Transfer Properties. J. Am. Chem. Soc. 2010, 132, 1348-1358.

9-11 Supplemental Information

Supplemental information as submitted for web publication.

In order to confirm that dual band three photon excited state emission was unique to "on-resonance" excitation near 800 nm, at a variety of excitation wavelengths were used. Specifically, excitation was varied from 700 nm to 950 nm in 25 nm increments. Figure 8-8 shows the emission spectra for the QOT2 sample under these conditions, with the on-resonance 800 nm excitation providing both emission bands (470 nm and 580 nm) and the off-resonance excitation showing only 470 nm emission.

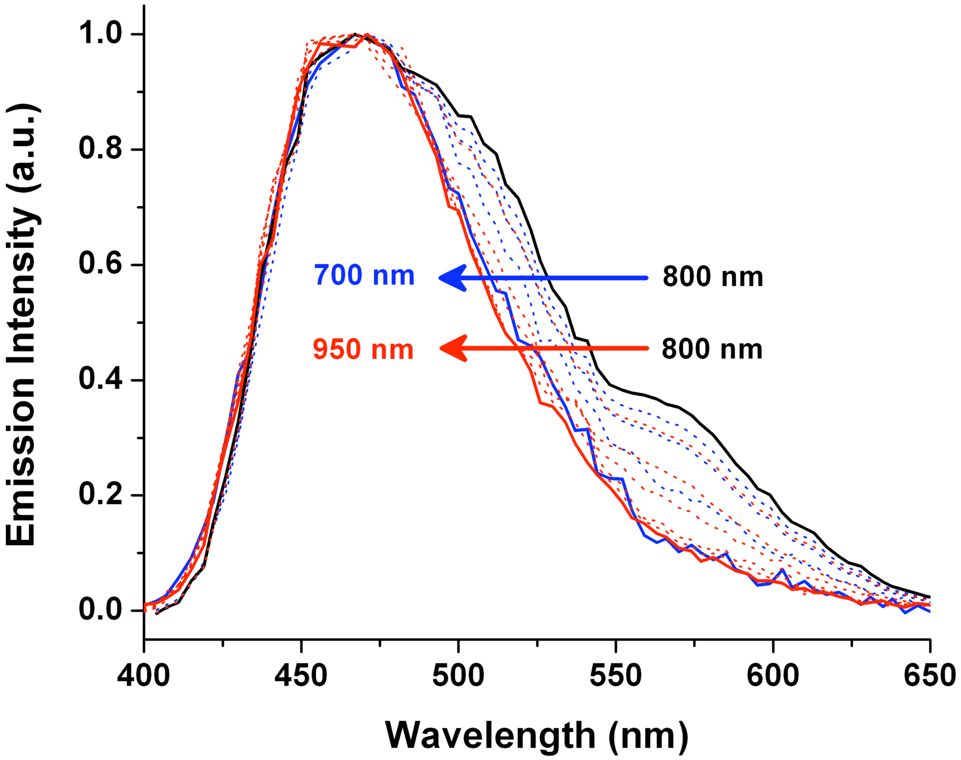

Figure 9-8. Emission Spectra for 700 to 950 nm Excitation

On-resonance 800 nm excitation emission is given in black. Higher energy excitation emission spectra are provided for 775 750, 725 (blue dash) and 700 nm (solid blue). Lower energy excitation emission spectra are provided for 825, 850, 875, 900, 925 (red dash) and 950 nm (solid red).

Additionally, to confirm that 3PA fluorescence is unique to the on-resonance excitation, power dependence studies for emission from 700 nm and 950 nm excitation were performed. Figure 8-9 displays log(fluorescence) – log(excitation power) relationship for these two excitation regimes. Both display purely quadradic (slope ~2) response typical of 2PA processes and entirely dissimilar to the 3PA emission observed from 800 nm excitation.

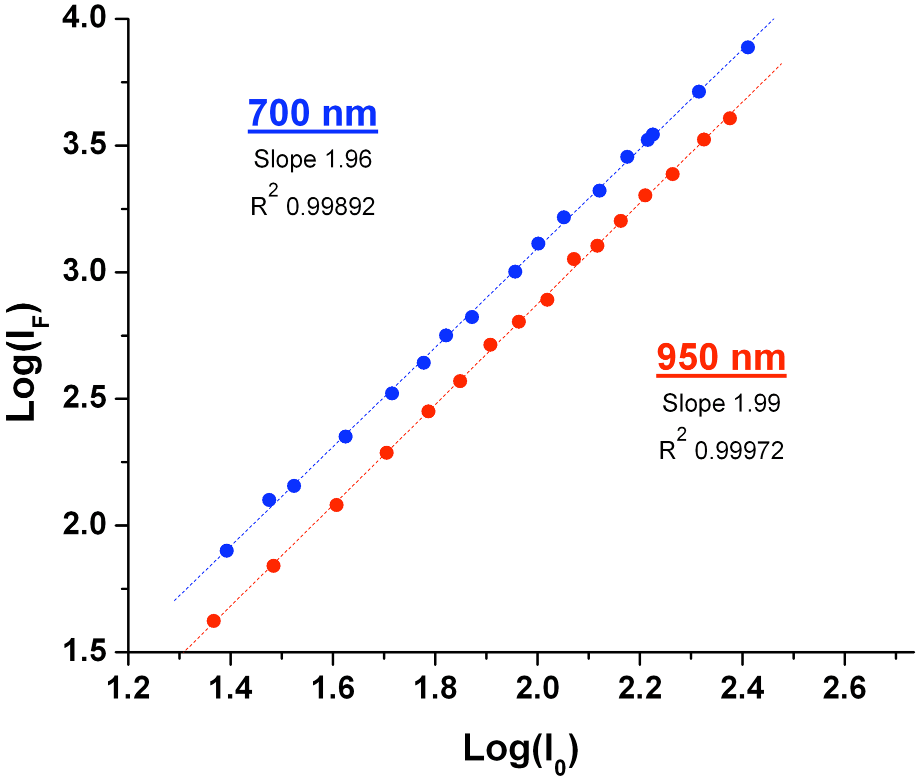

Figure 9-9. Log-Log Power Dependence of Off-Resonance Excitation Emission

Higher energy excitation at 700 nm is depicted in blue, with lower energy excitation depicted in red.

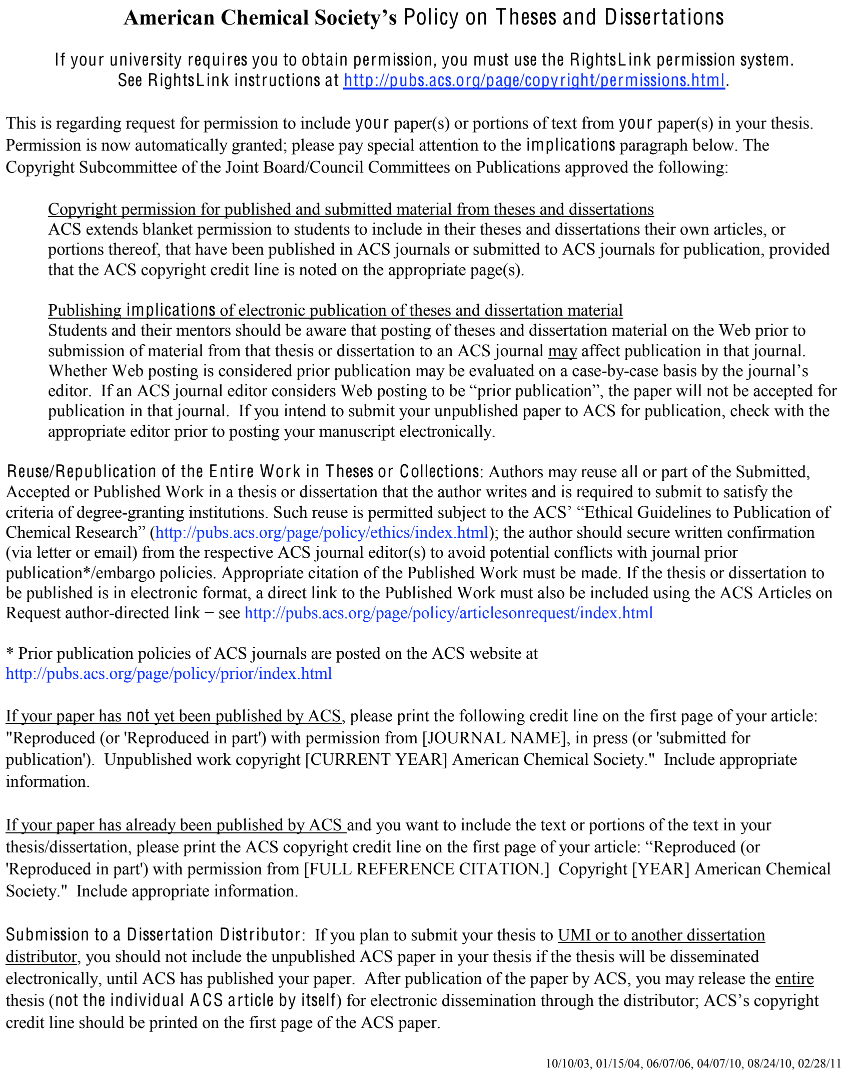

American Chemical Society's Policy on Theses and Dissertations

If your university requires you to obtain permission, you must use the RightsLink permission system.
See RightsLink instructions at http://pubs.acs.org/page/copyright/permissions.html.

This is regarding request for permission to include your paper(s) or portions of text from your paper(s) in your thesis. Permission is now automatically granted; please pay special attention to the implications paragraph below. The Copyright Subcommittee of the Joint Board/Council Committees on Publications approved the following:

Copyright permission for published and submitted material from theses and dissertations
ACS extends blanket permission to students to include in their theses and dissertations their own articles, or portions thereof, that have been published in ACS journals or submitted to ACS journals for publication, provided that the ACS copyright credit line is noted on the appropriate page(s).

Publishing implications of electronic publication of theses and dissertation material
Students and their mentors should be aware that posting of theses and dissertation material on the Web prior to submission of material from that thesis or dissertation to an ACS journal may affect publication in that journal. Whether Web posting is considered prior publication may be evaluated on a case-by-case basis by the journal's editor. If an ACS journal editor considers Web posting to be "prior publication", the paper will not be accepted for publication in that journal. If you intend to submit your unpublished paper to ACS for publication, check with the appropriate editor prior to posting your manuscript electronically.

Reuse/Republication of the Entire Work in Theses or Collections: Authors may reuse all or part of the Submitted, Accepted or Published Work in a thesis or dissertation that the author writes and is required to submit to satisfy the criteria of degree-granting institutions. Such reuse is permitted subject to the ACS' "Ethical Guidelines to Publication of Chemical Research" (http://pubs.acs.org/page/policy/ethics/index.html); the author should secure written confirmation (via letter or email) from the respective ACS journal editor(s) to avoid potential conflicts with journal prior publication*/embargo policies. Appropriate citation of the Published Work must be made. If the thesis or dissertation to be published is in electronic format, a direct link to the Published Work must also be included using the ACS Articles on Request author-directed link – see http://pubs.acs.org/page/policy/articlesonrequest/index.html

* Prior publication policies of ACS journals are posted on the ACS website at http://pubs.acs.org/page/policy/prior/index.html

If your paper has not yet been published by ACS, please print the following credit line on the first page of your article: "Reproduced (or 'Reproduced in part') with permission from [JOURNAL NAME], in press (or 'submitted for publication'). Unpublished work copyright [CURRENT YEAR] American Chemical Society." Include appropriate information.

If your paper has already been published by ACS and you want to include the text or portions of the text in your thesis/dissertation, please print the ACS copyright credit line on the first page of your article: "Reproduced (or 'Reproduced in part') with permission from [FULL REFERENCE CITATION.] Copyright [YEAR] American Chemical Society." Include appropriate information.

Submission to a Dissertation Distributor: If you plan to submit your thesis to UMI or to another dissertation distributor, you should not include the unpublished ACS paper in your thesis if the thesis will be disseminated electronically, until ACS has published your paper. After publication of the paper by ACS, you may release the entire thesis (not the individual ACS article by itself) for electronic dissemination through the distributor; ACS's copyright credit line should be printed on the first page of the ACS paper.

10/10/03, 01/15/04, 06/07/06, 04/07/10, 08/24/10, 02/28/11

Figure 9-10. General American Chemical Society Guideline on In-Press Usage and Author Publication in Thesis

Chapter 10

Ultrafast Charge Transfer in Broadband Molecular Wires

10-1 Original Publication Information

This chapter is be submitted for publication as the following document:

"Ultrafast Charge Transfer in Broadband Molecular Wires"
Jeffery E. Raymond, Zin Seok Yoon, Juan Casado, Peter Bauerle and Theodore Goodson III
The Journal of Physical Chemistry C, submitted Q3 2011

Modifications to the original document are cosmetic and used only to conform the format of this document or provide uniformity of enumeration.

10-2 Qualifying Statement

This chapter is not part of the major theme of this work. It focuses on a the charge recombination processes observed in a multichormophore molecular wire of the same class as the dimer discussed in chapter 9. It will be shown that the molecular wire has electronic behavior similar to the constituent parts and that charge recombination happens a less than 1 ps. No new techniques are introduced in this chapter.

10-3 Abstract

The excited-state radical behavior and the excited-state relaxation processes of a series of linear quinoidal oligothiophenes (QOT) have been investigated using femtosecond transient absorption spectroscopy. In contrast to oligothiophenes (OT) linked with single bonds between α-carbons of thiophene units, the current QOT system shows broadband and NIR response which is linearly related to the

conjugation length. This indicates pi orbital overlap which provides full realization of the head-to-tail conjugated path length. From the ultrafast relaxation observed on the <10 ps time scale and wavelength analysis of transient species, we found that the excited-state dynamics the generated radical in these chains can be explained by the transient absorption spectra and decay kinetics of constituent dimer and trimer units. We also found that the relaxation of constituent units occupied in longer chains show much faster decay kinetics when compared to that of the independent chromophores. The fact that the longest array shows the shortest excited-state lifetime (3.5 ps) infers that this material can be functionalized as a highly efficient charge transfer material.

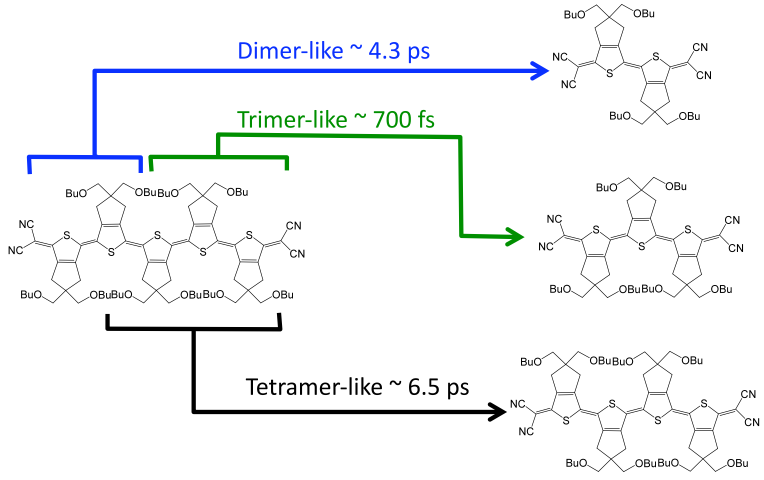

Broad Band NIR Molecular Wires
Multiple Excited State Configurations
Charge Recombination ~ 1 ps

Figure 10-1. Synopsis Table of Contents Image as Submitted

10-4 Introduction

The field-effect transistor (FET), first introduced by Lilienfeld in 1925 [1], is the foundation of modern electronic device design. More recently, the development of organic field-effect transistors (OFET) have shown marked progress towards the development of photo-electronic molecular devices such as photovoltaic cells [2], flexible displays [3] and radio frequency identification (RFID) tags [4]. The flexible, low-cost, easy-to-modify properties of OFETs have recently precipitated a high level of interest in OFET technologies, specifically when compared to the high cost, high environmental impact of the metallic or inorganic FET technologies currently in place [5]. In expectation of developing molecular devices, various materials have been tested for OFET response, such as π-conjugated polymers, acenes, carbon nanotube, etc. [6]. Among these, oligothiophene and polythiophene derivatives [7] are the most widely investigated classes of chromophore, due in large part to their synthetic availability, high stability in various redox states and charge mobility properties [8]. While oligothiophene and polythiophene derivatives have been known as p-type materials (hole transport), chemical modification can change the charge transport properties to n-type materials (electron transporters). Critical to characterization of charge transport characteristics, the optical properties of oligothiophene and polythiophene derivatives are mainly determined by their π-electronic systems, e.g., the allowed molecular conformation and the degree of π-orbital overlap between units.

In this regard, Otsubo et al. has recently developed long alpha–conjugated oligothiophene arrays containing up to 96 thiophene units with high solubility [9]. From steady-state absorption and emission measurement of these OT arrays, molecular extinction coefficient and fluorescence quantum yield show a linear structure-property relationship. However, the absorption red-shifts corresponding to an increase in thiophene units showed saturation behavior around 560 nm. Later, by introducing dicyanomethylene groups at both ends of an array, quinoidal oligothiophene (QOT) arrays have been synthesized with up to 6 thiophene units with high solubility [10] and their physical characteristics has been explored by ESR spectroscopy, Raman spectroscopy, and theoretical computations [11,12]. These studies showed efficient elongation of the π-conjugation pathway of QOT through conformational locking, an effect not observed in OTs bearing large numbers of thiophene units.

The optical application of multrichromophoric OFETs to functional devices demand an understanding of how excited-state energy transfer will occur from one moiety to another and how charge transfer will occur in the excited-state, specifically when induced by photoexcitation. These excited state processes are known to occur in the ps and fs regime. These extremely fast processes, critical to determining a species' viability for application, demand ultrafast time-resolved absorption or emission spectroscopic analyses for a true understanding of the structure-function relationship governing optoelectronic response. In this regard, we have been investigated the nonlinear optical properties and ultrafast excited-state dynamics of conjugated linear-type thiophene arrays, macrocyclic thiophene and thiophene dendrimers, along with a computational approach [13]. Those studies showed that the delocalized excited state character obtained in multichromophoric systems can be applied in quantum optical material applications. On a similar note rigid, linear QOT arrays can be suitable test beds in which to investigate the ultrafast optical properties of π-electron delocalization in a systematic manner, without the ambiguities induced by structures with higher order dimensionalities. According to previous reports on QOT arrays, the fluorescence spectra were unobservable at room temperature and at low temperature only weak fluorescence was observed. Thus, for QOT materials, which must be evaluated for functionality in devices at room temperature, time-resolved absorption spectroscopy is the most suitable approach for probing the excited-state properties. As it has been shown that photoexcitation of QOT oligomeric species manifest as a biradical species prior to relaxation, it is reasonable that the isolated electronic regions generated by the presence of an unpaired electron may best be observed in the ultrafast transient spectra [12].

In this study we characterize the excited-state properties of QOT arrays using femtosecond transient absorption spectroscopy. This is accomplished in order to utilize ground state bleaching, excited state absorption and wavelength dependence of the dynamics to display an intrinsic link between the component kinetics in large species to the individual dimer and trimer subunits which are contained within them.

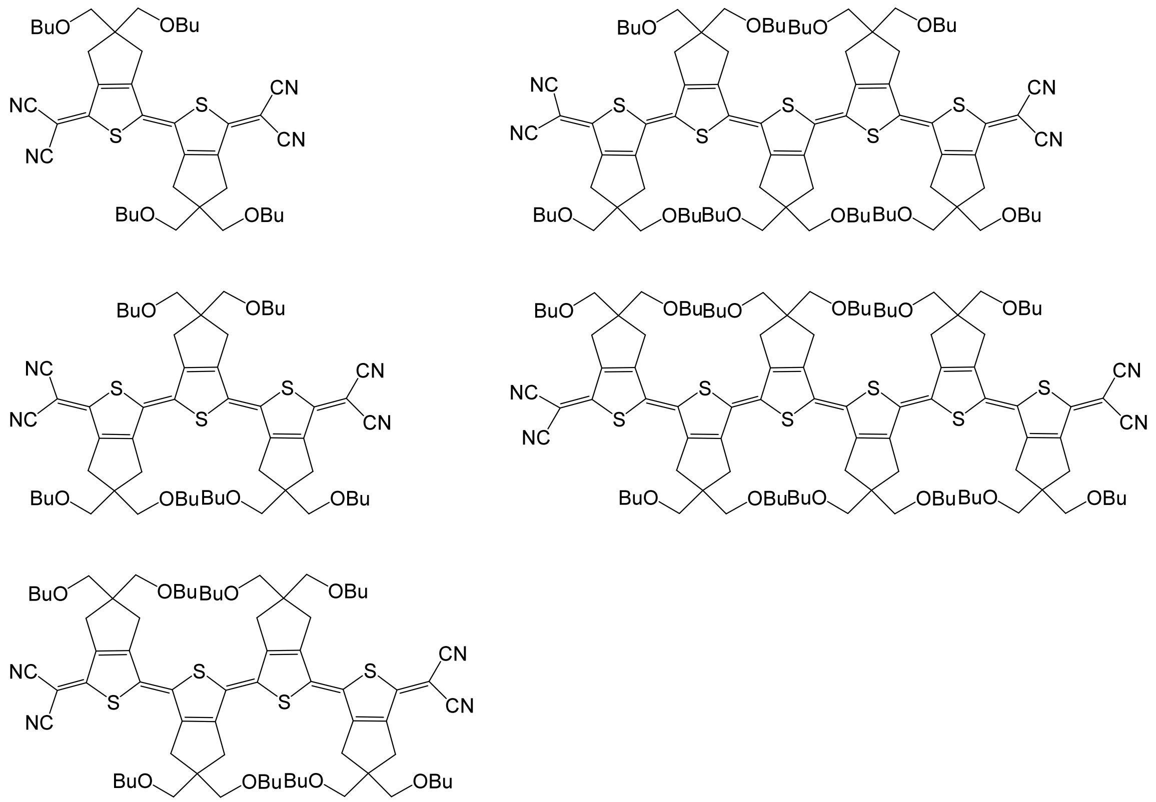

Figure 10-2. Molecular Structure of 2-, 3-, 4-, 5- and 6-meric Quinoidal Oligothiophene Arrays

10-5 Experimental Section

Materials. The syntheses of samples have been described previously [10]. All measurements were carried out with spectroscopic grade THF as the solvent, unless stated otherwise.

Steady-state Measurements. Ultraviolet (UV)-visible absorption spectra were recorded with an Agilent Technologies 8453 spectrophotometer. Steady-state fluorescence measurements were performed on a Fluomax-2 fluorometer.

Femtosecond Transient Absorption Measurements. Transient absorption was used to investigate the excited-state dynamics of the samples at different excitation wavelengths and description of the system is provided elsewhere [14]. Briefly, the output of an amplified laser beam was split to generate pump and probe beam pulses with a beam splitter (85% and 15%). The pump beam was produced by an optical parametric amplifier (OPA-800c). The pump beam used in the present investigation was obtained from either the second or the fourth harmonic generation of the signal beam and was focused onto the sample cuvette. The probe beam was delayed with a computer controlled motion controller and then focused on to a 2 mm sapphire plate to generate a white light continuum. The white light was then overlapped with the pump beam in a 1.5 mm quartz cuvette containing the sample and the change in absorbance for the signal was collected by a CCD detector (Ocean Optics). Data acquisition was controlled by software from Ultrafast Systems Inc. Typical power of probe beam was <0.1 μJ per pulse, while the pump beam ranged from 0.1 to 0.4 μJ per pulse with a repetition rate of 1000 Hz. Pulse duration was obtained by fitting the solvent response, which was ~130 fs. The sample was stirred with a rotating magnetic stirrer and no photodegradation of the sample was observed before or after the pump-probe experiment.

10-6 Steady State Absorption

Figure 9-3 shows the steady-state absorption spectra of quinoidal oligothiophene (QOT) arrays in THF, while figure 9-2 shows the molecular structure of each oligomer. With increasing chain length, the absorption red shift of the main band (the most intense bands in each spectrum) is observed. This continuous red shift shows that the pi-electron delocalization is efficient in our QOT arrays. In the 5mer and 6mer, small bands are also observed at higher energies than the main band, and appear in the same energy region as the 2mer and 3mer.

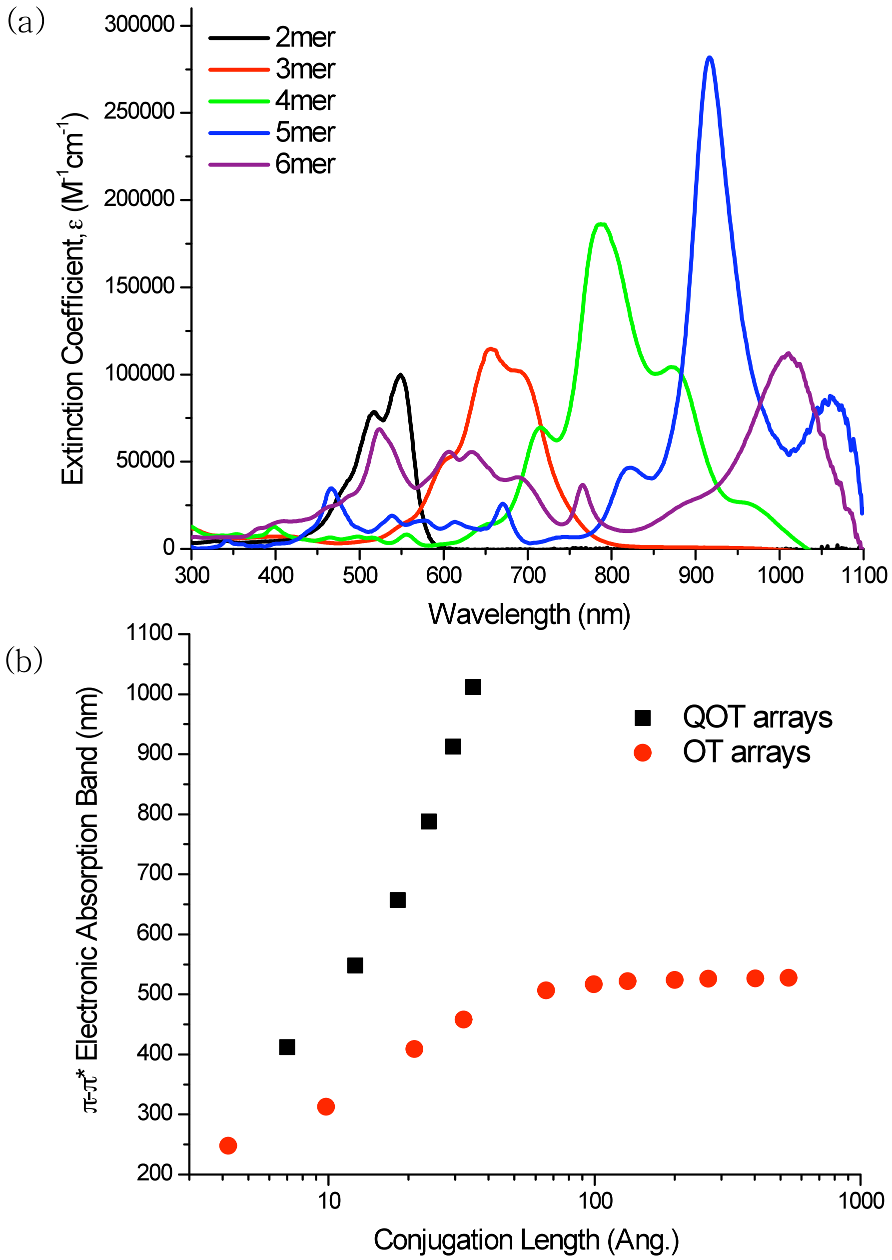

Figure 10-3. Steady-state Absorption Apectra of 2mer-6mer in THF (a) and Conjugation Length vs. Pi-Pi* Electronic Absorption Band Plot (b)

The conjugation length was estimated wit the following assumptions: total molecular structure is linear and both the C-C and C=C bond lengths are 1.4 angstrom, similar to benzene.

A critical observation can be made by comparing the absorption spectra of QOT arrays to those of oligothiophene (OT) arrays connected with a single bond between thiophene units [10,11]. In the QOT arrays, the absorption spectra show continuous red-shift with the increasing number of thiophene units, while OT arrays show saturation behavior at 560 nm. This is depicted in figure 9-3, where molecular conjugation length is compared to π-π* electronic absorption band maxima. This optical behavior, close to linear with regards to the unit number, in the QOT arrays indicates efficient ground state delocalization of π-electron conjugation, while the saturation behavior in the OTs show increasingly less efficient π-electron delocalization in the longer arrays. This provides clear evidence that QOT is an extremely promising species for molecular wire type behavior and viable for a number of applications where strong NIR response is also needed. Being intrinsically more rigid than OT, QOT may also be more suitable for highly ordered solid state devices.

10-7 Biradical Behavior and Ground State Relaxation of Dimer

In order to understand any findings obtained from femtosecond transient absorption, it is important to examine previous ultrafast spectroscopic studies and recall our knowledge of biradical excited states. Wang et al. reported that the excited-state energy relaxation process in a QOT dimer is related to the formation of a polaron, determined by observing the modulation of vibrational mode with a chirped frequency [11]. Afterwards, Ortiz et al. [12] demonstrated that, based on electronic and vibrational spectroscopy, the electronic ground state of QOT arrays is a singlet state which exhibits a biradical character, a result supported by theoretical calculations. Particularly relevant to our investigations, they predicted that the biradical character increases with increasing oligomer length. Extending this prediction to an expected material response, a conformational change from a quinoidal ground-state to a aromatic excited-state structure may lead to subsequent isolation of electronic states within larger oligomers. These studies and others [15] focus on polaron or radical ion formation as charge carriers and structural distortions upon photoexcitation in various conjugated oligomers. They set the stage for explaining charge transport and excited-state optical properties in many thiophene containing arrays. Lanzani et al. [16] investigated the excited-state charge transfer in a sexithiophene film sample using femtosecond pump-probe spectroscopic methods and proposed that the formation of polaron pairs is the origin of the fast non-radiative deactivation mechanism of the singlet excited-state, based on the spectral position of the excited-state absorption. In this report, they described that the lifetime of polaron pairs was estimated to be about 30 ps, and the π* state nonradiatively depopulates to the ground state by geminate recombination. The similar study has been performed by Brown et al. [17] for a poly(3-hexylthiophene) (P3HT) sample. Based on charge modulation spectroscopic observations, they suggest that there is a strong intermolecular interaction between P3HT units, which provides evidence for a delocalized polaron. Through DFT calculation, Fomine et al. [18] have described that polaron delocalization is relevant to the planarity between thiophene units. Interestingly, they concluded that the polaron delocalization increases with the number of thiophene units in a linear array and that the excited-state energy relaxation processes are related to the localization of polaron. This is consistent with the aforementioned studies and will be further elucidated in our subsequent assessment of QOT oligomer transient kinetics.

10-8 Femtosecond Transient Absorption

The excited-state spectroscopic characterization of delocalized π-conjugation systems can directly provide information on the potential application in molecular photonics/electronics. Due to QOTs low fluorescence at room temperature, the excited-state photophysical properties are best characterized by time-resolved absorption methods. Thus we performed femtosecond transient absorption experiments on QOT arrays in THF solvent at different excitation wavelengths, in order to characterize the excited-state dynamics of the radical forming, photo-induced π-π* transition.

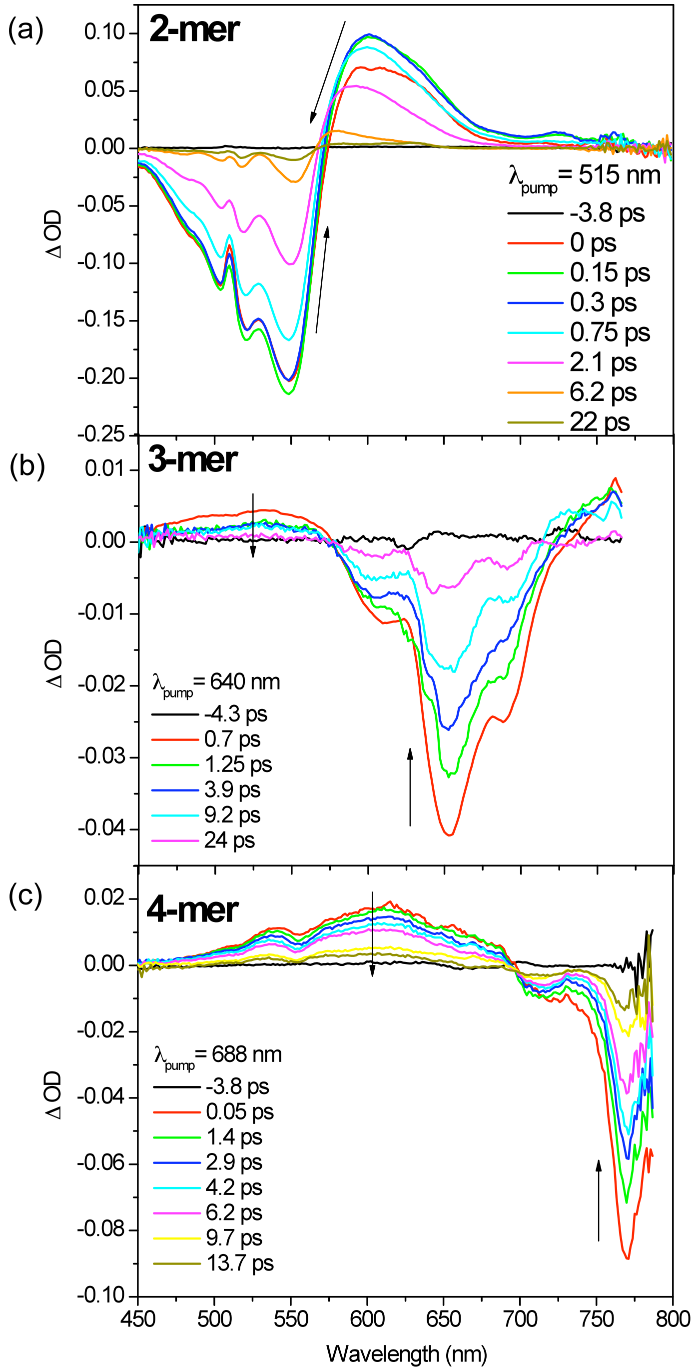

Figure 10-4. Femtosecond Transient Absorption Spectra of (a) 2-mer, (b) 3-mer and (c) 4-mer

In the 2-mer, a ground-state bleaching (GB) signal maximum was observed at 548 nm after photoexcitation at 515 nm, which is consistent with the absorption band position in steady-state measurements (figure 9-4). In the energetic region slightly lower than the GB band, an excited-state absorption (ESA) band can be observed, centered at 602 nm, with a smaller excited-state absorption band at 723 nm within our experimental detection range (450-800 nm). At earlier times (<5 ps) the bleaching signal showed a slight red-shift from 549 nm to 553 nm. During this same timeframe the excited-state absorption signal showed a blue shift from 601 nm to 579 nm. This is a reasonable shift in both regions as π* band relaxes vibronically and corresponds reasonably well to an ESA from π* to the σ* UV band during the relaxation. The bleaching recovery time constants were obtained by biexponential deconvolution fitting, resulting in a 2.91 ps relaxation time and a long time component with trivial amplitude.

For this dimer system, Wang et al. have previously investigated the conformational changes by torsion and C=C stretching between two thiophene units by analyzing the data obtained from sub-5 fs pump-probe absorption spectroscopy [11]. In their report, they propose that the two thiophene units can change structure from quinoidal to aromatic after photoexcitation, and the geometrical relaxation process to the ground state is related to polaron or bipolaron behavior. They obtained three decay time constants and assigned them as a transition from free exciton to self-trapped exciton state (200 fs), the relaxation to an intermediate state (1.8 ps), and direct ground state repopulation (>20 ps) [11]. In spite of a different excitation wavelength and pulse width, the observed decay time constants in previous and current studies show a consistent result, with the exception of the femtosecond time constant which is on the same order of our instrument response function. Similarly, the recent spectroscopic and electrochemical study by Ortiz et al. on biradical formation gives insight into the excited-state energy relaxation process of QOT-type dimers [12].

In the 3-mer (figure 9-4), a GB signal maximum was observed at 654 nm after photoexcitation at 640 nm. The GB position is also consistent to the observed band position of steady-state absorption measurements. Centered at the GB band, two regions of ESA could be observed, which are centered at 520 nm and at 750 nm. In this case, it should be emphasized that the two ESA regions showed slightly different kinetic behaviors. That is, the decay kinetics in the higher energy ESA signal (~520 nm) was able to be fitted with biexponential decay, and the weight-averaged time constant was 10.9 ps, relating to a π*-σ* similar to that observed in the 2-mer species. On the other hand, the lower energy ESA signal (~750 nm) was fitted with triple exponential decay functions, including a rise component (0.91 ps) and two decay components which weight average to ~10 ps. The different initial excited-state behavior in the red and blue ESA bands imply that the trimer can form energetically different types of excited-state species initially and is indicative of biradical formation isolating regions of a single chromophore. The different excited-state behavior becomes more obvious in longer chain chromophores, 4-, 5- and 6-mer.

In the 4-mer (figure 9-4), a GB signal maximum was observed at 772 nm after 688 nm photoexcitation. A broad ESA band was observed a higher energy region than the GB signal. The bleaching recovery time constants were obtained by biexponential deconvolution fitting, resulting in 6.6 ps time constant, again with a trivial amplitude long time component. The decay kinetics at the ESA signal (542 nm) was fitted with biexponential decay, and the weight-averaged time constant was 8.5 ps, reasonably close to the π* depopulation rate and again attributed to a π*→σ* transition.

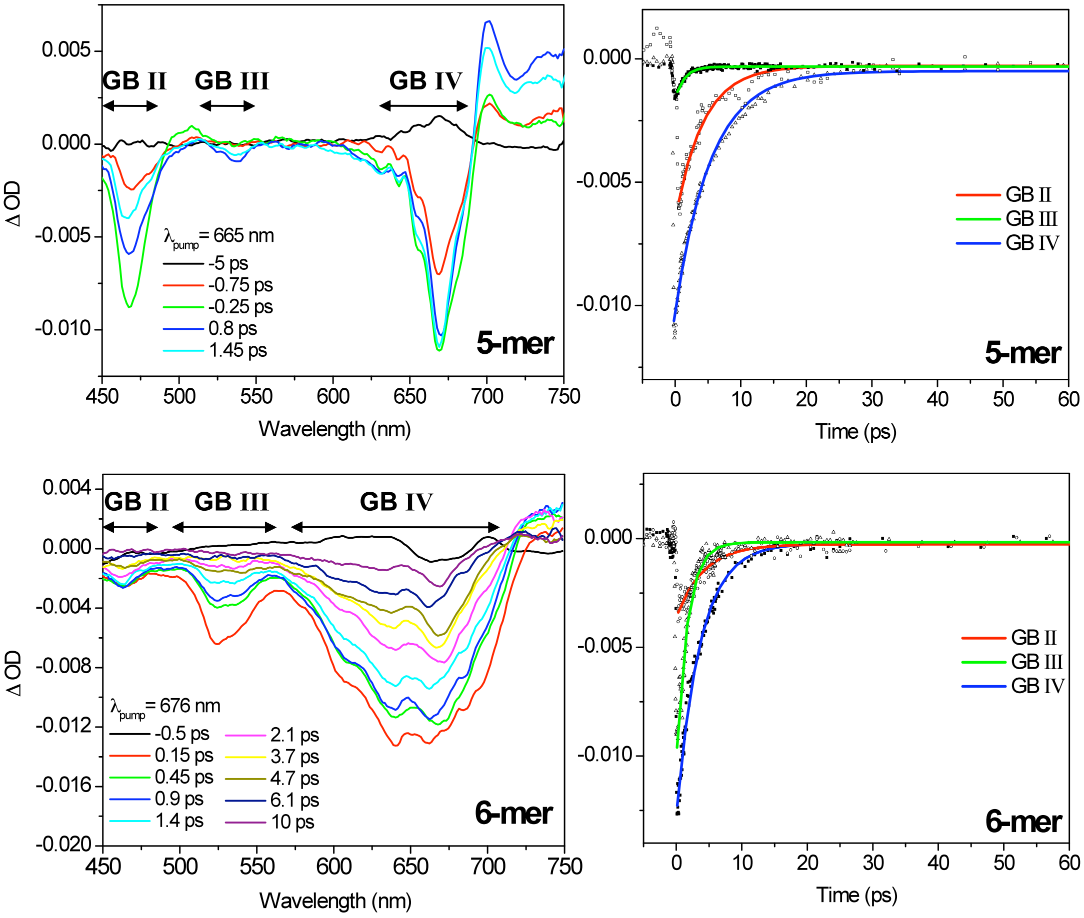

Figure 10-5. Femtosecond Transient Absorption Spectra of the (a) 5-mer and (c) 6-mer in THF

The decay kinetics of ground-state bleaching recovery in 2-mer type (GB II), 3-mer type (GB III) and 4-mer type (GB IV) excitonic regions are shown (b and d).

In the cases of the 5-mer and 6-mer (figure 9-5), broad GB bands could be observed in our detection window (450-750 nm). While the primary absorption bands for both species (~925 nm and ~1025 nm respectively) are outside of our detection range, these higher energy GB bands tell us an enormous amount about the excited state behavior of these species. The GB bands, denoted as GB II-IV, are centered at 460, 525 and 665 nm regions and correspond to blue-shifted radical 2-mer, 3-mer and 4-mer type behaviors for the 5-mer and 6-mer. The GB II-IV regions of higher energy secondary bands are observed in 5- and 6-mer steady-state absorption spectra. At first glance, the transient spectra of the 6-mer is much broader than those of the 5-mer. The higher density of energy states in the 6-mer are denoted by these broader bleach bands, and display that a greater variety of excited-state species are observable in the 6-mer over the 5-mer. With biradical formation being intrinsic to QOT photoexcited-states, the broader transient absorption bands of the 6-mer should be interpreted as a higher number of combined possibilities of radical isolated subunits (ie. monomer, dimer, and trimer). This is depicted conceptually in figure 9-6. In this case, observation of the same transient band energies with different broadness's and kinetics indicate that the biradical character follows a set of preferential configurations which are different and specific to each species.

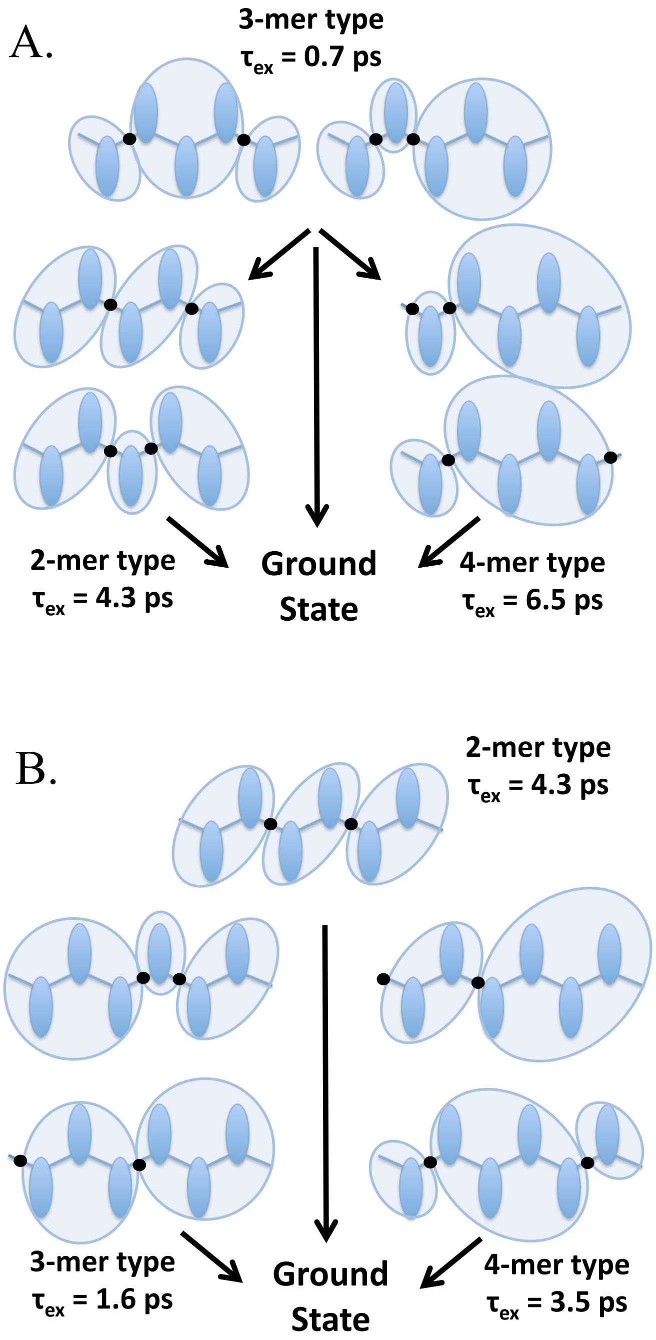

Figure 10-6. Conceptual Display of Biradical Electronic Region Isolation in (a) 5-mer and (b) 6-mer

Note that the 6-mer reaches lengths where radical isolation is capable of generating both 2-mer/3-mer and 2-mer/4-mer type behavior.

The excited-state decay kinetics of GB II-IV show distinctly different behavior (table 9-1). From deconvolution fitting at different wavelengths, we obtained different primary time constants of 4.3 ps for GB II band, 0.7 ps for GB III, and 6.5 ps for GB IV in the 5-mer. For the 6-mer, they are 4.3 ps for GB II, 1.5 ps for GB III and 3.6 ps for GB IV. These results show that the excited-state relaxation processes of the 5-mer and 6-mer are dependant on the dynamics of the radical dictated subunits within the chromophores. However, the decay time constants in GB II~IV are different from the decay time constants of the individual dimer, trimer or teteramer species. A reasonable explanation for this discrepancy is that the structural relaxation process of the excited-state in the subunits (for example, sub-trimer) is different from that of individual units (individual trimer). Specifically, for the trimer and trimer-type subunit, this points heavily to the availability of a multitude of faster or alternate relaxation processes, such as radical relocation. It should be noted that the relaxation of the trimer type units in both the 5- and 6-mer (0.7 and 1.5 ps) are on the same order as the ESA rise observed in the 3-mer (0.9 ps). This is a very strong indication that the same change resulting in the 3-mer rise time is precipitate the change of state observed in the diradical 3-mer type unit response.

Table 10-1. Summary of Time Constants Measured from Femtosecond Transient Absorption at Different Band Regions

		Dimer Region		Trimer Region		Tetramer Region	
Sample	λ_{pump}	τ_{GBII}	λ_{probe}	τ_{GBIII}	λ_{probe}	τ_{GBIV}	λ_{probe}
2-mer	515 nm	2.9 ps	554 nm	--	--	--	--
3-mer	640 nm	--	--	10.9 ps	650 nm	--	--
4-mer	699 nm	--	--	--	--	6.6 ps	762 nm
5-mer	665 nm	4.3 ps	462 nm	700 fs	525 nm	6.5 ps	665 nm
6-mer	676 nm	4.3 ps	467 nm	1.6 ps	520 nm	3.5 ps	642 nm

Throughout the spectroscopic and theoretical studies on oligothiophene derivatives mentioned previously, the polaron formation upon photoexcitation remained key to understanding the observed ultrafast excited-state dynamics in OT arrays. In our of QOT systems, the weight averaged excited-state decay rates become faster in increasing chain length (table 9-1) as the array sizes become larger than the 2-mer. Based on biradical formation, it is reasonable that the excited-state radical can induce a higher single bond character between the thiophene units, resulting in the structural change from a quinoidal to an aromatic structure. In other words, due to the conformational flexibility obtained by increased single bond character between thiophene units, faster nonradiative decay process are observed in longer arrays from the radical isolated subunits.

In addition to conformational dynamics, the energy gap law also provides an explanation for the observed decay time constants. That is, as the number of thiophene units increases, the HOMO-LUMO energy gap exhibits monotonic decrease as observed in steady-state absorption. The reduced HOMO-LUMO energy gap can accelerate the nonradiative decay rate in the longer arrays and can readily be associated with a polaronic structural change. Thus, based on the weak fluorescence and ultrafast decay time, we suggest that the excited-state dynamics in QOT arrays are dominated by the polaronic structural change associated with the reduced HOMO-LUMO energy gap and the kinetic differences arise as a result of the possible configurations of polarons/radicals along chains of differing sizes.

Generally, charge transfer processes in organic materials have been known as largely different from those in metals, semiconductors or inorganics [19]. While the electric conduction in metals occur by the drift of electron-hole pairs in the continuous energy levels of conduction bands, the electronic conduction in organic materials often occurs from drifting electrons in the subgap (self-trapped) states, inducing surrounding lattice deformations. This explains how charge transfer processes in organic materials are usually observed to be slower than that in metals. However, the current study shows that QOT arrays can exhibit ultrafast polaronic charge transfer, comparable to the charge transfer dynamics of metallic species, which make it suitable candidate for application on molecular electronics.

10-9 Conclusions

In spite of the various advantages of OFETs for practical application, conformational heterogeneity and inefficient charge transport have remained some of the most troubling problems for synthetic chemists and device engineers to overcome. In this study, we have provided direct spectroscopic evidence for ultrafast charge-separation and charge-recombination in conjugated QOT. Throughout the steady-state and time-resolved spectroscopic measurements, we observed that (i) QOT arrays exhibit linear response of absorption wavelength maxima to near-infrared region with increasing conjugation length, (ii) that the excited-state charge transfer rate becomes faster in increasing chain length and that (iii) the biradical dictated subunits show distinctly different kinetic behavior, can be individually assessed and directly related to breaks in quinoidal behavior. These results show that QOT arrays exhibit rigid molecular structure with efficiently delocalized π-electrons originated from strong intramolecular electronic interaction between thiophene units, which precludes large conformational change. The ultrafast responses of these molecular arrays by photoexcitation have been shown to be advantageous for practical application in as NIR-sensitive molecular wires. This current study, combined with previous OT investigations, suggests strongly that QOT arrays can play a role as efficient organic conductors. Furthermore, the observed results enable us to predict that in longer arrays (>6-mer) the absorption maxima will be driven further into the NIR regions with even shorter excited-state lifetimes, and will prove extremely promising for applications where NIR active molecular electronics could replace current solid state electronics.

10-10 References

(1) Horowitz, G. Adv. Mater. 1998, 10, 365-377.

(2) (a) Shimizu, Y.; Oikawa, K.; Nakayama, K. I.; Guillon, D. J. Mater. Chem. 2007, 17, 4223–4229. (b) Roncali, J.; Leriche, P.; Cravino, A. Adv. Mater. 2007, 19, 2045–2060. (c) Sirringhaus, H. Adv. Mater. 2005, 17, 2411–2425. (d) Barbarella, G.; Melucci, M.; Sotgiu, G. Adv. Mater. 2005, 17, 1581–1593. (e) Lo, S.-C.; Burn, P. L. Chem. Rev. 2007, 107, 1097-1116.

(3) (a) Gundlach, D. J. Nat. Mater. 2007, 6, 173–174. (b) Berggren, M.; Nilsson, D.; Robinson, N. D. Nat. Mater. 2007, 6, 3–5. (c) Zaumseil, J.; Sirringhaus, H. Chem. Rev. 2007, 107, 1296–1323.

(4) (a) Sirringhaus, H; Tessler, N.; Friend, R. H. Science 1998, 280, 1741–1744. (b) Huitena, H. E. A.; Gelinck, G. H.; van der Putter, J. B. P. H.; Kuijk, K. E.; Hart, C. M.; Cantatore, E.; Herwig, P. T.; van Breemen, A. J. J. M.; de Leeuw, D. M. Nature 2001, 414, 599. (c) Bao, Z. Adv. Mater. 2000, 12, 227–230. (d) Li, Y. N.; Wu, Y. L.; Ong, B. S. Macromolecules 2006, 39, 6521-6527. (e) Dimitrakopoulos, C. D.; Malenfant, P. R. L. Adv. Mater. 2002, 14, 99-117.

(5) (a) Mas-Torrent, M.; Rovira, C. Chem. Soc. Rev. 2008, 37, 827-838. (b) Coropceanu, V.; Cornil, J.; da Silva Filho, D. A.; Olivier, Y.; Silbey, R.; Bredas, J. L. Chem. Rev. 2007, 107, 926-952. (c) Shirota, Y.; Kageyama, H. Chem. Rev. 2007, 107, 953-1010. (d) Murphy, A. R.; Fréchet, J. M. J. Chem. Rev. 2007, 107, 1066-1096. (e) Anthony, J. E. Chem. Rev. 2006, 106, 5028-5048. (f) Newman, C. R.; Frisbie, C. D.; da Silva Filho, D. A.; Bredas, J. L.; Ewbank, P. C.; Mann, K. R. Chem. Mater. 2004, 16, 4436-4451.

(6) (a) Liu, S.; Wang, W. M.; Briseno, A. L.; Mannsfeld, S. C. B.; Bao, Z. Adv. Mater. 2009, 21, 1217-1232. (b) Javey, A.; Kim, H.; Brink, M.; Wang, Q.; Ural, A.; Guo, J.; McIntyre, P.; McEuen, P. Lundstrom , M.; Dai, H. Nat. Mater. 2002, 1, 241–246. (c) Javey, A.; Guo, J.; Farmer, D. B.; Wang, Q.; Yenilmez, E.; Gordon, R. G.; Lundstrom, M.; Dai, H. Nano Lett. 2004, 4, 1319–1322. (d) Klinke, C.; Chen, J.; Afzali, A.; Avouris, P. Nano Lett. 2005,

5, 555–558. (e) Kang, S. J.; Kocabas, C.; Ozel, T.; Shim, M.; Pimparkar, N.; Alam, M. A.; Rotkin, S. V.; Rogers, J. A. Nat. Nanotech. 2007, 2, 230–236. (f) Avouris, P.; Chen, Z.; Perebeinos, V. Nat. Nanotech. 2007, 2, 605–615.

(7) (a) Mishra, A.; Ma, C.-Q; Bäuerle, P. Chem. Rev. 2009, 109, 1141-1276. (b) Zotti, G.; Zecchin, S.; Vercelli, B.; Berlin, A.; Casado, J.; Hernandez, V.; Ortiz, R. P.; Lopez-Navarrete, J. T.; Orti, E.; Viruela, P. M.; Milian, B. Chem. Mater. 2006, 18, 1539-1545. (c) Pappenfus, T. M.; Chesterfield, R. J.; Frisbie, C. D.; Mann, K. R.; Casado, J.; Raff, J. D.; Miller, L. L. J. Am. Chem. Soc. 2002, 124, 4184-4185. (d) Janzen, D. E.; Burand, M. W.; Ewbank, P. C.; Pappenfus, T. M.; Higuchi, H.; Da Silva Filho, D. A.; Young, V. G.; Bredas, J.-L.; Mann, K. R. J. Am. Chem. Soc. 2004, 126, 15295-15308. (e) Chesterfield, R. J.; Newman, C. R.; Pappenfus, T. M.; Ewbank, P. C.; Haukaas, M. H.; Mann, K. R.; Miller, L. L.; Frisbie, C. D. Adv. Mater. 2003, 15, 1278-1282.

(8) (a) Locklin, J.; Li, D.; Mannsfeld, S. C. B.; Borkent, E.-J.; Meng, H.; Advincula, R.; Bao, Z. Chem. Mater. 2005, 17, 3366-3374. (b) Facchetti, A.; Letizia, J.; Yoon, M.-H.; Mushrush, M.; Katz, H. E.; Marks, T. J. Chem. Mater. 2004, 16, 4715-4727. (c) Nenajdenko, V. G.; Sumerin, V. V.; Chernichenko, K. Y.; Balenkova, E. S. Org. Lett. 2004, 6, 3437-3439. (d) Chang, P. C.; Lee, J.; Huang, D.; Subramanian, V.; Murphy, A. R.; Frechet, J. M. J. Chem. Mater. 2004, 16, 4783-4789. (e) Johansson, E.; Larsson, S. Synth. Met. 2004, 144, 183-191. (f) Ruiz Delgado, M. C.; Casado, J.; Hernandez, V.; Lopez Navarrete, J. T.; Fuhrmann, G.; Baeuerle, P. J. Phys. Chem. B 2004, 108, 3158-3167. (g) Meinardi, F.; Cerminara, M.; Blumstengel, S.; Sassella, A.; Borghesi, A.; Tubino, R. Phys. Rev. B 2003, 67, 184205. (h) Facchetti, A.; Mushrush, M.; Katz, H. E.; Marks, T. J. Adv. Mater. 2003, 15, 33-38. (i) Meng, H.; Zheng, J.; Lovinger, A. J.; Wang, B.-C.; Van Patten, P. G.; Bao, Z. Chem. Mater. 2003, 15, 1778-1787.

(9) Izumi, T.; Kobashi, S.; Takimiya, K.; Aso, Y.; Otsubo, T. J. Am. Chem. Soc. 2003, 125, 5286-5287.

(10) Takahashi, T.; Matsuoka, K.-I.; Takimiya, K.; Otsubo, T.; Aso, Y. J. Am. Chem. Soc. 2005, 127, 8928-8929.

(11) (a) Wang, Z.; Otsubo, T.; Kobayashi, T. Chem. Phys. Lett. 2006, 430, 45–50. (b) Wang, Z.; Kobayashi, T. Chem. Phys. Lett. 2007, 447, 221-226. (c) Wang, Z.; Kobayashi, T. New J. Phys. 2008, 10, 123021.

(12) Ortiz, R. P.; Casado, J.; Gonzalez, S. R.; Hernandez, V.; Lopez Navarrete, J. T.; Viruela, P. M.; Orti, E.; Takimiya, K.; Otsubo, T. Chem. Eur. J. 2010, 16, 470-484.

(13) (a) Varnavski, O.; Bäuerle, P.; Goodson, T. Opt. Lett. 2007, 32, 3083-3085. (b) Harpham, M. R.; Süzer, Ö.; Ma, C.-Q.; Bäuerle, P.; Goodson, T., III. J. Am. Chem. Soc. 2009, 131, 973-979. (c) Oliva, M. M.; Casado, J.; Navarrete, J. T. L.; Patchkovskii, S.; Goodson T.; Harpham, M. R.; Seixas de Melo, J.; Amir, E.; Rozen, S. J. Am. Chem. Soc. 2010, 132, 6231–6242. (d) Badaeva, E.; Harpham, M. R.; Guda, R.; Süzer, Ö.; Ma, C.-Q.; Bäuerle, P.; Goodson, T.; Tretiak, S. J. Phys. Chem. B 2010, 114, 15808–15817.

(14) Ramakrishna, G.; Bhaskar, A.; Goodson, T., III. J. Phys. Chem. B 2006, 110, 20872-20878.

(15) (a) Funston, A. M.; Silverman, E. E.; Miller, J. R.; Schanze, K. S. J. Phys. Chem. B 2004, 108, 1544-1555. (b) Zhao, Z.; Spano, F. C. J. Chem. Phys. 2005, 122, 114701. (c) Ye, A.; Shuai, Z.; Kwon, O.; Bredas, J. L. ; Beljonne, D. J. Chem. Phys. 2004, 121, 5567.

(16) (a) Lanzani, G.; Cerullo, G.; Stagira, S.; De Silvestri, S.; Garnier, F. Phys. Rev. B 1998, 58, 7740-744. (b) Lanzani, G.; Cerullo, G.; Stagoara, S.; De Silvestri, S. J. Photochem. Photobiol. A 2001, 144, 13-19. (c) van Hal, P. A.; Janssen, R. A. J.; Lanzani, G.; Cerullo, G.; Zaveleni-Rossi, M.; De Silvestri, S. Chem. Phys. Lett. 2001, 345, 33-38. (d) Cerullo, G.; Lanzani, G.; Muccini, M.; Taliani, C.; De Silvestri, S. Synth. Met. 1999, 101, 614-617. (e) Paa, W.; Yang, J.-P.; Rentsch, S. Appl. Phys. B 2000, 71, 443-449. (f) Paa, W.; Yang, J.-P.; Rentsch, S. Synth. Met. 2001, 119, 525-526.

(17) Brown, P. J.; Sirringhaus, H.; Harrison, M.; Shkunov, M.; Friend, R. H. Phys. Rev. B 2001, 63, 125204.

(18) (a) Fomine, S.; Guadarrama, P.; Flores, P. J. Phys. Chem. A 2007, 111, 3124-3131. (b) Flores, P.; Guadarrama, P.; Ramos, E.; Fomine, S. J. Phys. Chem. A 2008, 112, 3996-4003.

(19) Qiu, Y.; Zhu, L.-P. J. Chem. Phys. 2009, 131, 134903.

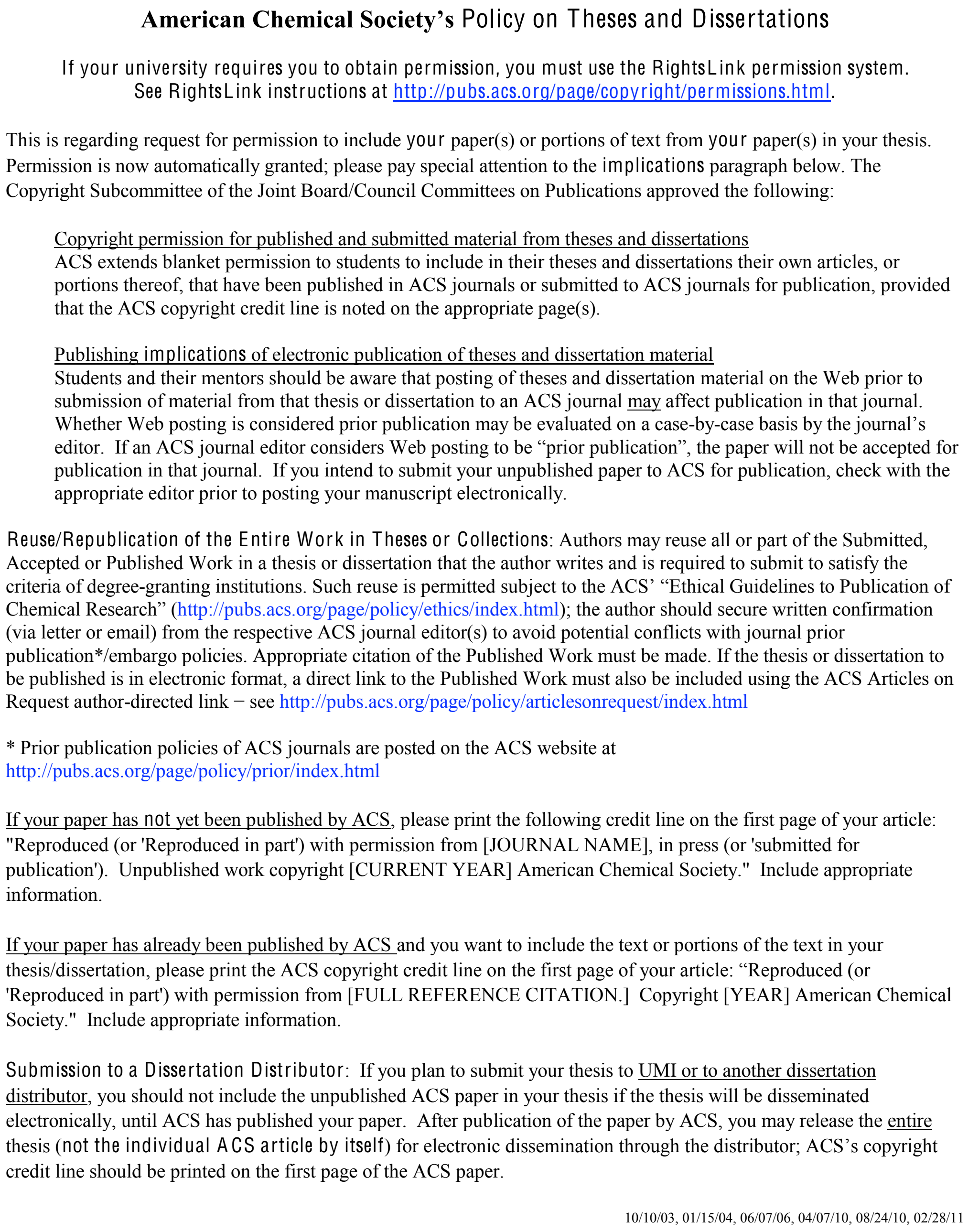

American Chemical Society's Policy on Theses and Dissertations

If your university requires you to obtain permission, you must use the RightsLink permission system.
See RightsLink instructions at http://pubs.acs.org/page/copyright/permissions.html.

This is regarding request for permission to include your paper(s) or portions of text from your paper(s) in your thesis. Permission is now automatically granted; please pay special attention to the implications paragraph below. The Copyright Subcommittee of the Joint Board/Council Committees on Publications approved the following:

> Copyright permission for published and submitted material from theses and dissertations
> ACS extends blanket permission to students to include in their theses and dissertations their own articles, or portions thereof, that have been published in ACS journals or submitted to ACS journals for publication, provided that the ACS copyright credit line is noted on the appropriate page(s).
>
> Publishing implications of electronic publication of theses and dissertation material
> Students and their mentors should be aware that posting of theses and dissertation material on the Web prior to submission of material from that thesis or dissertation to an ACS journal may affect publication in that journal. Whether Web posting is considered prior publication may be evaluated on a case-by-case basis by the journal's editor. If an ACS journal editor considers Web posting to be "prior publication", the paper will not be accepted for publication in that journal. If you intend to submit your unpublished paper to ACS for publication, check with the appropriate editor prior to posting your manuscript electronically.

Reuse/Republication of the Entire Work in Theses or Collections: Authors may reuse all or part of the Submitted, Accepted or Published Work in a thesis or dissertation that the author writes and is required to submit to satisfy the criteria of degree-granting institutions. Such reuse is permitted subject to the ACS' "Ethical Guidelines to Publication of Chemical Research" (http://pubs.acs.org/page/policy/ethics/index.html); the author should secure written confirmation (via letter or email) from the respective ACS journal editor(s) to avoid potential conflicts with journal prior publication*/embargo policies. Appropriate citation of the Published Work must be made. If the thesis or dissertation to be published is in electronic format, a direct link to the Published Work must also be included using the ACS Articles on Request author-directed link – see http://pubs.acs.org/page/policy/articlesonrequest/index.html

* Prior publication policies of ACS journals are posted on the ACS website at
http://pubs.acs.org/page/policy/prior/index.html

If your paper has not yet been published by ACS, please print the following credit line on the first page of your article: "Reproduced (or 'Reproduced in part') with permission from [JOURNAL NAME], in press (or 'submitted for publication'). Unpublished work copyright [CURRENT YEAR] American Chemical Society." Include appropriate information.

If your paper has already been published by ACS and you want to include the text or portions of the text in your thesis/dissertation, please print the ACS copyright credit line on the first page of your article: "Reproduced (or 'Reproduced in part') with permission from [FULL REFERENCE CITATION.] Copyright [YEAR] American Chemical Society." Include appropriate information.

Submission to a Dissertation Distributor: If you plan to submit your thesis to UMI or to another dissertation distributor, you should not include the unpublished ACS paper in your thesis if the thesis will be disseminated electronically, until ACS has published your paper. After publication of the paper by ACS, you may release the entire thesis (not the individual ACS article by itself) for electronic dissemination through the distributor; ACS's copyright credit line should be printed on the first page of the ACS paper.

10/10/03, 01/15/04, 06/07/06, 04/07/10, 08/24/10, 02/28/11

Figure 10-7. General American Chemical Society Guideline on In-Press Usage and Author Publication in Thesis

Chapter 11

Self-Assembled Mixed Metal Macrocycles for Ultrafast Photoswitching and Energy Transfer Applications

11-1 Original Publication Information

This chapter is be submitted for publication as the following document:

“Self-Assembled Mixed Metal Macrocycles for Ultrafast Photoswitching and Energy Transfer Applications”
Jeffery E. Raymond, Zin Seok Yoon, Yi-Tsu Chan, George R. Newkome and Theodore Goodson III
Chemical Sciences, submitted Q3 2011

Modifications to the original document are cosmetic and used only to conform the format of this document or provide uniformity of enumeration.

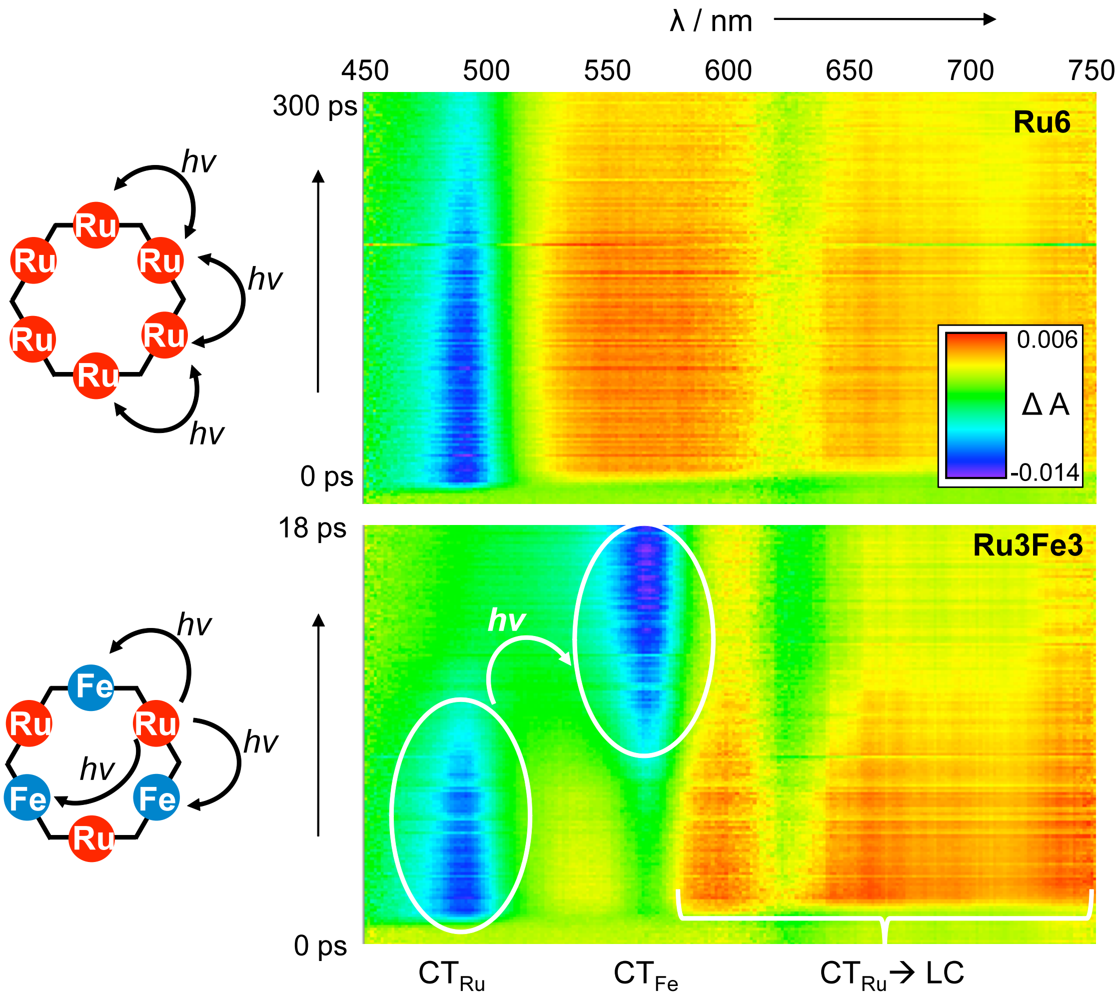

Figure 11-1. Table of Contents Image as Submitted

11-2 Qualifying Statement

This chapter is not part of the major theme of this work. It focuses on a the energy transfer processes observed in a multichormophore metal-organic macrocycle. While NLO processes such as ESA are discussed, neither TPA nor NSOM played a role in this study. It will be shown that the mixed metal macrocycle has electronic behavior which allows for photoswitching at <10 ps and strong energy trapping at longer times.

11-3 Abstract

In this work the steady state and ultrafast response of “click” assembled cyclic terpyridine hexamers with iron and ruthenium moieties are investigated for the explicit consideration of these systems as viable photoswitching and energy transfer materials. It will be shown that Ru containing macrocycles provide exceptional excited state absorption, Fe containing species provide a strong energy trapping response and that the mixed metal species is capable of both. The mixed metal response will be shown to be a result of resonance energy transfer and depend on how long after excitation one probes the system (<15 ps for photoswitching type response, >20 ps for energy trapping response). All of these behaviours will be shown to occur in the excited state despite complete electronic isolation of mer units in the ground state.

11-4 Introduction

There is a broad interest in metal-ligand complexes due to their applications in molecular materials and nano-science [1-3]. Among these materials terpyridine, a pyridine-derived tridentate ligand, and its derivatives have shown distinct architectural advantages over other polypyridyl derivatives, such as isomeric purity and inherent linearity [4-5]. Perhaps its most notable property is its ability to form metallo-bisterpyridyl complexes by self-assembly, resulting in multiple well-defined and highly reproducible molecular macrocyclic architectures [6-8]. As such, metallo-bisterpyridyl units have proven promising as building blocks for switchable ‘click chemistry’ in macrocyclic complexes where the bridging between tridentate ligands is selected to sterically favor ring closure [9,10].

One primary goal in the development and investigation of multichromophore assemblies is to facilitate controlled or enhanced optical properties for utilization in molecular optoelectronics. We have synthesized a well-known Ru(II)-bisterpyridine as well as its self-assembled hexameric macrocycles [6,11]. We have also generated Fe(II) and Ru-Fe hybrid hexameric macrocycle by self-assembly (figure 10-2). The foundation of this investigation is the observation of excitation energy transfer processes in an all-donor, an all-acceptor and a multiple donor-acceptor macrocycle [12,13]. Using steady-state absorption, fluorescence, and time-resolved femtosecond transient absorption spectroscopy, we will show that the incorporation of two different M-L building blocks allows for a functional material capable of both excited state absorption (ESA) and exciton trapping, two properties needed for applications such as photoswitching and energy transport.

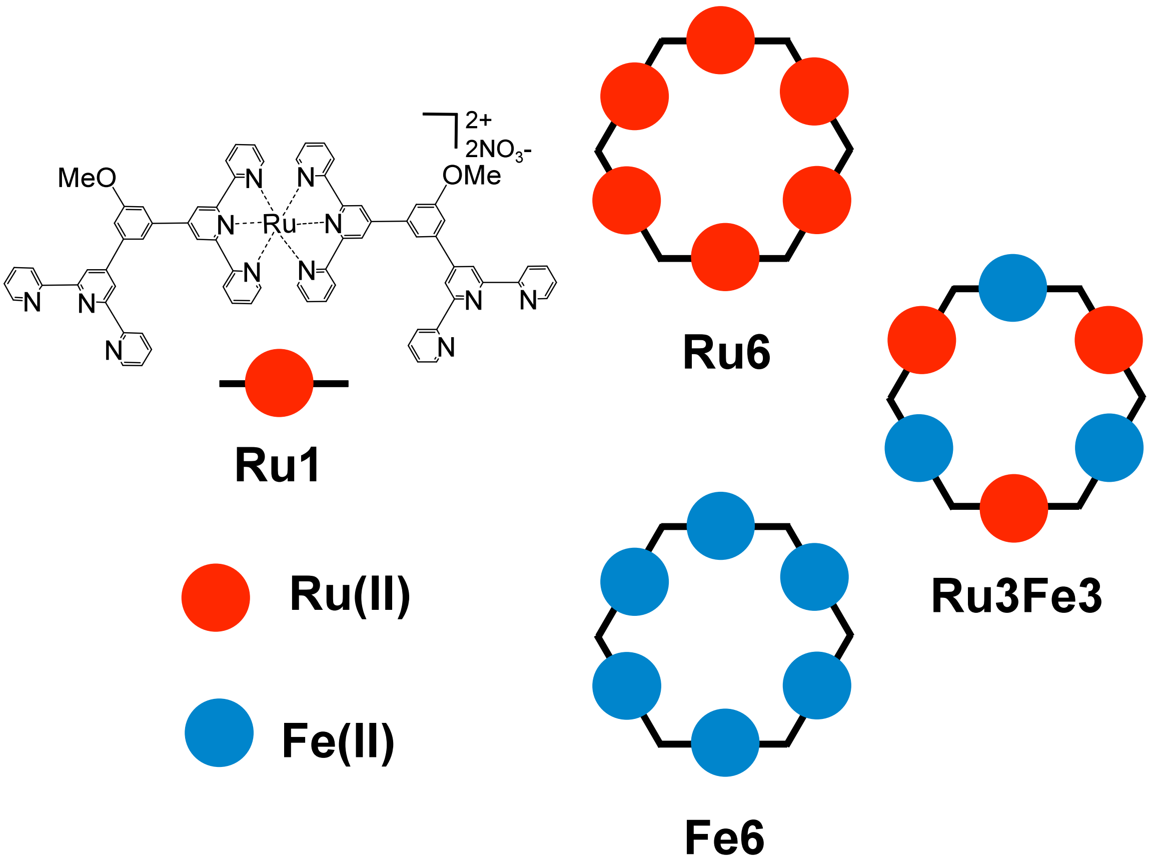

Figure 11-2. Schematic Molecular Structure of Self-Assembled Ru(II)-Fe(II) Macrocyclic Hexamers, Shown: Ru6, Fe6, and hybrid Ru3Fe3, and their reference monomer, Ru1

11-5 Steady State Spectroscopy

While the focus of this investigation is on the material response of these systems in the excited state, several critical properties of the system can be gleamed from the differences in steady state response observed. The normalized steady-state absorption spectra in figure 10-3 exhibit the hexamers Ru6, Fe6 and Ru3Fe3 as well as the single monomeric building block Ru1. In all samples, we observed two strong absorption bands at 287 and 312 nm, previously assigned as ligand-centered transition bands [6]. The nonexistence of a peak shift between species indicates a complete lack of coupling between the M and π* bands, while the slight change in peak ratios indicates subtle differences in the strain on the ligand dependent on the size of the metal ion and the structural restrictions of the multichromophoric systems. The absorption spectra of Ru6 and Ru1 display a broad band centered at 492 nm with exactly matching shapes, despite the multichromophoric nature of the Ru6 species. Using the normalized ligand centered absorption band as a reference, we observed that the 492 nm charge transfer band for the Ru6 species is larger. As there is no M- π* coupling, this result can be reasonably interpreted as the effect of two events. First, a ground state electronic configuration where the individual M-L interactions are electronically isolated. This isolation gives rise to a second finding, that even under lower level illumination some of the macrocycles species in solution are capable of absorbing multiple photons (i.e. can be come a multiexciton containing structure). Fe6 possesses absorption at 572 nm. Both absorptions (492 and 572 nm) were previously assigned as metal-to-ligand charge transfer transition bands and will be denoted as CT_{Ru} and CT_{Fe}.[6] The Ru3Fe3 macrocycle showed absorption in both CT_{Ru} and CT_{Fe} with no readily observed splitting or shift of band energy. This is unusual in systems where multiple types of metals are ligated in close proximity of each other. To confirm the lack of energy level splitting through Ru-Fe coupling, and further support our assertion that ground state electronic isolation between units exists, we plotted the absorption spectrum (Ru6+Fe6)/2 by averaging numerically the absorption spectra of Ru6 and Fe6 (figure 10-3 inset). This shows the absorption spectrum of Ru3Fe3 and (Ru6+Fe6)/2 to be identical. From these observations, it is evident that the electronic conjugation interaction between metal units is negligible in the ground state.

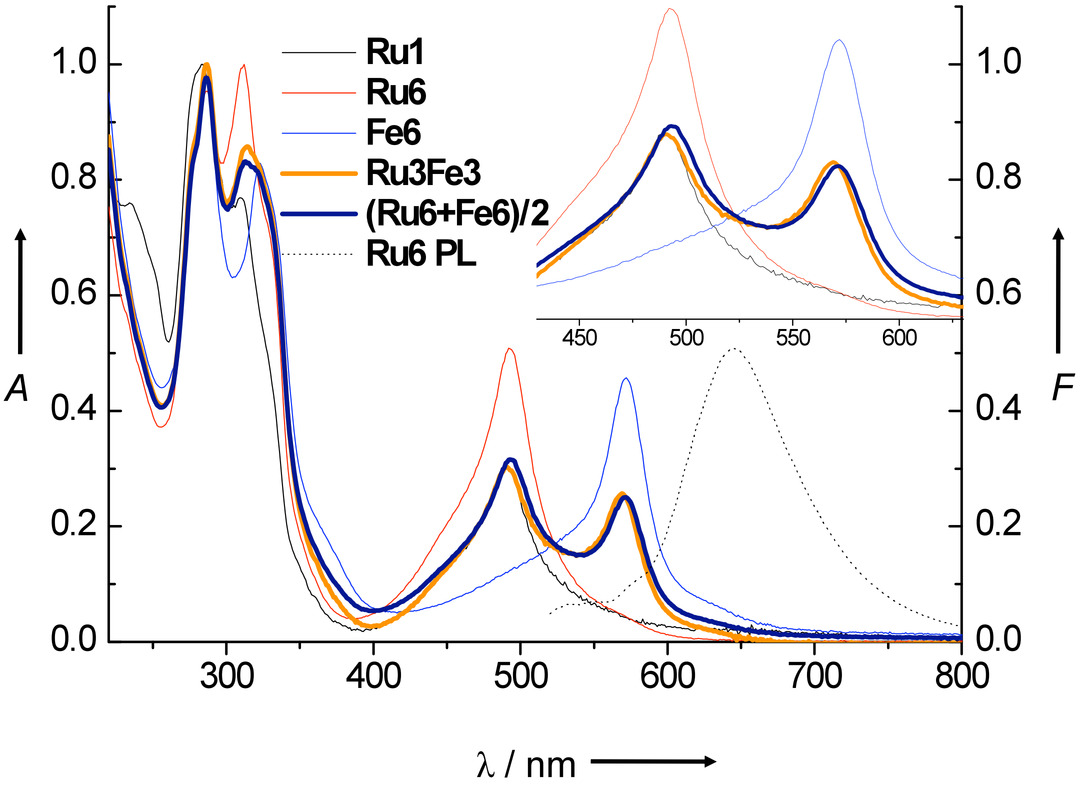

Figure 11-3. Steady-State Absorption Spectra of Ru1, Ru6, Fe6, Ru3Fe3 in ACN and the Numerically Averaged Absorption Spectrum of Ru6 and Fe6, (Ru6+Fe6)/2, and the Steady-State Fluorescence Spectrum of Ru6 in ACN

Inset shows the magnified MLCT absorption band.

When excited at CT_{Ru}, Ru6 showed fluorescence at 644 nm. The Stokes shift in the Ru sample was large (~4800 cm-1), indicating that there is a structural change between ground and excited state. However, the two rings containing Fe units, with or without Ru, showed no fluorescence. This finding is in sharp contrast to the observed isolation of states from the ground state absorption spectra. The emission results then indicate strong fluorescence quenching from the Fe moiety and infer a possibility of the Fe-L CT band as either being a non-emissive target of Dexter or Forester type energy transfer. Having confirmed in the absorption spectra a poor Ru-π-Fe electronic communication pathway, it stands that the majority of energy transfer in the Ru3Fe3 species occurs via resonance energy transfer (RET), as the distance between adjacent centers is near the fringe of Dexter limits (~10 ang.) and has already been shown to have low electronic (i.e. wavefunction) overlap through the ligand. Generally, RET occurs in a donor-acceptor system when the energy of the donor emission is slightly higher or comparable to the primary absorption of the acceptor. However, in the current system, we observed the acceptor absorption maxima being higher than that of the donor emission maxima, an effect which we will account for fully in the following discussion of transient absorption response.

The quantum yield of energy transfer (Φ_{ET}) can be estimated by steady-state fluorescence measurement with $\Phi_{ET} = 1\text{-}F_D/F_{0D}$, where F_D is the fluorescence intensity of the donor in the presence of acceptor and F_{0D} is that in the absence of acceptor [14]. Both of the Fe containing macrocycles showed nonfluorescent behavior, which indicates $F_D \sim 0$ and that Φ_{ET} is close to unity for Ru3Fe3. This has three strong implications for materials application of these types of "click" M-L systems:

(1) The Fe moiety acts as a phenomenal energy trap in this system.
(2) The molecular design of reversed energy level RET (higher absorption energy of acceptor and lower emission energy of donor) can be an efficient strategy for energy transfer.
(3) Both of these responses need not be restricted to systems where a strong electronic interaction across conjugated ligand bridges of close (<10 ang.) proximity is present.

11-6 Femtosecond Transient Absorption Spectroscopy

While the steady state response of these systems are illuminating, in order to fully understand energy pathways and optoelectronic capabilities of these materials a time-resolved femtosecond transient absorption study was performed [16]. Briefly, ultrafast transient absorption allows for the measurement of changes in absorption spectra shortly after photoexcitation. Typically two behaviors are discussed in this type of experiment: ground state bleaching (GB, $-\Delta A$) where a transition is no longer allowed after excitation and excited state absorption (ESA, $+\Delta A$) where a new electronic transition is possible after excitation. Both are discussed in terms of kinetic lifetimes from exponential fitting, with GB often indicating an occupied electronic state and ESA indicative of an occupied excited state being promoted to a still higher energy orbital. A particular emphasis was placed on controlling the excitation wavelengths to selectively tune for excitation of either CT_{Ru} or CT_{Fe} absorption bands in the Ru6 and Ru3Fe3 systems. The excited state lifetimes from exponential decay fitting are provide in table 10-1.

Table 11-1. Summary of Steady State Absorption and Emision Bands and Time Constants from Femtosecond Transient Absorption Experiments

Sample	λ_{abs} (nm)	λ_{emi} (nm)[a]	λ_{pump} (nm)[b]	λ_{probe} (nm)[c]	τ (ps)[d]
Ru1	492	644	492	483	640
Ru6	492	644	492	483	9.7, 302
Fe6	572	[a1]	572	567	inf
Ru3Fe3	492, 572	[a1]	492	483	1.8, 16, inf
			492	567	2.3, 19, inf.
			572	567	inf.

[a] Excitation at 492 nm. [a1] nonlfluorescent. [b] Pump wavelength in femtosecond transient absorption measurement. [c] Probe wavelength in femtosecond transient absorption measurement. [d] Time constants in picosecond unit, where infinite (inf) time constants were needed for bi- and triexponential decay fitting.

A two-dimensional plot of femtosecond transient absorption spectra and kinetics of Ru6 with the excitation at CT_{Ru} are presented in figure 10-4 (top). At the initial stage of photoexcitation, the Ru6 sample showed a ground-state bleaching (GB) at CT_{Ru} and broad ESA signal ranging from 530 to 750 nm. The ESA is consistent with CT*→L re-excitation and is a critical trait to photoswitching applications where an excited electron is needed in a π-conjugated system. The GB is extremely long lived (here shown to 300 ps), during the entirity of which strong ESA remains possible.

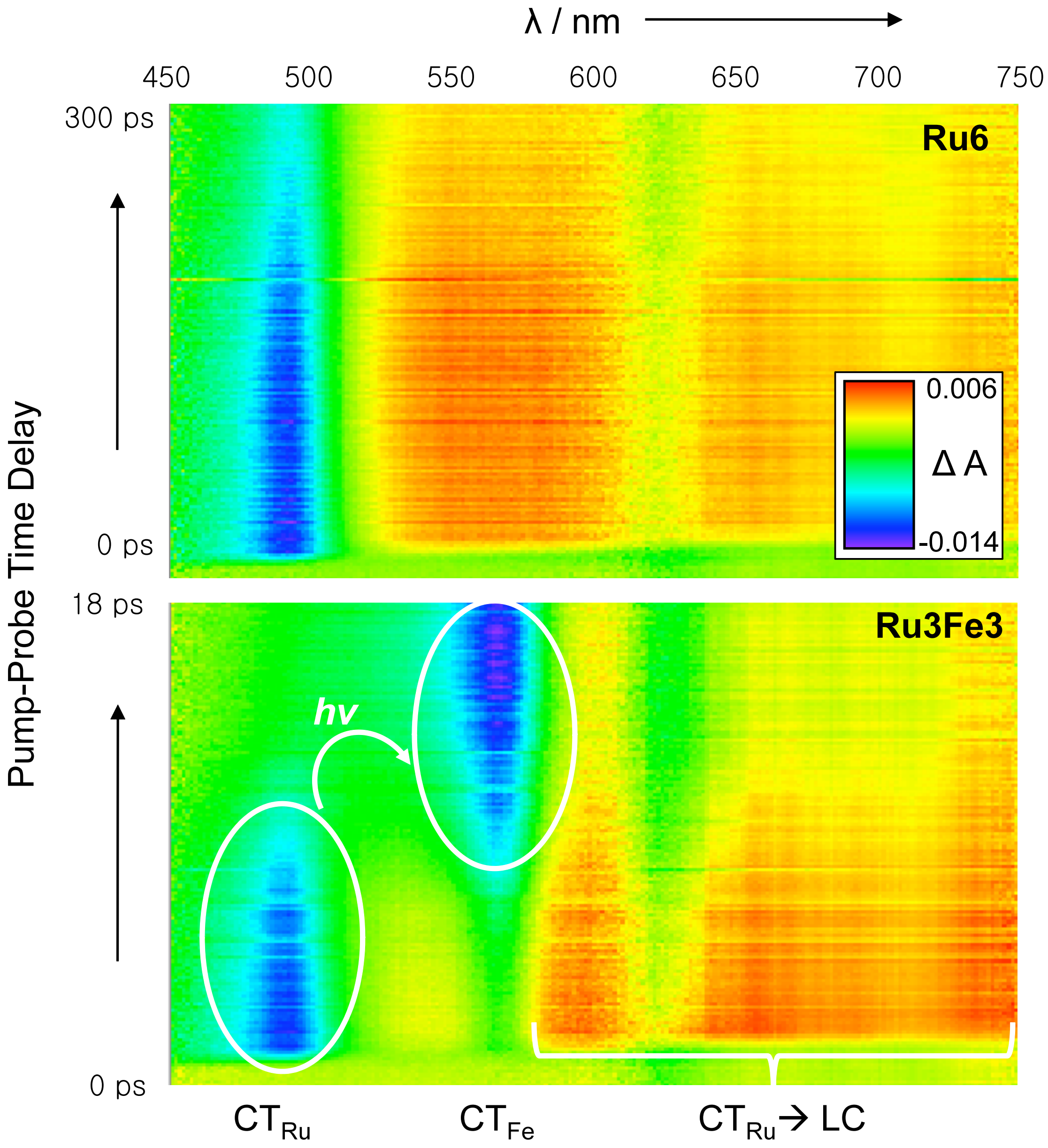

Figure 11-4. Two-Dmensional Plot of Femtosecond Transient Absorption Spectra of Ru6 and Ru3Fe3 in MeCN Under Excitation at 328 nm

The color panel indicates the ground-state bleaching (blue), no change (green) and excited-state absorption (red) bands.

On the other hand, the transient absorption spectra of Ru3Fe3 (figure 10-4 bottom) shows intense GB signals at CT_{Ru} after CT_{Ru} excitation, with GB at CT_{Fe} occuring shortly after. Also observed, at least during the lifetime of the CT_{Ru} bleach, was the same broadband ESA. The kinetics for the CT_{Ru} band provide two primary lifetimes, each readily attributable to a different relaxation process. The shorter time constant (1.8 ps) is indicative of a more immediate relaxation, most likely with a single RET "hop" to the iron and the longer lifetime (16 ps) being attributable to one or more RET "hopping" processes between Ru sites on the ring before being trapped by the iron moeity. It should be noted that the Ru6 sample showed even longer lifetimes, indicative of an even higher degree of hopping when an Fe 'trap' is not present. ESA lifetimes show the same kinetic behavior as the CT_{Ru} band, which should be taken as an indication that only CT_{Ru} excited states are able to be repromoted to the high energy ligand band. The transient ahsorption for the Fe6 sample showed know ESA in this region. This clarifies that only before relaxing into the 'trapped' CT_{Fe} band may $CT_{Ru} \rightarrow L$ transitions be achieved in the hybrid species. After initial excitation of Ru3Fe3, we observed the interconversion from $CT_{Ru}{}^* \rightarrow CT_{Fe}{}^*$ through the diminishing CT_{Ru} bleaching and increasing CT_{Fe} bleaching intensities. The rise time of the CT_{Fe} band has kinetics (2.3 ps and 19 ps) which map well onto the CT_{Ru} depletion times and indicates a low proabability that a intermediate state plays a major roll in this interconversion. The $CT_{Ru}{}^*$ to $CT_{Fe}{}^*$ interconversion process has its isosbestic point at 515 nm. After 14 ps, the bleaching signal of CT_{Fe} becomes more intense than that of CT_{Ru} and represents the point at which the $CT_{Ru}{}^*$/ $CT_{Fe}{}^*$ population inversion ends. In fact, from 68 to 300 ps, the spectral shape becomes preserved and closely resembles that of Fe6 at these times, both of which have $CT_{Fe}{}^*$ lifetimes beyond the range of our measurements (>10 ns). Thus, the ultrafast intensity change in the GB signals of CT_{Ru} and CT_{Fe} within several picoseconds conclusively shows strong exciton transfer into a trapped $CT_{Fe}{}^*$ state which prevents re-promotion through ESA (figure 10-5) and, when combined with steady state findings, has an efficiency near unity.

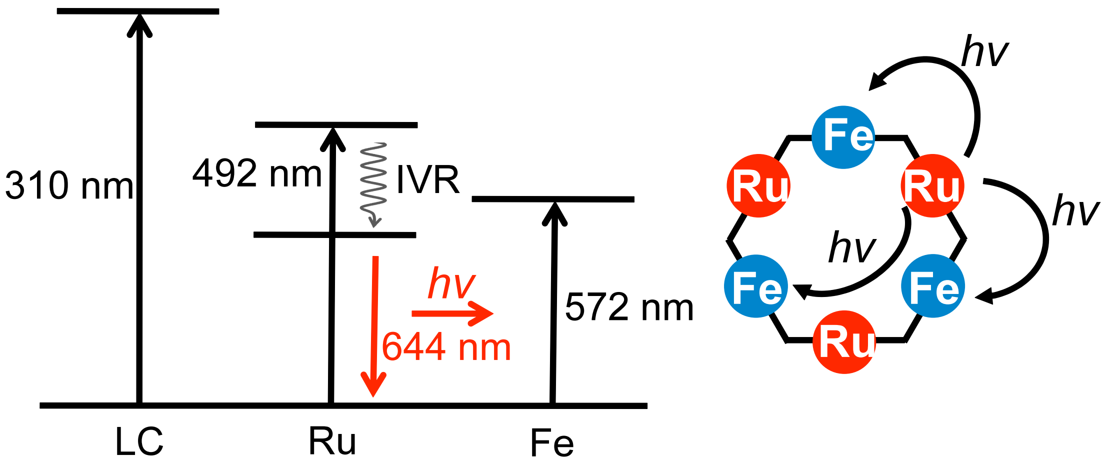

Figure 11-5. Schematic Energy Diagram of Ru3Fe3

To finalize our assertion that there is virtually no coupling through the π-conjugated ligands between the Ru and Fe moieties, we performed transient absorption with CT_{Fe} excitation (572 nm) on the Ru3Fe3 system (table 1). A strong, broad ground bleaching signal at CT_{Fe} was observed with only trivial bleaching in the CT_{Ru} band and was comparable to that observed at long times after CT_{Ru} band excitation as well as the Fe6 species. Additionally, no ESA of any kind was observed in transient absorption spectra (similar CT_{Ru} excitation after at longer times) which confirms that while CT_{Ru}→L transitions are allowed with ESA, the process of CT_{Fe} →L is forbidden.

11-7 Conclusions

In this study, we have observed the energy transfer processes in an all-donor (Ru), an all-acceptor (Fe) and multiple donor-acceptor macrocycle system. The quantum yield of energy transfer, close to 100 %, in the hybrid Ru-Fe hexamer, was determined to be mediated explicitly by RET. This RET is accomplished directly from Ru to Fe energy transfer or with a slighty slower process where additional hopping between Ru moeities occurs before eventual arrival at the Fe 'trapped' state. We display with this work that the individual components of which the macrocycles are composed can be self-assembled as architectures which provide either strong excited state absorption or singlet exciton trapping in homogeneous rings. In the case of the hybrid macrocycles, both properties can be obtained, with each dominating at different points during the excited state lifetime. It should also be noted that with photoswitching lifetimes in the ~10 ps range, and switching energies (ESA wavelengths) in the NIR, operating rates in the 10^9-10^{11} Hz range using relatively inexpensive light sources are a realistic possibility for the Ru3Fe3 system. We have also shown that a mismatch between the CT_{Ru} emission band and the CT_{Fe} absorption band does not hinder the aptitude for energy transfer in these structures. These properties give us a simple and elegant method for developing architectures from multiple donor-acceptor systems as a novel strategy for applications where photoswitching and efficient energy transfer is sought.

11-8 Experimental Section

Ultraviolet (UV)-visible absorption spectra were recorded with an Agilent Technologies 8453 spectrophotometer. Steady-state fluorescence measurements were performed on a Fluomax-2 fluorimeter. Femtosecond transient absorption was used to investigate the excited-state dynamics of the samples at different excitation wavelengths and the description of the system has been provided elsewhere.[15] In breif, a ~100 fs pulsed laser source is used to excite the sample (pump) and subsequently a ~100 fs pulsed white light source (probe) is applied to the sample and changes in absorption with time are recorded and compared to pre-pump response. Changes in time of separation are maintained with a translational stage in order to modulated probe pulse arrival times. The solution solvent for all samples was spectoscopic grade acetonitrile. Kinetic fitting and deconvolution were performed using Surface Xplorer and Origin 7.0 software packages.

11-9 References

(1) B. H. Northrop, Y.-R. Zheng, K.-W. Chi, P. J. Stang, Acc. Chem. Res. 2009, 42, 1554–1563.

(2) J. B. Gilroy, T. Gädt, G. R. Whittell, L. Chabanne, J. M. Mitchels, R. M. Richardson, M. A. Winnik, I. Manners, Nature. Chem. 2010, 2, 566 –570.

(3) B. M. Rosen, C. J. Wilson, D. A. Wilson, M. Peterca, M. R. Imam, V. Percec, Chem. Rev. 2009, 109, 6275–6540.

(4) U. S. Schubert, H. Hofmeier, G. R. Newkome, in Modern Terpyridine Chemistry, Wiley-VCH, Weinheim, 2006, pp 37-68.

(5) N. Tuccitto, V. Ferri, M. Cavazzini, S. Quici, G. Zhavnerko, A. Licciardello, M. A. Rampi, Nature Mater. 2009, 8, 41-46.

(6) I. Eryazici, C. N. Moorefield, G. R. Newkome, Chem. Rev. 2008, 108, 1834-1895.

(7) G. R. Newkome, P. Wang, C. N. Moorefield, T. J. Cho, P. P. Mohapatra, S. Li, S.-H. Hwang, O. Lukoyanova, L. Echegoyen, J. A. Palagallo, V. Iancu, S.-W. Hla, Science 2006, 312, 1782-1785.

(8) S.-H. Hwang, C. N. Moorefield, F. R. Fronczek, O. Lukoyanova, L. Echegoyen, G. R. Newkome, Chem. Commun. 2005, 713–715.

(9) Z. Li, W. Wu, Q. Li, G. Yu, L. Xiao, Y. Liu, C. Ye, J. Qin, Z. Li, Angew. Chem. 2010, 122, 2823 –2827.

(10) A. Stublla, P. G. Potvin, Eur. J. Inorg. Chem. 2010, 3040–3050.

(11) G. R. Newkome, T. J. Cho, C. N. Moorefield, P. P. Mohapatra, L. A. Godìnez, Chem. Eur. J. 2004, 10, 1493-1500.

(12) Z. Li, W. Wu, Q. Li, G. Yu, L. Xiao, Y. Liu, C. Ye, J. Qin, Z. Li, Angew. Chem. 2010, 122, 2823 –2827.

(13) M.J. Jezewska, R. Galletto, W. Bujalowski, Biochemistry 2003, 42, 11864-11878.

(14) J. P. S. Farinha, J. M. G. Martinho, J. Phys. Chem. C 2008, 112, 10591-10601.

(15) G. Ramakrishna, A. Bhaskar, T. Goodson III, J. Phys. Chem. B 2006, 110, 20872-20878.

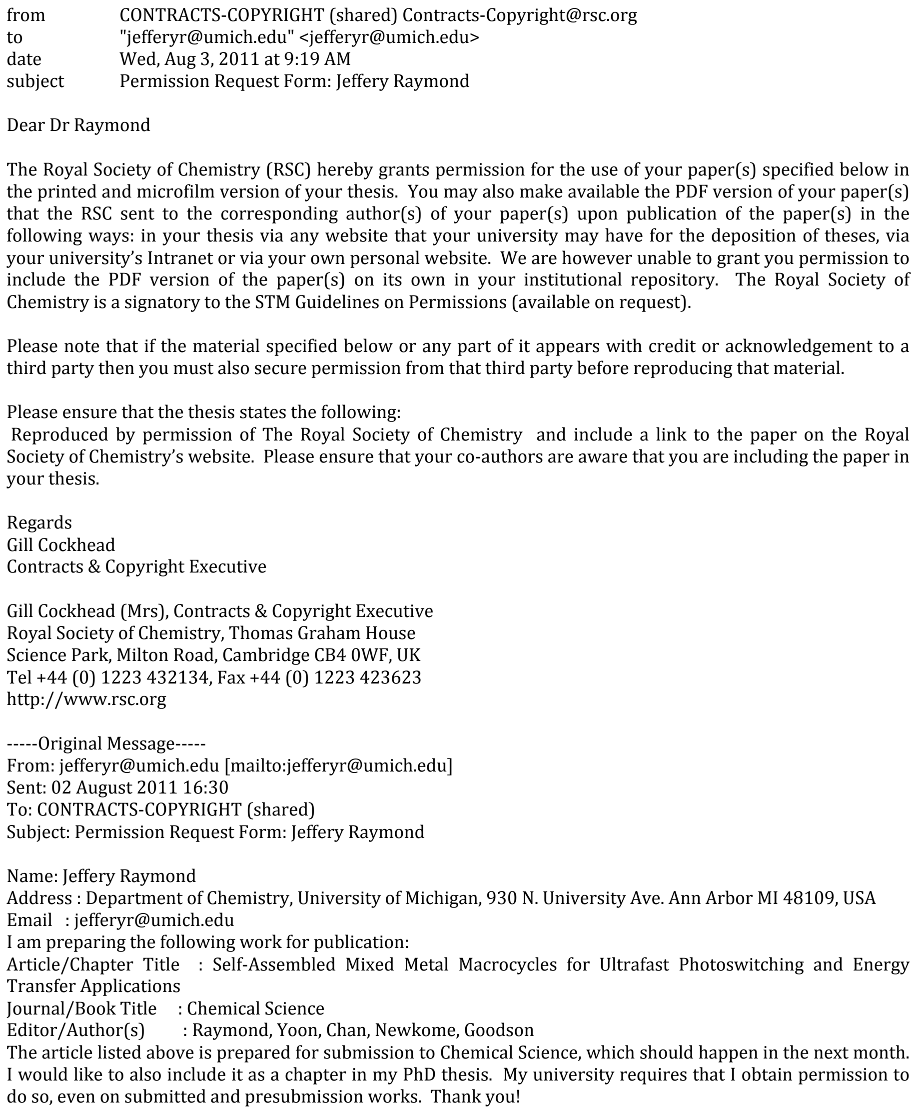

from CONTRACTS-COPYRIGHT (shared) Contracts-Copyright@rsc.org
to "jefferyr@umich.edu" <jefferyr@umich.edu>
date Wed, Aug 3, 2011 at 9:19 AM
subject Permission Request Form: Jeffery Raymond

Dear Dr Raymond

The Royal Society of Chemistry (RSC) hereby grants permission for the use of your paper(s) specified below in the printed and microfilm version of your thesis. You may also make available the PDF version of your paper(s) that the RSC sent to the corresponding author(s) of your paper(s) upon publication of the paper(s) in the following ways: in your thesis via any website that your university may have for the deposition of theses, via your university's Intranet or via your own personal website. We are however unable to grant you permission to include the PDF version of the paper(s) on its own in your institutional repository. The Royal Society of Chemistry is a signatory to the STM Guidelines on Permissions (available on request).

Please note that if the material specified below or any part of it appears with credit or acknowledgement to a third party then you must also secure permission from that third party before reproducing that material.

Please ensure that the thesis states the following:
Reproduced by permission of The Royal Society of Chemistry and include a link to the paper on the Royal Society of Chemistry's website. Please ensure that your co-authors are aware that you are including the paper in your thesis.

Regards
Gill Cockhead
Contracts & Copyright Executive

Gill Cockhead (Mrs), Contracts & Copyright Executive
Royal Society of Chemistry, Thomas Graham House
Science Park, Milton Road, Cambridge CB4 0WF, UK
Tel +44 (0) 1223 432134, Fax +44 (0) 1223 423623
http://www.rsc.org

-----Original Message-----
From: jefferyr@umich.edu [mailto:jefferyr@umich.edu]
Sent: 02 August 2011 16:30
To: CONTRACTS-COPYRIGHT (shared)
Subject: Permission Request Form: Jeffery Raymond

Name: Jeffery Raymond
Address : Department of Chemistry, University of Michigan, 930 N. University Ave. Ann Arbor MI 48109, USA
Email : jefferyr@umich.edu
I am preparing the following work for publication:
Article/Chapter Title : Self-Assembled Mixed Metal Macrocycles for Ultrafast Photoswitching and Energy Transfer Applications
Journal/Book Title : Chemical Science
Editor/Author(s) : Raymond, Yoon, Chan, Newkome, Goodson
The article listed above is prepared for submission to Chemical Science, which should happen in the next month. I would like to also include it as a chapter in my PhD thesis. My university requires that I obtain permission to do so, even on submitted and presubmission works. Thank you!

Figure 11-6. Email Transcript of Royal Society of Chemistry Permission Granted to Publish in Thesis

Chapter 12

Closing Remarks

This body of work constitutes a major advance in the fields of nonlinear optical enhancement, both at the macromolecular and solid state levels. It displays clearly that an empirically driven combination of ultrafast techniques and hyper-resolution imaging can rapidly assess functional organic materials for use in a variety of applications. This work represents a significant advancement of the per particle assessment of TPA materials by way of TPA-NSOM.

By controlled interactions between individual building blocks, environment and light, multiple order of magnitude NLO enhancement is obtainable. By careful construction of experimental techniques which target observation of these enhancements on the nanoscale, namely TPA NSOM, it is possible to rapidly assess ensemble effects and the structure-function relationships which drive them.

Appendix A

Two Photon Near Field Scanning Optical Microscope Standard Operation Procedure

Introduction

This manual is general guide to the use of a modified NSOM system, in conjunction with a Mai Tai fs pulsed laser system and an OPAL temperature tunable parametric amplifier, for the express purpose of generating shear force AFM and two photon NSOM images.

Basic Set Up

The operation of the CDP NSOM Multiscope system first requires a functional excitation source. Detailed below are 4 possible table set ups for delivering fs pulses at various wavelengths for two photon NSOM operation.

Mai Tai→ NSOM (**MN**)
Default Set-Up

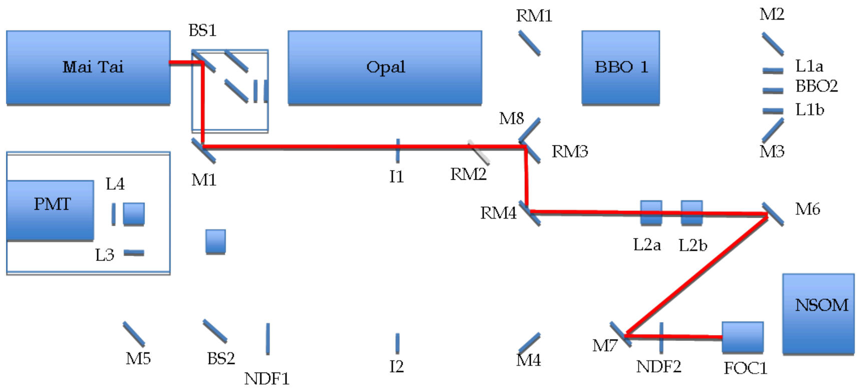

MN Configuration

This configuration is appropriate for delivering 690 to 1020 nm light to the NSOM coupler. It is accomplished via direct lasing from a Mai Tai fs pulsed laser.

Mai Tai → BBO → NSOM (**MBN**)

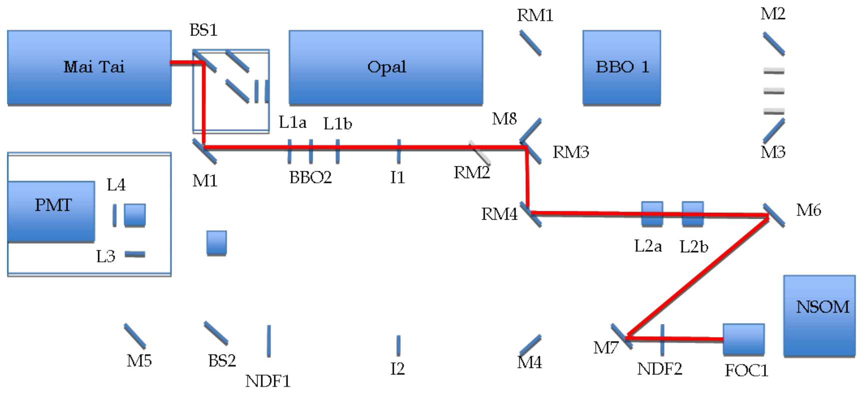

MBN Configuration

This configuration is appropriate for delivering 345 to 510 nm light to the NSOM coupler. It is accomplished by use of a Mai Tai laser source being applied to a nonlinear optical crystal (BBO) for second harmonic generation.

OPAL → NSOM (**ON**)

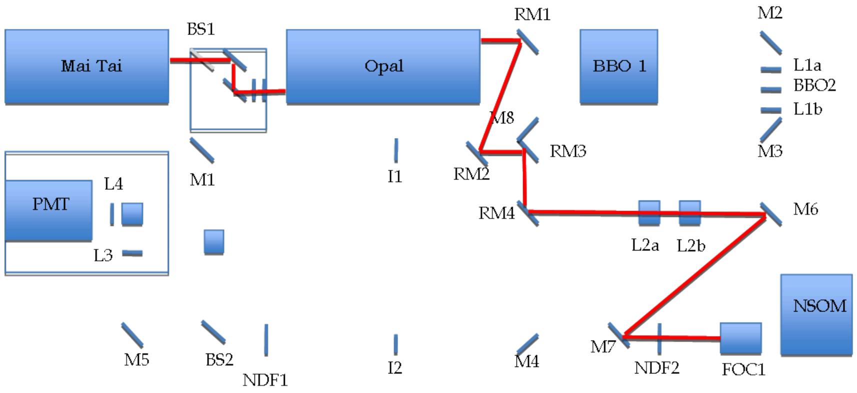

ON Configuration

This configuration is appropriate for delivering 1100 to 1500 nm light to the NSOM coupler. This accomplished by using a Mai Tai fs laser source to pump a OPAL parametric amplifier.

OPAL → BBO →NSOM (**OBN**)

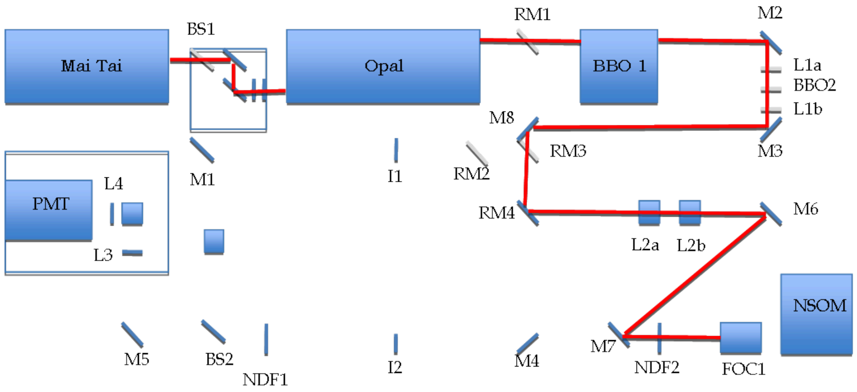

OBN Configuration

This configuration is appropriate for delivering 550 to 750 nm light to the NSOM coupler. It requires the use of a Mai Tai fs pulsed laser source to pump an OPAL parametric amplifier, with the subsequent OPAL output being up-converted via a BBO crystal.

In these configurations the proposed optics, which are in place as of the writing of the manual, are denoted with following abbreviations: BS- beam splitter, M-mirror, RM- removable mirror, I- iris, L- lens, NDF- neutral density filter, BBO- beta barium borate NLO crystal, FOC- fiber optic coupler.

General Operating Considerations

Specific notes about the experimental set up as used throughout the document:

1. The Mai Tai laser is extremely sensitive to any sort of back reflection. This is true to any sort of pulsed lasing system as any amount of disruption inside the inherently unstable cavity (where gain in the lasing media occurs) can result in collapse of mode-locking. This can be partially avoided by making sure that bulk adjustments of optics in the laser line are only made while the beam is blocked or the laser shutter is closed. Additionally, when cavity instability seems to be particularly problematic, one may also take the time to clean all optics in the beam path thoroughly before operation.
2. Coupling at the fiber is a long and tedious task. Also, day to day changes in the lasing conditions (humidity, temperature, vibrations) provide a scenario where a full alignment may be necessary often. Once a change has been made to the laser presets (ie prism and slit settings, as well as the PZT positioning mirrors) the current coupling is most likely out of alignment. This can most easily be tracked by keeping a good log of the laser output and settings as well as the maximum NSOM counts for a given intensity. A gross change (+/- 10% or more) should call for a physical realign at the fiber coupling device and the mirror just prior to the coupler. Any change of more than an order of magnitude most likely means that beam divergence has changed. This means that the columnating lenses prior to coupling should be adjusted as part of any full align process.
3. Individual probes can behave very different despite similar tapers, apertures, and fiber makes. This is due to slight variations in the core quality as well as a difference in the mechanical strain in a fiber. This results in very different behavior at the cleaved end despite a very clean cut (internal forces causing concave or convex cores). This means that the experimentor should try coupling both with and without the columnating lenses installed prior to coupling.
4. Using wavelengths greater than 850 nm can be problematic as the PMT is unresponsive at wavelengths greater than 850 nm, with notable drop off of sensitivity after 810 nm. This means that for longer wavelengths, one should accomplish alignment using either a thick film of a known TPA material at that wavelength or by using a BBO to up-convert the

excitation beam prior to imaging. However, as will be mentioned in the next comment, high energy light (<750 nm) should be very carefully modulated into the fiber as NLO effects and burning can occur.

5. The single mode fiber optics used for TPA-NSOM imaging are typically optimized for a specific wavelength, namely 780 nm, 810 nm or 830 nm. Regardless of the make, all of these fibers show reasonable throughput of pulses at 750 nm or longer. However, should higher energy photons be used, one must regulate the excitation judiciously with a neutral density filter. For 800 nm excitation, all incident intensities of 100 mW or below have been seen to be safe for extended operation. However, higher energy photons result in nonlinear response in the cable which can be interpreted falsely as true signal. Additionally, the opportunity for linear absorption processes to result in burning is grossly enhanced a lower wavelengths. Recommended coupling intensities are <5 mW for 650 nm-750 nm excitation, and <1 mW for light of shorter wavelengths than 650 nm.

Note that troubleshooting and operating the Mai Tai and OPAL systems is beyond the scope of this document. Please see the instrumentation documentation for more help with these systems.

Walk Through of Nominal Operation of TPA NSOM

This section is designed to provide a very general checklist for the day to day operation of the NSOM system.

1. Turn on the lasing sources to be used. Allow 30-90 minutes for the systems to reach equilibrium, especially in instances where temperature and humidity have been fluctuation since the last usage of the laser.
2. Open the NSOM box and inspect the tip distance from surface. If not already >1 mm from surface, manually adjust the tip to at least 1 mm from the surface. This can be done manually, or perhaps more safely, with the [Park] operation in the uScope software once it is open. Close the NSOM box.
3. Turn on the NSOM control box.
4. Open the uScope software for NSOM.
5. Wait 15-30 minutes for the NSOM to sit with high voltage (driving amplitude) on the probe tuning fork.
6. [Adjust] the probe in the uScope software to observe the current operating parameters. If you do not need to change samples or align collection, advance to step 25.
7. Record the initial parameters.

8. To remove the probe arm, perform the following in this order: raise the probe to at least 5 mm from the surface manually, unhook the probe leads from the microscope, remove the fiber bracing magnet, unscrew the mount screw while stabilizing the probe arm, remove the probe arm and place it on the probe arm holder, unclip the ground from the sample mount plate, remove the plate.
9. After replacing the sample, replace the plate and observe the sample under low magnification using bottom illumination.
10. Focus on the illumination source under the sample and center the top objective over it.
11. Switch to top illumination and focus on the substrate/sample.
12. Switch to high resolution objective and move the sample plate until a region of interest is centered in the field of view, turn off the illumination and remove the objective from over the sample.
13. Return the probe arm by way of the following steps: attach the ground cable without moving the sample plate, place the probe arm assembly back on the mount (gently), secure the fiber with a magnet without putting undue strain on the top of the fiber near the tuning fork assembly, reconnect the probe lead, secure the probe arm to the mount while attempting to keep the probe centered over the bottom illumination.
14. Using the jewelers lens and a small piece of plastic, gently tap the probe towards the surface until the probe reflection is visible.
15. Use the low resolution objective to be certain that the fiber is centered over the bottom collection aperture.
16. Connect the bottom aperture collection cable to the PMT.
17. Close the NSOM box and [Adjust] the system again.
18. [Contact Search] and then using the [double up arrow] to back off of the surface by 10 steps.
19. Turn on the PMT.
20. Place a power meter before the fiber coupler, and adjust the power to 1 mW.
21. Remove the power meter and optimize the coupling using the following iteration: adjust the y-z knobs on the fiber coupler, adjust the mirror prior to the coupler, adjust the z distance, repeat.
22. Everytime counts get higher than 1 million, decrease power and continue. Eventually power will be at a minimum for the neutral density filter's capability. This is when a filter should be inserted into the PMT to block much of the excitation beam.
23. Move power back up to a setting between 1 and 10 mW and repeat 21 and 22 until throughput typical of the current probe is observed.
24. If the researcher suspects a far field signal interfering with alignment, instead of a sample, use an aluminum foil covered slide with a very small pin hole poked in it to do alignment without the interference. If counts drop drastically in this mode, suspect gross misalignment or a damaged probe.

25. With alignment complete, [Contact Search] and allow the system to come to equilibrium (Z drift will stop occurring in the oscilloscope).
26. Choose initial scan parameters that confirm good feedback (2um x 2um and 200 pixels at 1 and 5 um/s speeds.
27. After confirming a reasonable feedback, image using larger fields of view at speeds capable of good emission collection and resolutions appropriate for the features being observed.
28. [Save Scan] should be done after each scan, regardless of the image's viability in order to keep an effective record of scan quality.
29. After usage, [Park] the probe twice, turn off PMT, turn off the NSOM control box and block the laser beam.
30. Power down the excitation sources only after recording the final settings and outputs.

Working in the uScope.exe Console

Understanding how to manipulate the NSOM interface is critical to successfully imaging with this system. Specifically, the TPA NSOM functionality will only be as useful as the AFM quality allows it to be. Ultimately, being able to keep the probe close to the surface and have a well defined topography is going to dictate how well the system elucidates structure/function in a nano- and micro- material.

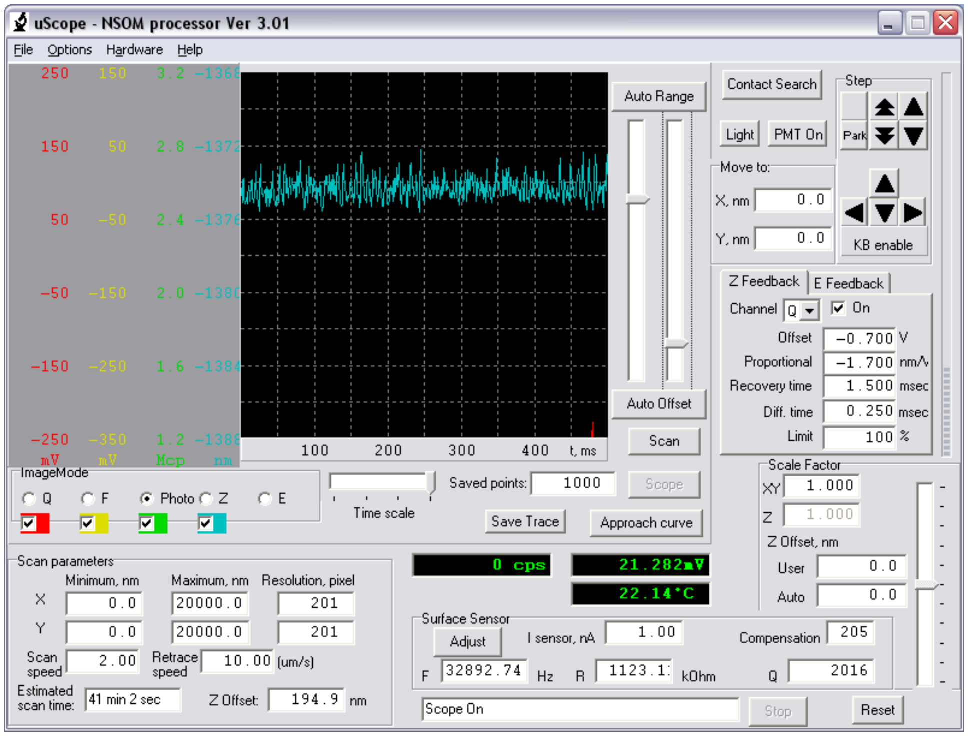

Move to:
X, nm 0.0
Y, nm 0.0

Channel Q ☑ On
Offset -0.700 V
Proportional -1.700 nm/V
Recovery time 1.500 msec
Diff. time 0.250 msec
Limit 100 %

XY 1.000
Z 1.000
Z Offset, nm
User 0.0
Auto 0.0

ImageMode
○ Q ○ F ● Photo ○ Z ○ E
☑ ☑ ☑ ☑

Saved points: 1000

0 cps
21.282mV
22.14°C

Scan parameters

	Minimum, nm	Maximum, nm	Resolution, pixel
X	0.0	20000.0	201
Y	0.0	20000.0	201

Scan speed 2.00
Retrace speed 10.00 (um/s)
Estimated scan time: 41 min 2 sec
Z Offset: 194.9 nm

I sensor, nA 1.00
Compensation 205
F 32892.74 Hz
R 1123.1 kOhm
Q 2016

Scope On

Control Panel for the uScope NSOM Software

The most obvious feature in the console is the digital oscilloscope. It can be selected to show Q, F, Z, and Photo channels. Typically, the Z and Photo channels will be the only channels taken into consideration when operating the NSOM. Scale values are displayed to the left and a scale and range adjustment slider can be found to the right, as well as a [Auto Range] button and [Auto Offset]. To switch between channels use the image mode circular buttons. The check boxes below the channel switching buttons dictate which channels the oscilloscope shows and which channels will be recorded during imaging. There is no good reason to ever turn these off. The time scale bar underneath the oscilloscope is just that, and can be slid to give different views of the readings at different time ranges. The number of points it shows is also something one could change, though 1000 seems to work just fine.

In the bottom left corner are the scan parameters. These dictate how fast a scan goes, how much surface to scan, the number of measurement points that will be taken on each line and the number of lines to scan. X-Y minimum and maximums will show the field of view. Settings up to +/- 20000 may be set, though typically this size of scan takes prohibitively long. Typical start values are 0→5000, 0→5000. Because of the nature of image manipulating software, it is best to be symmetric in set point selection. Also, it is good to select pixel values that divide the field of view into reasonable pixel sizes. A good start point is 250 for a 5um x 5um scan (20 nm/pixel). Because of the nature of the probe, scan speed/retrace speed set points should never be more than 2 for scan and 10 for retrace. These values are the number of um per second the probe will cover. For the best AFM and NSOM resolutions, slower is better. A good start point is 1/5. Time estimate is calculated based on the settings selected and the Z Offset is an arbitrary zero value for height which need never be adjusted as the offset is determined by the software itself.

The surface sensor panel is set in the lower left. An initial point of caution: never press the [Adjust] button unless certain that the probe has been parked once. [Adjust] is an action you will need to perform in order to determine your probes frequency and Q factor. The resulting R is a function of Q factor and I. I, the current, is typically the only number you will adjust in this panel. It is the current set point for operating the probe and can be thought of as the driving force/amplitude of the probe. Empirically, by changing I and observing the change in small features at high resolution, it has been observed that for most probes the amplitude of the tip oscillation is about 1 nm for every 0.7 nA. While CDP suggests setting of 4-8 nA, of 1.5-6 nA have worked with this system. For most probes, 2.5 nA is a good starting point, going higher for large area scans at low resolution. After adjusting, it is okay to take down the compensation, usually set near 205, down a few points (2-3). The compensation is a prescaling factor and magnifies signal. In a noisy environment, adjusting the compensation down one or two points can decrease the likelihood of a outside event accidently halting your scan with a error regarding the signal. Moving this number down more than 4 is not suggested.

Above the surface sensor panel is the scale factor panel. Technically one could scale all imaging immediately here if there was a need. It has never been used in this laboratory.

Above the scale factor panel is the feedback panel. This is a very important part of the interface as the settings determine the final quality of a scan and an incorrect setting can lead to probe breakage. First, only ever use the Z feedback tab (the other tab is meant for STM scanning). Also, a user will most likely only ever use the Q feedback channel. The F feedback channel can give reasonable images, but is prone to going to contact at fast scan speeds and large pixel sizes. The Offset value translates into a required amount of force. For fiber probes, it should always be negative. This negative value means that the probe is positioned outside the region of strongest van der Waals interaction (farther from the surface). The instrument then feels an attraction which registers as a negative voltage. The Offset will dictate the distance from the surface the probe attempts to maintain while scanning. If set with too high a magnitude, the risk of snapping away from the surface exists. If set to low, probe-surface contact could be made. A good start point for a given probe is -0.8, then adjust if the to higher magnitudes if there are surface contact errors from the software and adjust to lower magnitudes if during a scan the surface is lost. CDP suggests a value of -0.3 to -2.5 V, though the author has not used higher than -1.2 V. The proportionality is the amount of Z movement that comes with changes in voltage. As the piezo tubes that control the Z height only can handle a certain amount of voltage, the proportionality effectively limits maximum z heights that can be measured. The higher the value, the larger the height profile. Conversely, the fineness of the z resolution is dictated by this value such that the lower the value the finer the z steps and the better the height profile accuracy is. For looking at fine structure, a low setting of -1.0 nm/V is appropriate. For larger z values and less fine measurements, -2.0 nm/V has worked well. At a setting of -2.5 nm/V heights of 1 um have been obtained. The diff. time is just the time to obtain a certain gain in voltage (rate of voltage/z change). For typical operation values of 0.1 to 0.5 ms can be used, though the lowest you can work with the better. Therefore, most operations will take place at 0.1 ms unless one is performing a slow, high resolution scan of small features. Then closer to 0.5 is better. Limit value is just a set point for how much of maximum voltage can be applied to the z piezo. It should be left at 100%. Last, the On button. After [Adjust]ing a probe, a feedback channel must be selected and turned on before contact mode and imaging can occur. Check the box to engage the feedback channel. Note, when this happens the microscope control panel until the blue bar to the right of the feedback channel stops moving.

Finally, there are the step buttons. These are the most dangerous buttons to push and should be understood fully before using. The four directional arrows over the KB enable button should never be touched when the probe is anywhere near the surface. These buttons represent x (left-right) and y (up-down) stage translations and if touched at or near contact, the probe will be damaged. The author recommends never using the KB enable button as it makes the arrow buttons on the keyboard do x-y translations as well, making it even easier to break a probe through accidental engagement of translation. Above this is the step panel. This panel controls z height and should also be treated with the utmost care. Double arrow up raises the z height continuously. This is not dangerous. Double arrow down should not be used unless the user is watching the tip through the jeweler's lens. This is a viable method for approaching contact if one is uncomfortable with tapping the probe down. The arrows up and down do a single 1 um step up and down. The park button is a macro that takes the probe 50 steps up from the surface and should be pressed preferentially when breaking contact mode. Next to this channel is the PMT on/off button (needed for NSOM) and the Light button, which turns on a small light in the microscope hood for operating in the hood while the lights are off. The Contact Search button is the only button that should be used when going from above the sample to the sample. It automatically seeks out the Offset voltage and should be taken as the only way to obtain contact mode.

Final Notes

Spend some time with blank substrates or standards when first working with this system. From probe to probe, the optimum operating parameters can be very different. Spending some time to tweak your I, Offset, scan speed and Proportionality settings can pay off in terms of safe probe use and saving time.

The force between the tip and the surface changes on different surfaces. Glass is the presumed standard, but mica and polymer films should be anticipated. Mica will have a higher surface energy and it may be appropriate to use a higher offset magnitude, while polymers have lower surface energies and can require lower offset magnitudes. Also, if the sample is wet or the material on the substrate has weak intermolecular interactions to the substrate. This will mean that you should have the scan and retrace speeds the same so you don't drag solvent and/or material with your retrace. Also, slower is better here.

The software does not like huge steps. Any setting near a 10 um scan size with 100 or less pixels may fail. Also, when scanning greater than 1 um, speeds of less than 0.5 um/s may not work.

Selecting filters for the PMT is a critical part of emission imaging. Typically a low pass cut off filter with OD>8 at 700 nm or above should be used. These can be stacked if needed. If trying to image a specific emission band in a system where there are two emissions, use a low pass filter that cuts off higher wavelength emission or a high pass filter that cuts off lower wavelength emission. When doing absorption imaging it may be necessary to use a filter to decrease the overall counts below the nonlinearity threshold of the PMT, which begins at 1 million.

It is the author's opinion that a new user make two alignment slides. One should have Al coating with a small pinhole in it to do alignment slighty above contact. This will block fiber bleed and lead to a better alignment over the bottom collection aperture. The other slide should be a heavily dye doped polymer thin film. This will give a bright response to excitation and, with three low pass filters in place, will guarantee that the light reaching the sample is from the aperture. This is due to the low flux of any far field excitation incident on the film being too low to trigger emission.

Finally, pay attention to the physical effects of the laboratory space. Any solid object bridging the ground and the air table will wreck havoc on the AFM. Typically, sub-microsecond vibrations exist in the floor do to cooling pumps, fans and building air handling. These can be readily observed in the oscilloscope if you choose the right time frame, as in figure A-6. Another possible cause for irregular signal at contact is the AFM ground. The ground cable comes out of the back of the NSOM and is the only one ending in bare wiring. It should at all times be in contact with the table. Also, running additional leads to the table from other grounded sources can increase the grounding of the AFM. Any sharp and asymmetric oscillations in Z mean a periodic surge is causing the probe to leap violent toward and away from the surface. When this occurs, check all grounding sources and try new configurations until the signal goes away.

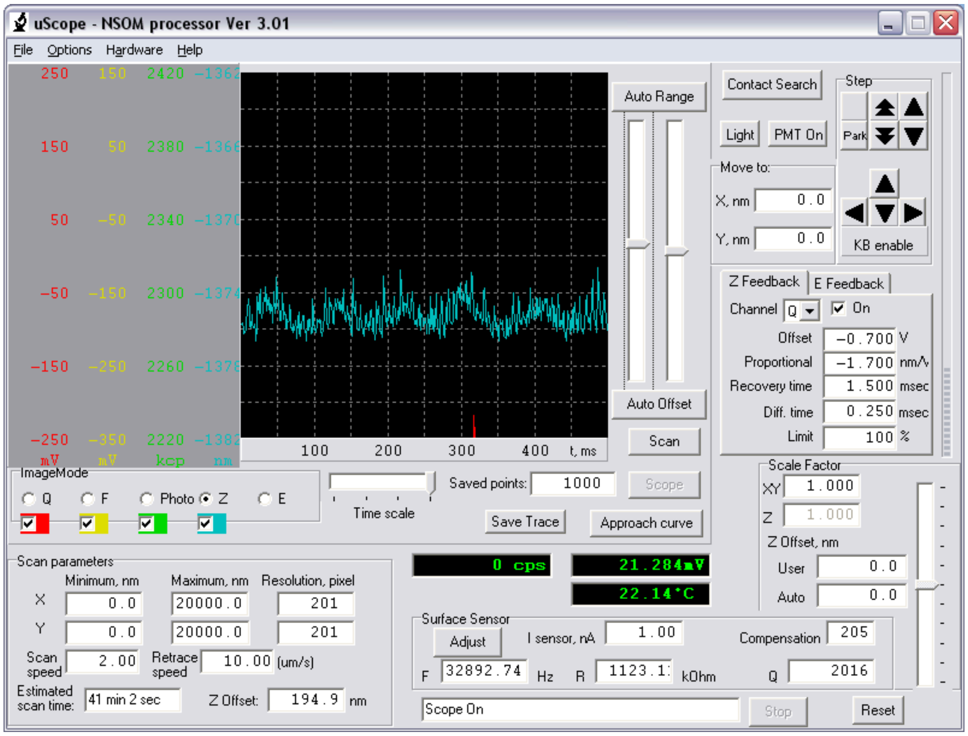

ImageMode: ○ Q ○ F ○ Photo ● Z ○ E ☑ ☑ ☑ ☑

Saved points: 1000

Move to: X, nm 0.0; Y, nm 0.0

Channel Q ☑ On

Offset −0.700 V

Proportional −1.700 nm/V

Recovery time 1.500 msec

Diff. time 0.250 msec

Limit 100 %

Scale Factor: XY 1.000; Z 1.000

Z Offset, nm: User 0.0; Auto 0.0

0 cps

21.284mV

22.14°C

Scan parameters

	Minimum, nm	Maximum, nm	Resolution, pixel
X	0.0	20000.0	201
Y	0.0	20000.0	201

Scan speed 2.00 Retrace speed 10.00 (um/s)

Estimated scan time: 41 min 2 sec Z Offset: 194.9 nm

Surface Sensor: I sensor, nA 1.00; Compensation 205

F 32892.74 Hz R 1123.1 kOhm Q 2016

Scope On

Effect of a Plastic Board Leaning Against the Air Table 3 m from the NSOM

Appendix B

Generation of Small Aperture Fiber Optic Probes for TPA-NSOM

Introduction

This appendix is meant to provide guidance for the construction of uncoated fiber optic NSOM probes with shear force AFM capabilities. The information contained here was largely obtained empirically through use of the CDP MoScan Multiscope System. This document is a reproduction of the standard procedure for probe production and the vernacular is chosen to increase approachability of the techniques outlined to a novice/non-expert user.

All techniques and guidance are provided in an informal format for reference to future users of the system and should not be taken as the sole available mode for construction of NSOM probes for this system. This document also assumes that the user is at least passingly familiar with usage of the NSOM system. A supplementary document to the CDP instruction manual has been generated elsewhere to assist users (Appendix A). Specifically, a method for generating a functional shear force AFM probe using the assembly provided by outside vendors and in-house pulled fiber optic tips will be given. An assumption that functioning or once functioning AFM probes which have lost NSOM functionality are available is made.

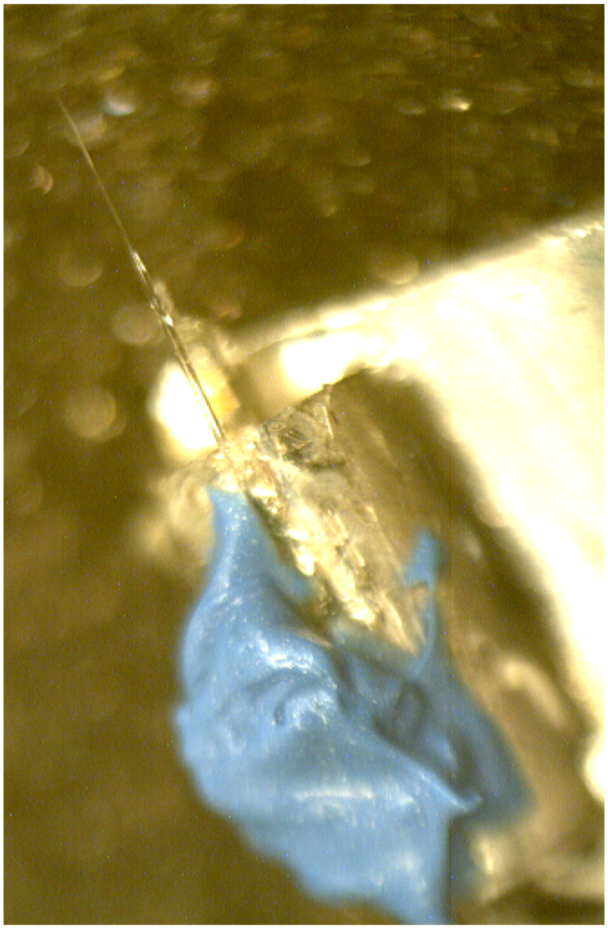

Finished TPA-NSOM Probe

Nomenclature for this Document

Fiber	the entire fiber optic cable, including the tip
Tip	the tapered end of the fiber optic cable where the aperture resides
Housing	the metal cylinder inside of which the tuning fork is bound to the voltage leads
Tuning Fork	the quartz tuning fork attached to the voltage leads
Binding	the cross bar which tethers the tuning fork to the tip/fiber
QSE	quick set epoxy (super glue)
TPE	two part metalated epoxy (plastic weld)
SGM	silicone gasket material
[A]	the adjust button (software panel)
F	frequency of the tuning fork, in Hz (software panel)
I	applied amperage at the leads (software panel)
Q	quality factor, at these frequencies should be taken as the FWHM for the frequency distribution divided by F (software panel)
C	compensation factor, a linear number applied by the software to scale the Q signal to operating parameters in the software (software panel)
R	resistance applied at the leads to generate the specified amperage at the tuning fork coupling (software panel)
SW	software, specifically uscope.exe provided by CDP Inc.
SWP	software panel, the interface observed on the NSOM controlling computer
Assembly	the leads, plug, plate, casing and tuning fork as a single unit, obtained from an outside vendor
Probe	a functioning NSOM probe, includes the assembly, fiber and binding
Leads	the voltage and feedback leads which plug into the NSOM and connect to the tuning fork
Plate	the aluminum piece to which the casing and leads are bound which screws into the arm when a probe is in use
Plug	the terminal of the lead which interfaces with the NSOM
Adhesive	general term for the QSE/TPE/SGM layering which secures the fiber to the outside of the casing in a finished probe
Tack	a very, very small amount of QSE used to attach the binding to the tuning fork, the binding to the fiber, or the fiber to the casing
Arm	The metal rod to which the plate is screwed
Mount	The arm, attached to the base which sits on the NSOM post
Post	The central component of the AFM z-control module, which rests on a ceramic core
Clamp	table mounted clamp for securing a probe
High Res	high resolution setting for the optical microscope (x20 lens)
Low Res	low resolution setting for the optical microscope (x10 lens)
Cam	microscope mountable digital camera
Cam SW	software for capturing digital images, ScopePhoto

Examples of Construction Materials

QSE (left), TPE (center), SGM (right) and a hobby knife (bottom).

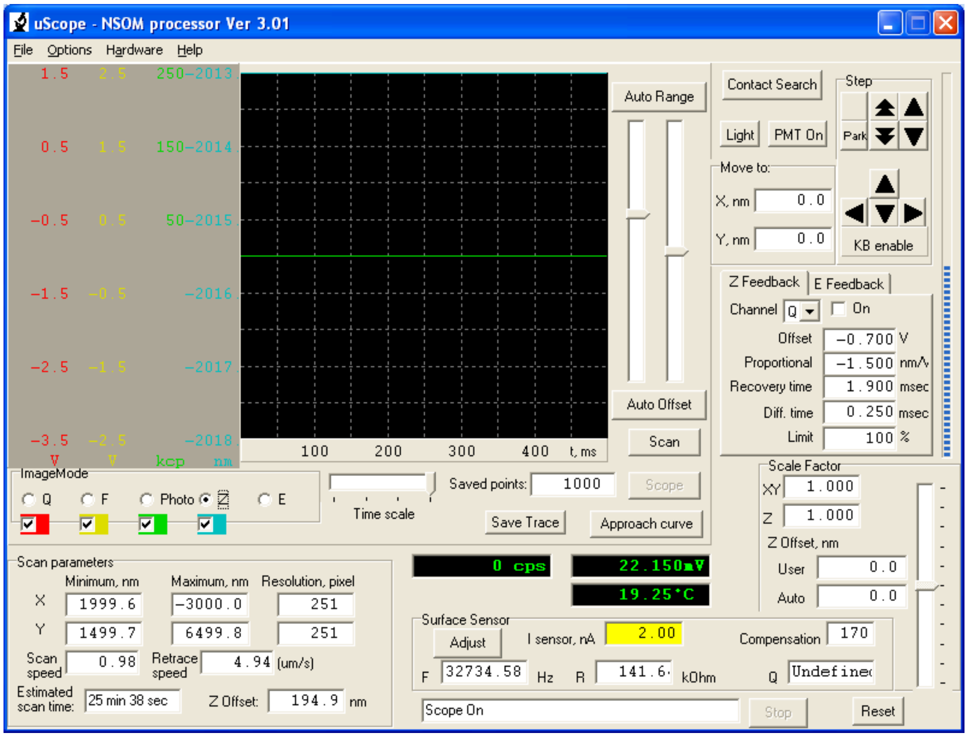

ImageMode: ○ Q ○ F ○ Photo ● Z ○ E

☑ ☑ ☑ ☑

Move to:
X, nm 0.0
Y, nm 0.0

Channel Q ☐ On
Offset -0.700 V
Proportional -1.500 nm/V
Recovery time 1.900 msec
Diff. time 0.250 msec
Limit 100 %

Saved points: 1000

Scale Factor
XY 1.000
Z 1.000
Z Offset, nm
User 0.0
Auto 0.0

0 cps
22.150mV
19.25°C

Scan parameters

	Minimum, nm	Maximum, nm	Resolution, pixel
X	1999.6	-3000.0	251
Y	1499.7	6499.8	251

Scan speed 0.98
Retrace speed 4.94 (um/s)
Estimated scan time: 25 min 38 sec
Z Offset: 194.9 nm

Surface Sensor
I sensor, nA 2.00
Compensation 170
F 32734.58 Hz
R 141.6 kOhm
Q Undefined

Scope On

Example of the Microscope Control Panel

Note that during the construction phase, the primary region of interest is the bottom right "Surface Sensor" region where I can be adjusted and F, R, C, and Q can be observed. Located here also is the "Adjust" button, denoted as [A] in this text.

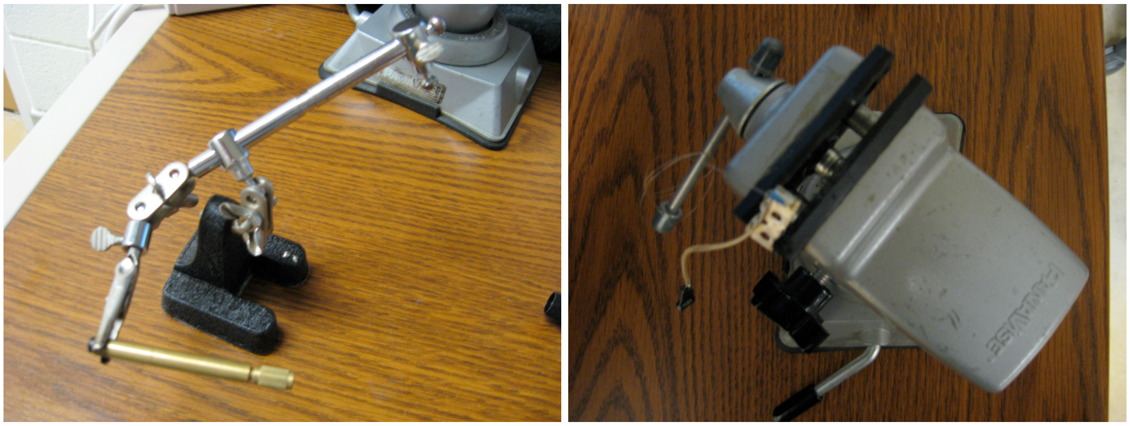

Table Top Tools for Probe Fabrication

The clip arm assembly with fiber holder attached (left) and the clamp with probe assembly held within the vise (right).

Selecting an Assembly

The first order of business when building a probe is to make sure you have a tuning fork that is working correctly. You should check the probe out by attaching it whole to the instrument and press [A] to get the specifics on the functioning probe. Reasonable values in the SW panel are as follow:

F	25000 – 35000	32000 typical
C	100 – 250	215 typical
Q	500 – 4000	2000 typical
I	set to 2.00 or whatever I setting you used during operation	
R	varies vastly based on tuning fork and I setting	

If you know that the current probe works for AFM, or recently did, note these settings and the I for operation. If the previously viable I returns a [Q could not be determined] message, try a higher I setting. This should be done in increments of 0.2 until you obtain a Q value from [A].

The I setting is directly proportional to the amplitude of the tuning fork operation and can be thought of as the oscillation strength. Therefore a setting of I that is too low will not provide enough signal to determine the Q factor of a probe. Even if Q can be determined, a low I setting may make the probe too sensitive to background noise during oscillations. This can lead to software failure messages, images with high Z drift or damage after a failure message. However, an unnecessarily high I setting will risk a voltage failure from the microscope. Additionally, larger than needed oscillations result in large tip dithering which negatively impacts the AFM x-y resolution as well as any optical images generated. A large dither may also provide greater opportunity for probe contact/damage during scanning, especially when scanning at high speeds or with large pixel sizes. Typically an I of 4 or less is used.

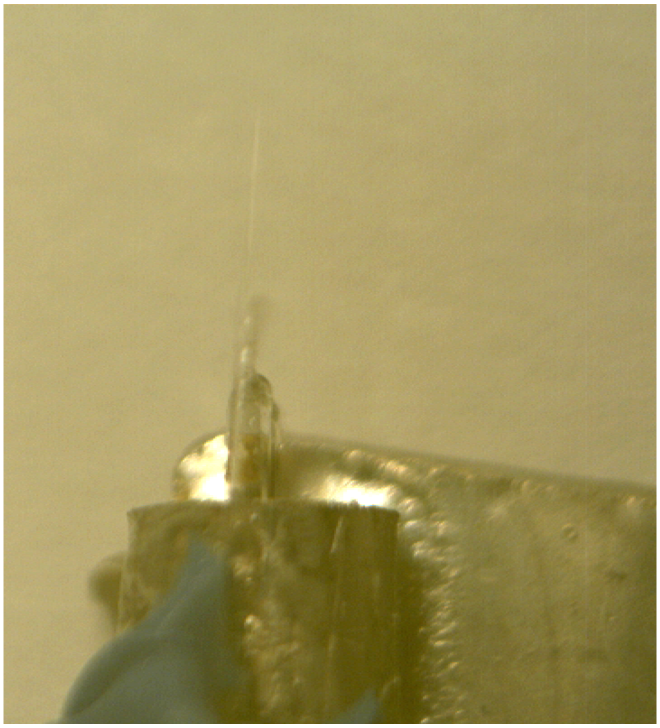

Functional AFM Probe

A functional AFM probe which has lost NSOM functionality.

Probe Clean-Up

Tip Removal. Ideally, you will reuse your binding and just “pluck” the fiber away from the binding. This is assuming you have a tuning fork that you know will provide decent AFM. This operation should be under low res magnification so you can pull the probe from the binding in a direction that does not force the binding to snap and you can see what direction the pull should be performed at. Feel free to use the Cam if needed and watch your movements on the computer. Note that when plucking the fiber there are two attachment points. The first is at the binding wire and is the easiest to break from. The second is at the adhesive. The adhesive is very tough - you will not be pulling the fiber whole from the adhesive bond. Instead, you will be snapping the fiber off at the base of the adhesive bond. This can be done most easily with a set of fine tweezers or with careful use of a fine blade. Even with great care, you may not successfully retain the binding. Should some binding become damaged/detached in part you can try to remove any residual binding that is still attached to the tuning fork if you want, though it may not be worth the risk. If attempted it should be done with even greater care than the probe-binding removal. If you choose to attempt removal of the residual piece of the binding, DO NOT make contact with the tuning fork directly – any physical contact can ruin the frequency of operation or detach it. The residual binding mass will have a trivial effect on the probe though the asymmetry it adds may effect the Q factor to some degree. Either way, you should not attempt to remove any tack left on the tuning fork – that is there to stay. Rather, expect to tack any new binding on top of the current tack, or next to it.

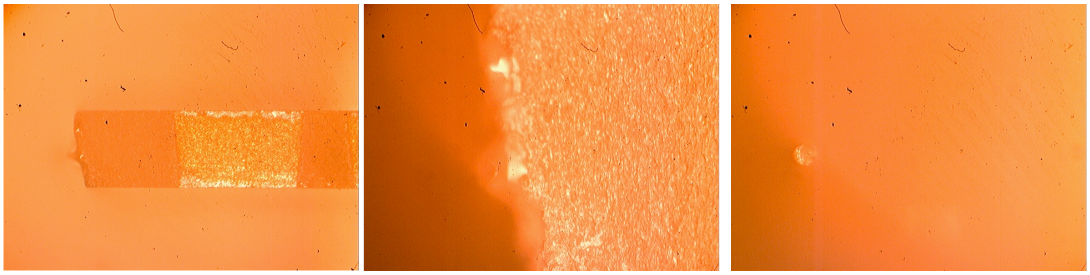

Tuning Fork with Binding

A tuning fork with binding (left), a high resolution image of the binding at the fork tip (center) and a high resolution image at a higher focal point showing the binding end (right).

Confirm Fork Viability. After removing the fiber and/or residual binding, attach the probe back into the NSOM and [A]. When calibrating a naked quartz tuning fork, expect Q factors in the range of 5000 to 10000. If you notice Q seems low, ramp up the current as detailed above. The current at which the Q factor stops changing is most likely the lowest operating current for reliable use of that tuning fork. Make a note of it. If you see that the Q could not be determined, this is because the amplitude is not sufficient. Again, ramp the current. However, an abnormally high current (>4) may be a sign of a bad coupling between the fork and the leads.

Technically, this could be fixed, but the author has not done so to date. Avoid using forks which require this level of current, though AFM from probes built off of forks requiring I=6 have worked in the past.

Clean Casing. When reusing tuning forks, make sure to clear all previous adhesive from the protective outer casing (metal). This should be done with the probe still attached to the arm and the mount in a table clamp. Snap off the tail end of the fiber if it is still attached to the casing. Use tweezers to remove and the SGM to the best of your ability. Then use a combination of tweezers and a sharp, small blade to remove the tougher epoxy resin layers. This will require precision and a fair amount of brute force. However, be very careful. It is extremely easy to slip, with several disastrous results possible: (1) The binding could be bumped off, a minor difficulty, but one that will add a lot more time to the process later. (2) The tuning fork could be touched, changing its properties or snapping it off all together, ruining that assembly. (3) There is a good chance that you could cut yourself if you slip. (4) You could sever the leads, which might be fixable, but has not been attempted by the author to date. Inspect the casing after cleaning by microscope to confirm cleanness. Scrape further if necessary. If there is any suspicion that you may have come in contact with the binding or forks, perform [A] again and note differences. Fork quality confirmation prevents a waste of time and resources on a probe that will never work correctly.

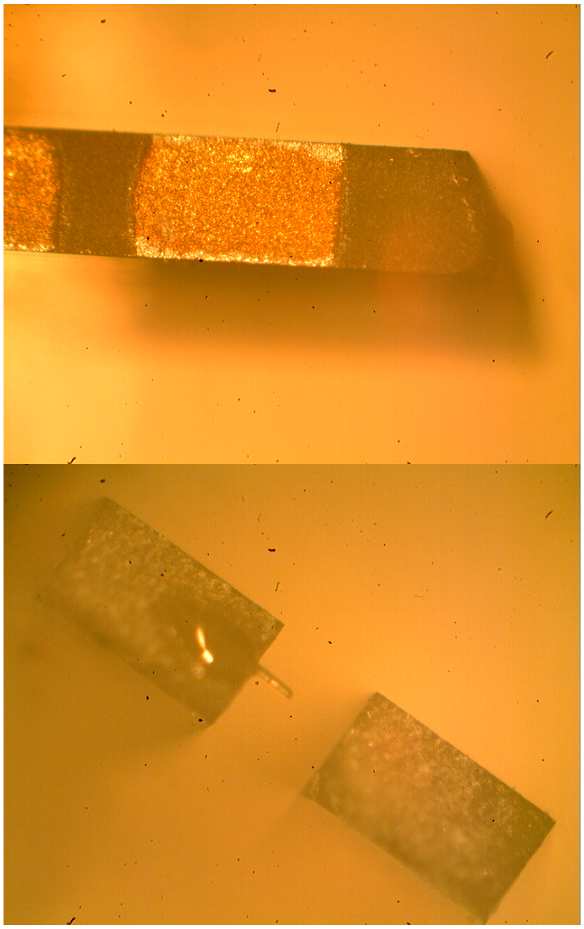

Reused “Naked” Tuning Forks

Examples of a reused tuning fork from the side (top) and looking at the end faces of the tuning fork (bottom). Note that the binding which would normally stick out is not protruding in the side view. The bottom view informs us that it was not saved from the previous probe. The residual adhesive remains, as well as some of the previous binding. If necessary, the binding could be removed, but the author is inclined to leave it due to the location. The adhesive should NOT be touched.

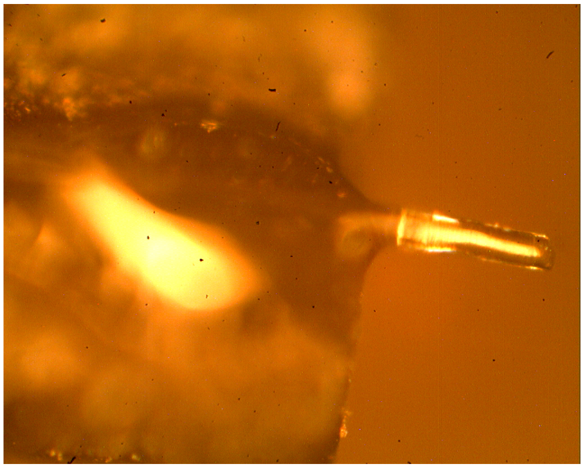

High Magnification of Residual Binding

Image (x200) of the residual binding, where a stripped F-SF fiber was used as the binder.

Selecting and Attaching a Binding

If you were able to retain a previously viable binding through the tip removal and cleaning processes, then this step is not needed. However, if your fork lacks a binding you must now attach one. This is done with QSE as tack and should be performed under the microscope, preferably with the Cam.

Positioning the Assembly. Position the assembly on the mount in such a way that the tuning fork is parallel to the ground. This sideways configuration has proven the best for getting a perpendicular binding and can be accomplished by unscrewing the arm enough to be able to rotate the assembly 90 degrees. Using low res, bring the side of the upper most tuning fork into focus so that the tuning fork end is visible.

Selecting a Binder. There are couple of materials that have been used successfully for binders. Specifically, nickel, tungsten and aluminum alloy wires of very small size diameter (0.001 inch). The author is uncertain which materials the original manufacturers used. However, the author has found that stripped fiber optic cable cleaved to a very short length works very well. It is possible that the material properties of a fiber binder-fiber tip provide for better coupling of signal to the tuning fork during contact. Two lengths have proven to be successful for binding. The first is one where the binder is long enough to span somewhere between one half of the tuning fork, plus the distance to the position where the fiber will lay (~1.5 mm). One half is an approximate distance – successful binding has been accomplished with binders spanning an entire fork to less than one quarter of the forks bottom face. This single fork binding provides the lowest change in Q, but is more difficult to lay perpendicular to the fiber and flush with the tuning fork and is also quite fragile. The second option for binding is where the cut binder is closer to 3 mm long, sufficient to span both fork bottoms and reach the fiber. This provides for easier positioning, but runs the risk of needing higher amperage to get similar signal.

Tacking (Single Fork). For the shorter binding to a single fork, disperse some QSE onto a clean surface. Using a single hair on a paint brush, obtain a small amount of QSE and, using the Cam, apply a small amount to the end of the fork to which you are binding. Less is better, as any major change in the mass/symmetry of the tuning fork can render it unusable or require increased I to operate. Quickly, before the fork QSE sets, use tweezers to pick up your binding. Using the same brush hair to apply a small amount of QSE to one end of the binder. Carefully place the binder onto the fork, using your eyes and the Cam to assure that the probe is perpendicular to the fork and reaches far enough past the casing to bind to the fiber later. Monitor the binder while it dries, making sure that it remains oriented correctly. If it should begin to shift, use a thin flexible material (like a stripped length of fiber optic cable) to adjust it back into position through small, gentle nudges. This is the authors preferred method.

Tacking (Double Fork). For the longer binding to two forks, disperse some QSE onto a clean surface. Using a single hair on a paint brush, obtain a small amount of QSE and, using the Cam, apply a small amount to the end of both forks. You will need even less than the single fork, as the two tack points will provide a much more stable placement. Again, before the fork QSE sets, use tweezers to pick up your binding. Using the same brush hair to apply a small amount of QSE to one end of the binder, neglecting the mid-section which will rest on the fork closest to the eventual fiber position. Empirically it has been found that having too much QSE on the double fork binder, specifically in between the forks can be disastrous and force you to rebind after you find that Q has been impacted too severely. Carefully place the binder onto the forks, using your eyes and the Cam to assure that the probe is perpendicular to the fork and reaches far enough past the casing to bind to the fiber later. Monitor the binder while it dries, making sure that it remains oriented correctly. If it should begin to shift, use a thin flexible material (like a stripped length of fiber optic cable) to adjust it back into position through small, gentle nudges. While the author finds this method provides a less robust probe in terms of AFM response under different imaging conditions, the binding is more mechanically stable, meaning that reapplication of a new fiber later will be easier.

Confirm Binding Viability. After the binding has dried, reorient the tuning fork into the normal configuration by adjusting the arm. Now [A] again. Both F and Q may decrease significantly after binding. Typical values after binding are changes in frequency of a couple thousand and a halving of the initial Q value, though sometimes the changes are much lower. [A] again, with changed I by +0.5 the first time and -0.5 the second time. Similar F and Q values should be obtained. If not, increase I until changes in I stop impacting F and Q, obeying all of the concerns relayed earlier regarding high I. The I at which your F/Q signals stop changing becomes the new operating current.

Fiber Placement

Fiber placement is the hardest component of the process, requiring steady hands and great care, as well as patience. Do not rush this step.

Preparing for Placement. First, compare the Q values in two positions of the recently or previously bound assembly. Some tuning forks are very sensitive to orientation and rotating the tuning fork 90 degrees off axis can change both F and Q by up to 20%. [A] both in the normal position, and then again with the forks parallel to the floor. Note any differences in signal. Leave the tuning fork in the parallel position, with the binder pointing directly towards the microscope objective. You should be able to focus straight down the binder and observe both its end and where it tacks with the uppermost fork. Once this range of focus is confirmed, obtain the clip arm assembly and z axis adjustable scissor lift. Position them on the microscope stage and remove all obstructions to movement in the area. Consider attaching the clip arm assembly to the lift with tape to avoid slippage during placement. Get comfortable manipulating the clip arm assembly and tighten/loosen joints as needed to obtain a firm but controllable tension when moving the clip arm. Make sure to have the fiber/tip you wish to bind available, fresh QSE on hand, and a fiber optic holder.

Fiber Handling. The fiber must be handled with care. Again, do not rush. Take the cleaved fiber end (not the tip) and feed it through the back side of the fiber holder until ~1 inch of fiber is sticking out on the tip end. Be very careful not to release either the holder or the fiber or else the fiber will slip all the way through and most likely your tip will be ruined. If at any time you suspect your tip has come in physical contact with anything, strongly consider throwing that tip away and starting with a new one. Not all tip contact damages the probe but most does, often at a scale not detectable under the optical microscope. Once the fiber has been back fed into the holder, tighten the holder grip (which should be on the side away from the tip). This assures that the fiber will not slip during manipulation and provides a degree of freedom for adjustment of the fiber position on the tip side of the holder. Next, place the fiber holder into one of the clips on the clip arm. This should be done slowly, with care. The clip should bite into one of the two rough surfaces on the holder, either the grip near the fiber end or the threads near the tip end. Try both and see which seems firmer and easier to manipulate for you. The author prefers the threaded end clipping better, but both have worked.

Fiber Positioning. By eye, use the clip arm to adjust the tip so that it is above the tuning fork and horizontally aligned. Position it so that it is about 1 inch above the casing, aligned in the direction of the tuning forks and a little off center. The tip, when looking straight down, should be at least 3 mm past the end of the tuning fork but no more than 6 mm past. Shorter than this, and it will be difficult to reach the slide surface. Longer probes have worked, but increasing the length/mass of the interacting fiber can make a probe unusable or very noisy/temperamental in AFM mode. Next you should lower the z lift until the fiber is just barely in contact with the casing (flush). The fiber should be near the center of mass for the tuning fork, but not quite touching the binding. Using the Cam and a second length of fiber optic cable, very gently nudge the fiber into contact with the binding. The binding should just barely be seen to move. During this adjustment use the light positive pressure against the casing to help control movement. Once you have positioned the fiber, the pressure against the casing must be high enough to hold the position. Any tension at all between the final fiber contact with the casing and the fiber contact with the binding will cause the probe to fail in testing. The fiber must rest naturally against the binding. Once you have positioned the fiber, carefully move away from the set-up. Do not bump or move anything.

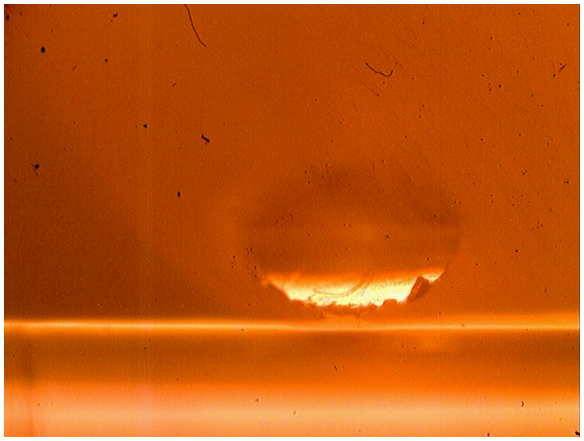

Binder Contact with Probe

Under high resolution, the contact between the binder (here a stripped F-SF fiber) and the fiber tip. View shows edge of fiber on bottom with the end of the binder visible in cross section.

Probe Testing. It is now time to test the probe's behavior with fiber-binding contact. First, minimize all disturbances in the room, including all pumps and music. Then [A]. It is critical while the software tests Q that you not move around, make noise, type or do anything which might compromise the adjustment. With the fiber touching the binding and the microscope hood up it is necessary that you take these extra steps or you will get a false probe failure signal. Four possible outcomes will result from this adjustment:

(1) First, the probe may be a success. In this case, a nominal Q and F value will be obtained, both lower than the tuning fork with binding alone. If so, go to the next step.

(2) If the SW returns a "Q could not be determined" message, then you may be able to increase I as detailed earlier. If this works and drives the amplitude of vibration up to a point where Q and F can be determined and I is not too high, go to the next step.

(3) If a Q value is found, and it is the same as that observed in the bound tuning fork without fiber, then the fiber-binding contact is not sufficient or there is no contact at this point. Using the Cam, very gently adjust the fiber into the binding and [A] again. You may need to do this several times, or you may have to fully reposition the fiber in order to get good fiber-binding contact which allows for the fiber to be felt by the SW.

(4) Last, the SW may return a "Probe unusable" message. This indicates that your contact with the binding is way too tight or that the length/mass of the tip over-hang is too great. Either way, you will need to fully reposition the fiber.

If all attempts fail to bring about a good coupling between binding and tip, there is one last option you may choose to try. This involves putting a very small amount of QSE on the fiber and just bringing it close enough for the surface tension to cause the QSE to span the gap. This QSE bridge will shrink as it hardens, making a very fragile binding which can be destroyed under almost any form of rough handling. However, once dried, this binding method has consistently worked (>75%). Drawbacks include a far shorter working life (you will break this probe eventually) and the fact that if it doesn't work then you are potentially out one fiber and/or binding.

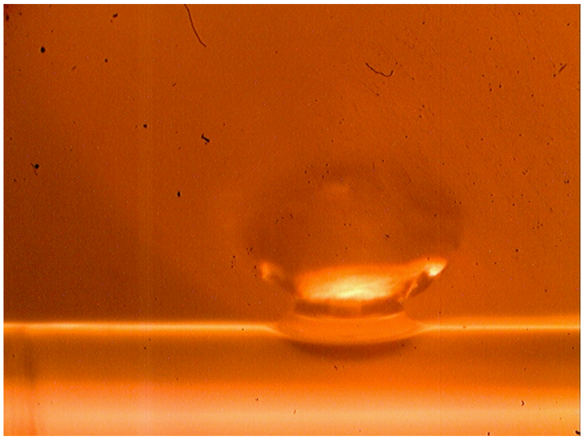

Binder-Tip Coupling Using QSE (High Magnification)

Displaying side of fiber (bottom), binding cross section (oval) and QSE (between).

Adhering the Fiber to the Assembly

The general adhesion regime is that an initial small tack will be placed so that further adhesives do not disturb the fiber placement. Then full tacking can occur. A supportive, less brittle adhesive will be placed over the bulk of the fiber-casing interface. The final adhesive will be a soft rubber which will prevent fiber dissociation during handling and storage.

Initial Bonding. Application of the initial adhesive is the most difficult component of this step. Take extra caution to avoid touching the fiber, clip arm, or the tip. Using an extremely thin applicator, like a 1/1000 inch diameter wire, obtain a small bead of QSE. Bring the bead over a central point of contact between the fiber and the casing. Bring the bead down slowly until contact is made with the top edge of the fiber. Do not lift the applicator straight up. Rather, move the applicator laterally, neither up-down nor in the direction of the fiber. This has the effect of unloading the bead of QSE such that it has minimal possibility of disrupting the fiber while still delivering the QSE for an initial bond. Allow this initial QSE to dry at least

5 minutes. Re-check [A] to confirm that the probe is still viable. Ideally, both F and Q will be the same as after fiber placement on the binding.

Reinforcing Bond. With the fiber tacked to the casing, larger quantities of QSE can be applied with minimal fear of disrupting the fiber. This can be done using a single drop off a toothpick or similar implement. Placement should be such that the drop falls on the fiber near the end of the housing but not in such a way as to get any on the upper parts of the tuning fork, which are situated directly below the lip of the casing. Typically, this will overlap the region where the initial bonding tack was placed. Allow 15 minutes to dry. Re-check [A] to confirm that the probe is still viable.

Intermediate Bonding. The TPE should be brought out and mixed, typically with a 1:1 ratio. The set time varies for different brands, so ensure you are aware of your usage window by referring to the packaging. Mix on a clean surface, using a small spatula or a hobby knife. When at first you note a change in viscosity/tackiness, immediately use a hobby knife to apply ~1 mm coating onto the fiber/casing region. Do not apply the TPE as close to the tip end as your QSE application. The final material the fiber touches before it travels to the binding should be strictly QSE, not TPE. This prevents the TPE from interacting with tip vibration. Towards the upper end of the casing TPE placement should only be placed up to 3 mm from the casing lip where the leads protrude. As directed by the product used, allow the TPE to dry/set. Re-check [A] to confirm that the probe is still viable.

Handling Protection. With the fiber adhered and coated over the majority of the casing, a cure-in-place silicone gasket material can be used to further protect the probe from damage during use. Without this rubber protection on the fiber end near the leads, the fiber will eventually snap at that point during usage. This occurs from gross bending near the TPE bonding and can happen during probe handling, in coupling (during NSOM operation) and during storage/retrieval. Squeeze a small amount of SGM onto a clean surface. With a clean hobby knife, apply the gasket material starting at the middle of the TPE coating and working towards the leads. Make sure that some of the SGM makes it between the fiber and the coupling near the edge of the casing where most fiber snaps occur. Residual SGM which creeps up the fiber is acceptable. SGM should not be applied on the tip end of the fiber/casing bond. Allow 1 hour to dry. Re-check [A] to confirm that the probe is still viable.

See earlier images for finished products appearance.

Final Probe Testing

Preparing for Inspection. Now that the probe is assembled, unscrew the fiber holder and slip the entire clip arm/fiber holder assembly off of the fiber. Clear any tools away from the work area as well as any other obstructions. Rotate the arm and probe so that the tip is pointing directly down (normal operating mode), remove the mount from the post and place it on the storage pedestal. Obtain a flat mica sheet and prepare the slide and the NSOM for normal operation.

Preliminary AFM Scan. Remount the probe and obtain contact mode as in normal operation, using the final I setting you have decided on. Note any changes in F or Q, which should be trivial. Scan 5 um x 5 um at 1 um/s : 5 um/s and 251 resolution. Note any drift in the sample height. Small increases in height from x- to x+ and larger increases in height from y- to y+ should be expected. Correcting for these is beyond the scope of this document. However, all drift should be linear for a given access. If it is, note your final probe operating conditions, label your probe, its spot in the probe holding case, and put the probe away for use. Observe the scan in 3D if needed. If asymmetry in the drift is obvious, this implies that the tip is not oscillating symmetrically.

Correcting Tip Orientation. If asymmetry is observed when scanning the flat mica sheet, park the probe and shut off the microscope. Remove the mount, arm and probe. Secure the mount in the clamp and loosen the screws which attach the assembly to the arm without removing them. Adjust the assembly so that the assembly rests as low on the arm as possible, within screw constraints. Observing only the tuning forks and the edge of the arm, note their relation to each other. If the forks are pointing forward from the mount, slide the front part of the assembly up until the forks are orthogonal to the arm. If the forks are pointing towards the mount, slide the back part of the assembly up until the forks are orthogonal to the arm. When doing this, make sure that the screw hole on the end you are not adjusting up remains flush with the screw. Once you are satisfied that the tuning forks are perpendicular to the arm, tighten screws, return to NSOM operation and scan again as detailed in the step above. Repeat until all drift, for a given axis, is linear. Once complete, note your final probe operating conditions, label your probe, its spot in the probe holding case, and put the probe away for use.

Fiber Tip Manufacturing

Fiber Selection. NSOM must be done with single mode fiber optics, preferably with the smallest possible thickness of coating, with fibers that do not fluoresce, introduce nonlinearities, absorb or heat appreciably under the excitation regime to be used. The length of cable from coupling point to sample is short enough to justify avoiding the use of polarization maintaining fibers. At first glance it may seem like a good idea to use these, however the construction method of these fibers lead to a bifurcated probe after pulling. This is due to the irregular distributions of refractive index in these types of fibers. Additionally, the de-phasing which occurs in a fiber optic cable over the operating length (~45 cm) is only nominally higher than that of air over the same distance. Specifically, I have worked with the F-SF Newport single mode fiber the most, as it conveys 800 nm to 830 nm well and is still functional out at longer wavelengths where a parametric amplifier may be used. If visible wavelength imaging is needed, one might consider using the F-SA or F-SV models, optimized for 488 nm and 633 nm respectively. Also, since attenuation, heat and emission are all possible side effects, I recommend that visible excitation NSOM use only a CW source of low intensity unless pulsed excitation is needed. Preliminary attempts to use a second harmonic generating crystal (BBO) to use fs pulsed light for one photon NSOM resulted in a 1-2 hour operating lifetime for the probe. The core, cladding and coating diameter specifications for the F-SF fibers are 5.6 um, 125 um and 250 um respectively

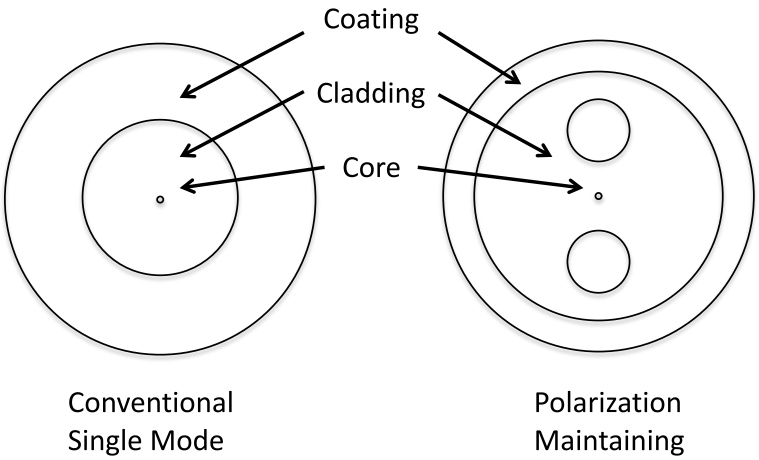

Standard and Polarization Maintaining Fiber Cross Sections

The conventional fiber (right) and the polarization maintaining fiber (left). Note that the polarization maintaining fiber has two parallel regions in the cladding on either side of the core. These have different refractive indices and material properties which contribute to asymmetric tips when pulled.

Sutter P-2000 Micropipette Puller Operation. The micropipette puller is where you will pull your fibers into tips. It is a multiuser instrument, and this means that the system can often behave very different between uses. It will be important to know how to adjust the programming as needed to generate serviceable tips each usage. The program structure is such that each program can have up to eight cycles. For fiber pulling, only the first line of the program will be used, e.g. one cycle. The parameters for each cycle is as follows:

Heat:	Setting range:	0 – 999
	This gives the output power for the CO_2 laser. Changes should be made in at least 10 unit jumps as single digit changes are virtually meaningless. This setting has the highest impact on tip diameter. Suggested: 300	
Filament	Setting range:	0 – 15
	This gives the raster scan length for the beam. Only a setting of 0 should be considered for fiber pulling. Suggested: 0	
Velocity	Setting range:	0 – 255
	This is the velocity of pull under constant strain the puller looks for before initiating the heat turn off. The heat turn off point in	

	conjunction with the delay dictate when hard pull is initiated. This setting impacts tip diameter almost as much as the heat setting. Suggested: 16
Pull	Setting range: 0-255 This dictates the force of the hard pull. Less sensitive than the velocity value, adjust pull in units of 10. Greater force leads to cleaner, less asymmetric pulls. However, too high a setting will potentially snap underheated fibers. Suggested: 175
Delay	Setting range: 0-255 Delay dictates the time between the heat turning off and the hard pull. The setting for both occurring at the same time is 128. Adjust this setting only one at a time, it is extremely sensitive to change. Never have a value >127. In other words, heating must still be on when the hard pull initiates. Suggested: 126

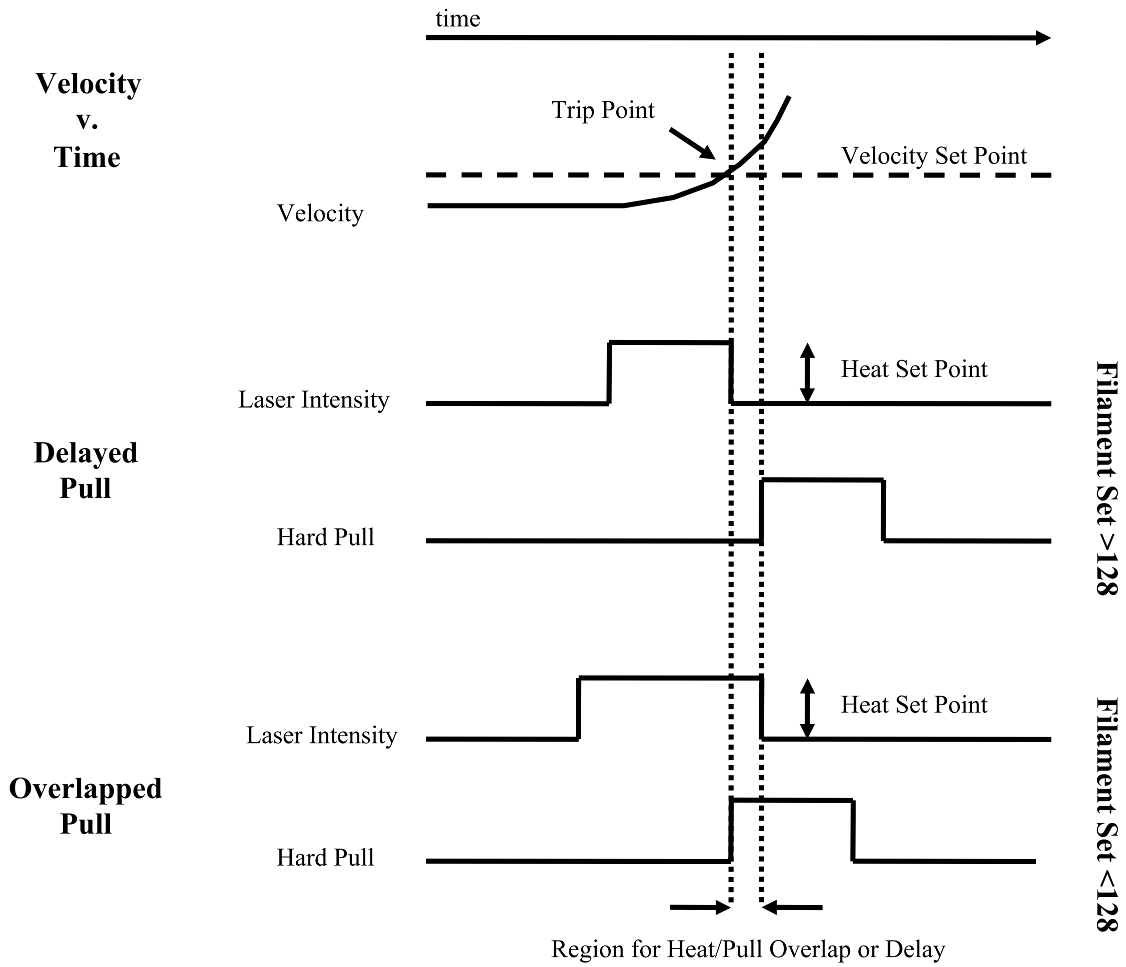

Fiber Pulling for Different Filament Setpoints

Displaying depiction of fiber velocity, a delayed pull and overlapped pull with time.

Pulling Strategies and Methods. Because the instrument is multiuser, it can be difficult to reproduce the results obtained on different days. Therefore the author suggests strongly that when pulling fibers you make a day of it. This means checking with the puller owning lab for a several hour block. Be prepared with 20 premeasured fibers of length 90 cm which have had the center 3 cm stripped of coating with the coating stripper tool. Do not touch the stripped region with your hands or any other solvent/oil containing surface. Use optical glass paper and only a small drop of pure methanol to clean the 3 cm region and remove any particles left by the stripping process. Also bring 20 premeasured 20 cm fibers with similar sections of coating removed and prepped at center of mass on the fiber. The 20 cm fibers will be used to find the settings which will be used to generate fibers of longer length (e.g. these short tips are just for calibration). Using the set points suggested above, pull short fibers and examine them under a sample prep microscope nearby. At high magnification, you will still only be able to look for four indicators of probe viability:

Crazing:	This is obvious cracks in the cladding near the tip, and indicates that a slower pull or higher heat is needed.
Asymmetry:	This is different taper angles on each side of the tip. It indicates that the beam is off center. If it happens every pull look to the P-2000 manual or get help centering the beam (vertical is the only adjustment that will be needed). Alternately, by changing the filament setting to 1 you can make the beam raster area larger, which may work if the asymmetry is small.
Streamers:	This is when the core gets too liquid at hard pull. They can be observed as small wisps at the end of the tip. Under these circumstances, reduced heat, adjusting delay back closer to 128 or a harder pull can all help.
Taper angle:	Typically you can tell by eye how sharp the taper is in regards to appropriate aperture size. Through practice the author has determined that tapers from 10 degrees out to 25 degrees have all generated functioning probes. Taper will adjust for all settings. Mostly you want to make sure that it is smooth and has no sudden changes in geometry. Heat, filament and pull all effect this aspect.

Also note any differences in the right and left tips generated from each pull. The author suspects that the timing or force may be a bit different on the left and right sides, leading to geometry differences between tips generated in the same pull. A method which generates a good tip on one side and a bad one on the other is very close to making two good tips. Under these circumstances, just keep adjusting the system until this happens.

Other difficulties include obvious scorching and harsh breaks where no pulling occurs. Scorching means that the fiber was not clean or that the fiber was not centered, resulting in the coating being too close to the focal point. Harsh breaks are due to either improper seating in the fiber holder or a severely misaligned laser. The author has also seen instances of some pulling with a jagged end. If the pull started well but turned ugly, this means that the system is far out of alignment, generating enough heat to eventually trigger a pull, but not actually heating the entire cross section in its entirety. The system may require a full realignment, which the P-2000 manual provides for.

Final Tip Characterization Before Coupling. The easiest way to do this is to return to the NSOM and use the high power objective to inspect your probes. Once a tip is in focus, go to the coupling end, strip 5 cm of coating and look at the fiber end under the jewelers lens. Sometimes the end will appear to have been cleaved flush, which is great. Most of the time you will need to take a hobby knife and try cleaving it flush yourself. This will take 5-10 tries usually, so try to take off as little as possible with each cut. Small irregularities at the very edge of the cladding are okay, as long as the rest of the cut provides a close to perfect cross section.

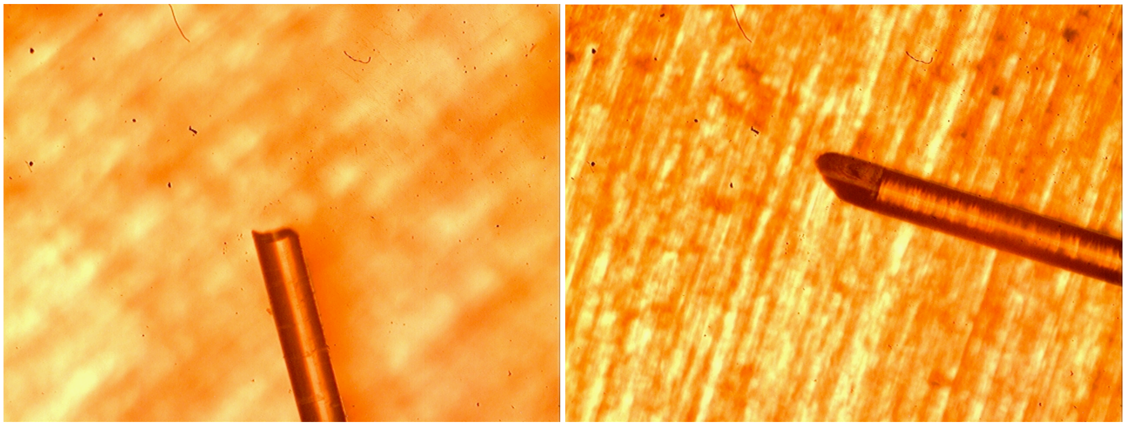

A Good (Left) and Poor (Right) Example of Cleaving

Next, place the cleaved end in the fiber chuck and couple low powered but visible Mai-Tai light into the fiber (suggest 0.1 – 1.0 mW of 700 nm light). Place a white piece of paper ~ 1 mm from the tip, being extremely careful not to contact the tip. Observe the pattern on the paper. If it is localized and symmetric with a low amount of far field defraction rings, then the tip is good. If you see a gross amount of light coming from the fiber as you view it from the side, then continue to align coupling until bleed is minimized. If it continues to produce large bleed, this implies that there is core damage internally from pulling. Do not use this probe.

Final Probe Characterization. Assuming a good tip was used to make a functioning AFM probe, the NSOM probe aperture should be characterized with the particle emission technique [1] and two studies published using probes assembled as above are also available [2-3]

Final Notes

A few final notes on this process should include a reiteration of several things stated earlier. Firstly, never touch your tip or your tuning fork. Nothing good will come of it. Secondly, use the NSOM documentation and P-2000 documentation in conjunction with any operation concerning either. Thirdly, the methods and materials outlined here are simply the best the author has been able to configure based on extended exposure to NSOM imaging. Lastly, this technique includes many terms which have a broad context in common usage. Please make sure to refer to the initial definition of terms outlined in the beginning of the text.

References

(1) Kim, J.; Kim, D.C.; Nakajima, K.; Mitsui, T.; Aoki, H. J. Korean Phys. Soc. 2010, 56, 1748-1753
(2) Raymond, J.E.; Goodson, T. Proc. SPIE 2009, 7413, 1-14
(3) Raymond, J.E.; Goodson, T. J. Phys. Chem. Lett., 2011, 2, 329-333

Appendix C

Application of Organic Nonlinear Optical Materials

Outlined below examples of various motivations for the investigation of self assembled organic nonlinear optical materials.

Green Chemistry. The investigation of ensemble effects of any material property has green chemistry overtones. This is a relatively mundane but important consideration: can a material give you more response per molecule without additional chemistry or solvents? Aggregate and 'click' chemistry type self assembly are two typical strategies for investigating the capabilities of a molecule without resorting to synthetic techniques which consume additional energy, use additional resources or generate additional waste.

In Situ Imaging. *In situ* imaging applications where near infrared light (NIR) can be used to excite two photon labels and probes. The two photon cross-section (TPACS, also denoted as σ_2 or δ_2) as well as the fluorescence quantum yield (Φ_F) and peak emission wavelength are all extremely sensitive to changes in environment. The NIR excitation of most two photon processes means that deep tissue imaging is possible as the human body has a transmission window in this region. It stands that any enhancement in the two photon emission properties will benefit both diagnostic and research capabilities by decreasing the overall amount of two photon material needed. This decreases the likelihood of the probe changing the system studied in a fashion that makes results more ambiguous. It should also be noted that the absolute limit of spatial resolution for two photon imaging is inherently higher than one photon imaging by a factor of two.

Remote Sensing. The same properties which make a two photon material appropriate for *in situ* biological imaging are also sought in remote photo responsive sensor arrays. Just like biological systems, there is an atmospheric ‘window’ in the NIR region. The exceptional responsiveness of two photon materials to changes in environmental conditions make them ideal for applications like ion detection and biomacromolecule detection in ambient conditions.

General Replacement of Si Materials. The current state of the somewhat aged Si semiconductor industry is such that it still requires huge amounts of energy to generate ultrapure Si wafers. Mining operations of electronics grade quartz remain extremely costly, both financially and environmentally. Also the most recent years of computational advancement have been characterized by enhanced parallel processor design without truly innovative advances in materials at a mass production scale. This is in addition to the unsolved problem of recycling electronics from the current regime safely and cost effectively. All of these lead to a push to generate organic materials capable of shouldering some of this growing burden by either enhancing current Si technologies beyond the current status quo, replacing technologies completely or surpassing current capabilities through photoelectronics possible in organic materials.

Optical Switching Applications. For some time now field effect transistors have been the standard for computation. However, the operating rate at which an individual component can be switched has placed considerable focus on constructing better computational arrays and less on materials development. As the Si semiconductor switching limits come closer to being reached, it may be necessary to transition to optical switching (where ‘on’ and ‘off’ are modulated by excitation of an electron to a conduction band). While semiconductor and carbon nanotube research show much potential, another avenue is single molecule transduction in which an organic macromolecular system provides the switching. A two photon photoswitching response adds further to the viability of a material as the density of gates can then approach the limits of two photon resolution, which as stated earlier, is twice as high as single photon processes.

Organic Photovoltaics. While the cost of inorganic solar materials has dropped dramatically in recent years, there is still a need for inexpensive and high volume solar materials. Organics, either as hybrid or pure, offer an alternative to conventional solar cells in several ways. First, the raw material is often significantly less expensive per kg. Second, any material that is sprayable, conformal or paintable will find usage (even if low efficiency) in next generation green building materials. Lastly, organic photovoltaics will come with significant cost benefits in terms of infrastructure: ease of processing, better recycling streams, higher portability, etc. While this is not a two photon absorption application, other nonlinear optical processes like excited state absorption (ESA) often play a role in enhanced photon collection and charge transport.

Optical Limiting. Optical limiting as a field of study is concerned with gross reduction of flux in a media when high intensities are present, often through any means necessary. The goal in most optical limiting applications is the reduction of photon throughput to a level that will not damage another device which the optical limiter has been designed to protect. The typical method by which this is achieved is through a combination of nonlinear optical processes, but is often dominated by TPA and/or ESA response in the material. Typical material/equipment protected by optical limiting include: satellites, telescopes, CCD cameras, human eyes, solar panels, sensor arrays and remote detectors. At the end of this chapter, a detailed discussion of how optical limiters can prevent damage from pulsed laser sources will be made with a special focus on the exceptional capabilities of materials studied in this work.

Practical Application of Organic NLO Materials: Optical Limiting

Discussion of the nonlinear optical properties of a material can seem a bit arbitrary, especially when material response is reported per molecule. Below, the TPA properties of several materials found in later chapters of this book will be outlined and the optical limiting capabilities of these systems will be provided in terms of the two photon responsiveness. The theoretical constraints for this discussion follow.

Transmission can be determined from the following equations given that all effects except two photon absorption can be neglected:

$$T = \frac{I}{I_0} = \frac{1}{1 + LI_0\beta} \quad \text{(I.)}$$

$$\beta = \frac{\sigma_2}{hv} N \quad \text{(II.)}$$

$$N = \frac{\rho}{M} N_A \quad \text{(III.)}$$

$$T = \frac{1}{1 + LI_0 \frac{\sigma_2}{hv} \frac{\rho}{M} N_A} \quad \text{(IV.)}$$

The variables are defined as: I, final intensity; I_0, initial intensity; L, thickness; β, bulk material TPACS; σ_2, molecular TPACS; hv, energy of single photon; N, number density; ρ, mass density; M, molecular weight; N_A, Avogadro's Number.

TPA materials are a special breed of optical limiting systems in that they are most effective against pulsed, focused excitation sources where maximum intensities can exceed terawatts per cubic centimeter. In effect they are particularly capable of limiting the throughput of a series of extremely high energy events, which also includes very bright "one-off" events like explosions. This stands in contrast to other optical limiting systems such as reverse saturable absorption and holographic liquid crystal systems, both of which are more appropriate for megawatt and lower continuous wave excitation sources.

A set of standards the author encountered while working with the optical limiting group at the Air Force Research Laboratory for assessing two photon materials in optical limiting roles concerned two scenarios: present field laser technology and anticipated field laser technology. Specifically, there is an active Department of Defense interest in being able to laser harden instrumentation and eyewear so that targeted pulsed laser systems will not be harmful to them. The present state of the art for laser systems which can be used in the field to provide high power fs pulsed light are all-in-one sealed box turn key systems which are currently commercially available. For the purpose of this discussion we will use a pulse duration of 100 fs and an operating rate of 80KHz (80,000 pulses per second). A typical maximum output of this type of system is an average of 3 Watts incident power. For this scenario, it is also important to have a realistic assessment of mass production capabilities at the current time. This will almost certainly involve some type of polymer film, doped with the TPA material. The assumption we will make for this discussion is a loading of 1% by unit volume. For consideration of future need one could consider an over either an overall power increase, a decrease in repetition rate (i.e. increased amplification) or a decrease in pulse duration, all of which result in over all increase in the maximum incident power. As an overall power increase and a decrease in pulse duration are both significantly harder (to accomplish in a technical sense) in the authors opinion, we will presume that next generation turn key systems will include an amplifier similar to those commercially available now and that a repetition rate of 1000 Hz will be incident on the materials. However when anticipating a lasing capability increase, one should also assume a materials processing capability increase. In that vein, an assumption of a neat film will be made.

Hence we will consider transmission under these two conditions;

1. Current Needs: 80,000 Hz 3W laser, 100 fs pulses, 1mm 1% loaded polymer film
2. Future Needs: 1,000 Hz 3W laser, 100 fs pulses, 1mm neat film

The results of these calculations are present in the following table and figure.

Optical Limiting in Two Photon Active Organic Films

Sample	Measurement		TPACS (GM)	Beta (cm/W)	1 KHz, Neat Film		80 KHz, 1% in PS		% Increase in Beta
	TPEF	NSOM			Max Fluence (W)	Limiting Onset (W)	Max Fluence (W)	Limiting Onset (W)	
D-pi-A LC	x		90	5.88E-09	1.92E-10	3.48E-09	1.54E-06	2.84E-05	-
LC 250 nm Rods	x	x	100	6.53E-09	1.80E-10	3.28E-09	1.43E-06	2.69E-05	107.69%
LC 60 nm Rods	x	x	420	2.74E-08	4.58E-11	8.57E-10	3.67E-07	6.96E-06	419.62%
Fl. Porph. Dimer	x		570	9.43E-09	1.22E-10	2.53E-09	1.07E-06	2.10E-05	-
Fl. Porph. NP		x	2,800	4.63E-08	2.71E-11	5.65E-10	2.17E-07	3.77E-06	493.09%
Fl. 11-mer Ring	x		410,000	6.15E-07	2.04E-12	4.34E-11	1.63E-08	3.28E-07	6564.42%
Fl. 19-mer Ring	x		1,000,000	8.72E-07	1.44E-12	2.75E-11	1.15E-08	2.12E-07	9304.35%
C. Porph. Dimer	x		720	1.18E-08	1.06E-10	1.80E-09	8.50E-07	1.43E-05	-
C. 4-mer Ring	x		28,700	1.18E-07	1.06E-11	1.82E-10	8.52E-08	1.75E-06	997.65%
*RhB PS NP**	x	x	660,000,000	2.42E-10	5.19E-09	1.06E-07	4.15E-07	8.67E-06	-

* RhB PS NP: As the standard, and being already doped in polystyrene, the 80 KHz results are using the same number density as the 1KHz results.

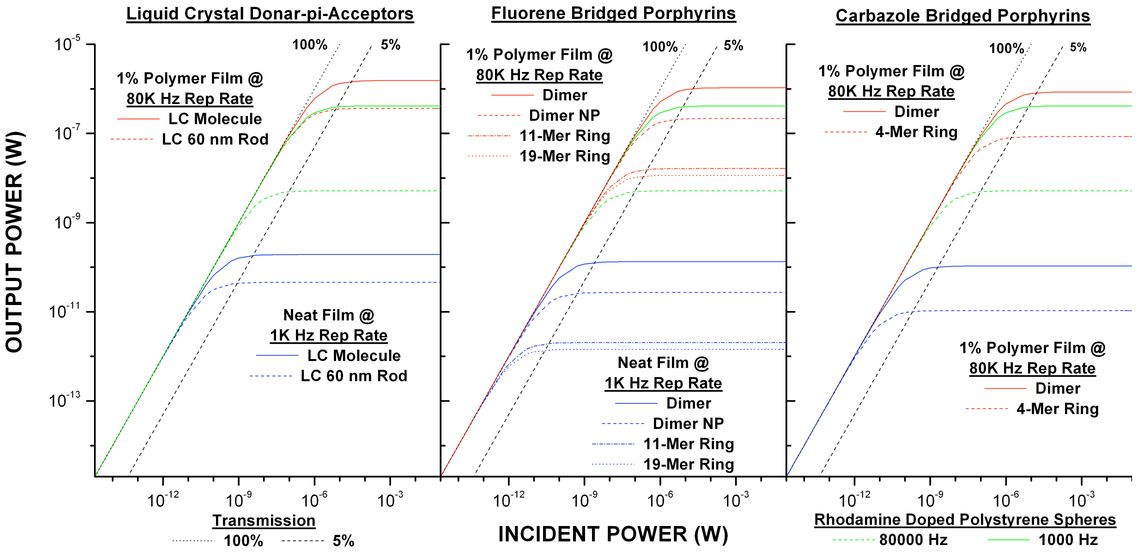

Output Power of Organic Films Under Different Excitation and Manufacturing Regimes

All neat films at 1000 Hz reported in blue, all 1% polymer films in red, and the standards are reported in green. Both 100% and 5% transmission rates are shown in black, and the 5% transmission should be taken as the point of optical limiting onset. The first panel presents the liquid crystal system, the second panel shows the fluorine bridged porphyrin system, while the third panel shows the carbazole bridged porphyrin system.

The three categories of material under consideration are the liquid crystal chromophores in chapter 2 and the subsequent nanorods produced by self assembly, the fluorine bridged porphyrin dimer and rings presented in chapters 3 and 6 and the carbazole bridged dimer and ring system presented in chapter 7. In addition to this a standard developed for TPA NSOM, Rhodamine B impregnated polystyrene nanospheres, are included under both conditions for reference. It should be noted that the loading potential for these spheres is already known, so a 1% sample was not considered for the current day 80 KHz calculations and that the neat film was also assumed there.

The table outlines the final findings and detail the laboratory methods used to determine the response of each system, beta values, % beta increase through self assembly, maximum fluence, and when the onset of strong optical limiting begins. While the more than an order of magnitude increase in optical limiting power in the liquid crystal rods and carbazole porphyrin tetramers (figure 1-1, panels 1 and 3) is significant, the absolute response of the 19-mer macrocycle is extremely telling. The 19-mer macrocycle was, at the time of publication, the highest TPACS single molecule to have been reported. This shows markedly in the power cut off abilities of the system, almost 100 times enhanced over a similar number of units in the lone chromophore system. Considering the neat film, it can be seen that optical limiting occurs such that no more than ~1 pW will get through the 1 mm film, even with intensities of 3 W. This means that for a 3 W system, fully operating on a target instrument, the maximum throughput is 12 orders of magnitude less than the incident flux. As this is a pulsed system though, really one must consider the maximum flux during the pulse, which is much higher than the average flux. Specifically, the maximum flux of the next generation amplified field laser considered here would be ~3 GW/cm^{-2} during a pulse under the operating conditions specified. However, the incident power that would be felt by any instrument protected by a 1 mm film of the 19-mer ring would be only 10 mW. This is with incident maximum intensities of less than 10 mW being roughly felt at 100%. In fact, as long as pulse width remained the same, no change in repetition rate or average power will generate more than 10 mW of incident power on the instrument at any time. This degree of optical limiting is a tremendous achievement for a 1 mm film and displays how critical it is to use ensemble effects to optimize a chromophores TPA response in order to get the absolute highest degree of response.